12.815 Atmospheric radiation and convection

December 8, 2015

Pr Sara Seager and Pr Kerry Emanuel

Notes written by Tom Beucler

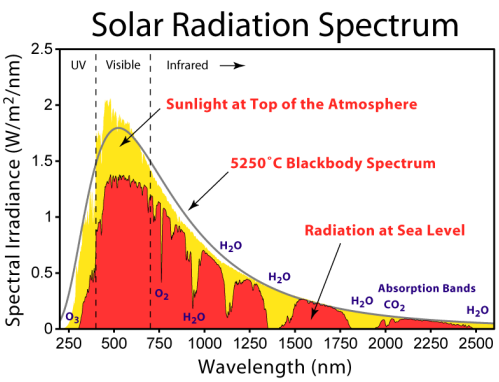

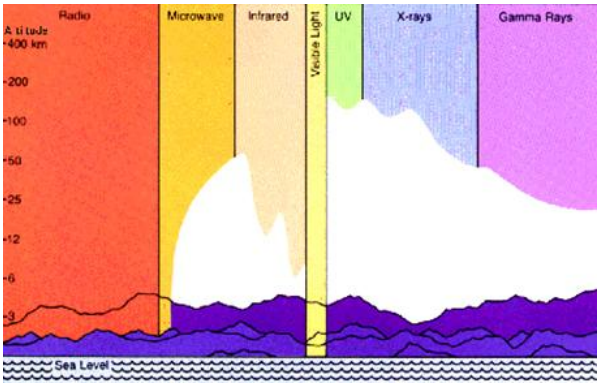

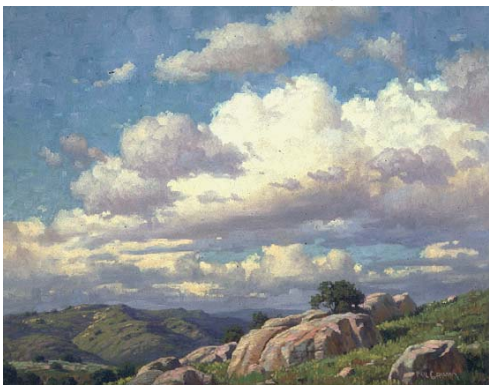

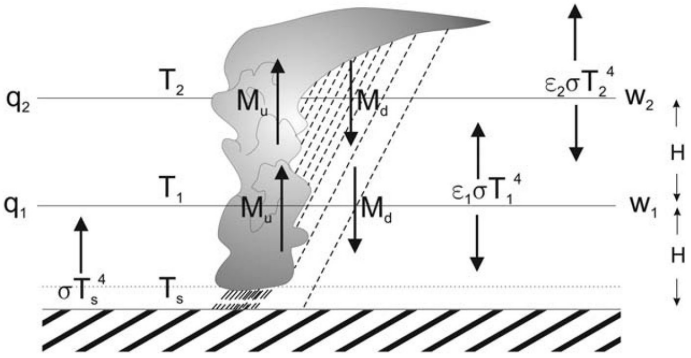

Contents

Notations, glossary and conventions

Vectors are denoted by upper right arrows (eg $\overrightarrow{X}$) and matrices by a bold font (eg $\boldsymbol{M}$).

Symbol	Description	Units	Cross-reference
A	Area	m^2	2.2
a_p	Planetary albedo	1	1.2
A_ν	Absorptance	1	10.4.2
b	Buoyancy	$\mathrm{m.s}^{-2}$	4.3
B	Rotational constant in energy units	J	7.4
B_λ	Planck function in wavelength	$\mathrm{W.m}^{-2}.\mu\mathrm{m}^{-1}.\mathrm{sr}^{-1}$	2.5
B_ν	Planck function in frequency	$\mathrm{W.m}^{-2}.\mathrm{Hz}^{-1}.\mathrm{sr}^{-1}$	2.5
c	Speed of light	$\mathrm{m.s}^{-1}$	2.3
c_l	Specific heat capacity of liquid water	$\mathrm{J.kg}^{-1}.\mathrm{K}^{-1}$	8.2
c'_p	Specific heat capacity of moist air at constant pressure	$\mathrm{J.kg}^{-1}.\mathrm{K}^{-1}$	8.2
c_{p_d}	Specific heat capacity of dry air at constant pressure	$\mathrm{J.kg}^{-1}.\mathrm{K}^{-1}$	4.3
c_{p_v}	Specific heat capacity of water vapor at constant pressure	$\mathrm{J.kg}^{-1}.\mathrm{K}^{-1}$	8.2
c'_v	Specific heat capacity of moist air at constant volume	$\mathrm{J.kg}^{-1}.\mathrm{K}^{-1}$	8.2
c_{v_d}	Specific heat capacity of dry air at constant volume	$\mathrm{J.kg}^{-1}.\mathrm{K}^{-1}$	8.2
c_{v_v}	Specific heat capacity of water vapor at constant volume	$\mathrm{J.kg}^{-1}.\mathrm{K}^{-1}$	8.2
e	Partial pressure of water vapor	$\mathrm{N.m}^{-2} \equiv \mathrm{Pa}$	4.2
e^*	Saturated water vapor partial pressure	$\mathrm{N.m}^{-2} \equiv \mathrm{Pa}$	8.2
f	Normalized broadening function in frequency	Hz^{-1}	7.6
$\mathcal{F}$	Radiative flux	$\mathrm{W.m}^{-2}$	1.2
$\mathcal{F}_b$	Surface buoyancy flux	$\mathrm{W.kg}^{-1}$	6.2
$\mathcal{F}_{[\lambda_1,\lambda_2]}$	Broadband flux	$\mathrm{W.m}^{-2}.\mu\mathrm{m}^{-1}$	2.2
$\mathcal{F}_\lambda$	Monochromatic flux	$\mathrm{W.m}^{-2}.\mu\mathrm{m}^{-1}$	2.2
g	Gravity constant	$\mathrm{m.s}^{-2}$	4.1
g	Specific free enthalpy	$\mathrm{J.kg}^{-1} \equiv \mathrm{m}^2.\mathrm{s}^{-2}$	8.2
h	Planck's constant	$\mathrm{J.s} \equiv \mathrm{m}^2.\mathrm{kg.s}^{-1}$	2.5
h	Moist static energy (MSE)	$\mathrm{J.kg}^{-1} \equiv \mathrm{m}^2.\mathrm{s}^{-2}$	8.2
h^*	Saturated MSE	$\mathrm{J.kg}^{-1} \equiv \mathrm{m}^2.\mathrm{s}^{-2}$	11.2
h_d	Dry static energy (DSE)	$\mathrm{J.kg}^{-1} \equiv \mathrm{m}^2.\mathrm{s}^{-2}$	8.2
h_w	Liquid water enthalpy	$\mathrm{J.kg}^{-1} \equiv \mathrm{m}^2.\mathrm{s}^{-2}$	8.2
$\mathcal{H}$	Relative humidity	1	8.2
I_λ	Intensity in wavelengths units	$\mathrm{W.m}^{-2}.\mu\mathrm{m}^{-1}.\mathrm{sr}^{-1}$	2.2
I_ν	Intensity in frequency units	$\mathrm{W.m}^{-2}.\mathrm{Hz}^{-1}.\mathrm{sr}^{-1}$	2.3
j	Quantum rotational number	1	7.4
j_ν	Mass emission coefficient in frequency	$\mathrm{W.kg}^{-1}.\mathrm{Hz}^{-1}.\mathrm{sr}^{-1}$	2.3
J_λ	Mean intensity	$\mathrm{W.m}^{-2}.\mu\mathrm{m}^{-1}.\mathrm{sr}^{-1}$	2.2
k	Mass extinction cross section	$\mathrm{m}^2.\mathrm{kg}^{-1}$	2.3
k	Specific enthalpy	$\mathrm{J.kg}^{-1} \equiv \mathrm{m}^2.\mathrm{s}^{-2}$	4.3
$\overrightarrow{k}$	Vertical unit vector	1	2.2
k_B	Boltzmann constant	$\mathrm{J.K}^{-1}$	2.5
L_v	Latent heat of vaporization of water vapor	$\mathrm{J.kg}^{-1} \equiv \mathrm{m}^2.\mathrm{s}^{-2}$	8.2

M	Mass	kg	4.1
$\overline{m_d}$	Mean molecular weight of dry air	$\mathrm{kg.mol^{-1}}$	4.2
M_u	Convective updraft velocity	$\mathrm{m.s^{-1}}$	11.1
m_v	Molecular weight of water	$\mathrm{kg.mol^{-1}}$	4.2
n	Number density	$\mathrm{m^{-3}}$	3.1
$\overrightarrow{n}$	Normal unit vector	1	2.2
N	Buoyancy/Brunt-Vaisala frequency	$\mathrm{s^{-1}}$	5.3
p	Pressure	$\mathrm{N.m^{-2}} \equiv \mathrm{Pa}$	4.1
$\mathcal{P}$	Scattering phase function	1	9.2
$\overrightarrow{p}$	Electric dipole moment	C.m	7.3
p_d	Partial pressure of dry air	$\mathrm{N.m^{-2}} \equiv \mathrm{Pa}$	4.2
q	Specific humidity	1	8.2
q^*	Saturated specific humidity	1	8.2
$\dot{Q}$	Radiative heating rate per unit mass	$\mathrm{W.kg^{-1}}$	6.2
r	Mixing ratio of water vapor	1	4.2
R^*	Ideal gas constant	$\mathrm{J.K^{-1}.mol^{-1}}$	4.2
R'	Specific gas constant of moist air	$\mathrm{J.K^{-1}.kg^{-1}}$	8.2
R_d	Specific gas constant of dry air	$\mathrm{J.K^{-1}.kg^{-1}}$	4.2
r_l	Mixing ratio of liquid water	1	8.2
r_p	Planetary radius	m	1.2
r_T	Total mixing ratio of water	1	4.2
R_v	Specific gas constant of water vapor	$\mathrm{J.K^{-1}.kg^{-1}}$	8.2
s	Moist entropy	$\mathrm{J.K^{-1}.kg^{-1}}$	8.2
s	Path length	m	2.3
s^*	Saturated specific entropy	$\mathrm{J.kg^{-1}.K^{-1}}$	8.3
S_0	Solar constant	$\mathrm{W.m^{-2}}$	1.2
s_d	Dry specific entropy	$\mathrm{J.kg^{-1}.K^{-1}}$	1.4
t	Time	s	2.2
T	Absolute temperature	K	1.2
T_e	Effective emission temperature	K	1.2
T_v	Virtual temperature	K	4.2
T_ν	Transmittance	1	10.4.2
T_ρ	Density temperature	K	4.2
u	Zonal velocity	$\mathrm{m.s^{-1}}$	4.1
u	Path length of absorbing gases	$\mathrm{kg.m^{-2}}$	10.4.2
v	Meridional velocity	$\mathrm{m.s^{-1}}$	4.1
v	Quantum vibrational number	1	7.5
$\overrightarrow{v}$	Velocity field of the fluid	$\mathrm{m.s^{-1}}$	8.2
V	Volume	$\mathrm{m^3}$	4.1
w	Vertical velocity	$\mathrm{m.s^{-1}}$	4.1
x	Abscissa	m	4.1
x	Size parameter	1	9.2
y	Ordinate	m	4.1
z	Altitude	m	1.4
z_0	Roughness length	m	6.3
z_{0T}	Roughness thermal length	m	6.2

α	Specific volume	$\mathrm{m}^3.\mathrm{kg}^{-1}$	4.1
α_c	Specific volume of liquid water	$\mathrm{m}^3.\mathrm{kg}^{-1}$	4.2
α_d	Specific volume of dry air	$\mathrm{m}^3.\mathrm{kg}^{-1}$	4.2
Γ	Lapse rate	$\mathrm{K.m}^{-1}$	4.3
Γ_d	Dry adiabatic lapse rate	$\mathrm{K.m}^{-1}$	4.3
Γ_m	Moist adiabatic lapse rate	$\mathrm{K.m}^{-1}$	8.3
ϵ	Ratio of water vapor molecular weight to dry air's	1	4.2
ε_λ	Emissivity in wavelength	$\mathrm{W.m}^{-3}.\mu\mathrm{m}^{-1}.\mathrm{sr}^{-1}$	2.5
ε_ν	Emissivity in frequency	$\mathrm{W.m}^{-3}.\mathrm{Hz}^{-1}.\mathrm{sr}^{-1}$	2.5
θ	Zenith angle\Colatitude	rad	2.2
θ	Potential temperature	K	5.3
θ_e	Equivalent potential temperature	K	289
θ_lv	Liquid water virtual potential temperature	K	283
θ_ρ	Density potential temperature	K	8.2
κ	Absorptivity	m^{-1}	2.5
κ	Thermal diffusivity	$\mathrm{m}^2.\mathrm{s}^{-1}$	6.1
λ	Wavelength	μm	2.2
ν	Frequency	$\mathrm{s}^{-1} \equiv \mathrm{Hz}$	2.3
ν	Mechanical diffusivity	$\mathrm{m}^2.\mathrm{s}^{-1}$	6.1
$\tilde{\nu}$	Electromagnetic wavenumber	cm^{-1}	7.1
ρ	Density	$\mathrm{kg.m}^{-3}$	2.3
ρ_d	Density of dry air	$\mathrm{kg.m}^{-3}$	4.2
ρ_v	Density of water vapor	$\mathrm{kg.m}^{-3}$	4.2
σ	Stefan-Boltzmann constant	$\mathrm{W.m}^{-2}.\mathrm{K}^{-1}$	1.2
σ	Cross-section	m^2/molecule	7.6
τ	Optical depth	1	2.4
ϕ	Longitude	rad	2.2
φ	Passive tracer	Depends	6.3
Ω	Solid angle	sr	2.2
$\tilde{\omega}$	Single scattering albedo	1	9.2
$\overrightarrow{\Omega}$	Unit direction vector	1	9.2

Acronym	Definition	Cross-reference
CAPE	Convective Available Potential Energy	8.3
CIN	Convective Inhibition Energy	8.3
LCL	Lifted Condensation Level	8.3
LHF	Latent Heat Flux	11.2
LFC	Level Free Convection	8.3
LNB	Level Neutral Buoyancy	8.3
LW	Longwave	10.2
RCE	Radiative-Convective Equilibrium	1
RE	Radiative Equilibrium	1.2
SHF	Sensible heat flux	11.2
SW	Shortwave	10.2
TOA	Top Of the Atmosphere	1.2

1 Introduction

Radiative-convective equilibrium (RCE) is the simplest thermodynamic framework to describe planetary atmospheres, where the radiative cooling/heating is balanced by convective heating/cooling. It shows the importance of studying atmospheric radiation and convection together, in order to better understand atmospheric physics.

1.1 Basics of Earth's radiation

Looking at the composition of the Earth's atmosphere on 1, we see that Oxygen (O_2) and Nitrogen (N_2) constitute 99% of the dry atmospheric mass, whereas Carbon dioxide (CO_2), Argon (Ar) and the remaining gases only constitute a very small portion of it.

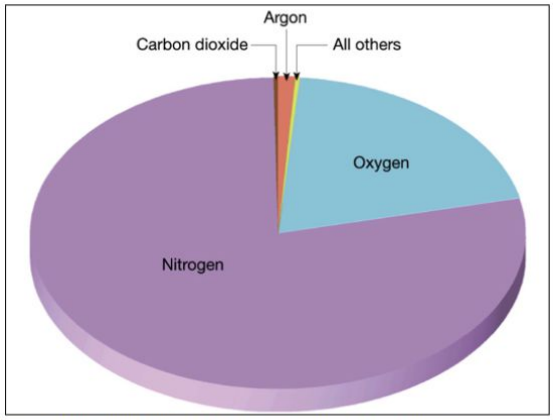

Table 1–2 Principal gases of dry air

Constituent	Percent by Volume	Concentration in Parts Per Million (PPM)
Nitrogen (N_2)	78.084	780,840.0
Oxygen (O_2)	20.946	209,460.0
Argon (Ar)	0.934	9,340.0
Carbon dioxide (CO_2)	0.036	360.0
Neon (Ne)	0.00182	18.2
Helium (He)	0.000524	5.24
Methane (CH_4)	0.00015	1.5
Krypton (Kr)	0.000114	1.14
Hydrogen (H_2)	0.00005	0.5

figure and table from Lutgens and Tarbuck, *The Atmosphere*, 8th edition)

Figure 1: Composition of Earth's atmosphere

The right part of figure 2 presents the Earth's mean energy budget:

- First, note that only half of the incoming solar radiation is absorbed by the surface; the rest is absorbed by the atmosphere or reflected.
- Then, we can see on the right part of the diagram that the surface gets more energy from the back radiation than the solar radiation: this is the greenhouse effect.
- Finally, the budget of energy would not close if we were to only look at the radiation part. Roughly one quarter of the energy emitted by the surface comes from convective surface fluxes. Most of it is latent heat (which means there is a net positive water vapor flux from the surface to the atmosphere), especially in the Tropics.
- In the end, we have a net balance of energy for the Earth's climatic system: there is as much energy coming out than coming in.

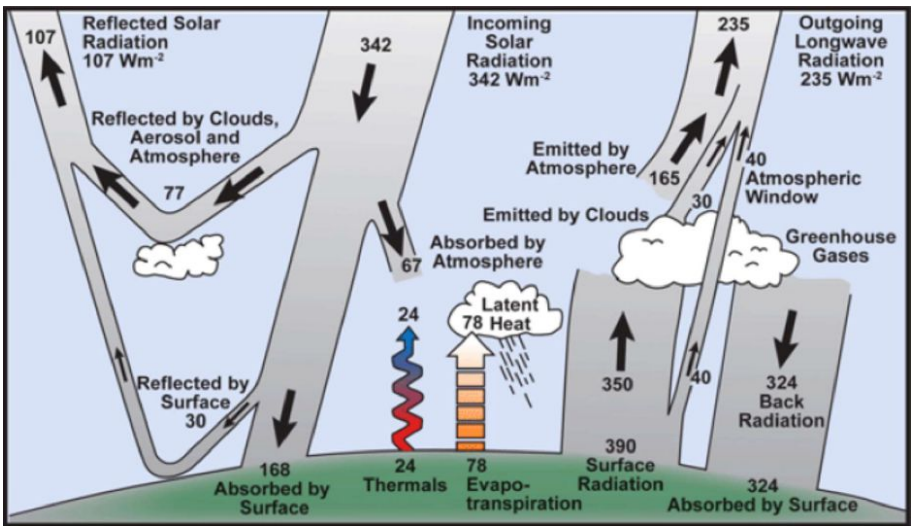

Figure 2: Earth's mean energy budget

We now look at the spectral distribution of the radiation transmitted by the atmosphere on 3. The smooth curves are the Planck functions for the Sun (red) and the Earth (purple, blue, and black depending on the latitude) if they are approximated as black bodies. We can see that the two spectra have almost no overlap, and we will approximate them as separate, and use the terms:

- Shortwave/solar radiation for the solar part of the spectrum.
- Longwave/terrestrial radiation for the terrestrial part of the spectrum.

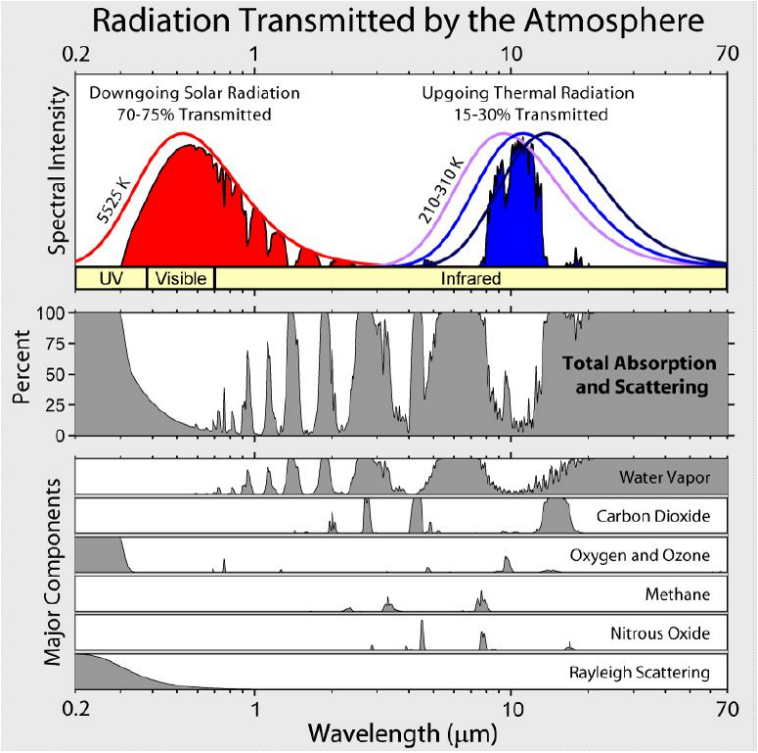

Figure 3: Radiation transmitted by the atmosphere

We can see that the most energetic part of the shortwave radiation (roughly the UV part) is absorbed by oxygen and scattered, and that some visible shortwave bands are absorbed by water vapor (which is important in the Tropics). The greenhouse gases, which absorb in the longwave part of the spectrum, comprise (in order of importance) water vapor (H_2O), carbon dioxide (CO_2), methane (CH_4) and Nitrous Oxide (N_2O). The visible band is the least absorbed band, which explains why our eyes have evolved to see in this band.

1.2 Radiative equilibrium

Radiative-equilibrium (RE) is the state the atmosphere and surface would reach in the absence of non-radiative enthalpy fluxes. It is a hypothetical state: the troposphere is never in RE, whereas the stratosphere is not that far from RE. The Stefan-Boltzmann law stipulates that if the radiation emitted by a black body is integrated over all the wavelengths, the flux of energy is given by:

$$\mathcal{F} = \sigma T^4 \tag{1}$$

where $\sigma = 5.67.10^{-8}\text{W.m}^{-2}.K^{-4}$ is the Stefan-Boltzmann constant. For instance, the solar radiative flux is equal to $\mathcal{F}_{\text{solar}} = 6.4.10^{7}\text{W.m}^{-2}$. According to Stefan-Boltzmann law 1, it corresponds to a surface temperature $T_{\text{solar}} \approx 6000\text{K}$. To model RE, we assume that a constant proportion a_p of the incoming total solar radiation is reflected back to space ($a_p \approx 30\%$ is by definition the Earth's albedo). As the Earth is a sphere of radius r_p, its cross section is πr_p^2, and the total absorbed solar radiation is $S_0(1-a_p)\pi r_p^2$ where $S_0 \approx 1360\text{W.m}^{-2}$ is the solar constant. As the total surface area of the Earth is $4\pi r_p^2$, the absorption per unit area is approximately given by:

$$\frac{S_0}{4}(1-a_p) \approx 240\text{W.m}^{-2} \tag{2}$$

Most of this absorption is done by the surface, but clouds also play an important role in absorbing the solar radiation. If the Earth didn't have an atmosphere, it would need to emit back the same radiative energy per unit area. If in addition it was a black body, we

could obtain its temperature through Stefan-Boltzmann law 1:

$$\sigma T_e^4 = \frac{S_0}{4}(1 - a_p) \;\Rightarrow\; T_e \approx 255K \approx -18^{\circ}C \tag{3}$$

The previous equation 3 defines the effective emission temperature T_e. This temperature is too cold compared to the observed average surface temperature $T_{\text{obs}} \approx 288\text{K} \approx 15^{\circ}C$ because we have neglected the greenhouse effect. As a first attempt to model the greenhouse effect, we assume that:

- The atmosphere is a single layer of gas.
- It is transparent to shortwave radiation.
- It is opaque to longwave radiation.
- In the longwave domain, the surface and the atmosphere emit radiation like black bodies.

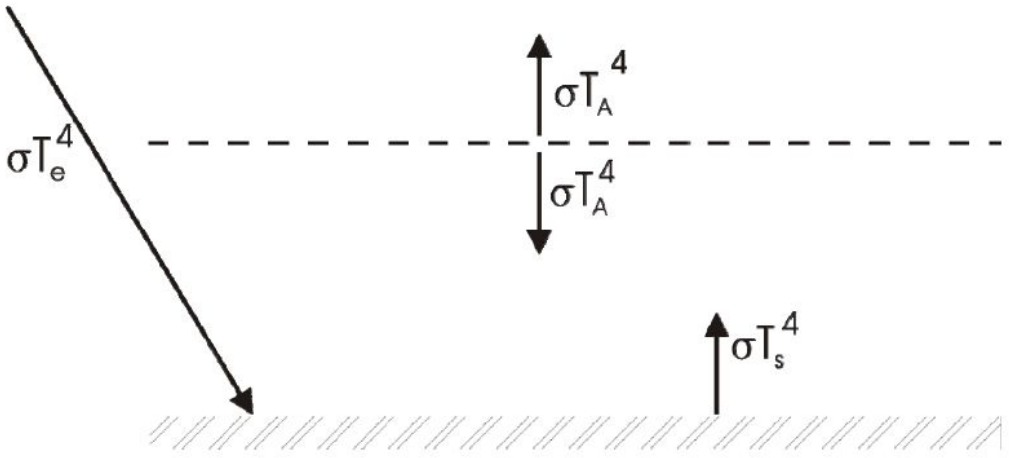

Figure 4: Schematic of the highly idealized RE model

To compute the temperature T_A of the atmosphere and the temperature T_S of the surface, we use:

- The Top Of the Atmosphere (TOA) energy balance:

$$\sigma T_A^4 = \frac{S_0}{4}(1 - a_p) = \sigma T_e^4 \;\Rightarrow\; \boxed{T_A = T_e}$$

- The surface energy balance:

$$\sigma T_S^4 = \sigma T_A^4 + \frac{S_0}{4}(1 - a_p) = 2\sigma T_e^4 \;\Rightarrow\; \boxed{T_S = 2^{\frac{1}{4}} T_e} \approx 303K$$

In this model, the surface temperature is higher than both the atmospheric and the effective emission temperatures because the radiative cooling of the Earth has to compensate for the incoming solar radiation and the heat emission from the atmosphere. The surface temperature T_S is now too large compared to the observed temperature $T_{\text{obs}} \approx 288\text{K}$, for several reasons:

- The model is so highly simplified that we didn't expect to match the observations.
- The Earth's surface does not only loose heat through radiative heat transfer, but also through convection.

1.3 Greenhouse gases

Fourier was the first to realize that something was missing in the Earth's radiative budget, but historically, Tyndall was the first to understand quantitatively what a greenhouse gas was. His experimental setting, depicted in figure 5, allowed him to test how much radiation a given gas absorbed. He showed that the main constituents of the atmosphere, ie Oxygen and Nitrogen, are actually transparent to solar and terrestrial radiation. Thus, if the Earth was only constituted of these two gases, its surface temperature would be the effective emission temperature $T_e \approx 255\text{K} \approx 0\text{F}$.

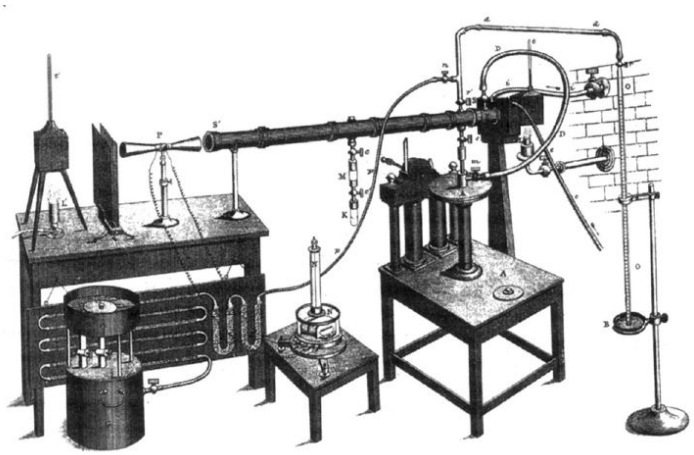

Figure 5: Tyndall's experimental setting

. It was by studying water vapor, carbon dioxide, methane... that he realized that a tiny fraction of the atmospheric mass ($< 1\%$) was entirely responsible for the greenhouse effect. This difference in radiative behavior is due to the structure of the molecules: O_2 and N_2 are diatomic whereas H_2O, CO_2 and CH_4 are triatomic and have more vibrational and rotational degrees of freedom, as depicted on figure 6.

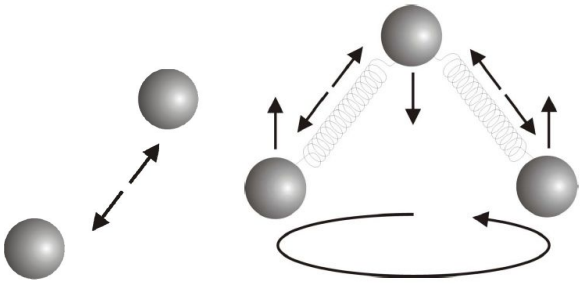

Figure 6: Schematic of a diatomic (left) and a triatomic (right) molecule's degrees of freedom

Clouds (especially low clouds) are also partly responsible for the greenhouse effect.

1.4 From RE to RCE

On figure 10, a full numerical calculation of the annual mean temperature profile in RE is represented in blue. It assumes a greenhouse gas profile that does not vary with time, except for the water vapor profile. The latter is prescribed by assuming a constant relative humidity $\mathcal{H}$, which is approximately the ratio of the water vapor density to its saturation value. We see that the atmospheric temperature in RE decreases sharply near the surface, and then increases more slowly above the tropopause, which is completely unrealistic for the troposphere but acceptable for the stratosphere. The temperature's discontinuity near the surface comes from the discontinuity of emissivity between the surface (1) and the atmosphere (small emissivity). This unrealistic feature motivates the introduction of convection in our model. Convection refers to the fluid motion originating from variations in the fluid's density and the presence of a gravity field. More crudely, because of the buoyancy force, hot air rises and cold air sinks, as shown on figure 7.

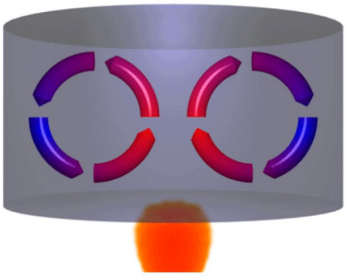

Figure 7: Schematic of two convective cells

The fact that the atmosphere is convecting simplifies its study, as molecular diffusion is negligible compared to convective processes. As convection is always more efficient than radiation in a non-dimensional sense, the atmosphere will always be close to a state of convective neutrality rather than in RE. A good example is the fact that boiling water never goes above the evaporation's temperature of water because convection is so efficient at removing the warm water vapor from the boiling interface. We will prove later in the class that an atmosphere is convectively stable if its entropy profile is strictly increasing with altitude:

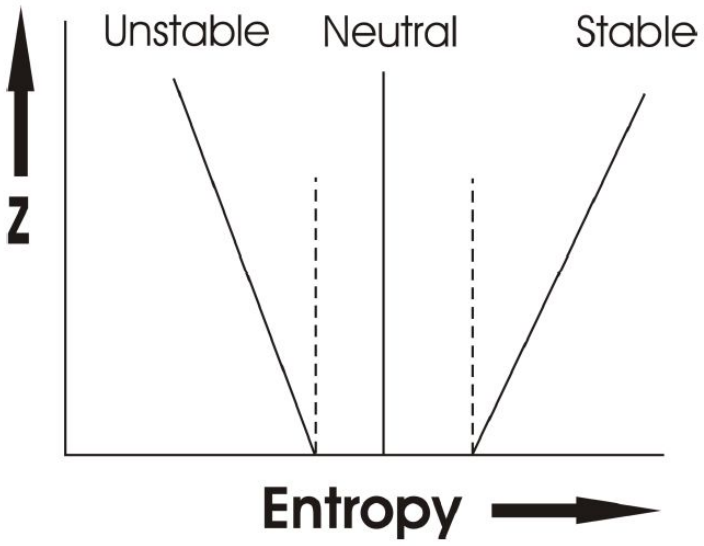

Figure 8: Convective stability of the atmosphere

. Convection will bring back the entropy profile back to its neutral state $\frac{ds}{dz} = 0$ whenever the atmosphere is convectively unstable (ie $\frac{ds}{dz} < 0$). Note that convection does not produce energy but only transfers it (from potential energy it produces kinetic energy). Taking convection into account allows us to numerically compute the temperature profile in RCE, represented by a green line on figure 10. More precisely, whenever the entropy decreases with altitude, we set it back to constant in a way that conserves energy (usually it will warm the atmosphere). We then adjust the mixing ration of water using the assumption of fixed relative humidity. If we compare RCE to RE:

- The adiabatic lapse rate (the rate at which temperature decreases with altitude) is much smaller, because we haven't allowed the entropy to vary with altitude.
- The temperature is much warmer in the troposphere, and the temperature discontinuity has been suppressed. The fact that the entire troposphere is warmer can be explained by the positive feedback between specific humidity and temperature at fixed relative humidity. This positive feedback is more effective in the lower troposphere, where the near surface layers becomes almost opaque.
- The stratosphere is not exactly identical, because of the change of tropospheric temperature affects the amount of infrared emitted upwards, which changes the amount of absorption in the stratosphere. This underlines the non-locality of radiative processes.

The presence of condensed water (clouds) makes the real atmosphere much more complicated/exciting to study, as we can see by looking at the photo of a cumulus cloud over the Indian Ocean on figure 9This underlines the complex topography of clouds, with non trivial consequences on scattering and radiative transfer.

Figure 9: Photo of a cumulus cloud over the Indian Ocean

Latent heat release by the condensation of water vapor makes atmospheric convection non adiabatic. However, by assuming thermodynamic equilibrium between liquid water and water vapor in the atmosphere, we will see that in one dimension, we can simply redefine the entropy to include the effects of condensation on the convective stability of the atmosphere. To a good approximation, the atmosphere is neutrally stable to convection, and this new entropy variable is approximately conserved with height in the troposphere, as we can see by doing balloon-based soundings of the tropical atmosphere (figure 10). Because the radiative cooling of the atmosphere makes it convect, and the convection redistributes the water in the atmosphere, which has strong radiative effects, moist RCE (RCE that takes into account the effect of condensation) is a two-way street between radiation and convection. Here, we avoid this complexity by assuming a constant relative humidity profile again, leading to the temperature profile represented by a red line on figure 10.

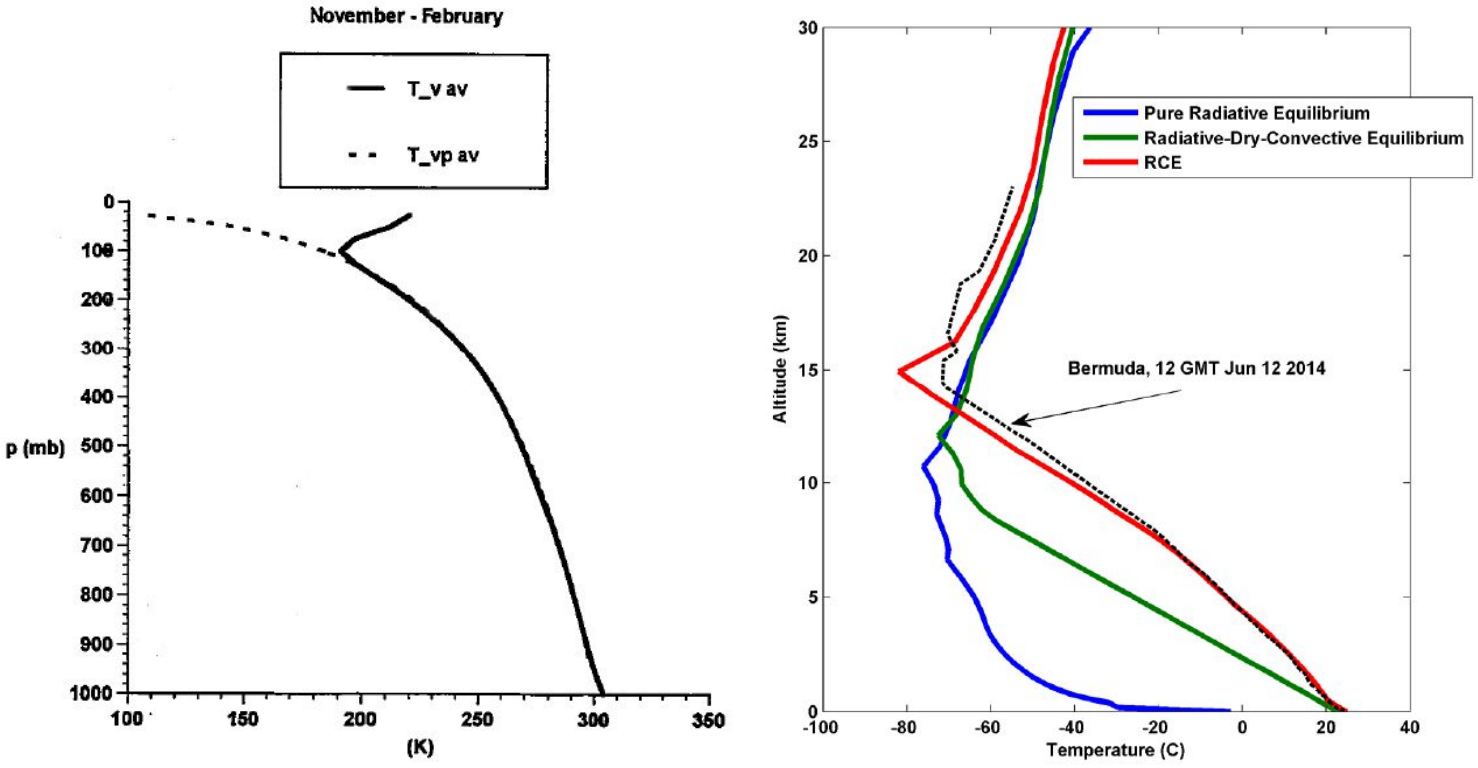

Figure 10: Left: Tropical sounding of the atmosphere (full line) compared to a theoretical profile conserving entropy in the vertical (dashed line)
Right: Temperature profiles in pure RE (blue line), dry RCE (green line), moist RCE (red line) and in a tropical sounding (black dashed line)

If we compare the moist RCE to its the other profiles:

- The adiabatic lapse rate is less steep than in dry RCE and in RE.
- More generally, the troposphere is warmer than in RE, which explains why radiation cools the Earth's troposphere while convection warms it by releasing latent heat.
- Typical tropical soundings, such as the one represented by a black line on figure 10, are quite close to moist RCE in the troposphere.
- In the stratosphere, typical soundings are even colder than the moist RCE because of the Brewer-Dobson circulation, a wave-driven stratospheric circulation which is thermally indirect (it makes cold air ascend and warm air descend).
- As the lower stratosphere is colder than in RE, the air is being radiatively heated. It is compensated by the fact that convection actually cools the lower stratosphere: Buoyant plumes overshoot after reaching their level of neutral buoyancy near the tropopause, and when the air parcels fall back down, there is a net transfer of mass downwards which cools the atmosphere.

If we are interested in the spatial features of RCE, it is possible to simulate it in a box with periodic boundary conditions. The radiation profile is specified for computational reasons, and the evolution of convection is studied. On figure , the colors show the moist entropy distribution near the surface. This calculation include an island producing a diurnal cycle of convection, but we will see later in the class that convection doesn't even need an island to spontaneously self-aggregate.

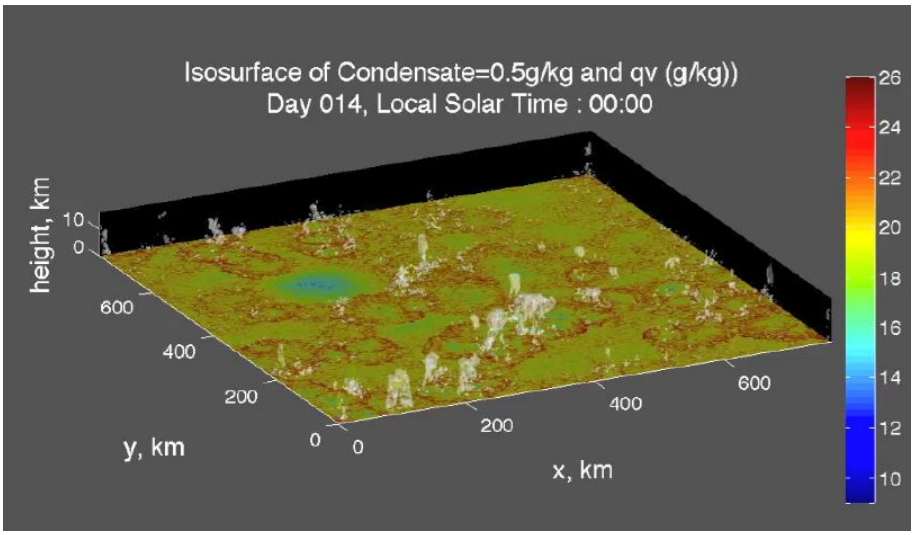

Figure 11: Simulation of convection in a box

2 Radiation overview

2.1 Introduction

We remember the Earth's mean energy budget presented in 2. We now focus on the radiation part (incoming and reflected, shortwave and longwave), and the physical mechanisms responsible for the absorption and scattering of radiation, which will eventually lead to the radiative transfer equation 9. Looking at the solar radiation spectrum on figure 12, we can see that the radiation at sea level mostly deviates from the blackbody spectrum because of absorption bands. Each absorption band corresponds to one/several molecules. In the shortwave domain, the main absorber is Water vapor (H_2O), followed by Ozone (O_3). Note that the previous spectrum does not include clouds, which are also strong absorbers in the shortwave domain. A way to think about this shortwave spectrum is to imagine a "blackbody spectrum with bites taken from it by the absorbing molecules".

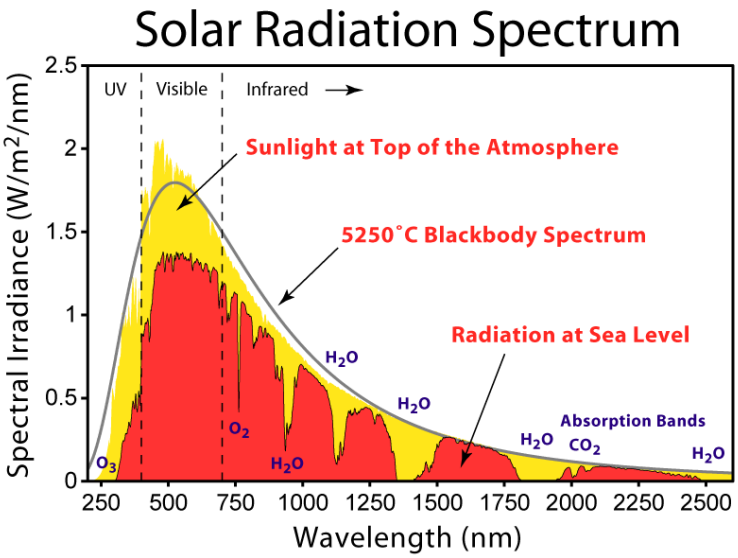

Figure 12: Solar radiation spectrum

On figure 13, we can see a simulation of how our solar system would look if we were to observe it 30l.y. away, if the interstellar medium was transparent. To each planet has been associated a blackbody spectrum, and the absorption bands have been added on the Earth spectrum.

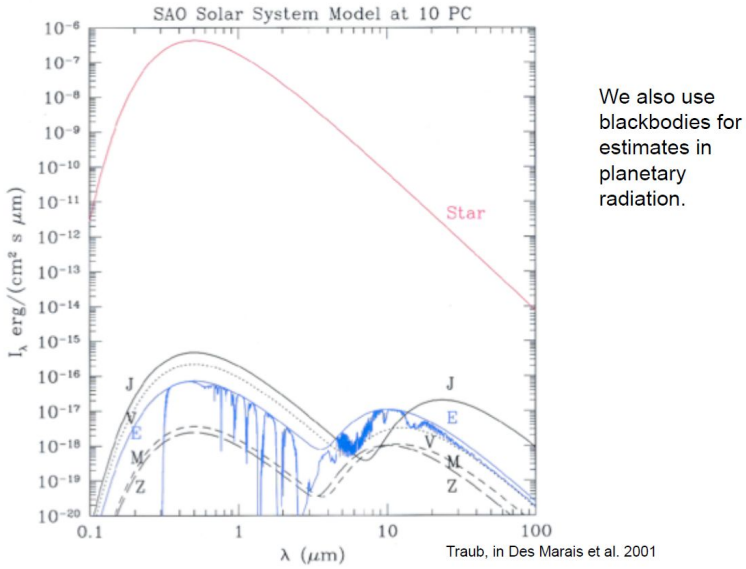

Figure 13: Monochromatic intensity as a function of wavelength for the Sun and the planets from the Solar system if all were observed from a 30l.y. distance

We note that:

- The intensity of the star's spectrum is much larger the sum of the intensity of the planets spectra (beware of the logarithmic scale): Only a small part of the solar radiation is reflected by the planets.
- There are two separated spectral peak, a left one corresponding to the shortwave radiation reflected from the Sun and a right one corresponding to the longwave radiation thermally emitted from the planets surfaces.

We now look at the Earth's thermal emission spectrum, which is depicted on figure 14.

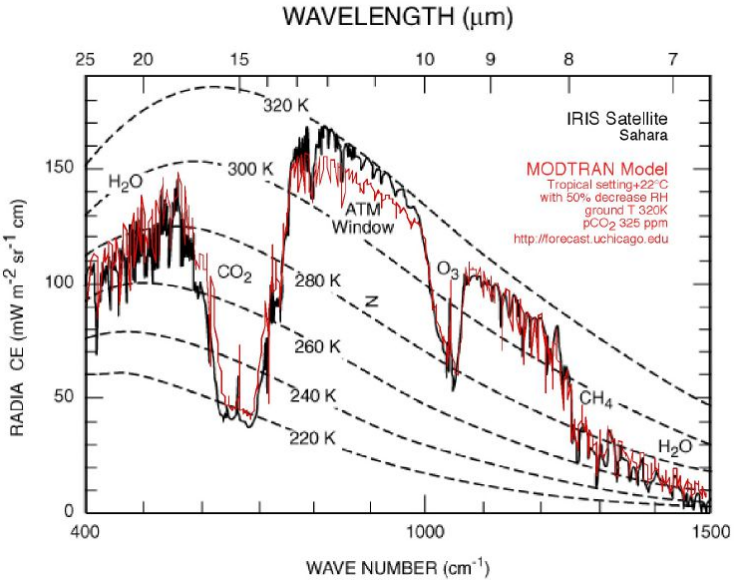

Figure 14: Radiance of the Earth as a function of the wave number

It has been obtained from satellite data (black curve) and from running the MODTRAN model (red curve).

- The main absorption bands correspond to the greenhouse gases listed in 1.3.
- Numerous small absorption bands on the spectrum are due to water vapor, the main greenhouse gas in the atmosphere.
- From the atmospheric longwave window below 1000cm^{-1}, where we can "see the ground", we can see that the place where the spectrum was observed was hot (almost $320\text{K} \approx 47°C$), consistently with the fact that the observations took place in the Sahara desert.
- In the middle of the Ozone's absorption band, there is a peak of lessened absorption due to the intrinsic absorption of O_3.
- In the middle of the Carbon Dioxide's absorption band, there is a peak of lessened absorption due to the positive temperature gradient in the stratosphere, as we will see later in class.

An online MODTRAN model of the Earth's thermal emission spectrum is available at [http://climatemodels.uchicago.edu/modtran/]. In this model, the temperature's profile does not adapt to the changes in atmospheric chemistry, making it a tool to understand the longwave absorption of the atmosphere, but not to realistically simulate this spectrum. Finally, we look at the thermal emission spectrum of the exoplanet Gemini, which has a pretty hot surface ($600 - 750\text{K}$) and orbits at $\sim 13\text{au}$ of its star Eridani (cf left part of figure 15).

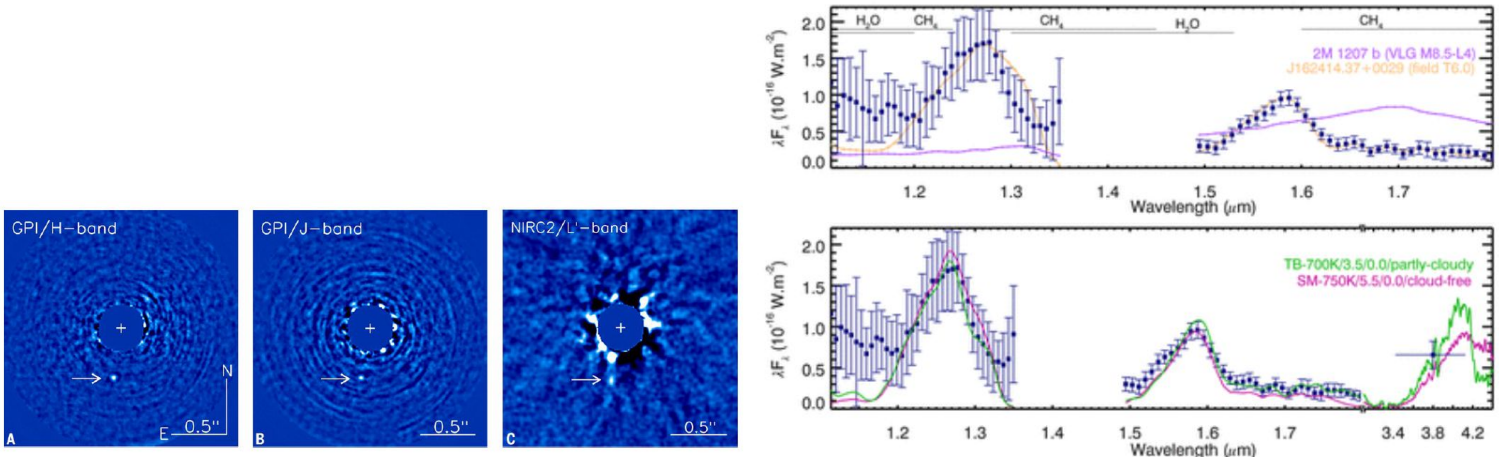

Figure 15: Gemini planet imager discovery (left) and thermal emission spectrum (right)

Looking at the exoplanet's thermal emission spectrum on the right of figure 15 and comparing the observations with the blackbody curves allows us to identify two components of the exoplanet's atmosphere:

- On the left side, between 1μm and 1.2μm, we see H_2O emission features, without the individual bands that we can not resolve at this distance.
- On the right side, above 1.5μm, we can see CH_4 emission features.

The error bars are quite large, but it is still a good measurement given how far the exoplanet is. Note that if you wanted to detect the light coming from such an exoplanet from Earth, you would have to take into account the Earth's absorption spectrum 14 and look through an atmospheric window, keeping in mind that the local water vapor features might affect the quality of the observation. This explains why telescopes are set in high and dry places, such as the mountains of Chili.

2.2 Definition of flux and intensity

2.2.1 Flux

By definition, the flux (more rigorously the flux density) $\mathcal{F}$ is the rate at which radiation is incident on or passes through a surface, in units of W.m^{-2}:

$$\mathcal{F} \stackrel{\text{def}}{=} \frac{d^2 E_\lambda}{dA dt} \tag{4}$$

where E_λ is the energy continuously transported by radiation, dA is an infinitesimal area, and dt an infinitesimal time. If we take the example of a Summer day at the beach, you could compute the solar flux by looking at how much the sun heats a small area of your skin. As the day progresses, the sunlight strikes the surface at an increasingly oblique angle, spreading the same energy over a larger and larger area, as we can see on figure 16. As a consequence, the flux on the specified area (eg the small area of your skin) decreases.

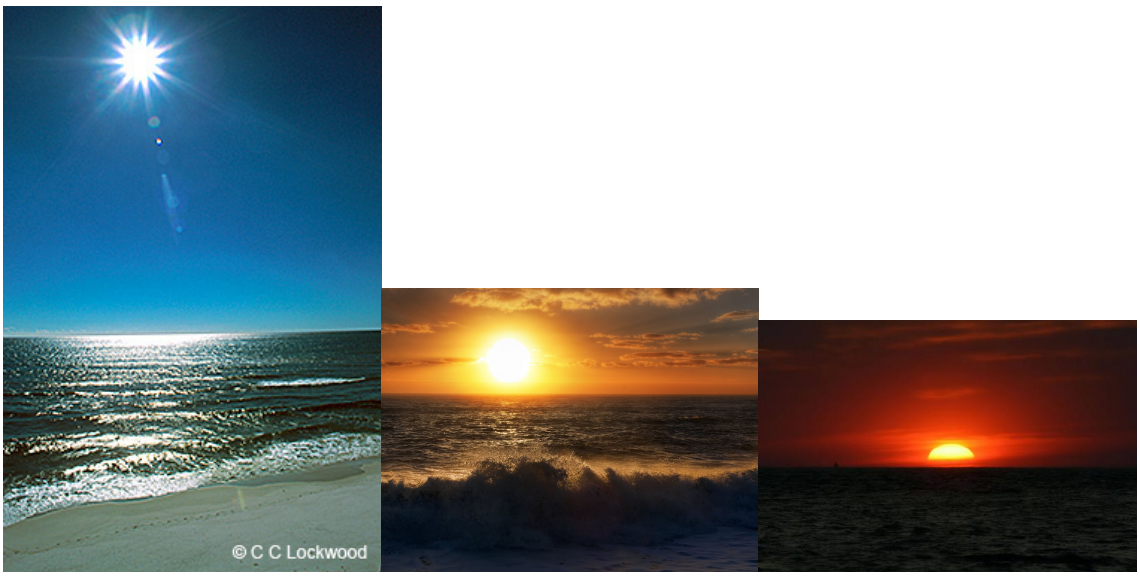

Figure 16: Sun over the beach at noon (left) in the end of the afternoon (middle) and at dusk (right)

Note that the flux itself makes no distinction concerning where the radiation is coming from, as it is the sum of the radiation you get over all the directions. If we are interested:

- In a specific wavelength, we define the monochromatic flux, in units of W.m^{-2}.μm^{-1}:

$$\mathcal{F}_\lambda \stackrel{\text{def}}{=} \frac{d\mathcal{F}}{d\lambda} = \lim_{\Delta\lambda \to 0} \mathcal{F}_{[\lambda, \lambda+\Delta\lambda]} \tag{5}$$

- In a given band $[\lambda_1, \lambda_2]$, we define the broadband flux, in units of W.m^{-2}.μm^{-1}:

$$\mathcal{F}_{[\lambda_1,\lambda_2]} \stackrel{\text{def}}{=} \frac{\int_{\lambda_1}^{\lambda_2} F_\lambda d\lambda}{\lambda_2 - \lambda_1} \tag{6}$$

For instance, we could be interested in the visible band, approximately $[400\mu\text{m}, 800\mu\text{m}]$.

2.2.2 Intensity

The intensity provides the strength and direction of the various sources contributing to the incident flux on a surface. For visible radiation, intensity roughly corresponds to the "brightness" your eyes can see looking backwards along a ray on incoming radiation. Coming back to the example of the sun over the beach on figure 16, the sun (a localized high intensity source) has a much higher intensity and is much "brighter" than the clear sky (a uniform low intensity source). Clouds may also appear "brighter" or "darker" depending on their thickness and their angle from the sun. More rigorously, the intensity is the monochromatic flux, measured on a surface making an angle θ with the reference surface, per unit solid angle traveling in a particular direction:

$$I_\lambda(\Omega,\theta) \stackrel{\text{def}}{=} \frac{1}{\cos\theta}\frac{d\mathcal{F}}{d\Omega} = \frac{d^4E_\lambda}{\cos\theta dA d\Omega d\lambda dt} \Leftrightarrow F_\lambda = \int_{(\Omega)} I_\lambda(\overrightarrow{n}\cdot\overrightarrow{k})d\Omega = \int_{(\Omega)} I_\lambda \cos\theta d\Omega \tag{7}$$

where we have adopted the notations on the left of figure 17.

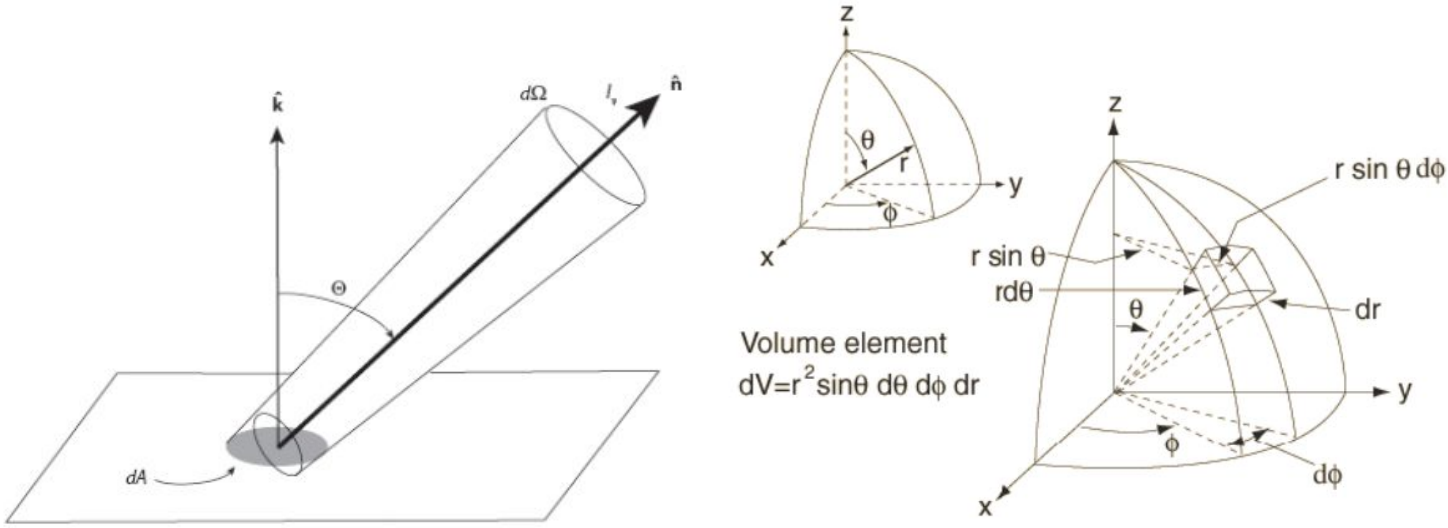

Figure 17: Schematic of incident radiation (left) and spherical coordinates (right)

The solid angle Ω, in units of sr, can be mathematically defined by adopting the spherical coordinate system presented on the right of figure 17, and considering an elementary area $d\sigma$:

$$d\Omega \stackrel{\text{def}}{=} \frac{d\sigma}{r^2} = \sin\theta d\theta d\phi \tag{8}$$

2.2.3 Summary

The table below summarizes the definitions of some key quantities in radiative transfer. Note that these terms are described differently depending on the book/journal you read:

Quantity [Units]	Name	Definition
I_λ	Intensity	$\frac{d^4E_\lambda}{\cos\theta dA d\Omega d\lambda dt}$
J_λ	Mean intensity	$\frac{1}{4\pi}\int_{(\Omega)} I_\lambda d\Omega$
$\mathcal{F}_\lambda$	Monochromatic flux	$\frac{d^3E_\lambda}{dAd\lambda dt} = \int_{(\Omega)} I_\lambda \cos\theta d\Omega$
$\mathcal{F}$	Flux/flux density	$\frac{d^2E_\lambda}{dAdt} = \int_0^{+\infty} F_\lambda d\lambda$
f	Total flux	$\frac{dE_\lambda}{dt} = \int_{(A)} \mathcal{F} dA$

2.3 The radiative transfer equation

The radiative transfer equation can be written:

$$\underbrace{\frac{dI_\nu(s,\nu,\mu,t)}{ds}}_{\text{Change intensity}} = -\underbrace{\rho k(s,\nu,t) I_\nu(s,\nu,\mu,t)}_{\text{Exctinction=Loss}} + \underbrace{\rho j_\nu(s,\nu,\mu,t)}_{\text{Emission=Gain}} \tag{9}$$

where:

- I_ν is the intensity in frequency units, linked to the intensity in wavelengths units by:

$$I_\nu = |\frac{d\lambda}{d\nu}| I_\lambda = \frac{cI_\lambda}{\nu^2} \tag{10}$$

  where we have used $c = \lambda\nu$.

- s is the distance traveled by radiation in the medium (aka path length) and ρ is the density of the medium.

- k is the mass extinction cross section in units $\mathrm{m}^2.\mathrm{kg}^{-1}$. Alternatively, we can use the absorption coefficient $\kappa = \rho k$ in units m^{-1}. The extinction cross section depends on how fast photons are absorbed by the medium and computing it is a quantum mechanical problem.

- j_ν is the mass emission coefficient in units $\mathrm{W.kg}^{-1}.\mathrm{Hz}^{-1}.\mathrm{sr}^{-1}$. Alternatively, we can use the emission coefficient $\varepsilon_\nu = \rho j_\nu$ in units $\mathrm{W.m}^{-3}.\mathrm{Hz}^{-1}.\mathrm{sr}^{-1}$. The emission coefficient depends on scattering and is also very hard to compute.

- $\mu = \cos\theta$ is the cosine of the angle between the surface through which radiation goes and the reference surface.

In 9, we can see that we have a competition between extinction/emission, ie processes that remove/add photons from/to the beam. If we consider the three fundamental radiative processes:

1. Absorption of radiation contributes to the extinction.
2. Emission of radiation contributes to the emission.
3. Scattering of radiation contributes to both the extinction and the emission.

2.4 Optical depth

The optical depth τ is a measure of transparency. If you think of an object in a fog, such as on figure 18:

- When the object is immediately in front of you: $\tau = 0$.
- As the object moves away, τ increases.
- τ depends on the frequency of the electromagnetic radiation.

Figure 18: Mountain behind a fog

Mathematically, we define τ as a dimensionless vertical scale:

$$d\tau \stackrel{\text{def}}{=} -\kappa dz = -\rho k dz = -\rho k \cos\theta ds \tag{11}$$

The negative sign arises from the fact that we are looking down into the atmosphere. Physically the optical depth can be better understood by considering the last photon that makes it to the observer. In a very "optically thick" atmosphere, a lot of molecules absorb and emit photons on the way, which explains why the last photon making it to the observer has been emitted "recently", as we can see on figure 19.

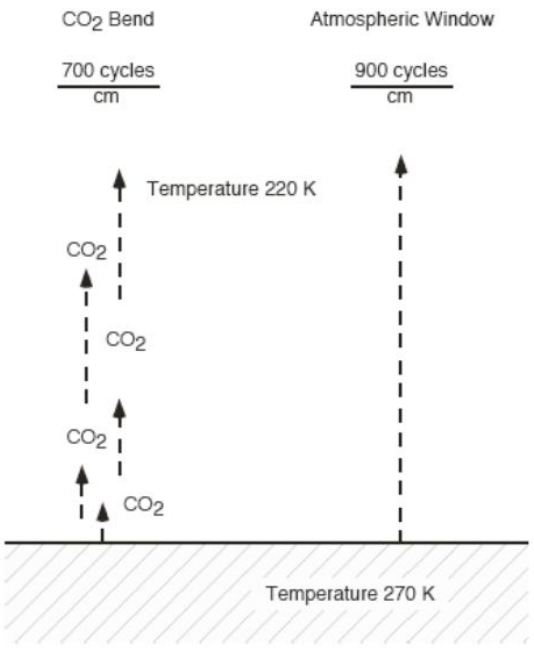

Figure 19: Difference between an "optically thick" band (left) and an atmospheric window (right) for the path of photons

2.5 Blackbody radiation

2.5.1 Blackbody

A blackbody is a "perfect" radiator that absorbs all radiation incident on it and remits radiation in a frequency spectrum depending only on its temperature. Blackbody radiation is furthermore isotropic, ie independent of direction. An ideal blackbody is one which is in equilibrium with the Planck distribution: it absorbs all the radiation incident upon it and emits radiation in the Planck distribution for its temperature. In the real world, it is impossible to find an ideal blackbody. Examples of objects close to the ideal blackbody include:

- The inside of a cavity, such as a closed heated oven (cf figure 20), where the radiation is continuously being absorbed and remitted by the walls. A small opening in the cavity will act as a source of radiation, and almost give off radiation characteristic of an ideal blackbody.
- A dense cloud, in which multiple scattering occurs and the light can not escape.

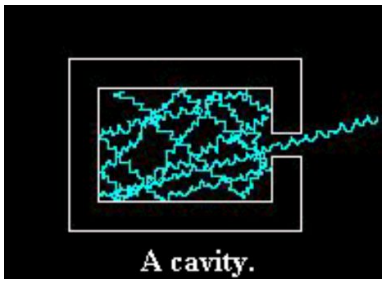

Figure 20: Schematic of a cavity with a small opening

2.5.2 Planck's law

When a blackbody is in thermal equilibrium, its intensity (note that the Planck functions are indeed given per unit steradians) is given by Planck's law:

- In frequency units:

$$\boxed{B_\nu(T) = \frac{2h\nu^3}{c^2[\exp(\frac{h\nu}{k_BT}) - 1]}} \tag{12}$$

- In wavelength units:

$$B_\lambda(T) = |\frac{d\nu}{d\lambda}|B_\nu = \frac{2hc^2}{\lambda^5[\exp(\frac{hc}{\lambda k_BT}) - 1]} \tag{13}$$

Note that the blackbody's intensity and spectrum depends only on the temperature of the body. The two asymptotes of the Planck's function are:

1. Wien's tail:

$$\lambda \to 0 \;\Rightarrow\; B_\lambda \to \frac{2hc^2}{\lambda^5}\exp(-\frac{hc}{\lambda k_BT}) \tag{14}$$

2. Rayleigh Jeans tail:

$$\lambda \to +\infty \;\Rightarrow\; B_\lambda \to \frac{2ck_BT}{\lambda^4} \tag{15}$$

2.5.3 Wien's law

Most objects emit radiation at many wavelengths. However, there is one wavelength where the object emits the largest amount of radiation. Wien's law gives the wavelength at which B_λ is maximum:

$$\boxed{\lambda_{\max} = \frac{b}{T}} \tag{16}$$

where $b \approx 2.90.10^{-3}$m.K is Wien's constant. Inverting Wien's law for an object emitting at maximal intensity for wavelength λ allows us to find its brightness temperature. As we can see on figure 21, the hotter an object, the shorter the wavelength at which it will emit most of its radiation.

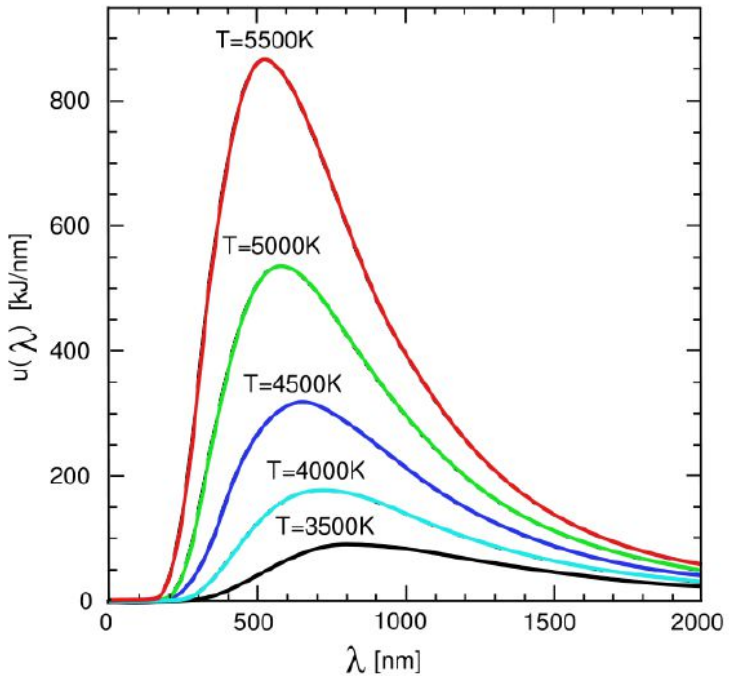

Figure 21: Planck's function as a function of wavelength for different brightness temperatures

If $\lambda_{\max}$ is a visible wavelength, then it will determine the color of the emitting source to a good approximation, which explains why colors can be associated to black bodies with brightness temperatures between 1000K and 10000K. The correspondence between wavelength and temperature can be seen in many situations, including in the experiment photographed on the left of figure 22 where molten lava is poured on ice: the hot lava is yellow-orange, corresponding to a brightness temperature of 3000K; it then becomes red (2000K) as it cools down to eventually become black as it solidifies, meaning that its wavelength of maximal intensity in now in the infrared.

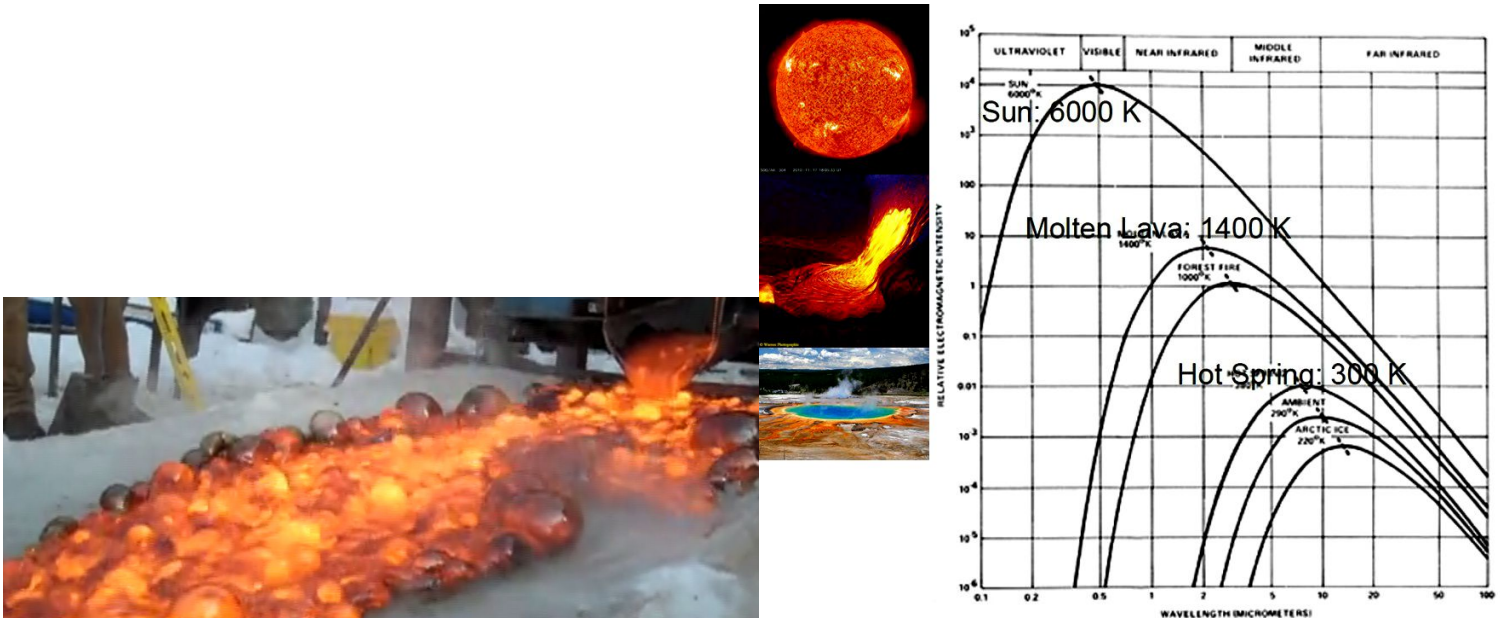

Figure 22: Molten lava on ice (left) and examples of brightness temperatures (right)

Other examples of real objects with their associated brightness temperatures can be found on the right of figure 22.

2.5.4 Stefan-Boltzmann law

In the sake of broadband analysis, we can integrate Planck's function 13 over a given band $[\lambda_1, \lambda_2]$:

$$\pi \int_{\lambda_1}^{\lambda_2} B_\lambda d\lambda = \sigma T_{b,\lambda}^4 \tag{17}$$

where $T_{b,\lambda}$ has the dimensions of a temperature and $\sigma \approx 5.67.10^{-8}\text{W.m}^{-2}\text{.K}^{-4}$ is the Stefan-Boltzmann constant. For example, by integrating a spectrum of the atmosphere over the band corresponding to the atmospheric window, it is possible to obtain the temperature of the ground, which is what we had done when analyzing 14. Integrating Planck's function over all the possible wavelengths allows us to derive Stefan-Boltzmann's law, that we had taken as a given in 1:

$$\boxed{\pi \int_0^{+\infty} B_\lambda d\lambda = \sigma T^4} \tag{18}$$

Inverting Stefan-Boltzmann law to find the temperature of a blackbody emitting a given radiative flux is the easiest way to compute its brightness temperature.

2.5.5 Kirchhoff's law

For a body of any arbitrary material emitting and absorbing thermal electromagnetic radiation in thermodynamic equilibrium, Kirchhoff's law states that the ratio of its emissivity ε_λ to its absorptivity κ is equal to the Planck function B_λ:

$$\boxed{\varepsilon_\lambda = \kappa B_\lambda(T)} \tag{19}$$

It will allow us to simplify the radiative transfer equation 9 in special cases.

2.6 Monte Carlo simulations of the radiative transfer equations

The radiative transfer equation 9 is difficult to solve in the case of three dimensional complicated surfaces or when the medium has discontinuities (eg cloud boundaries). As a consequence, Monte Carlo simulations of the radiative transfer equation have been developed, where each photon is individually emitted, scattered and absorbed with a given probability, as shown on figure 23.

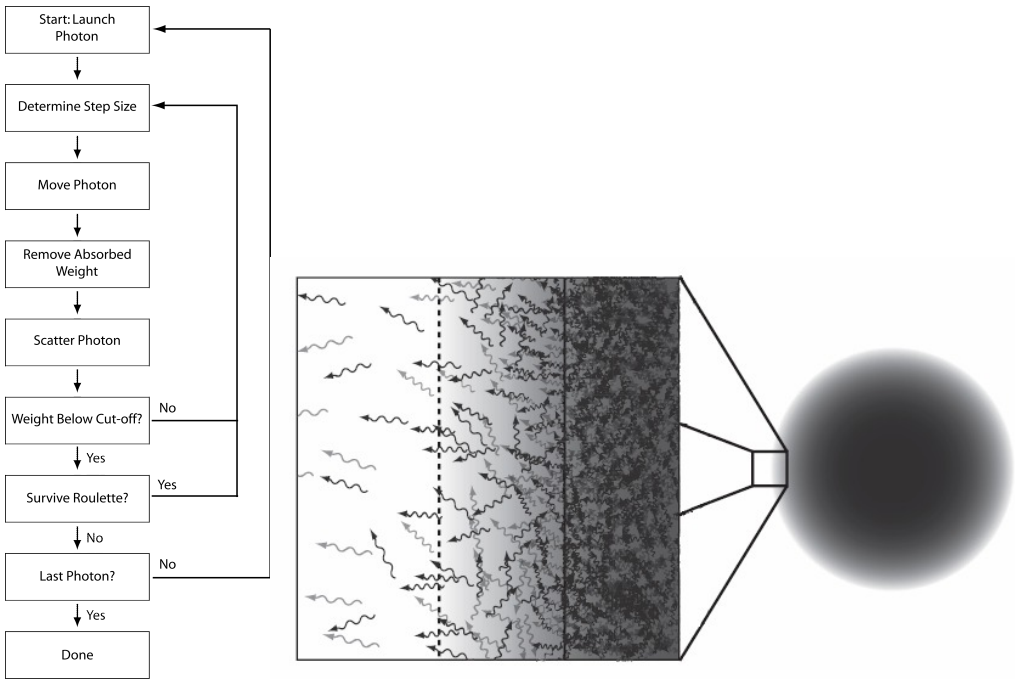

Figure 23: Steps of the Monte Carlo simulation of the radiative transfer equation (left) and schematic of the photons in the simulation (right)

The simulations are very computationally intensive (typically 10^8 photons are needed), and have been for instance used for biomedical applications or even radiation through stellar disks. They give an interesting discrete viewpoint of radiation, where electromagnetic radiation is equivalent to a beam of traveling photons.

3 Modeling Transmission and Emission

3.1 Absorption vs emission lines

3.1.1 Absorption coefficient

The absorption coefficient κ (in units m^{-1}) can be computed by summing over the absorbers cross-sections σ_{ij} (in units m^2) :

$$\kappa = \sum_j \kappa_j = \sum_j \sum_i n_{ij}\sigma_{ij} \tag{20}$$

where i refers to different energy levels and j to different atoms/molecules, while n_{ij} is the number density in units m^{-3}. The cross sections of different absorbers at different frequencies can be found on database such as [http://vpl.astro.washington.edu/spectra/allmoleculesli For instance the cross-sections of CO_2 and CH_4 are shown on figure 24.

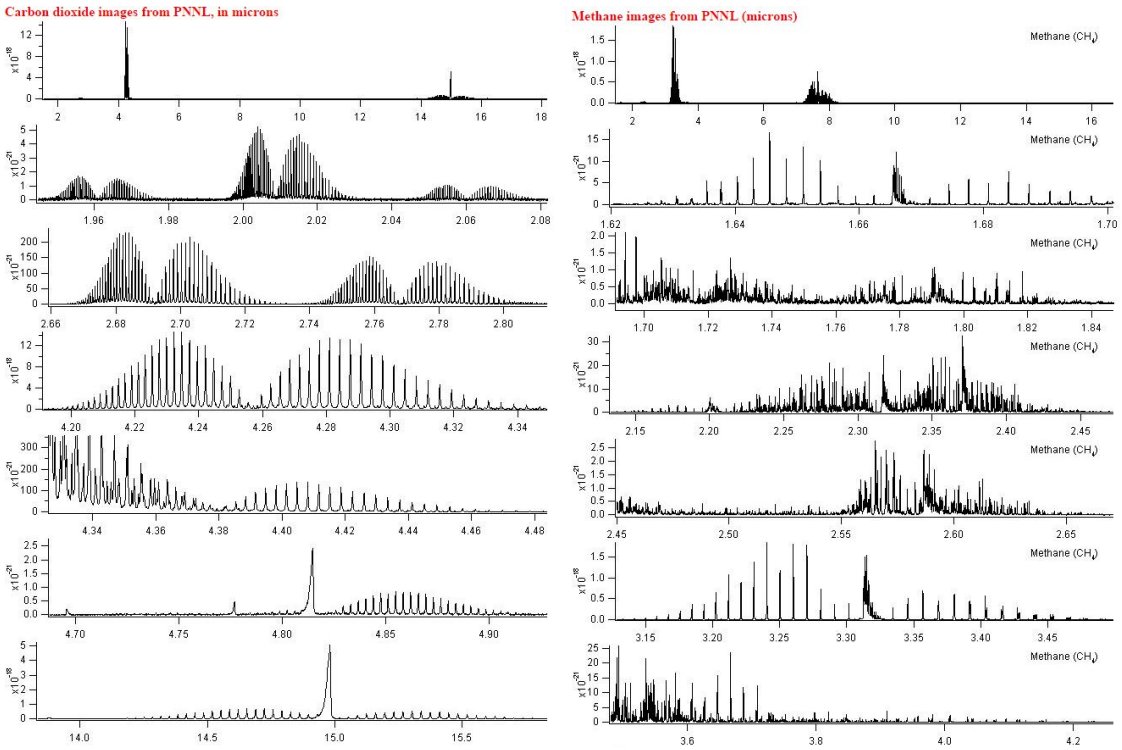

Figure 24: Cross-sections of CO_2 (left) and CH_4 (right) in units cm^2/molecule for increasing wavelengths in units μm (up to down)

All of these cross-sections must be considered when studying the interaction of a given greenhouse gas with light.

3.1.2 Origin of absorption and emission lines

We have seen in 2.5 that a hot blackbody emits a continuous spectrum. A cloud of cooler gas placed between the blackbody and the observer will absorb some discrete wavelengths of this continuous spectrum, corresponding to the discrete quantized energy levels of its molecular constituents (cf figure 25).

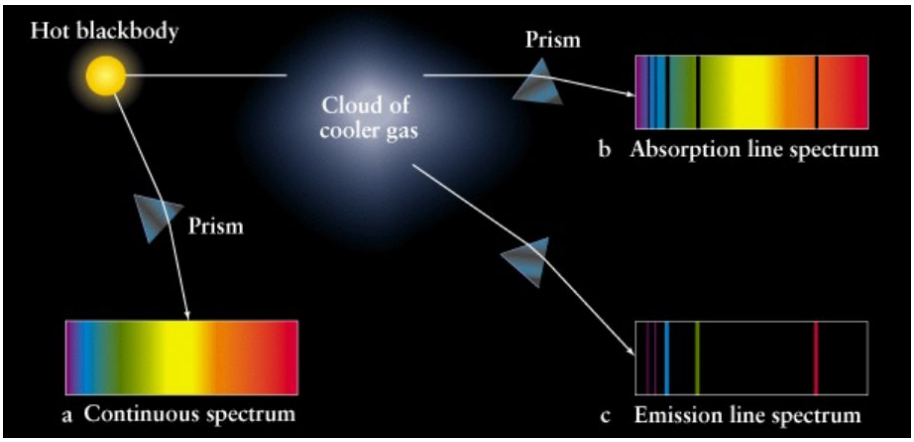

Figure 25: Spectra observed for different configurations of a hot blackbody and a cloud of cooler gas

We now assume that the deepest layer of a planetary atmosphere emits a continuous spectrum, like a blackbody. If we look from above, depending on the vertical temperature gradient, three different situations arise:

1. If the atmosphere is isothermal (left of figure 26), the spectrum emerging from the top of the atmosphere will be the same continuous blackbody spectrum.

2. If the temperature decreases with altitude (middle of figure 26), the cooler layer of gas on top of the hot blackbody will behave like the cool gas on figure 25, and an absorption spectrum will result.

3. If the temperature increases with altitude (right of figure 26), we will have emission lines from the hotter layers of the atmosphere on top of the black body.

Figure 26: Three options for the vertical temperature gradient: zero (left), negative (middle) and positive (right)

3.1.3 Earth's absorption and emission lines

Looking at the Earth's vertical temperature structure, we can distinguish four layers based on the vertical temperature gradient's sign (left of figure 27).

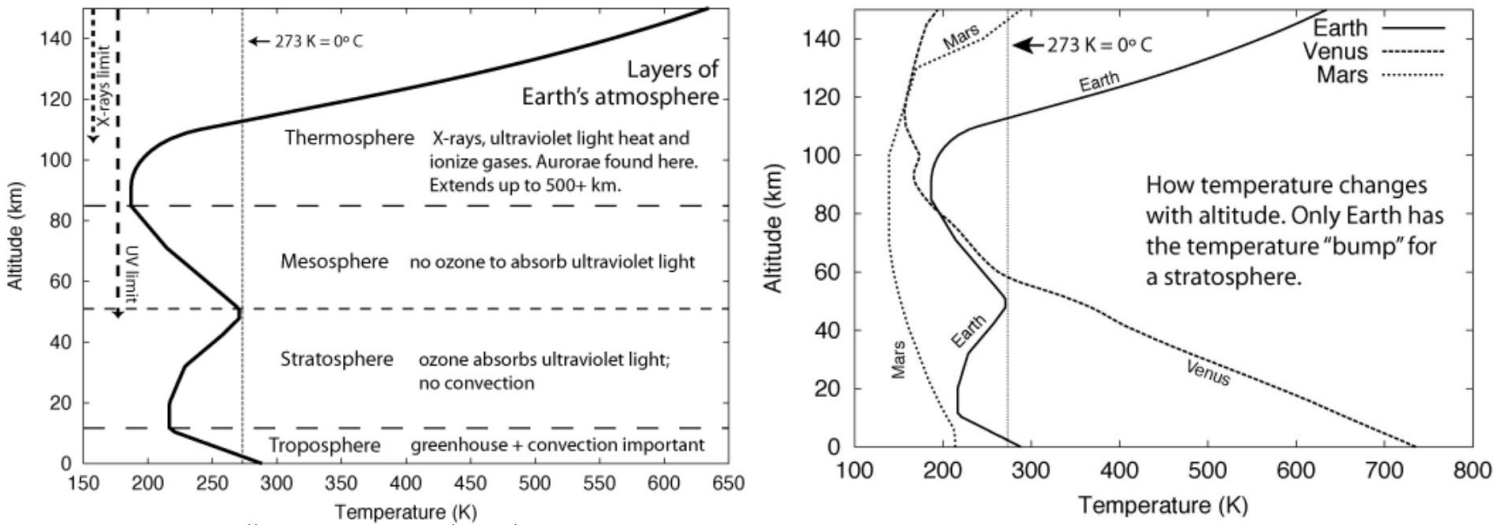

Figure 27: Earth, Venus and Mars's temperature structures

We are mostly concerned with the two lowest layers of the Earth's atmosphere: the troposphere and the stratosphere, which constitute the vast majority of the atmospheric mass. Note that the Earth has a stratosphere mostly because of the Ozone's shortwave absorption, and that it is not true for other planets such as Venus or Mars (right of figure 27). We can see the uniqueness of the Earth's temperature structure by comparing the longwave absorption of Venus, Earth and Mars on figure 28. The Earth is the only planet to have the small emission peak in the middle of the CO_2 absorption band, because of the positive temperature gradient in the stratosphere. This peak is small because the density of Carbon Dioxide decreases almost exponentially with altitude, and emits only at the wavelength where it cross section is large, as we can see on figure 24.

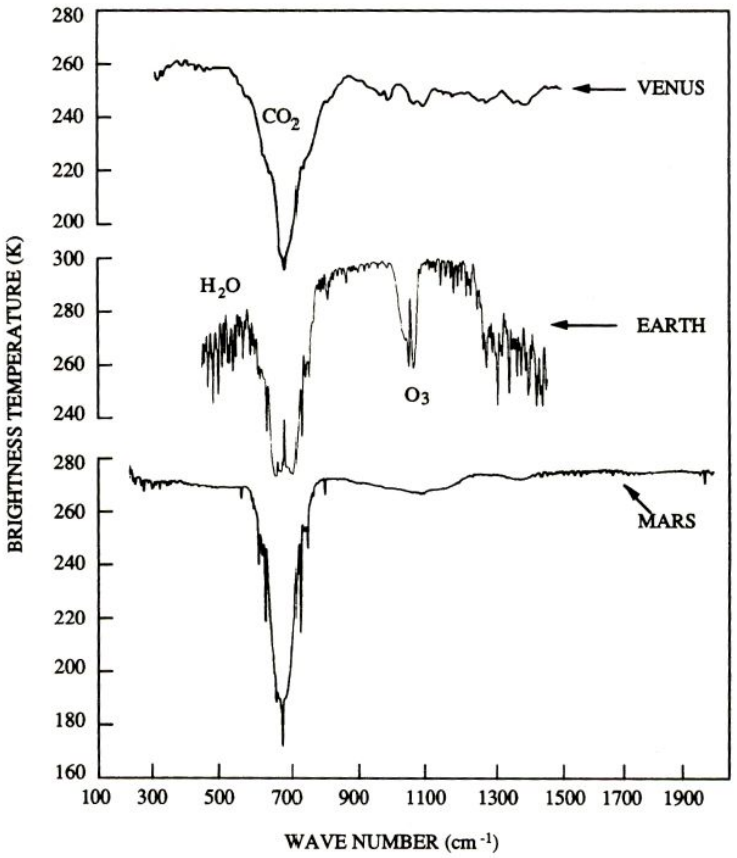

Figure 28: Longwave brightness temperature vs wavenumber for different planetary atmospheres

3.2 Local thermodynamic equilibrium

A material is said to be in thermodynamic equilibrium when it is in thermal, chemical and mechanical equilibrium. Local thermodynamic equilibrium (LTE) implies thermodynamic equilibrium over a small volume of the atmosphere, and is only valid locally, where any temperature, pressure or chemical gradients are small given the photon mean free path. We do not assume the equilibrium to hold for radiation and allows it to depart from that of a black body. Coming back to 20, we were left to compute the level populations n_i for each given atom/molecule j of the system. We recall the discrete energy levels of the hydrogen atom (left of figure 29), and that photons can allow electrons to jump from one level to the other (right of figure 29).

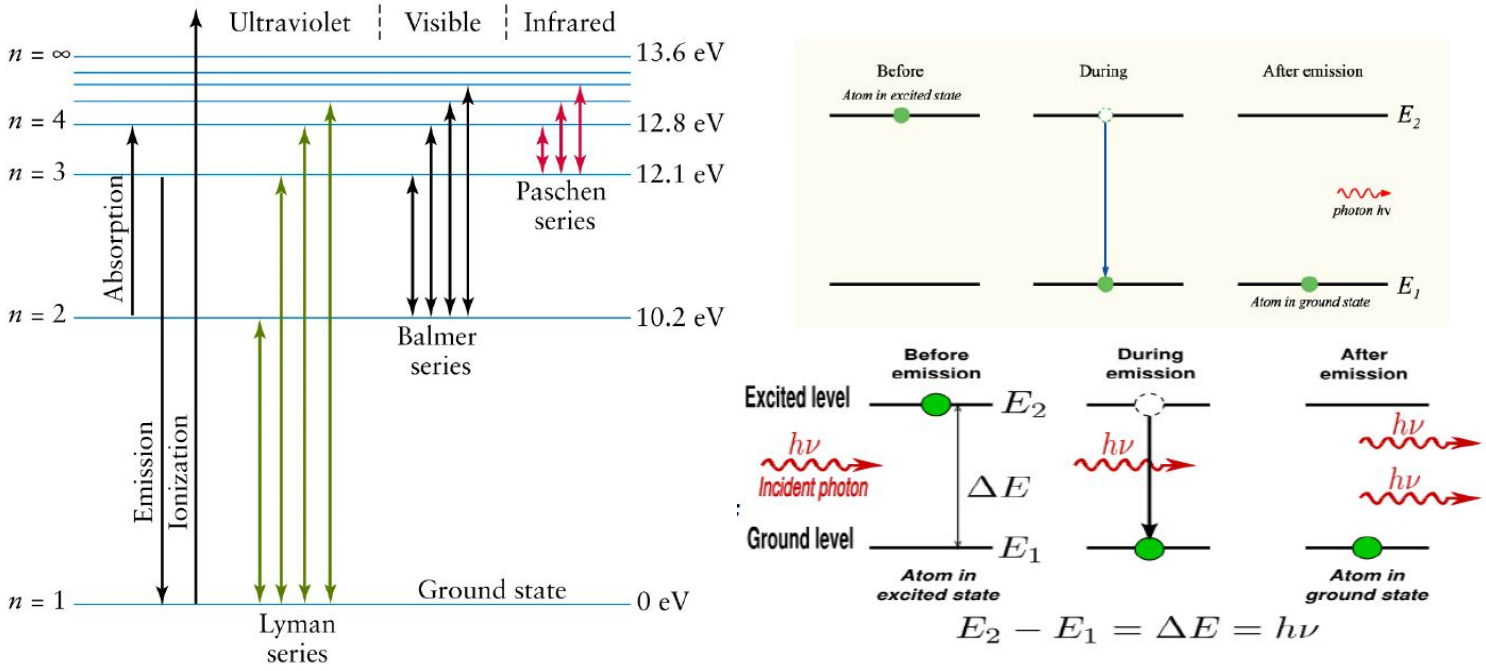

Figure 29: Hydrogen energy levels (left) and effects of photons on level populations (right)

From the role of photons in energy level's transitions, we can expect radiation to have an influence on the level populations, making the radiative transfer equation 9 extremely hard to solve as the absorption coefficient κ depends on the intensity I in this case. For instance, the latter case happens when a planet is very close to a big star and highly irradiated by it: we then need to write a radiative equation at each level of energy of the important atoms/molecules. However, if LTE applies, collision processes dominate over radiative effects. Collisions control the population's level by coupling the radiation field to the matter's temperature via the kinetic energy of the gas (cf figure 30), and drives the population's density to Boltzmann's distribution:

$$\boxed{\frac{n_i}{\sum_i n_i} = \frac{g_i \exp(-\frac{h\nu_i}{k_B T})}{\sum_i g_i \exp(-\frac{h\nu_i}{k_B T})}} \tag{21}$$

where n_i is the number density at the energy level i associated to the frequency ν_i, and g_i is the degeneracy of level i (there is 1 vibrational level and $2i+1$ rotational levels).

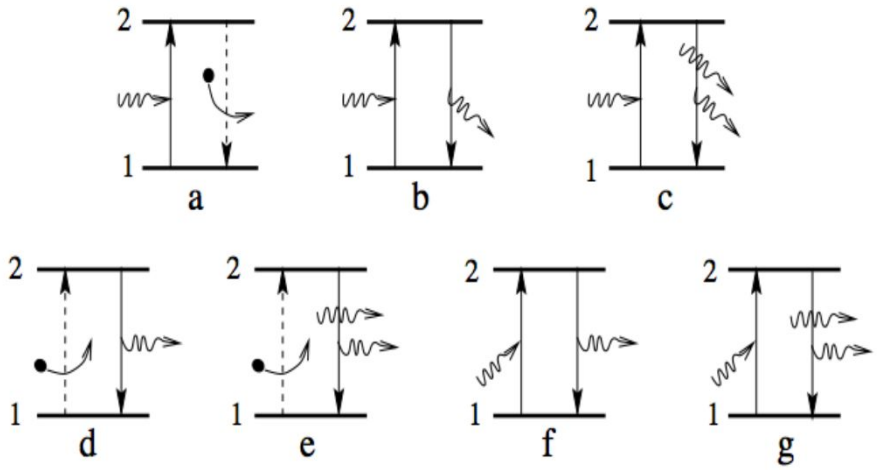

Figure 30: Different collision situations in a two energy level system

Consequently, in LTE, all properties of the matter only depend on the local kinetic temperature and the density, making 9 much easier to solve. In the Earth's atmosphere, LTE will only be valid under $60-70$km, where pressure is high enough for collisional

processes to dominate. LTE breaks down in the upper atmosphere because of the open boundary to space. Another common situation where LTE breaks down is when average electronic energy levels are artificially pumped (eg lasers, fluorescent light bulbs, gas discharge tubes, light-emitting diodes...).

3.3 Thermal emission from a solution to the radiative transfer equation

3.3.1 Plane parallel atmosphere

Let's consider incident radiation at an angle θ in a given atmosphere, as represented on figure 31.

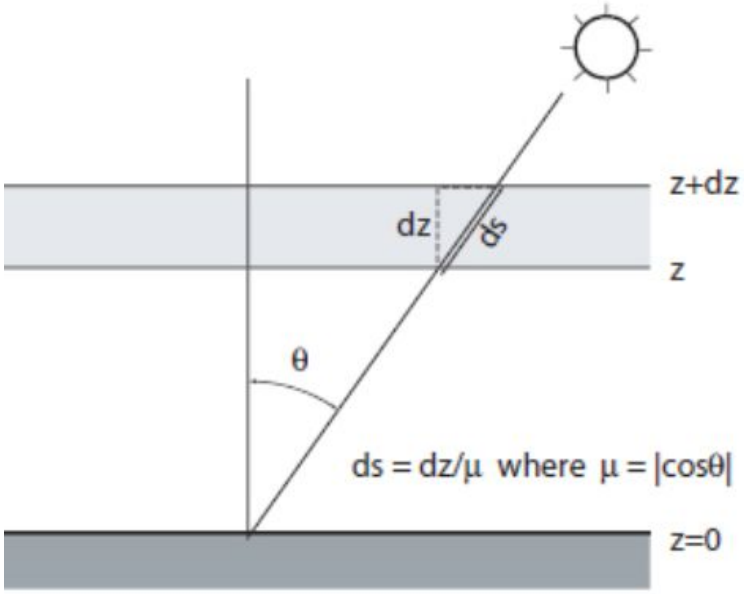

Figure 31: Schematic of incident radiation in a slab atmosphere

We make the plane parallel atmosphere, which includes two assumptions:

1. At a given location, we ignore the horizontal variations in the radiative properties of the atmosphere. It is valid for a highly stratified atmosphere, where physical properties such as temperature, pressure and density vary much more strongly in the vertical than in the horizontal direction. It is not valid for objects with horizontal structures, such as clouds.

2. We ignore the curvature of the planet, approximately valid for:

$$\frac{H}{\cos\theta} \ll r_p \tag{22}$$

where H is the scale height of the atmosphere, θ the incident angle and r_p the planet's radius. For the Earth where $H \approx 8$km and $r_p \approx 6400$km, the approximation is always valid, and most photons make it through the Earth's atmosphere without ever "feeling" the effects of its curvature.

3.3.2 Solution to the radiative transfer equation in LTE

We work in a plane parallel atmosphere and assume that LTE holds. We write the radiative transfer equation 9 and use the optical depth τ defined in 11 as the vertical coordinate; using the notations introduced in 31:

$$\mu\frac{dI(\tau,\lambda,\mu,t)}{d\tau} = I(\tau,\lambda,\mu,t) - \frac{\varepsilon(\tau,\lambda,\mu,t)}{\kappa(\tau,\lambda,t)} \tag{23}$$

In LTE, Kirchhoff's law 19 holds and we obtain:

$$\mu\frac{dI(\tau,\lambda,\mu,t)}{d\tau} = I(\tau,\lambda,\mu,t) - B(\tau,\lambda,t) \;\Rightarrow\; \mu\frac{d}{d\tau}[I\exp(-\frac{\tau}{\mu})] = -B\exp(-\frac{\tau}{\mu}) \tag{24}$$

Integrating the previous equation 24 from $\tau' = 0$ (top of the atmosphere) to $\tau' = \tau$ (corresponding to an altitude z):

$$\underbrace{I(0)}_{\text{Intensity satellite}} = \underbrace{I(\tau)}_{\text{Intensity}} \underbrace{\exp(-\frac{\tau}{\mu})}_{\text{Transmittance if } \mu=1} + \underbrace{\int_0^\tau \frac{B(\tau')}{\mu} \exp(-\frac{\tau'}{\mu}) d\tau'}_{\text{Path-integrated emission}} \tag{25}$$

Note that the intensity seen from the satellite $I(0)$ is not affected by the emission $B(\tau')$ from points through which the intervening atmosphere is opaque ($\tau \gg 1$).

Going back to the online longwave MODTRAN spectrum [http://climatemodels.uchicago.edu/modtran/], we can use the model to study the following questions:

1. *Identify the major gases in Earth's IR thermal emission spectrum (hint: increase or decrease the concentration to see which spectral feature is affected).*
2. *Methane has a current concentration of* 1.7ppm *in the atmosphere, and is doubling at a faster rate than is* CO_2.
   (a) Is 10 *additional* ppm *of Methane more or less important than* 10ppm *of Carbon Dioxide in the atmosphere at current concentrations?*
   (b) Would a doubling of Methane have as great an impact on the heat balance as a doubling of Carbon Dioxide?
3. *How do clouds affect the appearance of Earth's IR spectrum?*
4. *Choose a greenhouse gas and increase the gas by a large amount. What is the surface temperature increase required to preserve the same total outgoing flux?*

3.4 Transmission

To understand transmission, we consider the case where there is no scattering nor emission, so that the only extinction in the intensity comes from the absorption. In this case, we start from $\tau' = 0$ and are interested in the intensity at a given optical depth $\tau' = \tau$ with no emission ($\varepsilon = 0$), so that the integral of equation 24 reduces to Beer-Lambert's law:

$$\underbrace{I(\tau)}_{\text{Intensity}} = \underbrace{I(0)}_{\text{Initial intensity}} \underbrace{\exp(-\frac{\tau}{\mu})}_{\text{Transmittance if } \mu=1} \tag{26}$$

For example, if the atmosphere is transparent, its absorptivity is $\kappa = 0$, and Beer-Lambert's law 26 gives $I(\tau) = I(0)$. In contrast, if the atmosphere is opaque κ is high enough so that $I(\tau) \approx 0$ as soon as the ray travels a short physical distance z. We are now interested in planetary examples of radiation transmission.

1. The sun is red at sunset because it has to go through a "longer atmospheric path" (cf figure 32), meaning that the optical depth is larger. As Rayleigh's scattering (which applies as long as the parcels of the atmosphere are smaller than the radiation's wavelength) scales like λ^{-4}, blue light (short visible wavelengths) is scattered out of the solar radiation when it takes the "long path", and only red light remains, making the sun look red.

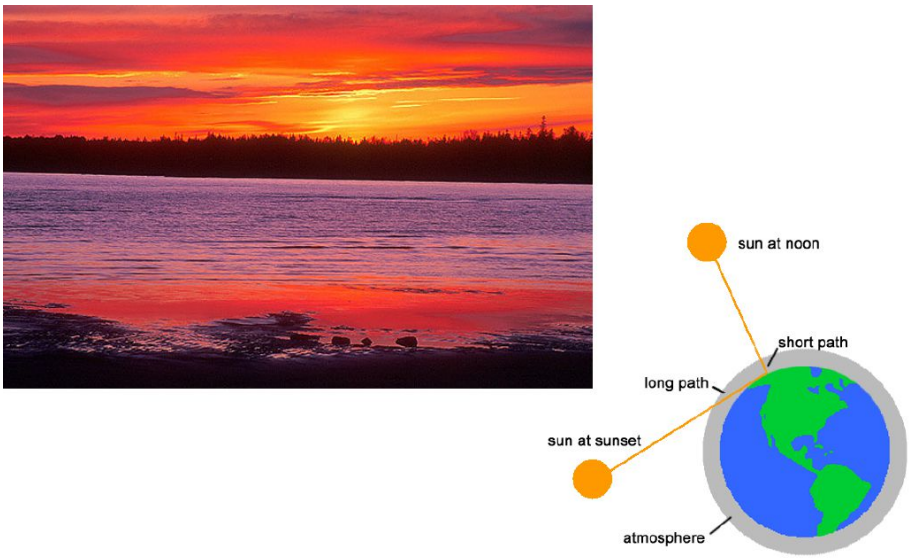

Figure 32: Why is Sun red at sunset?

2. We can also look at the differences between Limb and Nadir remote sensing methods, which look at microwave wavelength (cf figure 33).

Figure 33: Limb and Nadir sounding (left) and the System Microwave limb sounder (MLS, right)

Nadir sounding looks from above at the zenith sky atmospheric transmission (left of figure 34): The main absorption features come from Water vapor, Carbon Dioxide and Ozone. The atmospheric windows ($8-12\mu$m, $3-5\mu$m) are used to measure the concentration of other atmospheric trace gas species. Unlike Nadir, the Limb sounder looks forward from its satellite Aura, which allows it to measure a given slice of the atmosphere. As the transmission through the atmosphere is much better at these higher altitudes, it can measure tracer species which would be very hard to detect looking at the surface of the Earth. In that purpose, it makes passive measurements in broad bands at five distinct frequencies, and is able to produce maps of the potential temperature of nine tracers with concentrations that can be very small (down to pptv, cf right of figure 34).

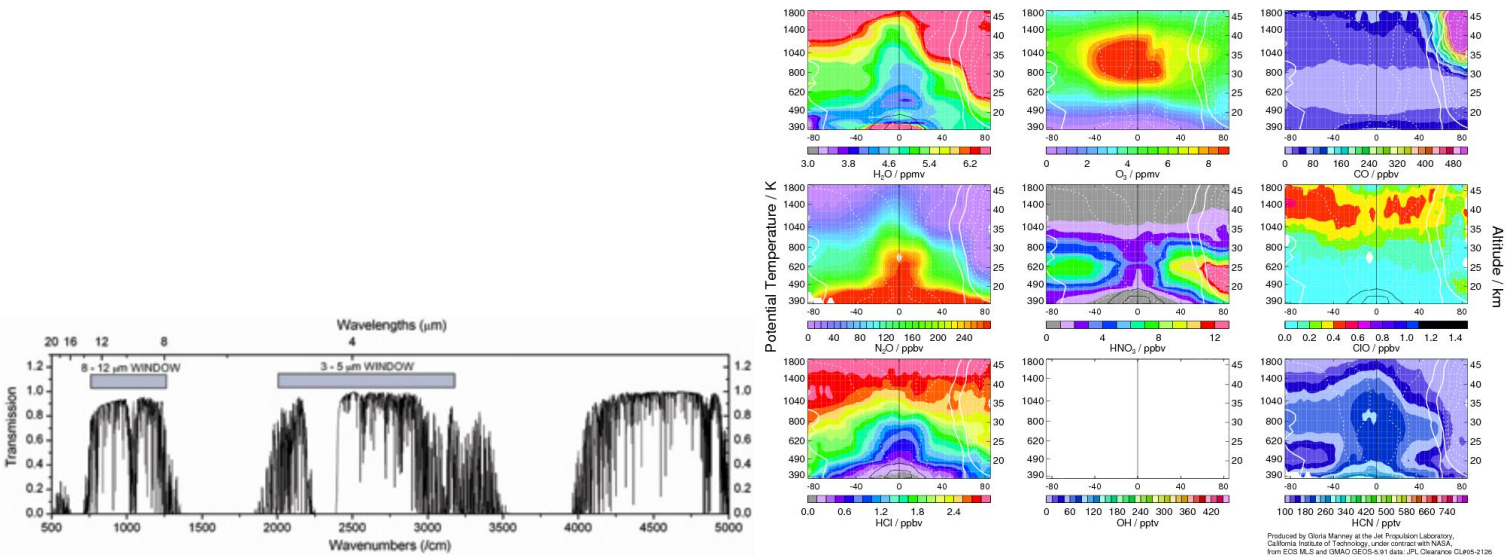

Figure 34: Nadir transmission spectrum (left) and MLS potential temperature maps (right)

3. It is possible to simulate what Earth would look like if it were observed as an exoplanet, in front of the Sun. Figure 35 shows the relative transmission the Earth at different wavelengths. If we look at the most energetic part of the spectrum ($\lambda \sim 0-0.5\mu$m), it is possible to see the Ozone and the Water Vapor absorption peaks forming as we get closer to the surface of the Earth.

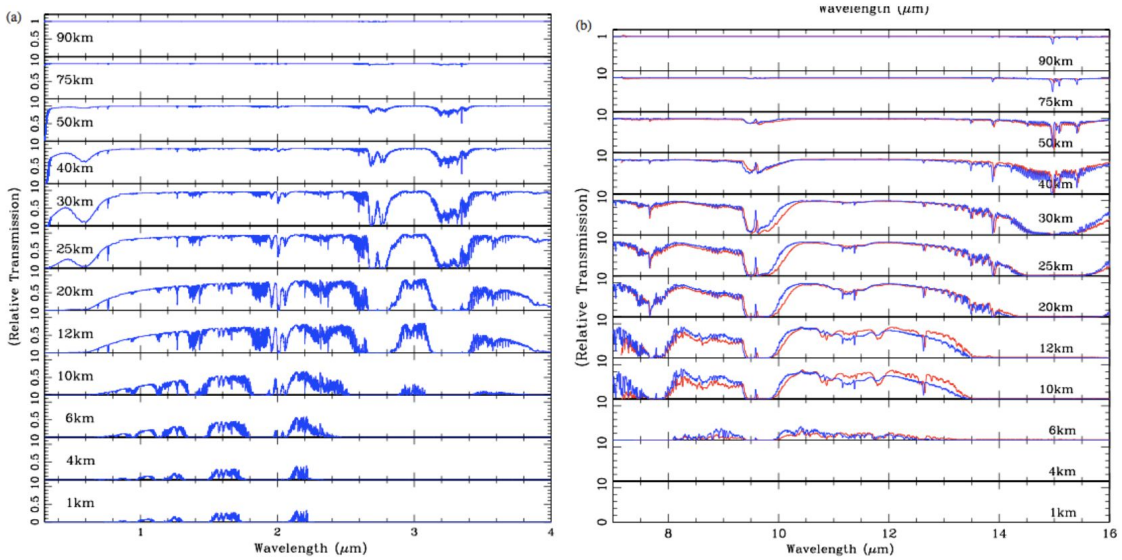

Figure 35: Relative transmission of the "exoplanet Earth" at different altitudes as a function of the wavelength, for $0-4\mu$m (left) and for $7-16\mu$m (right)

However, it doesn't explain the big amount of absorption between 0.5μm and 1μm as we get closer to the surface. To analyze these transmission figures in more details, looking at the relative transmission of the Earth's main absorbers on figure 36 is helpful, and we can see that the big absorption on the left is actually due to aerosols. In the less energetic part of the longwave domain, we can see on figure 36 that the greenhouse gases are strong absorbers with very large effective height, which explains why nothing makes it through the atmosphere near the surface on the right of figure 35.

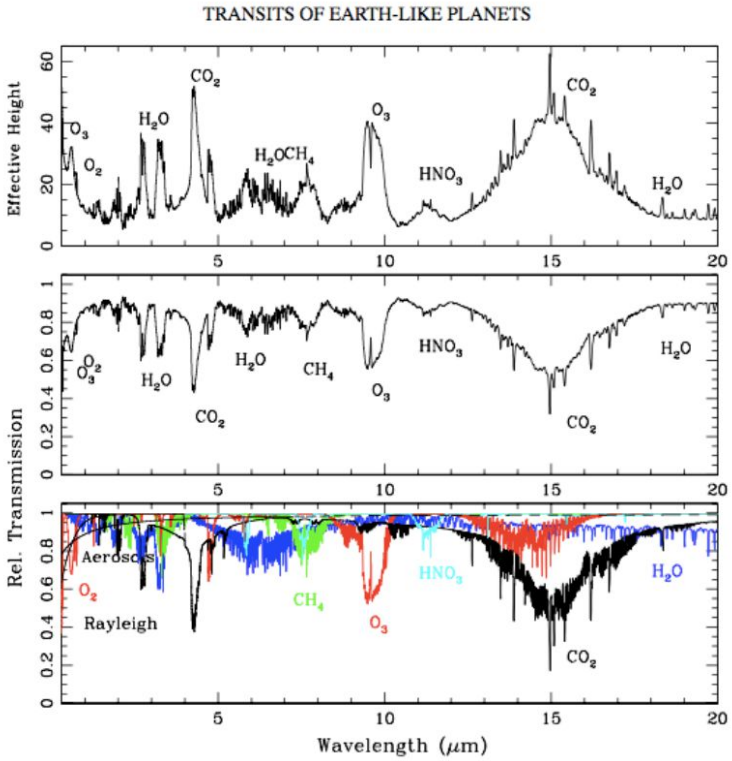

Figure 36: Effective height and relative transmission of the main atmospheric constituents

4. Finally, understanding transmission allows to infer exoplanet atmospheres compositions, when they are in front of a star (left of figure 37). Indeed, when the exoplanet transits across a star, additional light is absorbed by the planetary atmosphere, which makes it look bigger because we have additional absorption peaks in the star's emission spectrum (right of figure 37).

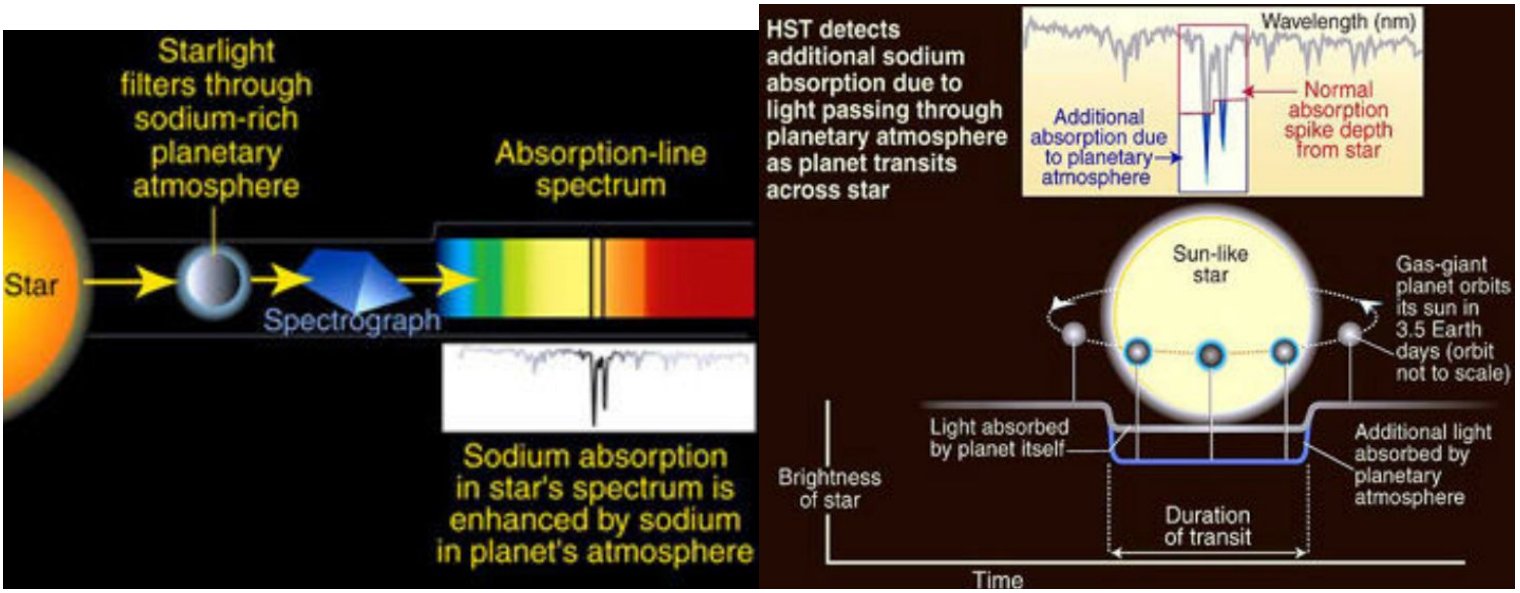

Figure 37: Absorption peaks of an exoplanet transiting across a star

Taking the example of a super Earth, we expect different transmission spectra depending on its composition (left of figure 38). If the main atmospheric constituent is a light constituent, such as H_2, its scale height is very large and we expect the transmission spectrum to include large features allowing us to measure the tracer gas concentrations. However, if the main constituents of the atmosphere are heavy (eg water), the signal will move forward without attenuation for high altitudes or will be entirely absorbed if it travels too close to the surface, which makes it impossible to infer the exoplanet's atmospheric composition. In the latter case, it is possible to observe the exoplanet for a longer time, hoping to detect characteristic features (eg water). In the example shown on the right of figure 38, the additional time does not help inferring the composition of the exoplanet's bulk interior or/and atmosphere, and more precise measurements would not provide more information on that topic.

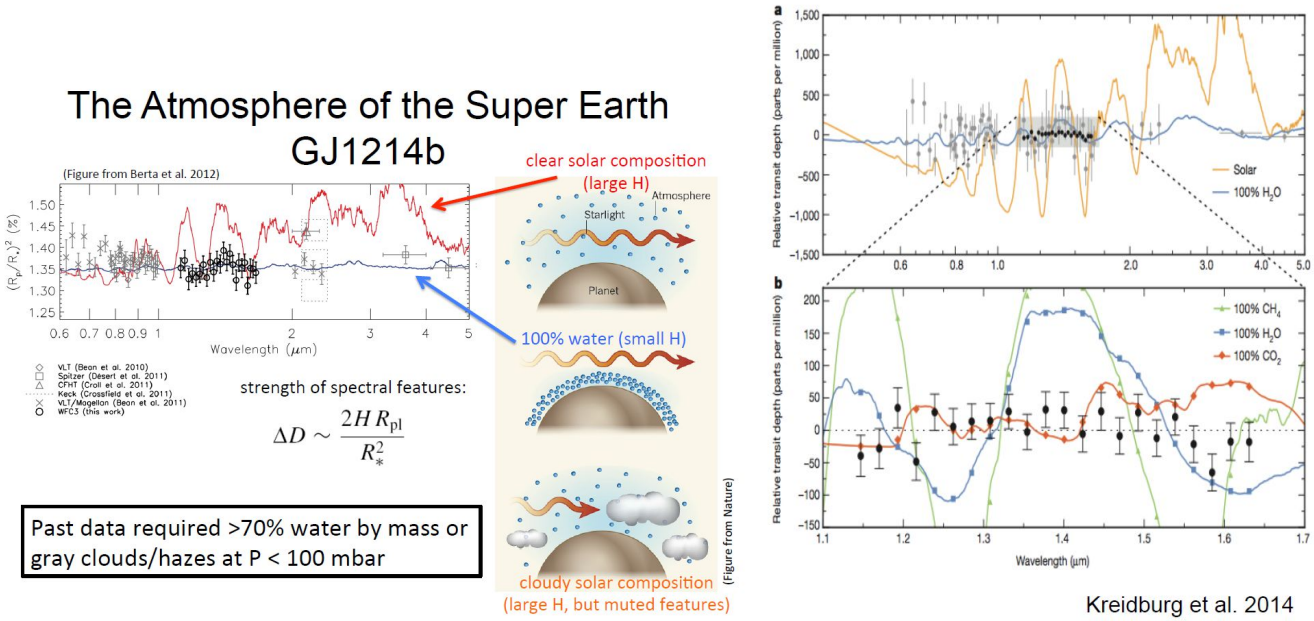

Figure 38: Trying to find the composition of the atmosphere of the Super Earth GJ1214b

If the emission spectrum shows a large scale height with big features along with mutated features, the presence of clouds is suspected on the exoplanet, but being assertive is only possible in specific cases, which explains why so many exoplanets are "suspected to have clouds".

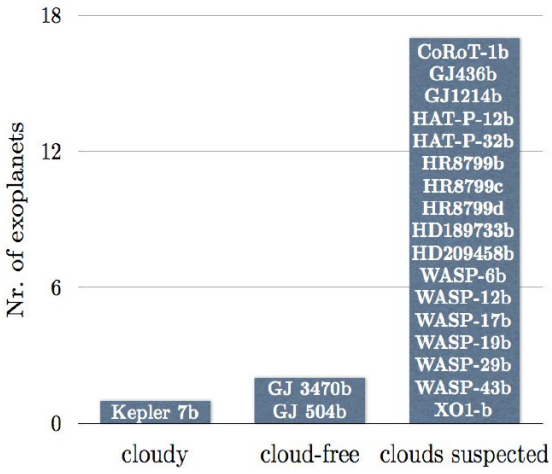

Figure 39: Clouds on exoplanets

When the chemical composition of the atmosphere is known and the atmosphere is suspected to have solid aerosol, laboratory experiments can help determine if it possible for clouds to form on a given exoplanet, as well as probing the scattering properties of these aerosol/clouds.

3.5 RE and consequences on the Earth's climatic budget

We have defined radiative-equilibrium (RE) in 1.2: in a purely radiative context, we can see RE as an energy conservation statement. In a small atmospheric volume, an imbalance in the amount of radiation coming in and out can be seen as a radiative heating/cooling rate. When the amounts coming in and out are the same, the system is in RE and it is possible to compute the atmospheric temperature profile. In RE, an analogy can be drawn between a bathtub and the climatic system. The flow of water through different levels of a fountain represents the flow of photons through the atmospheric layers, with absorption/emission analogous to the mixing/evacuation of the water. From this analogy, it is possible to obtain new insight on the anthropogenic emissions and their consequences on the climatic system:

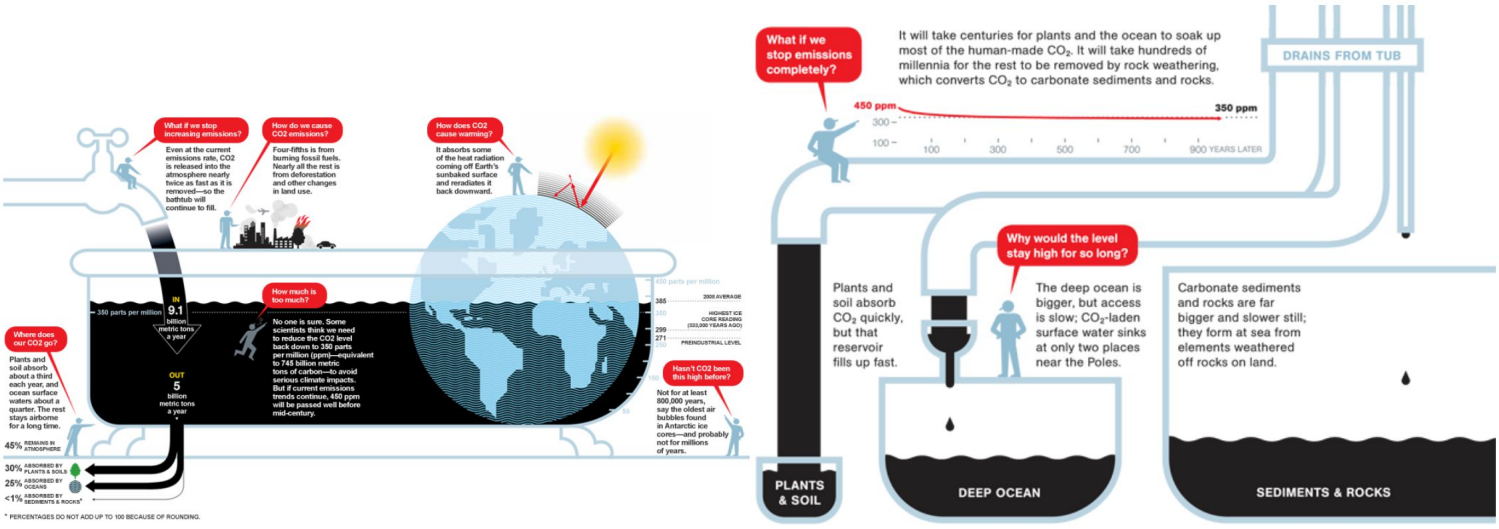

Figure 40: The bathtub analogy for the Earth's Carbon and climatic budgets

We now want to formulate a global version of RE, using the definitions 2.2. Assuming that the absorptivity κ and the emissivity in frequency units ε_ν are isotropic, the balance between absorption and emission integrated over all the atmosphere can be written:

$$4\pi \int_0^{+\infty} \kappa(\tau,\nu) J_\nu(\tau,\nu) d\nu = \int_0^{+\infty} d\nu \int_{(\Omega)} d\Omega \varepsilon_\nu(\tau,\nu) \tag{27}$$

If we assume LTE 3.2, Kirchhoff's law 19 applies and:

$$\int_0^{+\infty} d\nu \int_{(\Omega)} d\Omega \varepsilon_\nu(\tau,\nu) = \int_0^{+\infty} d\nu \int_{(\Omega)} d\Omega \kappa(\tau,\nu) = 4\pi \int_0^{+\infty} \kappa(\tau,\nu) B_\nu(\tau,\nu) d\nu \tag{28}$$

Combining equations 27 and 28 leads to the global statement of RE:

$$\boxed{\int_0^{+\infty} d\nu \kappa(\tau,\nu)[B_\nu(\tau,\nu) - J_\nu(\tau,\nu)] = 0} \tag{29}$$

4 Buoyancy of dry, moist and cloudy air

4.1 Buoyancy

To our knowledge, the concept of buoyancy was historically formulated by Archimedes (250BC). In a fluid with velocity (u,v,w), the vertical momentum equation can be written:

$$\frac{Dw}{Dt} = -\alpha \frac{\partial p}{\partial z} - g \tag{30}$$

where $\alpha = \frac{1}{\rho}$ is the specific volume, p the fluid's pressure, and z the vertical coordinate aligned with the gravity vector $\overrightarrow{g} = -g\overrightarrow{e_z}$. We are interested in variations about the hydrostatic equilibrium, denoted by over-lines and defined by:

$$\overline{\alpha} \frac{\partial \overline{p}}{\partial z} \overset{\text{def}}{=} -g \tag{31}$$

In that purpose, we decompose (α, p, u, v, w) in a hydrostatic component and a perturbation, that we assume to be small:

$$\begin{bmatrix} \alpha \\ p \\ u \\ v \\ w \end{bmatrix} = \begin{bmatrix} \overline{\alpha} \\ \overline{p} \\ 0 \\ 0 \\ 0 \end{bmatrix} + \begin{bmatrix} \alpha' \\ p' \\ u' \\ v' \\ w' \end{bmatrix} \tag{32}$$

Consequently, the vertical momentum budget 30 can be approximated to:

$$\frac{Dw}{Dt} = \frac{\partial w'}{\partial t} + u'\frac{\partial w'}{\partial x} + v'\frac{\partial w'}{\partial y} + w'\frac{\partial w'}{\partial z} \approx \frac{\partial w'}{\partial t} \approx -\alpha' \frac{\partial \overline{p}}{\partial z} - \overline{\alpha}\frac{\partial p'}{\partial z}$$

$$\boxed{\frac{\partial w'}{\partial t} = \underbrace{g\frac{\alpha'}{\overline{\alpha}}}_{\text{Buoyancy}} - \underbrace{\overline{\alpha}\frac{\partial p'}{\partial z}}_{\text{Non hydrostatic pressure perturbation}}} \tag{33}$$

Physically, variations in the density of the fluid generate a vertical acceleration, which is the buoyancy term. The non-hydrostatic pressure perturbation usually scales like the square of the perturbation velocity, which means that it is a small term counteracting the buoyancy force. Integrating the buoyancy term over a finite volume of fluid gives Archimedes law:

$$F_{\text{buoyancy}} = \int_{(V)} \overline{\rho} g \frac{\alpha'}{\overline{\alpha}} dV = -g \int_{(V)} \rho' dV = -gM' = -(M_{\text{immersed object}} - M_{\text{displaced fluid volume}})g \tag{34}$$

where V [m^3] refers to a volume and M [kg] to a mass.

4.2 Moist variables

Because of gravity, density is not constant in the atmosphere. Water vapor/liquid water (H_2O) weights less/more than the main molecular components of the atmosphere (O_2, N_2), which means that variations in the concentration of atmospheric water vapor/condensed water will have consequences on the atmospheric density α^{-1}:

$$\alpha = \frac{V_{\text{air}} + V_{\text{condensed water}}}{M_{\text{dry air}} + M_{\text{water vapor}} + M_{\text{liquid water}}} = \alpha_d \frac{1 + \overbrace{r_T}^{10^{-2}} \frac{\overbrace{\alpha_l}^{10^{-3}}}{\alpha_d}}{1 + r_T} \approx \frac{\alpha_d}{1 + r_T} \tag{35}$$

where we have defined:

- Dry air as the all the constituents of the atmosphere, except water, which mass concentration evolves on much longer time scales. From now on, we will use the subscript d for dry air, v for water vapor and l for liquid water.
- The specific volume of dry air when the mass of water vapor is negligible:

$$\alpha_d \overset{\text{def}}{=} \frac{V_{\text{air}}}{M_{\text{d}}} \tag{36}$$

- The specific volume of condensed water when the mass of liquid water and water vapor are negligible:

$$\alpha_l \overset{\text{def}}{=} \frac{V_l}{M_{\text{d}}} \tag{37}$$

- The total mixing ratio of water:

$$r_T \overset{\text{def}}{=} \frac{M_v + M_l}{M_d} \tag{38}$$

In practice, we do not take into account the deviation of the atmosphere from the ideal gas law, so that the specific volume of dry air is given by:

$$\alpha_d = \frac{R_d T}{p_d} \tag{39}$$

where we have introduced the partial pressure of dry air p_d and the specific gas constant of dry air:

$$R_d \overset{\text{def}}{=} \frac{R^*}{\overline{m_d}} \tag{40}$$

involving the ideal gas constant R^* and the mean molecular weight of dry air $\overline{m_d}$, that we compute from the molecular weight m_i and the mass M_i of each atmospheric molecule i:

$$\overline{m_d} \overset{\text{def}}{=} \frac{\sum_i M_i}{\sum_i m_i^{-1} M_i} \tag{41}$$

We now want to relate p_d to p using the mixing ratio r. From Dalton's law:

$$\frac{p}{p_d} = \frac{p_d + e}{p_d} = \frac{R^* T (\frac{\rho_d}{\overline{m_d}} + \frac{\rho_{\text{v}}}{m_{\text{v}}})}{\frac{R^* T \rho_d}{\overline{m_d}}} = \frac{1 + \frac{r}{\epsilon}}{1 + r_T} \tag{42}$$

where we have defined:

- The partial pressure of water vapor e.
- The mixing ratio of water vapor:

$$r \overset{\text{def}}{=} r_T(M_{\text{l}} = 0) = \frac{M_v}{M_{\text{d}}} = \frac{\rho_{\text{v}}}{\rho_d} \tag{43}$$

- The ratio of the molecular weight of water vapor to the molecular weight of dry air:

$$\epsilon \overset{\text{def}}{=} \frac{m_v}{\overline{m_d}} \approx 0.622 \tag{44}$$

Combining equations 35 and 42, we obtain:

$$\boxed{\alpha \approx \frac{R_d T}{p} \frac{1 + \frac{r}{\epsilon}}{1 + r_T}} \tag{45}$$

Note that in the absence of condensation, the previous expression 45 along with the definition of the mixing ratio 43 give:

$$\alpha = \frac{R_d T}{p} \frac{1 + \frac{r}{\epsilon}}{1 + r} > \frac{R_d T}{p} = \alpha_d \tag{46}$$

This explains why moist air is more buoyant than dry air, which is the basis to understand convection in the absence of latent heating. For meteorological purposes, and in order to write equations 45 and 46 in a more simple way, we can introduce:

- The density temperature:

$$T_\rho \overset{\text{def}}{=} T \frac{1 + \frac{r}{\epsilon}}{1 + r_T} \tag{47}$$

- The virtual temperature:

$$T_v \overset{\text{def}}{=} T_\rho(M_l = 0) = T \frac{1 + \frac{r}{\epsilon}}{1 + r} > T \tag{48}$$

4.3 Stability of dry air

We just saw that the specific volume was clearly not a conserved variable as an air parcel ascends in the atmosphere: we thus need to relate it to a conserved variable. For adiabatic reversible displacement of air parcels, the specific entropy s is conserved, making it a natural choice. To relate changes inα to changes in s, we will derive one of Maxwell's relations, from the first principle of thermodynamics. For a dry ideal gas, an infinitesimal change of specific enthalpy $k = u + p\alpha$ (where u is the specific internal energy) is related to pressure and entropy changes through the second thermodynamic identity:

$$dk = \alpha dp + Tds \tag{49}$$

Note that the second identity 49 can be derived from the first law of thermodynamics by using the definition of the specific enthalpy k:

$$dk \overset{\text{def}}{=} du + d(p\alpha) = -pd\alpha + Tds + d(p\alpha) = \alpha dp + Tds \tag{50}$$

Applying Schwartz's theorem for partial differentials to identity 49 gives us Maxwell relation:

$$\frac{\partial}{\partial s}[(\frac{\partial k}{\partial p})_s]_p = \frac{\partial}{\partial p}[(\frac{\partial k}{\partial s})_p]_s \;\Rightarrow\; (\frac{\partial \alpha}{\partial s})_p = (\frac{\partial T}{\partial p})_s \tag{51}$$

We can now use it to relate the changes in α at constant pressure to the changes in s:

$$\alpha = \alpha(p,s) \;\Rightarrow\; (d\alpha)_p = (\frac{\partial \alpha}{\partial s})_p ds = (\frac{\partial T}{\partial p})_s ds \tag{52}$$

Note that we have neglected the presence of water vapor for simplicity. We will incorporate it when we consider the stability of moist air. Coming back to the definition of buoyancy 33 and using our new equation 52:

$$b = g\frac{\alpha'}{\overline{\alpha}} = \frac{g}{\overline{\alpha}}(\frac{\partial \overline{T}}{\partial p})_s s' = \Gamma_d s' \tag{53}$$

where primes denote the difference of a variable between the air parcel and the environment. We have defined the dry adiabatic lapse rate:

$$\Gamma_d \overset{\text{def}}{=} \frac{g}{\overline{\alpha}}(\frac{\partial T}{\partial p})_s \overset{\text{hydrostatic}}{=} -(\frac{\partial T}{\partial z})_s \overset{\text{ideal gas}}{=} \frac{g}{c_{p_d}} \approx \frac{1°\text{C}}{100\text{m}} \tag{54}$$

where c_{p_d} is the specific heat of dry air at constant pressure. Equation 53 gives a direct relation between the entropy profile and convective stability:

- If $\frac{\partial s}{\partial z} > 0$: Suppose an air parcel has an entropy perturbation $s' > 0$. Then, the buoyancy force will be oriented upwards $b > 0$, and the parcel will be displaced to an environment of higher entropy. As a consequence, s' will decrease, and the air parcel will stabilize. An environment with positive entropy gradient is thus stable.
- If $\frac{\partial s}{\partial z} = 0$, the atmosphere is neutrally stable.
- If $\frac{\partial s}{\partial z} < 0$, the atmosphere is convectively unstable.

In the troposphere, the adiabatic lapse rate Γ does not change dramatically, so that we will often approximate it as constant in class.

5 Convection from maintained and instantaneous point sources and buoyancy

5.1 The Buckingham Pi theorem

Dimensional analysis gives a lot of insight about the physics of a problem, by helping to identify its controlling parameters. Consider a physical system depending on n dimensional quantities q_i: $\varphi(q_1, q_2, ..., q_n)$. The Buckingham Pi theorem states that the dependence of the system can be reduced to m dimensionless parameters Π_i: $\varphi(\Pi_1, \Pi_2, ..., \Pi_m)$. If k is the minimal number of primary quantities needed to express the dimensions of the dimensional quantities q_i:

$$\boxed{m = n - k} \tag{55}$$

Theorem 55 is especially helpful for problems with a small number of parameters.

5.2 Maintained point source of buoyancy: Plumes

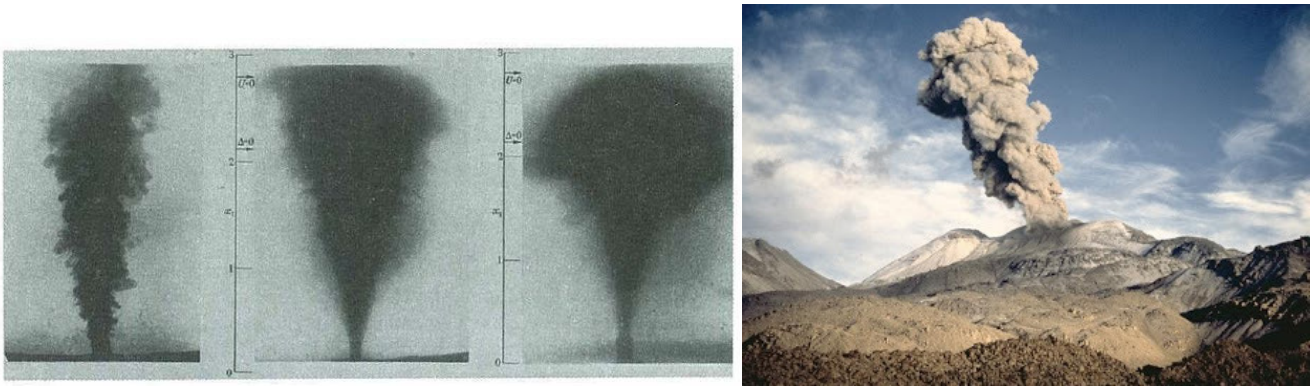

Figure 41: Plumes in neutrally and stably stratified fluid (left) and volcanic plume (right)

Imagine a steady point source of buoyancy: it will generate a plume. Examples of plumes include erupting volcanoes or laboratory plume experiments (cf figure 41). To model a maintained point source of buoyancy, we make the following assumptions:

- The atmosphere is unstratified.
- We approximate the plume as fully turbulent, which means that the convection is independent of molecular viscosities.
- We make the Boussinesq approximation, and neglect the density variations of the fluid, except when they are coupled with gravity (ie the buoyancy force).

By definition, the buoyancy flux $\mathcal{F}_b$ is the supply of buoyancy to the fluid:

$$\mathcal{F}_b \sim \text{Velocity} \cdot \text{Area} \cdot b \;\Rightarrow\; [\mathcal{F}_b] = L^4.T^{-3} \tag{56}$$

If we assume that the area of the source is infinitesimally small, the buoyancy flux and the altitude z are the only controlling parameter of the problem. According to the Pi theorem , the dependence of the system can be reduced to $2-2=0$ dimensionless parameters, which allows us to find their scaling through dimensional analysis. For instance, we find the scaling of:

- The vertical velocity in the plume:
$$[w] = L.T^{-1} \;\Rightarrow\; w \sim (\frac{\mathcal{F}_b}{z})^{\frac{1}{3}} \tag{57}$$
- The horizontal velocity in the plume:
$$[u] = L.T^{-1} \;\Rightarrow\; u \sim w \sim (\frac{\mathcal{F}_b}{z})^{\frac{1}{3}} \tag{58}$$
which means that mass is not conserved within the plume: there is an entrainment rate of air equal to the vertical velocity in the plume.
- The radius of the plume
$$[R] = L \;\Rightarrow\; R \sim z \tag{59}$$
which implies a conical cross-section, consistently with what we observe when laboratory experiments are made (figure 41).
- The buoyancy itself:
$$[b] = L.T^{-2} \;\Rightarrow\; b \sim (\frac{\mathcal{F}_b^2}{z^5})^{\frac{1}{3}} \tag{60}$$
- The volume flux:
$$[Q] = L^3.T^{-1} \;\Rightarrow\; Q \sim R^2 w \sim (\mathcal{F}_b z^5)^{\frac{1}{3}} \tag{61}$$

The success of dimensional analysis relies in the simplicity of our solutions, compared to the complexity of the problem. Laboratory experiments allows to compute the constant in front of the power law scalings found previously, and from similarity arguments we can extend the formulas to the geophysical world. They also allows us to check the consistency of our scaling law, helping us identify the main control parameters of the problem. Experimentally, Yih (1951) found that the following laws for the vertical velocity, the buoyancy and the radius:

$$w = 4.7(\frac{\mathcal{F}_b}{z})^{\frac{1}{3}} \exp(-\frac{96R^2}{z^2}) \tag{62}$$

$$b = 11.0(\frac{\mathcal{F}_b^2}{z^5})^{\frac{1}{3}} \exp(-\frac{71R^2}{z^2}) \tag{63}$$

$$R = 0.12z \tag{64}$$

Comparing formulas 62, 63 and 64 to 57, 60 and 59 confirms that dimensional analysis gives a proper scaling for (w, b, R), but that experiments are still needed to confirm that scaling and obtain the quantitative dependence of these quantities.

5.3 Instantaneous point source of buoyancy: Thermals

5.3.1 Unstratified problem

The previous laws rely on the fact that we only had two controlling parameters for the system. They do not apply when the point source of buoyancy is time-dependent. Another model with no time-dependence is the instantaneous point source of buoyancy. In this case, there is no maintained buoyancy flux; instead, at time $t = 0$, the point source of buoyancy releases a given amount of buoyancy:

$$B \overset{\text{def}}{=} \int_{\text{(Plume)}} b dV \;\Rightarrow\; [B] = L^4.T^{-2} \tag{65}$$

The controlling parameters for this problem are now (B, z), meaning that the Pi theorem 55 tells us that the system is controlled by $2 - 2 = 0$ dimensionless parameters. It is straightforward to derive different scaling laws for all the quantities studied in section 5.2. In particular, the vertical velocity scaling is:

$$[w] = L.T^{-1} \;\Rightarrow\; w \sim \frac{\sqrt{B}}{z} \tag{66}$$

If we compare this scaling law for the vertical velocity to the one obtained for the maintained point source of buoyancy 57, we can see that w decreases much faster with altitude in the case of an instantaneous point source of buoyancy. Physically, we know that the plume is slowing for two reasons:

1. The plume entrains and transfer momentum to a larger and larger volume of quiescent air around it.
2. The plume mixes the fluid on a larger and larger radius $R \sim z$.

In the case of an instantaneous point source, the plume is entraining a third dimension that was not present in the two-dimensional maintained point source case. Thus, the dilution process is more costful, which explains why the vertical variations in w are larger. If several point source of buoyancy are separated by a distance L, dimensional analysis only allows us to find the scaling laws at a large enough vertical distance from the plume $\Delta z \gg L$, where all the plumes look like "one merged plume". However, by doing laboratory experiments, it can be shown that the different plumes entrain themselves mutually, which mean that they merge relatively close to the ground, and that we can hope that are scaling laws apply for small z. An old application of this phenomenon was to align burners on both side of the runways of an airport to dissipate the fog and allow planes to take off.

5.3.2 Constant stratification

If the atmosphere follows a dry adiabat defined by equation 54, it can be shown that the potential temperature θ is conserved with altitude:

$$\theta \overset{\text{def}}{=} T(\frac{p_0}{p})^{\frac{R_d}{c_{p_d}}} \tag{67}$$

By definition, the dry entropy is also conserved with altitude:

$$s_d \overset{\text{def}}{=} s_0 + c_{p_d} \ln(\frac{T}{T_0}) - R_d \ln(\frac{p}{p_0}) = s_0 + c_{p_d} \ln(\frac{\theta}{T_0}) \tag{68}$$

where s_0 is the reference entropy at the reference temperature T_0 and the reference pressure p_0. Note that for a moist atmosphere with no phase change, we have seen in subsection 4.2 that the ideal gas specific constant has to be changed, and the specific heat capacity of the gas at constant pressure also changes. However, the ratio of these two quantities $R_d c_{p_d}^{-1}$ is found not to change very much when water vapor is taken into account, which means that θ is still approximately conserved with altitude if the atmosphere is unstratified. If the fluid is stably stratified, the dry entropy and thus the potential temperature both increase with altitude, which we can quantify by introducing the Brunt-Vaisala/buoyancy frequency:

$$N^2 \overset{\text{def}}{=} \frac{g}{\theta}\frac{d\theta}{dz} = \frac{g}{c_p}\frac{ds}{dz} \;\Rightarrow\; [N] = T^{-1} \tag{69}$$

We are now in measure of analyzing the problem of a thermal in an environment of constant stratification (ie the buoyancy frequency does not vary with altitude). Dimensional analysis tells us that the typical vertical scale H is governed by a dimensionless combination of the two controlling parameters of the problem: the buoyancy frequency and the total buoyancy of the thermal B, defined in 65:

$$[H] = L \;\Rightarrow\; H \sim (\frac{B}{N^2})^{\frac{1}{4}} \tag{70}$$

Qualitatively, the fluid parcel accelerates up until it has negative buoyancy at a height H, where the thermal will stop accelerating. We are now going to make progress by applying momentum and heat budgets to the plume, based on the Navier-Stokes equations integrated over the thermal, and several assumptions:

1. The flow is steady.
2. The radial profiles of mean vertical velocity and mean buoyancy are similar at all heights.
3. Based on scaling 58, the mean turbulent inflow is proportional to the vertical velocity: $u = -\alpha|w|$.
4. We make the Boussinesq approximation for the flow, ie we only consider fluid density variations when they are coupled with gravity.

We write the following conservation laws for the thermal:

- Mass conservation:
$$\frac{D}{Dt}(\frac{4\pi}{3}R^3) = -4\pi R^2 u = 4\pi R^2 \alpha |w| \tag{71}$$
- Momentum conservation:
$$\frac{D}{Dt}(\frac{4\pi}{3}R^3 w) = \frac{4\pi}{3}R^3 b \tag{72}$$
where we define the buoyancy based on a constant reference temperature θ_0:
$$b \stackrel{\text{def}}{=} g\frac{\theta - \theta_0}{\theta_0} \tag{73}$$
- Heat/Buoyancy conservation:
$$\frac{D}{Dt}[\frac{4\pi}{3}R^3(\theta - \theta_0)] = -4\pi R^2 u(\overline{\theta} - \theta_0) = 4\pi R^2 \alpha w(\overline{\theta} - \theta_0)$$
Using :
$$\frac{D}{Dt}[\frac{4\pi}{3}R^3(\theta - \theta_0)] = (\overline{\theta} - \theta_0)\frac{D}{Dt}(\frac{4\pi}{3}R^3) = \frac{D}{Dt}[(\overline{\theta} - \theta_0)\frac{4\pi}{3}R^3] - \frac{4\pi}{3}R^3 \underbrace{\frac{D}{Dt}(\overline{\theta} - \theta_0)}_{w\frac{d\overline{\theta}}{dz}}$$
we can write the buoyancy conservation as a function of the Brunt-Vaisala frequency defined in 69:
$$\frac{D}{Dt}(\frac{4\pi}{3}R^3 b) = \frac{4\pi}{3}R^3 w N^2 \tag{74}$$

We simplify the problem by introducing the following variables:

$$M \stackrel{\text{def}}{=} R^3 w \tag{75}$$
$$V \stackrel{\text{def}}{=} R^3 \tag{76}$$
$$F \stackrel{\text{def}}{=} R^3 b \tag{77}$$

The initial conditions for these variables are given by:

$$M = V = 0 \ @ \ T = 0 \tag{78}$$
$$F = F_0 = \frac{3B}{4\pi} \ @ \ T = 0 \tag{79}$$

We combine (M, V, F, t) with the buoyancy frequency N (controlling parameter) to obtain a set of dimensionless variables:

$$f \stackrel{\text{def}}{=} \frac{F}{F_0} \tag{80}$$
$$m \stackrel{\text{def}}{=} \frac{4\pi}{3}\frac{MN}{F_0} \tag{81}$$
$$v \stackrel{\text{def}}{=} (\frac{\pi N^2}{3\alpha F_0})^{\frac{3}{4}} V \tag{82}$$
$$t \stackrel{\text{def}}{=} NT \tag{83}$$
$$z \stackrel{\text{def}}{=} 4(\frac{\pi\alpha^3 N^2}{3F_0})^{\frac{1}{4}} z_{\text{dim}} \tag{84}$$

where z_{dim} is the dimensional altitude. The conservation statements 71, 72 and 74 can then be written in a very simple dimensionless form:

- Momentum budget:

$$\boxed{\frac{dm}{dt} = f} \tag{85}$$

- Buoyancy budget:

$$\boxed{\frac{df}{dt} = -m} \tag{86}$$

- Mass budget:

$$\boxed{\frac{dv^{\frac{4}{3}}}{dt} = |m|} \tag{87}$$

- Velocity definition:

$$\boxed{\frac{dz}{dt} = w = \frac{m}{v}} \tag{88}$$

The absolute value in the mass budget 87 means that the mass of the thermal can only increase. This is an indirect consequence of the second principle of thermodynamics, which implies that turbulent entrainment is irreversible. In dimensionless form, the initial conditions 78 and 79 become:

$$m = v = 0 \ @ \ t = 0 \tag{89}$$

$$f = 1 \ @ \ t = 0 \tag{90}$$

For the initial conditions 89 and 90, we find the following analytical solution for $0 \leq t \leq \pi$:

$$R = v^{\frac{1}{3}} = (1 - \cos t)^{\frac{1}{4}} \tag{91}$$

$$w = \frac{m}{v} = \frac{\sin t}{(1 - \cos t)^{\frac{1}{4}}} \tag{92}$$

$$b = \frac{f}{v} = \frac{\cos t}{(1 - \cos t)^{\frac{1}{4}}} \tag{93}$$

$$z = 4(1 - \cos t)^{\frac{1}{4}} \tag{94}$$

To compute the solutions for all $t > 0$, look at the values of the variables at $t = \pi$, solve the equation on $]\pi, 2\pi[$, and reiterate the process, giving the solutions plotted on figure 42.

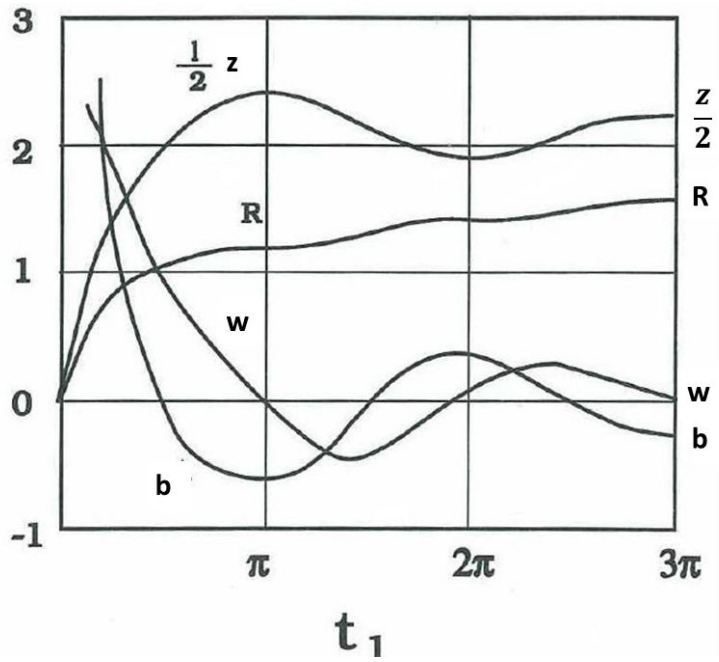

Figure 42: Plot of dimensionless solutions 91, 92, 93 and 94 vs dimensionless time 83

We can see that the radius of the thermal increases until the air parcel overshoots when its buoyancy becomes smaller than that of the environment at $t \approx \pi$. We can see that the vertical velocity w and the buoyancy b of the thermal undergo damped oscillations:

- Before the overshooting happens, the thermal entrains colder air, which decreases the momentum and the buoyancy of the thermal.
- Once it has overshot, the air parcels are less buoyant than the environment, and they entrain warmer air as they sink back in the fluid, increasing the momentum and the buoyancy of the thermal.
- Because of their inertia, the parcels sink down below the overshooting point, meaning that they are warmer than they environment, which means that the oscillation can repeat itself.

A concrete application of the plume scaling laws has been to estimate the risk of stratospheric pollution during the Gulf War. Imagine that oil wells are all set on fire for diverse reasons. Will the resulting plume enter the stratosphere if:

(a) The oil production of the country is 10^7barrels/day *where* 1barrel $=$ 160kg.

(b) There are approximately 1000 *active oil wells of roughly equal production.*

(c) The heating value of gasoline is about $4.7.10^7$J.kg^{-1}.

(d) The surface air density is about 1.2kg.m^{-3} *and its temperature is roughly* 300K. *The heat capacity at constant pressure of air is about* 10^3J.kg^{-1}.K^{-1}.

(e) The troposphere extends upwards to about 10kg *and has an average buoyancy frequency of* 10^{-2}s^{-1}.

If we compute the conservation laws for a plume in a fluid of constant stratification, we also get a nonlinear set of equations for (w, b, R), but this time there are no analytical solutions which means that the equations need to be integrated numerically. From the left of figure 41, we can see that the plume ascends and spreads out above the overshooting level. Experiments allow us to get more insight in the physics of the thermals of the plumes: for instance, we can see on figure 43 that the thermals are self-similar at a microscopic scale.

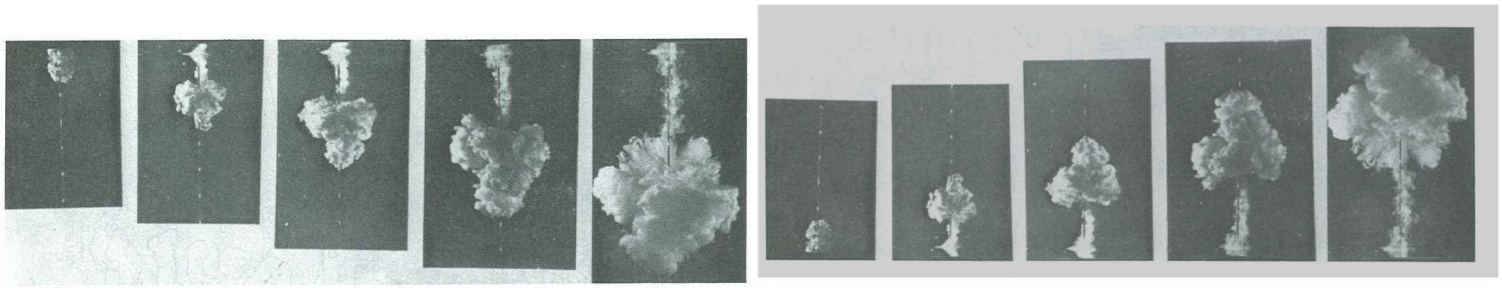

Figure 43: Successive photos of the descending thermal (left) and the same photo turned upside down (right)

Returning the left of figure 43 gives the right of figure 43, which is similar to an ascending cumulus cloud. The fact that we can't deduce the orientation of the photo by looking at it proves the symmetry in thermal ascent/descent. Work has also been done on how thermals expand with altitude and time: as we can see on the left of figure 44 and from dimensional analysis we find $z^2 \sim t$. Observing the motion of the parcels within the thermal shows that they undergo a toroidal motion (cf right side of figure 44).

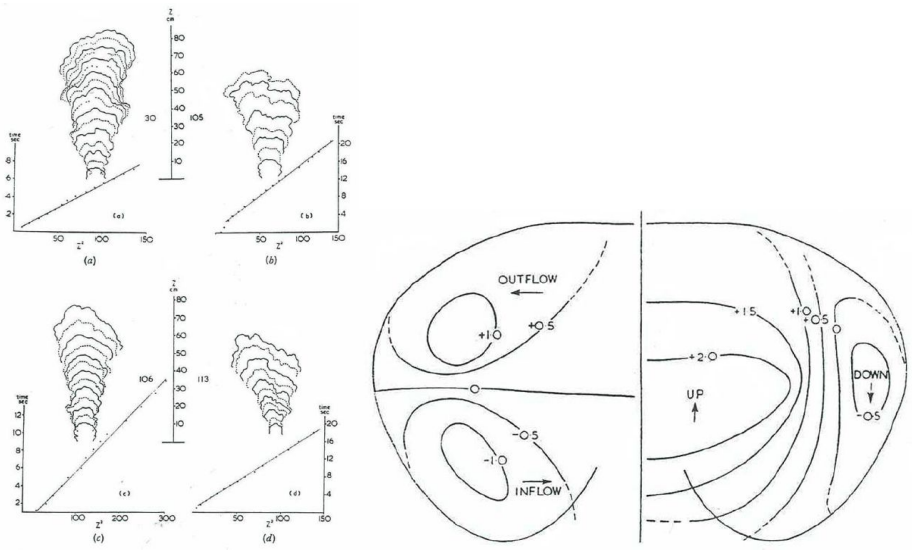

Figure 44: Successive outlines of thermals traced from photographs (left) and distribution of radial and vertical velocities in a thermal obtained by observing the motion of particles within it (right)

6 The Prandtl problem

6.1 Irrelevance of the Rayleigh-Bénard problem

Another case where dimensional analysis can be insightful is where the dimension of the buoyancy source is chosen to be infinite. The Rayleigh-Bénard problem, which has been stated at the very end of the nineteenth century, consists of a fluid of height H heated at the bottom and cooled at the top, giving to the fluid a buoyancy b (cf left of figure 45). It is the archetype of convection in classical fluid dynamics.

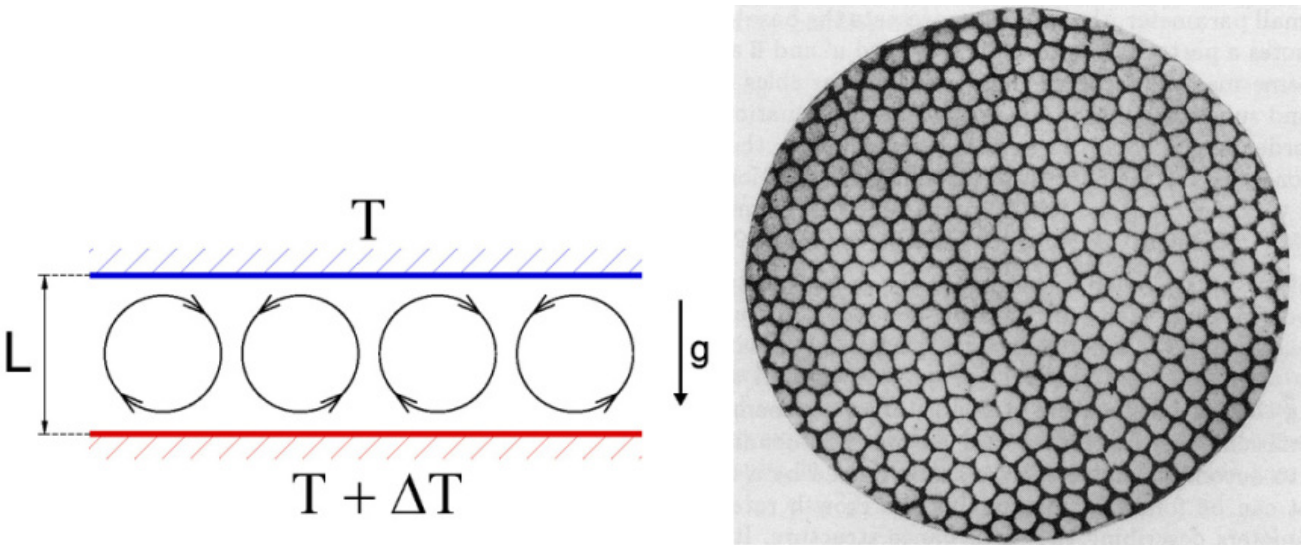

Figure 45: Rayleigh-Bénard convection cell (left) not to be confused with Bénard Marangoni cells (right) that rely on the surface tension of the fluid

Adding the mechanical diffusivity ν and the thermal diffusivity κ, Rayleigh-Bénard convection is governed by four dimensional parameters in total: (H, b, ν, κ). According to the Pi theorem 55, the dependence of the problem can be reduced to two dimensionless parameters:

- The Prandtl number:
$$\mathrm{Pr} \stackrel{\text{def}}{=} \frac{\nu}{\kappa} \tag{95}$$
- The Rayleigh number, proportional to the buoyancy b of the fluid:
$$\mathrm{Ra} \stackrel{\text{def}}{=} \frac{bH^3}{\nu\kappa} \tag{96}$$

Linear stability analysis proves that the system will become linearly unstable for $\mathrm{Ra} \geq \frac{27\pi^4}{4}$. Consequently, convection cells will appear in the fluid. From the most unstable wavenumber, it can be shown that the wavelength of the first cell to appear is $\lambda = 2\sqrt{2}H$. This problem has received a lot of theoretical, numerical and experimental attention, and its details can be found all over the literature in fluid dynamics and applied mathematics. However, because the Rayleigh-Bénard problem assumes two flat surfaces, there will always be diffusive boundary layers, making the problem depend on the diffusivities (ν, κ). Even when experiments are done with Rayleigh number as high as 10^{23}, the energy dissipation and some scalings in the problem will always depend on those diffusivities. Because geophysical boundaries are rough (ie fractal), atmospheric convection does not depend on molecular diffusivities in practice, which explains why the rich literature on Rayleigh-Bénard problem does not necessarily help understanding atmospheric convection better.

6.2 Prandtl convective boundary layer

In 1925, Prandtl introduced a problem more relevant to atmospheric convection: a fluid is cooled at constant rate everywhere and heated at its lower boundary, which produces a constant flux of total buoyancy $\mathcal{F}_b$ $[\mathrm{m}^2.\mathrm{s}^{-3} \equiv \mathrm{W.kg}^{-1}]$ (cf figure 46).

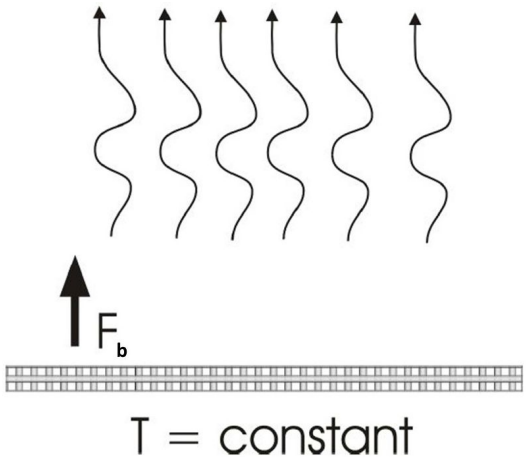

Figure 46: Schematic of the Prandtl problem

We make the Boussinesq approximation again, and suppose that the cooling eventually drives the fluid to be unstable. The instability of the fluid leads it eventually to a statistically steady state where it is fully turbulent, so that the the buoyancy flux per unit area balances the vertically integrated sink of buoyancy imposed to the fluid; from the first law of thermodynamics:

$$\dot{Q} = -c_p \frac{D\theta}{Dt} = -\frac{c_p \theta_0}{g} \frac{Db}{Dt} \tag{97}$$

where we have used the definition of buoyancy 73 and introduced the radiative heating rate of the cooling $\dot{Q}$ [W.kg^{-1}]. Integrating the local balance 97 over an atmospheric column, we can relate the buoyancy flux to the radiative heating rate:

$$\mathcal{F}_b = -\frac{g}{c_p \theta_0} \int_0^{+\infty} \dot{Q} dz \tag{98}$$

Because of this homogeneous cooling, the Prandtl problem is much more difficult to set up in a laboratory, which might explain why experimental studies of it are much less frequent. However, dimensional analysis is simpler in this case, as the rough boundary makes the turbulence independent of the molecular diffusivities in practice. Dimensionally, we have two controlling parameters $(\mathcal{F}_b, z)$, and two dimensions (L, T). According to the Pi theorem 55, any variable of the system is controlled by 0 parameter and can once again be written as a combination of the controlling parameters:

- The turbulent velocity scales like:
$$q \sim (\mathcal{F}_b z)^{\frac{1}{3}} \tag{99}$$
- The buoyancy scales like:
$$b \sim (\frac{\mathcal{F}_b^2}{z})^{\frac{1}{3}} \tag{100}$$
Similarly to the scaling found for plumes (cf scalings 57 and 60), there is a singularity for $z \to 0$. For plumes, the explanation was that the source is never a strict point. In the case of a rough surface, the explanation relies in the fact that it is impossible to precisely define $z = 0$ as the surface is fractal, and there is no singularity in practice as we always work above the rough surface.
- The buoyancy frequency scales like:
$$N^2 = \frac{g}{\theta_0} \frac{d\overline{\theta}}{dz} \sim (\frac{\mathcal{F}_b}{z^2})^{\frac{2}{3}} \tag{101}$$
From the previous scaling 101, we can integrate the environmental potential temperature profile:
$$\overline{\theta}(z) = T_0 - C_1 \frac{\theta_0}{g} \mathcal{F}_b^{\frac{2}{3}} [(z_{0T})^{-\frac{1}{3}} - z^{-\frac{1}{3}}] \;\Leftrightarrow\; \mathcal{F}_b = \sqrt{\frac{(z_{0T}^{-1} - z^{-1})^{-1}}{C_1^3} [\frac{g}{\theta_0}(T_0 - \overline{\theta}_\infty)]^3} \tag{102}$$
where we have defined the thermal roughness length z_{0T} and the reference temperature T_0 such that $\overline{\theta}(z_{0T}) = T_0$. C_1 is an integration constant.

From the environmental potential temperature profile 102, we can see that there is a finite temperature difference between the ground of temperature T_0 and the constant temperature above the surface layer:

$$\overline{\theta}_\infty = \overline{\theta}(z \to +\infty) = T_0 - C_1 \frac{\theta_0}{g} (\frac{\mathcal{F}_b^2}{z_{0T}})^{\frac{1}{3}} \tag{103}$$

we can express the buoyancy flux above the surface layer:

$$\mathcal{F}_b(z \to +\infty) = \sqrt{\frac{z_{0T}}{C_1^3}[\frac{g}{\theta_0}(T_0 - \overline{\theta}_\infty)]^3} \tag{104}$$

The previous expression 104 is in a meteorological context to relate temperature differences to the surface buoyancy flux. However, the result strongly depends on how well the roughness length z_{0T} is measured, making it a key parameter in the problem. The thermal rough boundary is what makes the physics independent of the molecular diffusivities, which explains why the Prandtl problem is relevant in a geophysical context. Except for the surface layer, which is quite small, the potential temperature (and thus the entropy) is conserved with height, which is expected for a neutrally stable convective layer, and confirmed by model aircraft measurements (cf figure 47).

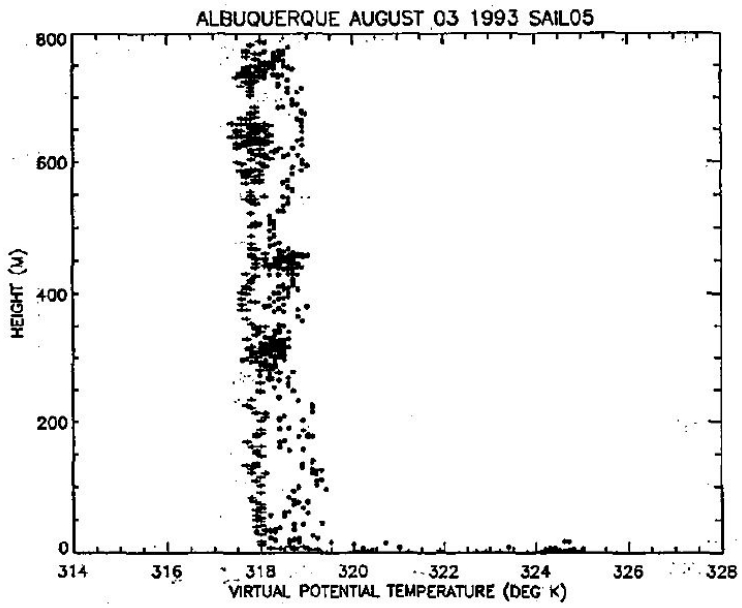

Figure 47: Virtual potential temperature profile from aircraft measurements (Renno and Williams, 1995)

We can see that real profiles are closer to convective neutrality than to radiative neutrality, confirming the relevance of the Prandtl problem to the atmosphere.

6.3 Mechanically generated turbulence

Now that we have a basic understanding of thermally generated turbulence, we are going to study shear-generated turbulence. Surface turbulent fluxes are generally observed to be even more sensitive to shear instability than to convective instability. We adopt a very similar setting than for the Prandtl problem:

- We consider a rough boundary of roughness length z_0.
- We make the Boussinesq approximation for the fluid.
- However, this time, instead of a heat sink, we impose a finite momentum source everywhere in the atmosphere, which accelerates the fluid in the $x-$direction:

$$\dot{M} = \int_0^{+\infty} \alpha_0 \frac{\partial p}{\partial x} dz \;\Rightarrow\; [\dot{M}] = L^2.T^{-2} \tag{105}$$

where α_0 is the incompressible specific volume and p the atmospheric pressure. Fluid accelerates in the $x-$direction. Because of this momentum source and the no-slip condition at the ground, we expect the mean flow $\overline{u}$ to increase with the height z. In equilibrium, the momentum transfer to the fluid must be balanced by a downward flux of momentum towards the ground: $\overline{u'w'} = \dot{M}$. Once again, we only have two controlling parameters $(\dot{M}, z)$ and two dimensions (L, T); the Pi theorem 55 states that the physics are controlled by zero dimensionless parameters.

- Unlike the case of thermally-generated turbulence, the velocity fluctuations do not depend on altitude:

$$u' \sim \sqrt{\dot{M}} \tag{106}$$

- The shear's scaling is given by:

$$\frac{d\overline{u}}{dz} \sim \frac{\sqrt{\dot{M}}}{z} \;\Rightarrow\; \frac{d\overline{u}}{dz} = C_3 \frac{\sqrt{\dot{M}}}{z} \tag{107}$$

Integrating the previous equation 107 from the roughness length to an altitude z, we obtain a logarithmic velocity profile:

$$\overline{u} = C_3 \sqrt{\dot{M}} \ln(\frac{z}{z_0}) \;\Leftrightarrow\; \dot{M} = \frac{\overline{u}}{C_3 \ln(\frac{z}{z_0})} \tag{108}$$

- Now consider a passive tracer φ with a source/sink everywhere in the atmosphere and a compensating sink/source at the ground, given by:

$$\mathcal{F}_\varphi = \int_0^{+\infty} \dot{\varphi} dz = \text{Flux of } \varphi \text{ through surface} \;\Rightarrow\; [\mathcal{F}_\varphi] = [\varphi].L.T^{-1} \tag{109}$$

We use dimensional analysis again to find the variations of $\overline{\varphi}$ with height:

$$[\frac{d\overline{\varphi}}{dz}] = [\varphi].L^{-1} \;\Rightarrow\; \frac{d\overline{\varphi}}{dz} \sim \frac{\mathcal{F}_\varphi}{z\sqrt{\dot{M}}} \;\Rightarrow\; \frac{d\overline{\varphi}}{dz} = -C_4 \frac{\mathcal{F}_\varphi}{z\sqrt{\dot{M}}} \tag{110}$$

Integrating the previous relation from $z' = z_0$ to $z' = z$:

$$\overline{\varphi} = \overline{\varphi_0} - \frac{C_4 \mathcal{F}_\varphi}{\sqrt{\dot{M}}} \ln(\frac{z}{z_0}) \;\Leftrightarrow\; \mathcal{F}_\varphi = \frac{\sqrt{\dot{M}}(\overline{\varphi} - \overline{\varphi_0})}{C_4 \ln(\frac{z}{z_0})} \tag{111}$$

In meteorology, it is hard to measure the very low wind at ground level. We thus measure it at an altitude z_a, which then allows us to compute the flux of any passive tracer φ at $z = z_a$ if we know its mean value at this height $\overline{\varphi}_a$:

$$\overline{u}(z_a) = \overline{u}_a = C_3 \sqrt{\dot{M}} \ln(\frac{z_a}{z_0}) \;\Leftrightarrow\; \mathcal{F}_a = \frac{\overline{u}_a(\varphi_0 - \overline{\varphi}_a)}{C_3 C_4 \ln^2(\frac{z_a}{z_0})} \tag{112}$$

When using formula 112, meteorologists and oceanographers are usually trying to obtain the flux of a tracer from the value of the wind. However, it is important to be cautious with causality. In our case, the wind is generated by the momentum source and the boundary layer, and wind values not too far from the surface are strongly dependent on the boundary layer in practice, which makes the actual problem more intricate than taking the wind as a given.

6.4 Competition between thermally and mechanically generated turbulences

In the real world, turbulence is both:

- Thermally generated by buoyancy fluxes $\mathcal{F}_b$ with dimensions $L^2.T^{-3}$.
- Mechanically generated by momentum sources $\dot{M}$ with dimensions $L^2.T^{-2}$.

From this two sources, it is possible to form a length scale, called the "Monin-Obukhov length":

$$L \overset{\text{def}}{=} -\frac{\dot{M}^{\frac{3}{2}}}{\mathcal{F}_b} \tag{113}$$

Note the negative sign in the definition 113, so that $L > 0$ for a convectively stable surface layer where $\mathcal{F}_b < 0$. During the day, we expect $\mathcal{F}_b > 0 \;\Rightarrow\; L < 0$, whereas we expect $\mathcal{F}_b < 0 \;\Rightarrow\; L > 0$ during the night, so that $L \to \pm\infty$ at dawn and dusk. Physically, L allows us to separate between the dominance of thermally/mechanically generated turbulence: For $z > L$, thermally generated turbulence dominates whereas shear generated turbulence dominates for $z < L$. In practice, $|L|$ lies somewhere between the surface and the top of the boundary layer. As L is usually fairly small, convection mostly feels shear turbulence. As we can see on figure 48, the typical profile of the physical quantities of interest lie between their thermal and mechanical limits.

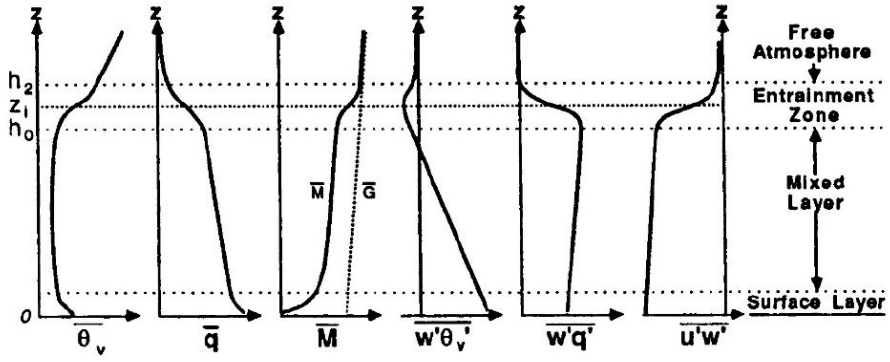

Figure 48: Typical profiles of quantities in a convective boundary layer

As a consequence, we need to interpolate the quantities between their two limits, based on physical intuition and field experiments:

- The velocity fluctuations need to be interpolated between 99 and 106:

$$u' \sim \sqrt{\dot{M}[1 + (\frac{z}{-L})^{\frac{2}{3}}]} \tag{114}$$

- The buoyancy frequency needs to be interpolated between 101 and the $z-$derivative of 111:

$$N^2 = \frac{g}{\theta}\frac{d\bar{\theta}}{dz} \sim -\frac{C_4 \mathcal{F}_b}{z\sqrt{\dot{M}}}[1 + (\frac{C_4}{C_1})^3(\frac{z}{-L})]^{-\frac{1}{3}}$$

  Fields experiments have been done in the seventies and show that:

$$N^2 \approx -\frac{0.74}{\kappa}\frac{\mathcal{F}_b}{z\sqrt{\dot{M}[1 + 9(\frac{z}{-L})]}} \tag{115}$$

  where we have introduced the Von Kármán constant:

$$\kappa = 0.41$$

A dimensionless way to compare the thermally to the mechanically driven turbulence is The gradient Richardson number, defined as the ratio of the thermal to the shear gradient:

$$\mathrm{Ri} \overset{\mathrm{def}}{=} \frac{\text{Thermal gradient}}{\text{Shear gradient}} = \frac{N^2}{(\frac{\partial \bar{u}}{\partial z})^2} \tag{116}$$

Miles theorem states that the flow becomes unstable when the shear is large enough to make the Richardson number $\mathrm{Ri} < \frac{1}{4}$. In conclusion, dry convection is always turbulent, and except in specific cases, the convective boundary layer is driven by shear instability/turbulence. Note that large scale wind blowing over the surface (measurable by an anemometer) reduces any kind of turbulence, since it tends to radiate the kinetic energy away as gravity waves.

7 Molecular spectroscopy

7.1 Introduction

We now dig in the details of radiative transfer, and look at how the spectrum is produced by the molecular constituents of the atmosphere. In particular, we remember the definition of the absorption coefficient 20, which implies a sum on the molecules and the energy level. From the absorption coefficient, it is possible to compute molecular lines as precise as on figure 49.

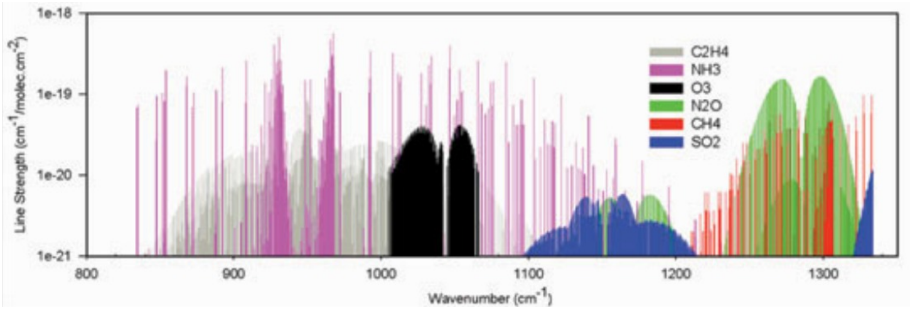

Figure 49: Example of molecular spectral signatures lying within the $8-12\mu$m atmospheric window

However, most geophysical models don't use such a sophisticated radiative scheme: for instance, the MIT GCM only has five bands. In planetary science, radiation is very important and models such as HITRAN allow researchers to start off with all the bands. In the field of molecular spectroscopy, the wavenumber of electromagnetic radiation (not to be confused with the angular wavenumber used in wave equations) is often used:

$$\tilde{\nu} \stackrel{\text{def}}{=} \frac{E}{hc} = \frac{1}{\lambda} = \frac{\nu}{c} \;\Rightarrow\; \tilde{\nu}[\text{cm}^{-1}] \approx \frac{10^4 \text{cm}^{-1}.\mu\text{m}}{\lambda[\mu\text{m}]} \tag{117}$$

For example, the absorption cross-sections are functions of the electromagnetic wavenumber; we have already seen the (CO_2, CH_4) ones on figure 24; other important molecular absorption cross-sections include (CO, H_2O) (figure 50)

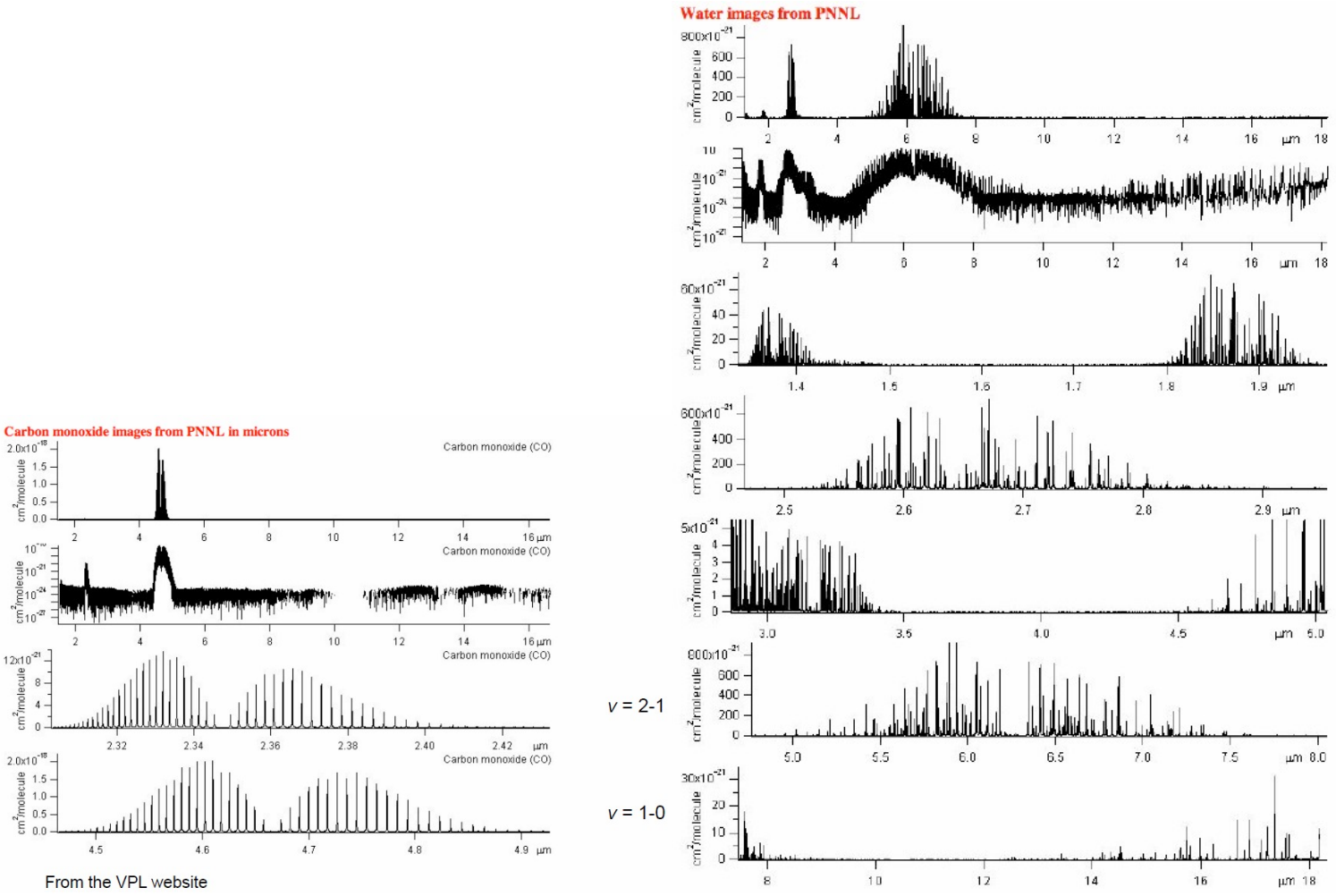

Figure 50: Absorption cross-sections for Carbon Monoxide (left) and Water (right)

. If we look at the two bottom lines of the Carbon Monoxide spectrum, it is possible to see rotation features within the vibration bands (from far they look equally spaced but we will see that they are not). Looking at the water vapor spectrum, we can see that

molecular spectroscopy can quickly become complicated complicated as soon as the molecule is triatomic, because of all the rotational and vibrational degrees of freedom. To compute the cross-sections from scratch, you have to take into account the line broadening for each molecule, before finding the contributions for each wavenumber, as detailed on figure 51.

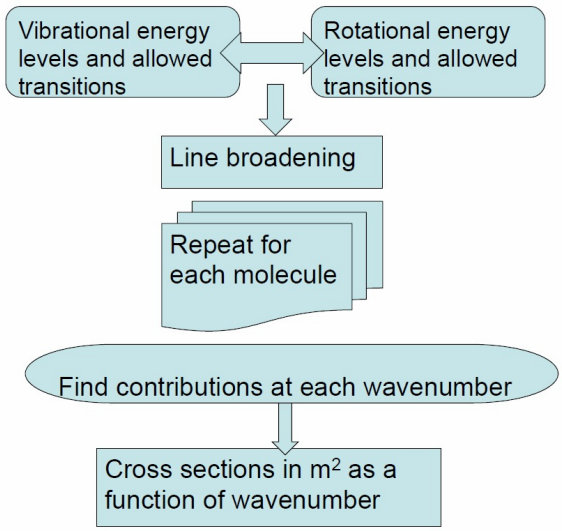

Figure 51: Method to compute the molecular cross-sections

Local thermodynamic equilibrium (LTE 3.2) is generally assumed, allowing us to use statistical mechanics to populate the different energy levels. However it is important to remember that LTE only applies when collision processes dominate over radiative effects, which is not the case when the temperature is very low, such as for the 3K background radiation in space.

7.2 Preamble of spectra

Molecules have specific frequencies at which they rotate and vibrate, which produce the vibrational bands in which rotational lines are embedded, as visible on the Carbon Dioxide's emission spectra (52).

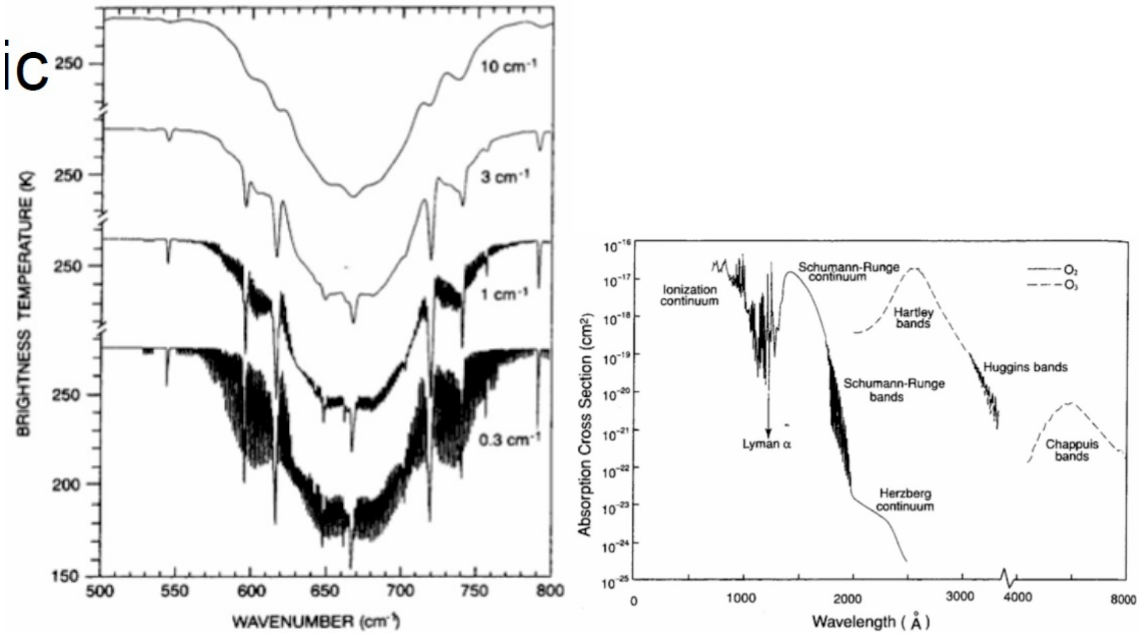

Figure 52: Spectra of a CO_2 atmosphere (left) and absorption cross-sections of O_3 and molecular oxygen in the UV spectral region

Electronic transitions are important if one wants to compute the absorption cross-sections in the UV (right of 52).

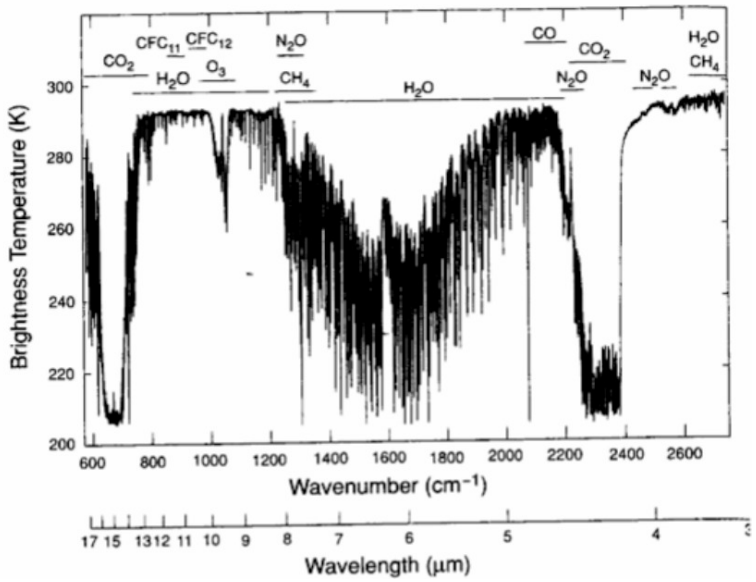

Figure 53: Observed IR spectrum displaying all the absorption gases

Looking at spectra from airplanes measurements on figure 53, we can see that real-world spectra are extremely complex. For a class of molecules, the complexity of the spectra increase with the size of the molecule:

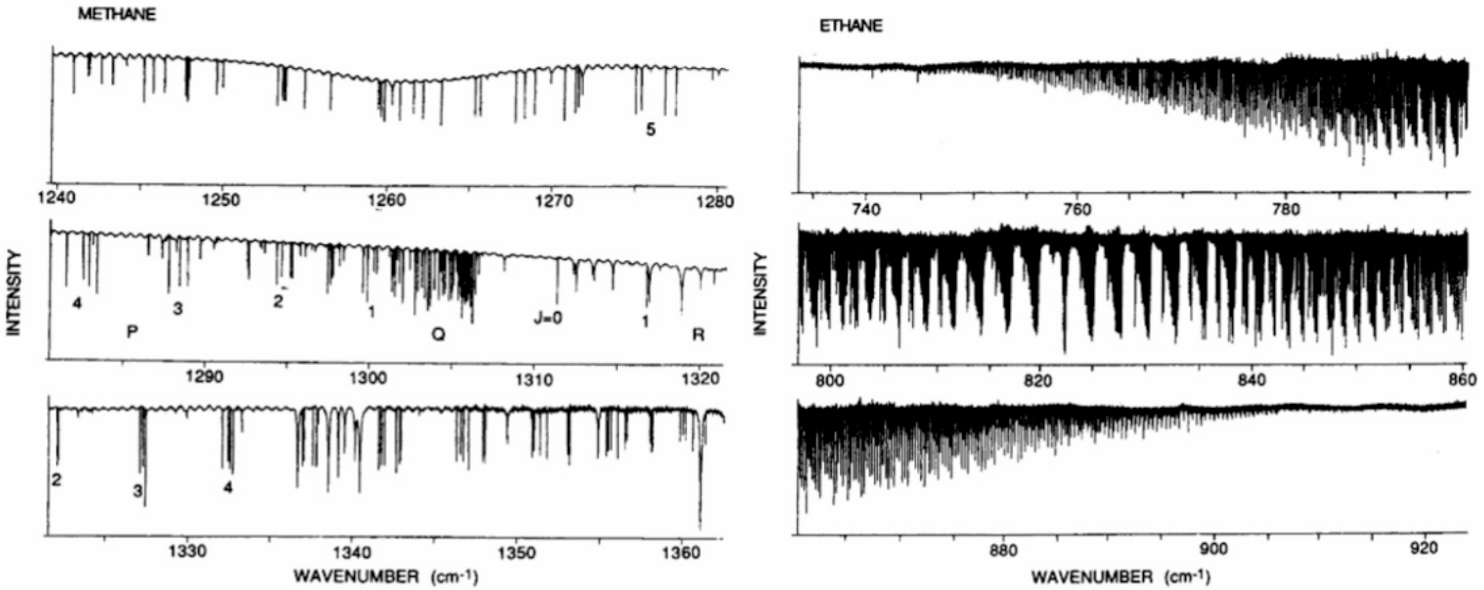

Figure 54: The ν_4 vibration-rotation band of methane (left) and the ν_9 vibration-rotation band of ethane (right) recorded at high spectral resolution

- The Methane (CH_4) spectra are already much more complicated than those studied previously, because the molecule is polyatomic and thus has many vibrational modes. This spectrum can be measured in laboratory.
- Ethane (C_2H_6) is even more complex, and exhibits a series of regulated branches in the $790 - 850\text{cm}^{-1}$ region.

We now look at planetary spectra on figure 55.

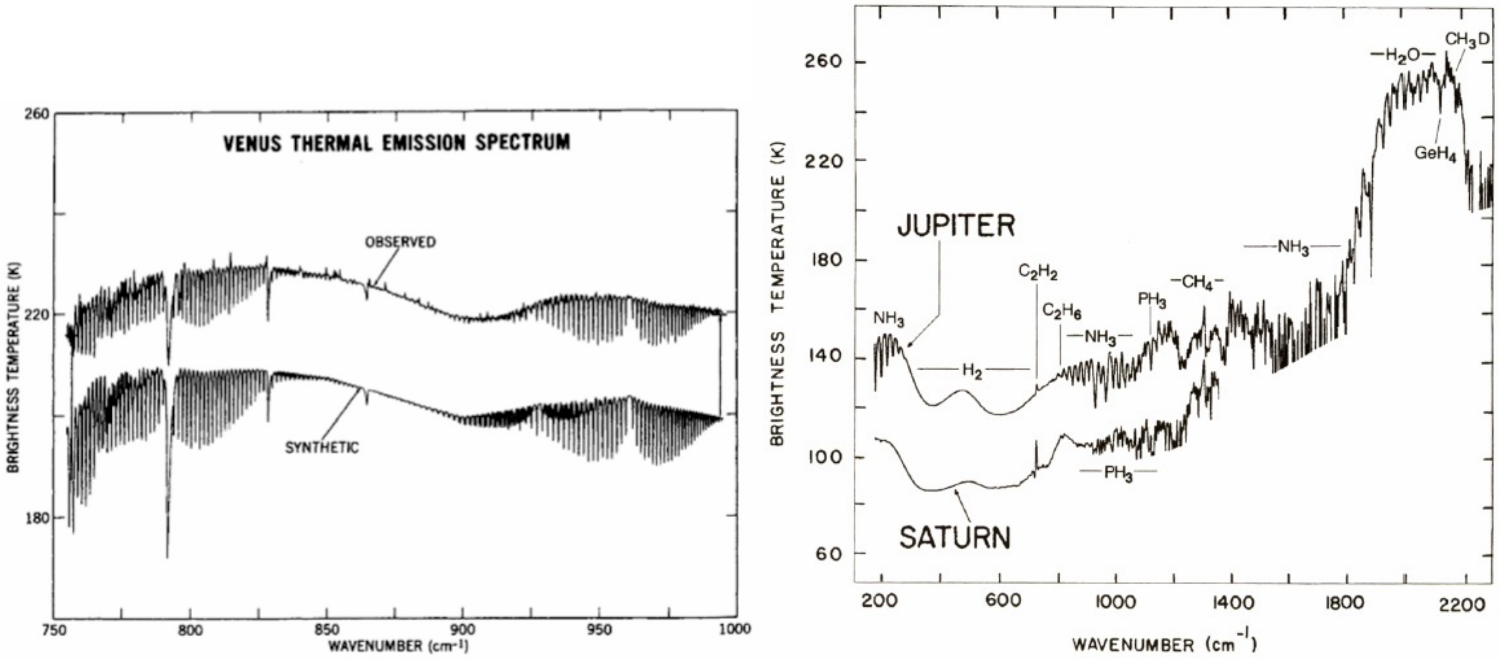

Figure 55: Measured and calculated thermal emission spectra of Venus (left) and spectra of Jupiter and Saturn (right)

- Venus spectra show the difference between when they are observed and the final product where Earth atmospheric lines need to be removed.
- We can see that the spectra of Jupiter and Saturn look quite similar. From the numerous lines, it is easy to understand why those spectra are so hard to process/synthesize, which is why so many radiative codes are shared in the planetary science community.

7.3 Molecular energy levels

The Hydrogen energy levels (figure 56) show that level correspond to a given energy and thus a given spectral series

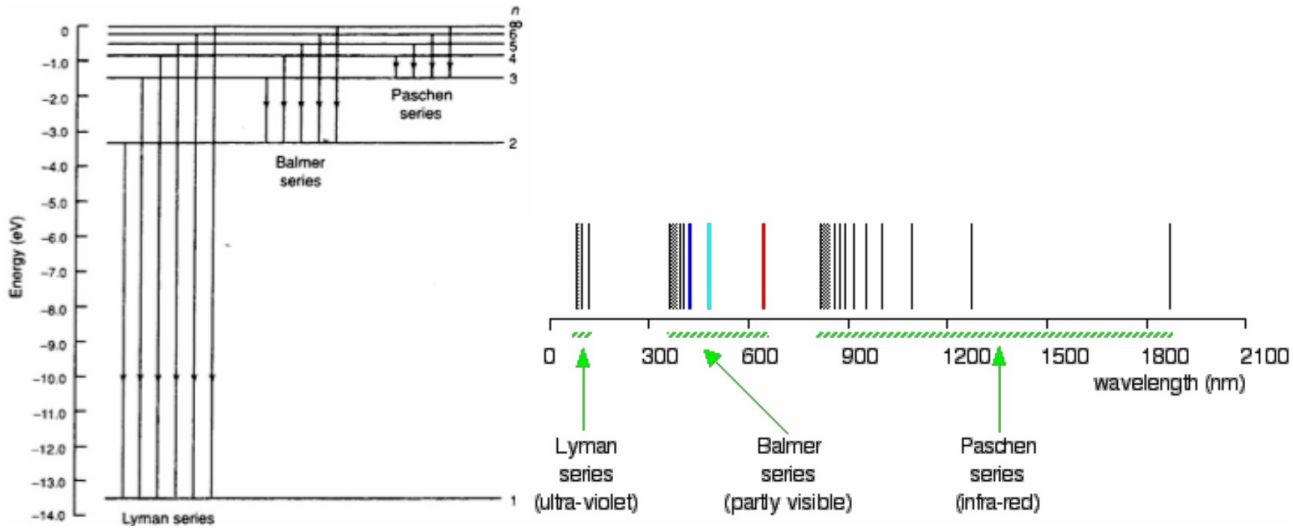

Figure 56: Energy level diagram for a Hydrogen atom showing the quantum number n for each level and some transitions that appear in the spectrum (left) and Hydrogen atomic lines (right)

. Molecular energy levels are much more complicated than Hydrogen electronic levels, since they have vibrational and rotational transitions. If we assume that the electronic energy only depends on the positions of the nuclei, the potential energy distribution function is a function of internuclear distance alone. Looking at this potential energy on figure 57, we can see that within electronic transitions, there are vibrational transitions and within them, there are rotational transitions.

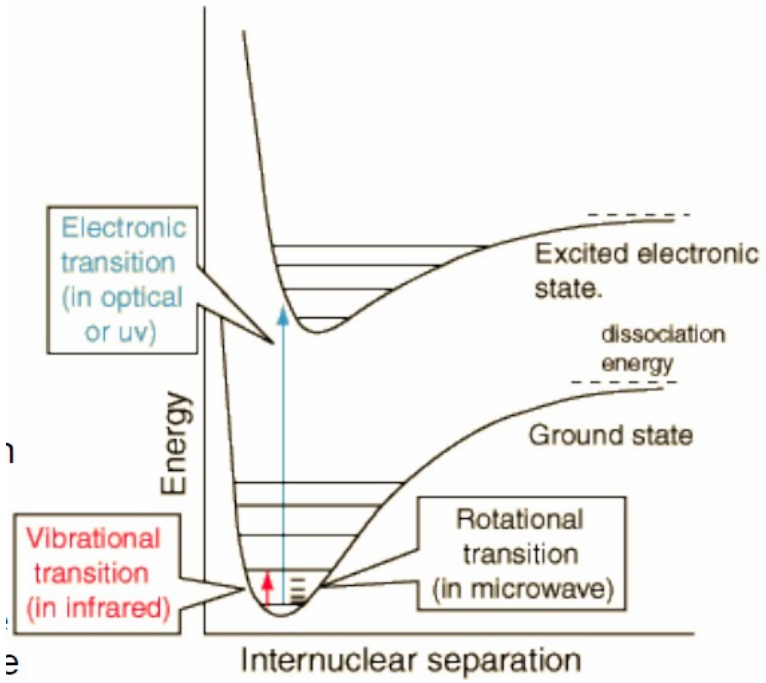

Figure 57: Potential energy as a function of the internuclear separation

Focusing on the internuclear separation $x-$axis of the graph, a high value corresponds to unbound electrons. The minimum of potential energy occurs where attractive electromagnetic forces balance repulsive forces between the molecules. In order to interact with the radiation field, molecules need to have a dipole moment $\overrightarrow{p}$, defined by:

$$\overrightarrow{p} \overset{\text{def}}{=} q\overrightarrow{M_- M_+} \tag{118}$$

where q is the charge of the dipole, M_- the barycenter of negative charges and M_+ the barycenter of positive charges. That's why Nitrogen and Oxygen, which are the main components of our atmosphere if you look at their mass concentration, have no radiative roles because their permanent dipole moment is zero (otherwise the Earth would be very hot). Examples of molecular dipole moments are given on figure 58.

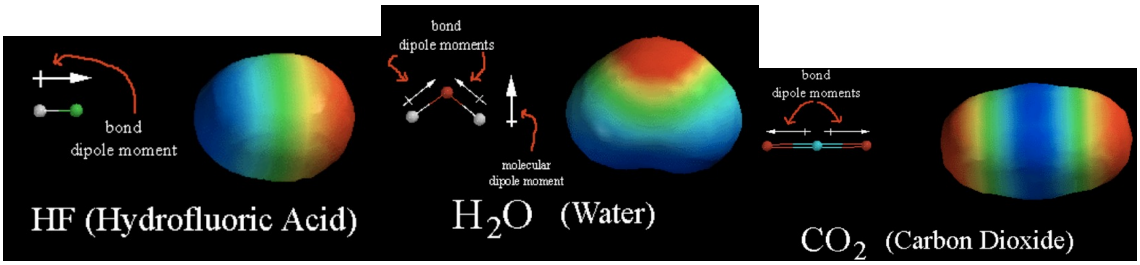

Figure 58: Three molecules with permanent dipole moments

Note that the molecule of Carbon Dioxide does not have a permanent dipole moment. However, dipole moment can be induced, as electronic excitations can lead to asymmetric charge distributions and thus provide a net dipole moment to the molecule. Note that molecules with flexible bonds such as Hydrogen (H_2) can be rearranged by collisions, which can make them absorb radiation at high pressure, as we can see on Jupiter and Saturn (collision induced absorption and emission which comes from inelastic collisions unlike collisional broadening). Looking at figure 59, we are reminded that:

- Molecular nitrogen (N_2), the most abundant atmospheric constituent, has neither electric nor magnetic dipole moment and therefore has no rotational absorption spectrum.
- Oxygen (O_2) has no electric dipole moment. However, unlike other diatomic gases, it has a permanent magnetic moment, which explains why it can have rotational absorption bands at 60GHz and 118GHz.
- Carbon dioxide (CO_2) and methane (CH_4) have no permanent electric nor magnetic dipole moments, and are therefore radiatively inactive with respect to pure rotational transitions. However, bending vibrational motions can break the linear symmetry of the

molecule and introduce an oscillating dipole moment whose presence permits combine vibration-rotation transitions at shorter wavelengths.

- The vast majority of the other molecules found in Earth's atmosphere exhibit permanent electric dipole moments and therefore also major rotational absorption bands.

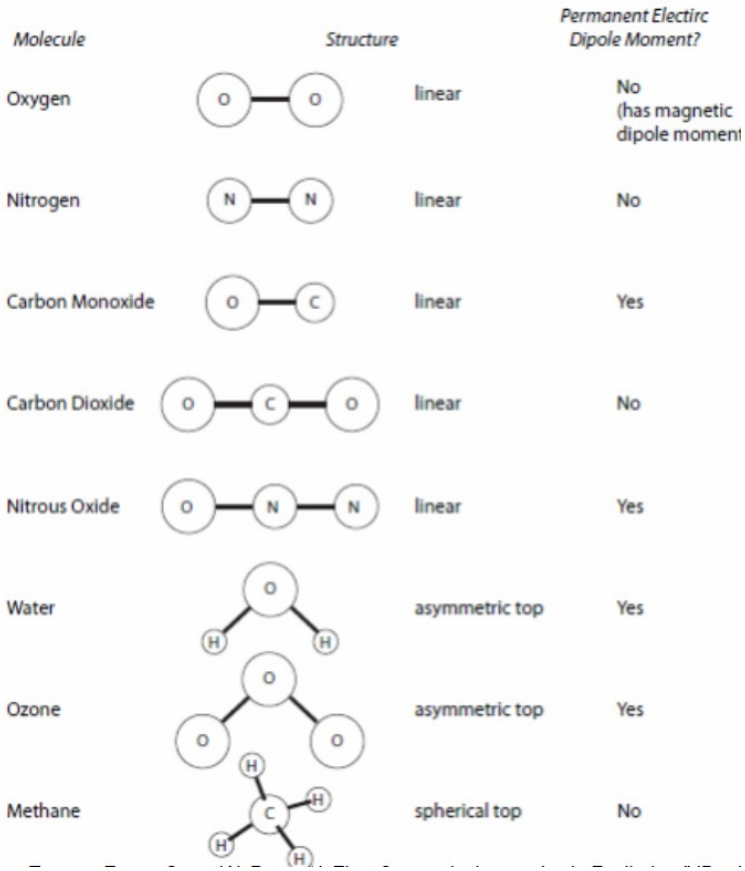

Figure 59: Molecules with permanent electric dipole moment

7.4 Molecular rotational energy levels

To understand the basics of molecular rotational energy levels, we will adopt the rigid rotor approximation, depicted on figure 60.

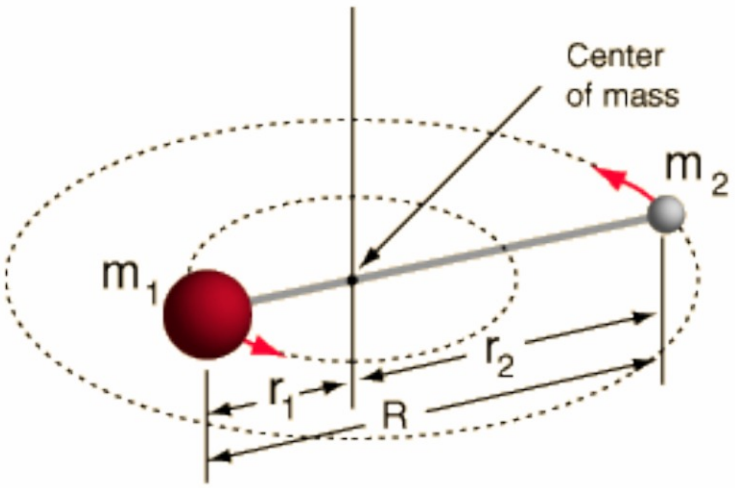

Figure 60: Rigid rotor approximation for a diatomic molecule

A basic mechanics reminder can be found on figure 61.

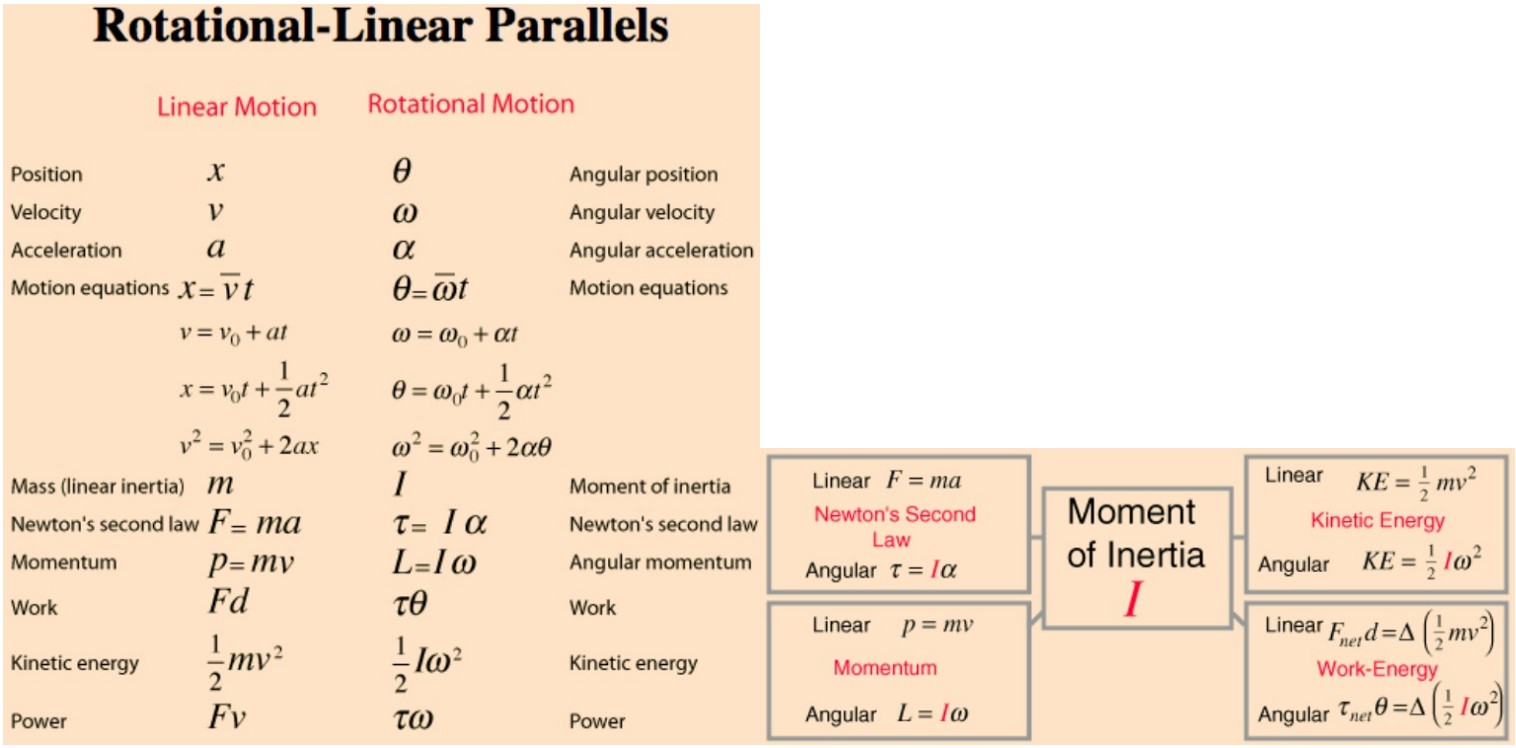

Figure 61: Rotational-Linear parallels (left) and Moment of inertia (right)

Following the notations defined on figure 60, we know that the axis of rotation of the rotor will coincide with its center of mass, which position is such that $m_1r_1 = m_2r_2$. The total distance is given by $R = r_1 + r_2$. For a two-body system, it is convenient to define a reduced mass:

$$m' \stackrel{\text{def}}{=} \frac{m_1m_2}{m_1+m_2} \tag{119}$$

The moment of inertia of the system is then given by:

$$I \stackrel{\text{def}}{=} m_1r_1^2 + m_2r_2^2 = m'R^2 \tag{120}$$

A classical rotor has no potential energy, only kinetic energy, given by:

$$E_c \stackrel{\text{def}}{=} \frac{m_1v_1^2 + m_2v_2^2}{2} = \frac{I\omega^2}{2} = \frac{L^2}{2I} \tag{121}$$

where we have defined:

- The angular frequency of the rotor:

$$\omega \stackrel{\text{def}}{=} \frac{v}{R} \tag{122}$$

- The angular momentum of the rigid rotor:

$$L \stackrel{\text{def}}{=} m_1\omega r_1^2 + m_2\omega r_2^2 = m'\omega R^2 = I\omega \tag{123}$$

We now complete our classical mechanics model by adding one element of quantum physics: Via Schrödinger equation, we can prove that the angular momentum of our rigid molecule can only take discrete values, given by:

$$L = \frac{hj(j+1)}{2\pi} \mid j \in \mathbb{N} \tag{124}$$

where h is the Planck constant. Combining equations 121 and 124 gives us the discrete rotational energy levels in our model:

$$E_j = \frac{I\omega^2}{2} = \frac{j(j+1)h^2}{8\pi^2I} \Rightarrow \boxed{E_j = Bj(j+1)} \tag{125}$$

where we have defined the rotational constant (in energy units):

$$B \stackrel{\text{def}}{=} \frac{h^2}{8\pi^2 I} \tag{126}$$

There are two selection rules for rotational transitions:

1. A permanent dipole is required.
2. A change in level j is constrained by $\Delta j = \pm 1$.

As a consequence, from 125 we find that the rotational energy levels (and hence the frequency levels) consist of a series of equally spaced lines (equally spaced in energy/frequency/wavenumber not in wavelength) separated by:

$$\Delta E = E_{j+1} - E_j = 2B(j+1) \tag{127}$$

The equal spacing in wavenumber can be seen on figure 62, and can be seen within the vibrational bands of the CO on the left of figure 50.

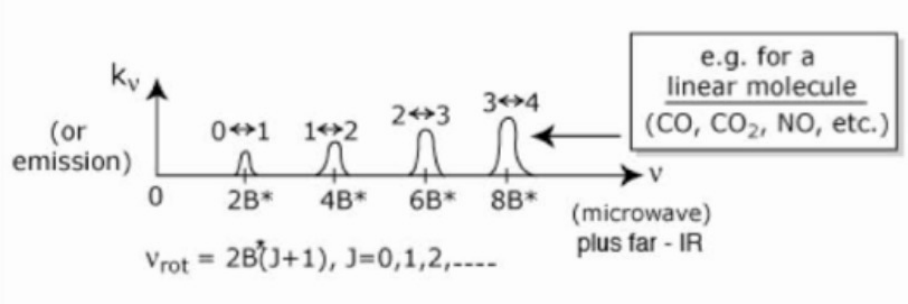

Figure 62: Rotational lines for a linear molecule

However, looking more closely at figure 50, the spacing of the rotational lines decreases continuously as the wavenumber increases. This can be explained by the fact that the centrifugal force between two atoms pulls them apart, increasing the rotor's moment of inertia, and thus decreasing the value of B. This force increases with the quantum rotational number j, which explains why its potential energy and thus the spacing between the lines decreases with increasing $j/\tilde{\nu}$. To find the "envelope of rotational lines", we assume local thermodynamic equilibrium, which means that the population of each level follows a Boltzmann distribution (see 21). Since there are $2j+1$ rotational levels, the ratio of the population N_j at level j to the population N_0 at the ground state is given by:

$$\frac{N_j}{N_0} = (2j+1)\exp[-j(j+1)\frac{B}{k_B T}] \tag{128}$$

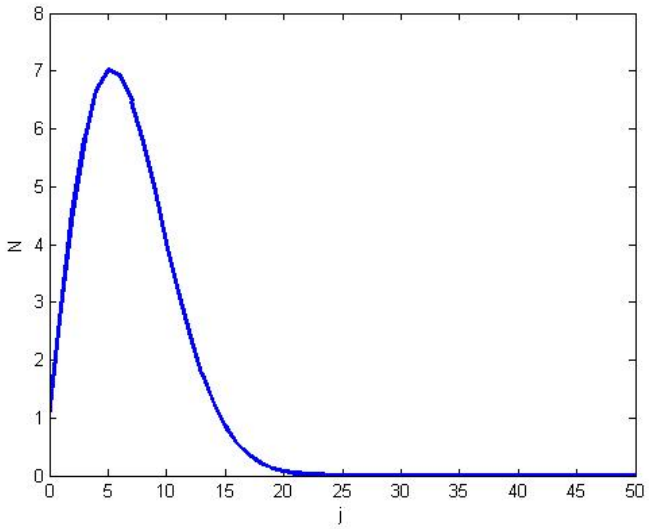

Figure 63: $\frac{N_j}{N_0}$ vs j for $\frac{B}{k_B T} = 1.5\%$ corresponding to room temperature for a typical linear diatomic molecule

We can see that the previous ratio 128 is maximal for finite j:

$$\frac{\partial}{\partial j}(\frac{N_j}{N_0}) = 0 \;\Leftrightarrow\; j_{\text{max ratio}} = \frac{1}{\sqrt{2}}(\sqrt{\frac{k_B T}{B}} - 1) \tag{129}$$

and the theoretical curve 63 of $\frac{N_j}{N_0}$ corresponds to the shape of the vibrational-rotational band observed on figure 50:

- First the ratio starts from 1 ($j = 0$) and increases until $j = j_{\text{max ratio}}$ and then decreases until it becomes smaller than 1. This is the part of the vibrational bands where the rotational lines are bigger and bigger.
- Then the ratio becomes smaller than 1, and goes towards 0 as $j \to +\infty$. This is the part of the vibrational bands where the rotational lines are smaller and smaller.

Finally, one last noticeable thing on figure 50 is that the rotational bands have black lines close to them. It corresponds to different isotopes of the same molecule which have slightly different rotational wavenumbers.

7.5 Molecular rotational-vibrational lines

In a linear diatomic molecule, all vibratory motions takes place along the line joining the atom: the atoms are in periodic motion with respect to their center of mass. As the molecules vibrates, rotational modes are also excited. However, we'll ignore rotation for now and only consider the discrete vibrational levels depicted by regular horizontal lines on figure 57.

7.5.1 Vibrational energy levels

To have a conceptual understanding of vibrational energy levels, we will once again use a simple mechanical analog: a mass attached to a spring of stiffness k (cf left of figure 64). For a small displacement z, the restoring force of a linear spring is simply given by $F_{\text{spring}} = -kz$, corresponding to a potential energy:

$$V = -\int_0^z F_{\text{sping}}(z')dz' = \int_0^z kz'dz' = \frac{kz^2}{2} \tag{130}$$

. Applying Newton's second law to the mass m, its acceleration is given by:

$$\frac{d^2z}{dt^2} = \frac{F_{\text{spring}} + F_{\text{gravity}}}{m} = -\frac{k}{m}z - g \tag{131}$$

so that the deviation of the spring from its equilibrium position $z' = z + \frac{mg}{k}$ verifies the harmonic oscillator equation:

$$\frac{d^2z'}{dt^2} + (2\pi\nu_0)^2 z' = 0 \;\Rightarrow\; z' = A\cos(2\pi\nu_0 t - \phi) \tag{132}$$

where we have introduced the natural frequency of the oscillator:

$$\nu_0 \overset{\text{def}}{=} \frac{1}{2\pi}\sqrt{\frac{k}{m}} \tag{133}$$

as well as the amplitude A and the phase ϕ of the oscillation at the initial time $t = 0$. A harmonic solution analogous to the one found in 132 is plotted on the right of figure 64.

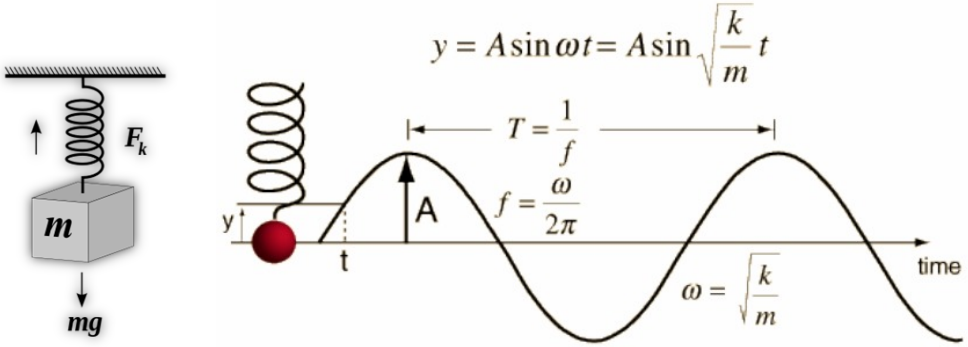

Figure 64: Mass-spring model (left) and simple harmonic motion of angular frequency ω and amplitude A (right)

To make an analogy with a diatomic molecule, we need to replace k with the bond force constant and m with the reduced mass of the molecule. Once again, we complete our mechanics model by borrowing one element from quantum physics: the energy levels are discrete, and their value E_v for a given vibrational level v is given by:

$$\boxed{E_v = h\nu_v = h(v + \frac{1}{2})\nu_0} \tag{134}$$

The energy levels of the oscillator, depicted on figure 65, are populated following Boltzmann distribution 21:

$$\frac{N_v}{N_0} = \exp(-v\frac{h\nu_0}{k_B T}) \tag{135}$$

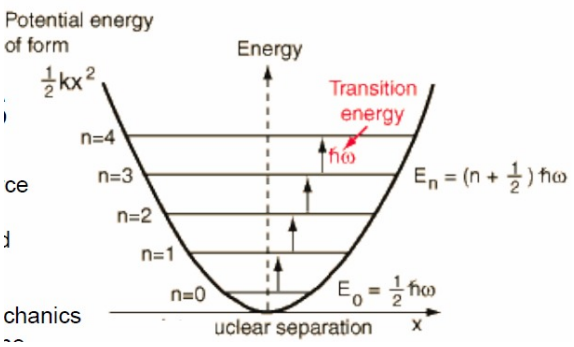

Figure 65: Potential energy of the harmonic oscillator and vibrational levels

In reality, the potential energy is not strictly a parabola and the oscillator is anharmonic. This changes the selection rules: all the integral changes of the quantum numbers are allowed. For example, $\Delta v = 2$ gives the first overtone band from the ground state $v = 0$ to the state $v = 2$, with twice the frequency of the fundamental mode. Simultaneous changes in two different vibrational quantum numbers give rise to combination/difference bands with frequencies that are the sum/difference of the fundamental frequencies. However, these are small transitions, negligible compared to the strong bands generated by the fundamental transitions.

7.5.2 Vibrational modes

To find the number of vibrational energy levels of a polyatomic molecule constituted by N nuclei, we note that each nuclei can move in the three spatial directions, giving $3N$ degrees of freedom. However, 6 of those degrees correspond to the molecular motion as a whole (the three coordinates of the center of mass and the three angles defining its orientation in space), so that:

- For $N > 2$, the total number of vibrational degrees of freedom is $3N - 6$.
- For a linear diatomic molecule $N = 2$, only two angles are needed to specify orientation and the number of vibrational degrees of freedom is $3N - 5 = 1$.

For example, methanol CH_4O has 6 atoms and thus $18 - 6 = 12$ vibrational modes. Three examples of molecules are given on figure 66.

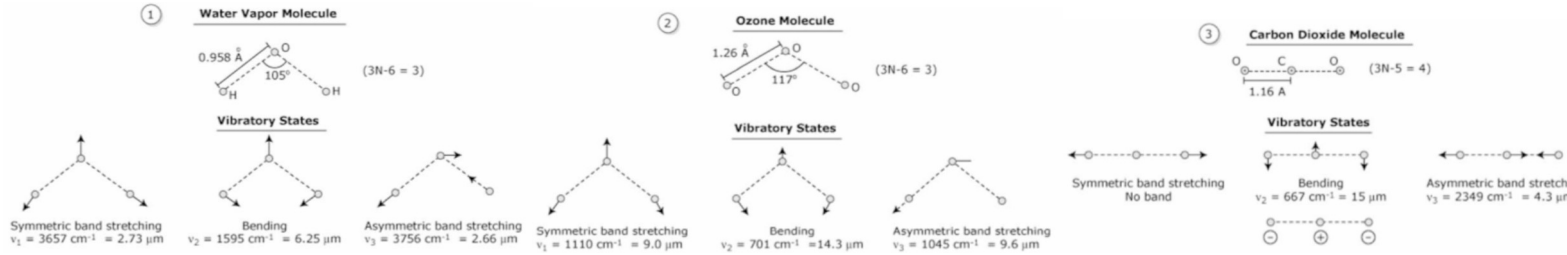

Figure 66: Vibrational states of H_2O (left), O_3 (middle) and CO_2 (right)

7.5.3 P and R rotational-vibrational branches

In reality, rotational transitions always accompany vibrational transitions. Imagine that an electron goes from a vibrational level v (the "ground state") to a vibrational level $v+1$ (the "excited state") on figure 7.3, which requires an energy $h\nu_0$. There are three possibility for its rotational transition, remembering the constraints on the quantum rotational number j studied in 7.4:

- $\Delta j = +1$, ie the rotational number in the ground state is more than the rotation number in the excited branch. This branch is called the R-branch for " rich" , and the energy transition is given by:

$$\Delta E_R = h\nu_0 + B[(j+1)(j+2) - j(j+1)] = h\nu_0 + 2B(j+1) \tag{136}$$

- $\Delta j = -1$, ie the rotational number in the ground state is less than the rotational number int eh excited state. This branch is called the P-branch for "poor", and the energy transition is given by:

$$\Delta E_P = h\nu_0 + B[j(j-1) - j(j+1)] = h\nu_0 - 2Bj \tag{137}$$

- $\Delta j = 0$, ie the rotational number in the ground state is the same than the rotational number in the excited state. This branch is called the Q-branch (because Q is between P and R) and the energy transition is given by $\Delta E_Q = h\nu_0$. For $\nu_0 \neq 0$, this transition is not allowed for diatomic molecules and the Q-branch is thus not observable for diatomic molecules in practice.

Note that in wavenumber space, the lines are separated by a distance $\frac{2B}{hc}$, allowing us to compute the rotational constant of a molecule by simply looking at its rotational-vibrational lines. Example of such lines can be found on figure 67.

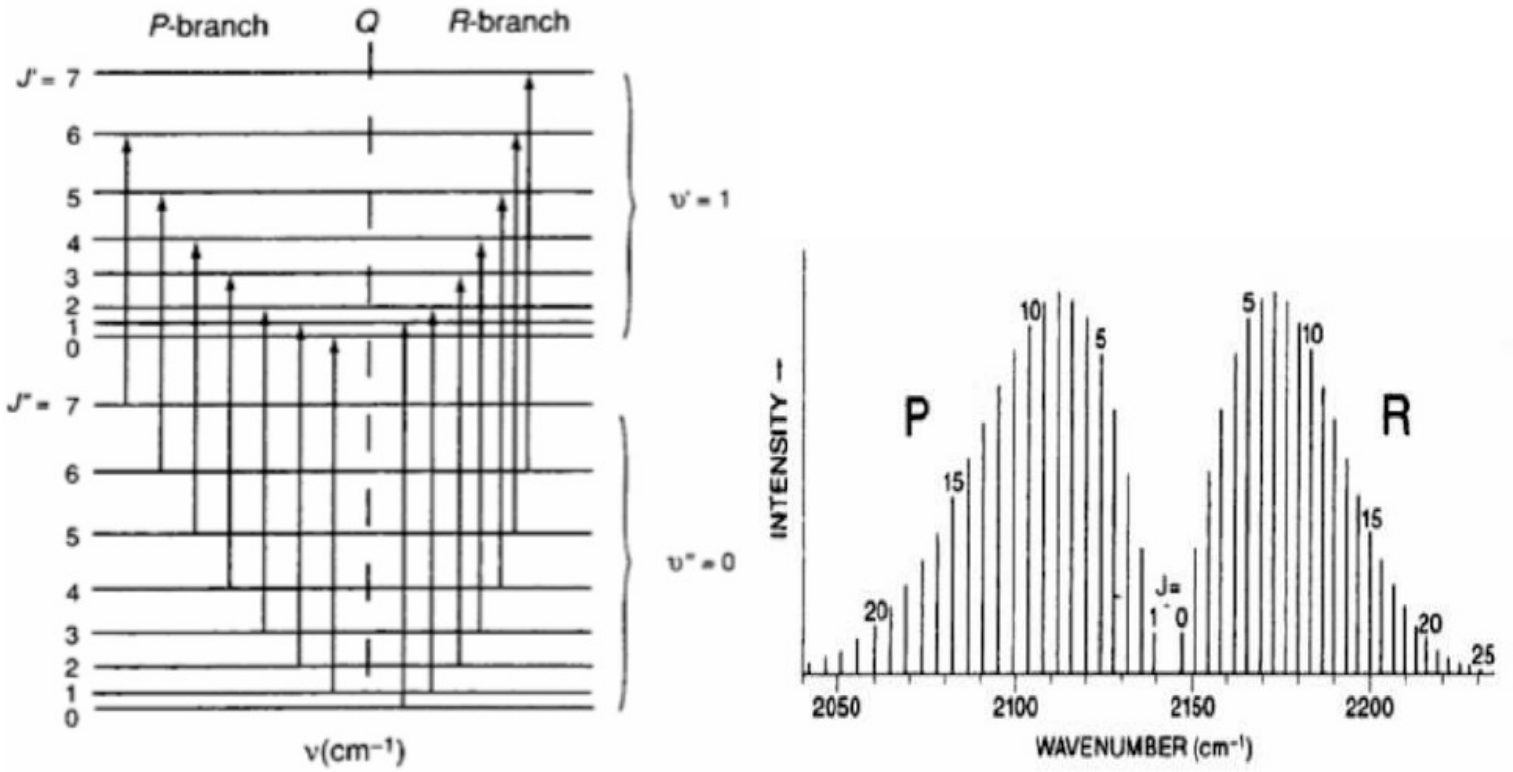

Figure 67: Rotational-vibrational lines schematic (left) and for Carbon Monoxide (right)

Those lines can also be observed on the cross-sections of Carbon Monoxide and Water 50. Rotational-vibrational lines of many molecules can be found on the HITRAN website [http://www.hitran.com/].

7.5.4 Summary

To summarize, the selection rules for vibrational-rotational transitions are reminded below on the left figure 68 for a given electric dipole moment $\overrightarrow{\mu}$. This gives rise to the P and R branches on the right of figure 68, which vibrational-rotational frequencies are given by:

$$\boxed{\nu_{\text{vib-rot}} = \nu_0 + \frac{2B}{h}\begin{cases} j+1 & [\text{R branch} \equiv \text{Vib rise} + \text{Rot rise}] \\ 0 & [\text{Q branch} \equiv \text{Vib rise} + \text{Rot unchanged}] \\ j & [\text{P branch} \equiv \text{Vib rise} + \text{Rot fall}] \end{cases}} \tag{138}$$

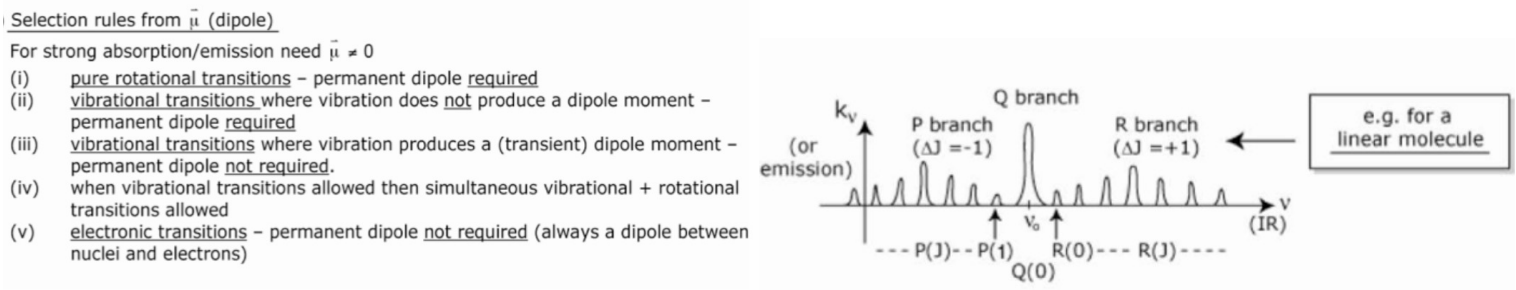

Figure 68: Selection rules for vibrational-rotational transitions (left) and rotational-vibrational lines (right)

7.6 Line broadening

7.6.1 Cross-section

For a given molecule at a given frequency, the cross-section σ [in m^2/molecule] is given by:

$$\boxed{\sigma_{\tilde{\nu}} = Sf(\tilde{\nu} - \tilde{\nu}_0)} \tag{139}$$

where:

- $\tilde{\nu}$ is the electromagnetic wavenumber and $\tilde{\nu}_0$ is the wavenumber of an ideal monochromatic line.
- S is the line strength, which normalized the cross-section over all electromagnetic wavenumbers:

$$S \overset{\text{def}}{=} \int_{-\infty}^{+\infty} \sigma_{\tilde{\nu}} d\tilde{\nu} \tag{140}$$

- f is the normalized broadening function, as all the lines are broadened in nature ($\delta-$functions are never observed):

$$1 = \int_{-\infty}^{+\infty} f(\tilde{\nu} - \tilde{\nu}_0) d\nu \tag{141}$$

7.6.2 Overview of line broadening

In nature, monochromatic emission is practically never observed: energy levels during energy transitions are changed slightly:

- By external influences
- Due to natural, Doppler and/or collisional broadening

Consequently, we always observe spectral lines of finite width, which position, strength and shape are affected by broadening. In general, line broadening is associated to a loss of information, as rotational lines are at least blurred if not merged.

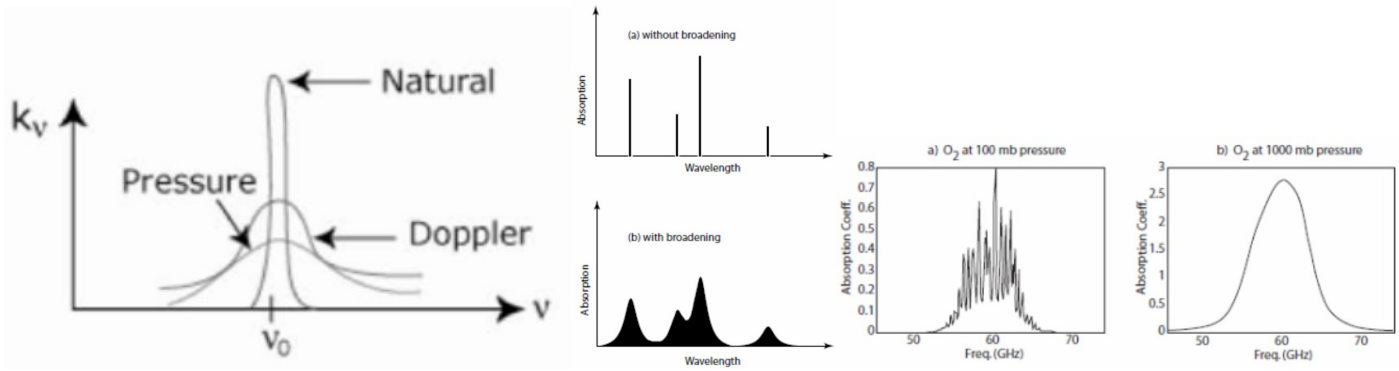

Figure 69: Three types of broadening (left), transformation of absorption spectrum by broadening (middle)
Right: Absorption coefficient of O_2 near 60GHz at 100mb where the individual lines making up the absorption band are visible and at 1000mb where pressure broadening obliterates the line structure.

7.6.3 Natural broadening

Natural broadening occurs because of Heisenberg's uncertainty principle applied to the energy of the upper and lower energy levels of transition. It is a purely quantum effect, and can only be observed in the absence of collisions (ie a single molecule). According to the uncertainty principle, the momentum and position of a particle (or alternatively its energy/frequency and the time of emission) can not be measured simultaneously because of its wave nature:

$$\Delta p \Delta x \geq \frac{h}{4\pi} \;\Rightarrow\; \Delta\nu\Delta t \geq \frac{1}{2\pi} \tag{142}$$

From relation 142, we can see that there will be a natural spread in frequency $\Delta\nu$ "the natural broadening of the line", especially when the time of emission Δt is small. The time of emission depends on how long the atom/electron stays in the excited state before emitting a photon, which is determined by quantum physics (cf figure 70).

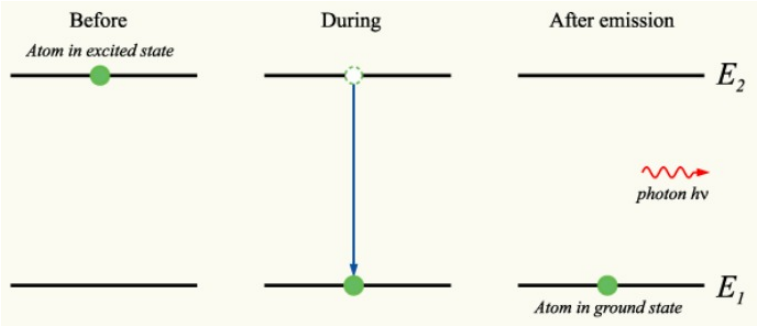

Figure 70: Desexcitation of an atom and consequences on natural broadening

For instance, for a strong (allowed) transition in the IR, a typical lifetime is $\Delta t = 10^{-1}$s, corresponding to the following spread in electromagnetic wavenumber:

$$\Delta\tilde{\nu} = \frac{1}{2\pi c\Delta t} \sim 10^{-10}\text{cm}^{-1} \tag{143}$$

7.6.4 Doppler broadening

Doppler broadening arises from difference in thermal velocities of atoms and molecules. We remember the Doppler effect, arising when a wave source is moving away from/towards the observer at a velocity v which decreases/increases the perceived the initial frequency ν_0 of the wave depending on the angle θ between the ray and the motion of the source:

$$\nu = \nu_0(1 + \frac{v\cos\theta}{c}) \tag{144}$$

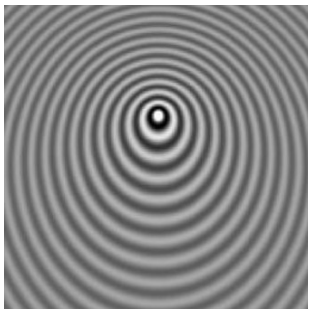

Figure 71: Doppler effect distorting the lines of constant phase emitted by the source moving upwards

To quantitatively understand the Doppler broadening using kinetic gas theory, we introduce the Doppler shift 144 in the Maxwell-Boltzmann distribution of velocities, and normalize the result to find the following normalized broadening function:

$$\boxed{f_D(\nu - \nu_0) = \frac{1}{\sqrt{\pi}\alpha_D}\exp[-(\frac{\nu-\nu_0}{\alpha_D})^2]} \tag{145}$$

We have introduced the following frequency:

$$\alpha_D \stackrel{\text{def}}{=} \nu_0 \sqrt{\frac{2k_B T}{mc^2}} \tag{146}$$

which multiplied by $\sqrt{2\ln 2}$ is the half-width at half-max of the profile. Roughly speaking, the Doppler broadening broadens the spectral line to make it Gaussian because the velocity profile of the molecules is Gaussian. As the mean speed of the molecule scales like $\sqrt{k_B T m^{-1}}$, the line width increases with temperature and decreases with molecular mass. However, a Maxwellian distribution of velocity only applies without any external influence, and we do not expect it to hold for the troposphere and the stratosphere where collisions are important.

7.6.5 Collisional or Lorentz broadening

To construct the profile resulting from collisional broadening, we assume that the molecular collisions are instantaneous, and that they change the phase of the molecular wave-train in a random manner, "smearing out" the emitted frequencies about the nominal frequency ν_0. If we assume that the molecular wave-trains are harmonic oscillators, and that the time between collisions has a Poisson distribution with a given mean t_0, it can be shown that the collisional broadening function is given by a Lorentz profile:

$$\boxed{f(\nu - \nu_0) = \frac{1}{\pi} \frac{\alpha}{(\nu - \nu_0)^2 + \alpha^2}}$$

where we have introduced the half-width at half-maximum, that can be once again computed from kinetic gas theory:

$$\alpha = \alpha_0 \frac{p}{p_0} (\frac{T_0}{T})^n$$

The subscript 0 refers to standard temperature and pressure ($p_0 = 1013$mb, $T_0 = 273$K). The parameters (α_0, ν_0) are not always well-measured and understood, especially for atmospheres of other planets. The Lorentz line shape has two notable deficiencies:

1. The far wings of actual absorption lines (ν small or large) have been found to be poorly represented by this shape.
2. The shape is only valid when $\alpha \ll \nu_0$.

This profile works reasonably well in the lower atmosphere, where high pressures make the Lorentz broadening dominant. However, in the upper atmosphere ($20 - 50$km), Doppler and Lorentz broadenings are both important, leading to a convolution of both profiles: the Voigt profile:

$$f_{\text{Voigt}}(\nu - \nu_0) = \int_{-\infty}^{+\infty} f(\nu' - \nu_0) f_D(\nu - \nu') d\nu' = \frac{1}{\pi^{\frac{3}{2}}} \frac{\alpha}{\alpha_D} \int_{-\infty}^{+\infty} \frac{d\nu'}{(\nu' - \nu_0)^2 + \alpha^2} \exp[-(\frac{\nu - \nu'}{\alpha_D})^2] \tag{147}$$

It is possible to simplify the Voigt profile 147 by switching to dimensionless variables:

$$t = \frac{\nu - \nu'}{\alpha_D}$$

$$y = \frac{\alpha}{\alpha_D}$$

$$x = \frac{\nu - \nu_0}{\alpha_D}$$

$$f_{\text{Voigt}}(\nu - \nu_0) = \frac{K(x, y)}{\sqrt{\pi} \alpha_D}$$

leading to:

$$\boxed{K(x, y) = \frac{y}{\pi} \int_{-\infty}^{+\infty} \frac{\exp(-t^2) dt}{y^2 + (x - t)^2}} \tag{148}$$

8 Moist convection

8.1 Introduction

Moist convection takes into account the fact that water changes phase in the atmosphere. Two important things to remember are:

1. That the latent heat of vaporization $L_v \approx 2.5.10^6 \text{J.kg}^{-1}$ is a very high number, making phase change an important event energetically. As phase changes generally imply thermodynamic equilibrium, it is possible to redefine entropy for a mixture of air and liquid water, which will make our stability considerations much easier.

2. Precipitation of water is an irreversible phenomenon, as it falls down and not up, creating entropy and drying the atmosphere down, making it sub-saturated. Fallout of precipitation is very important, as well as the fact that condensation is heterogeneous in the atmosphere, making it possible for small sub-saturation values.

Moist convection significantly differs from dry convection qualitatively and quantitatively, making it a challenging and interesting atmospheric science problem.

8.2 Moist thermodynamics

8.2.1 Definitions

We now need to take into account the highly variable water vapor and liquid water content to write the ideal gas law. Combining the ideal gas law incorporating moisture 45 with the definition of density temperature T_ρ 47:

$$\alpha = \frac{R_d T_\rho}{p} \tag{149}$$

where we remember that α is the specific volume, p the pressure and R_d the specific gas constant of dry air. We introduce the specific humidity, defined as the mass concentration of water vapor:

$$q \overset{\text{def}}{=} \frac{M_v}{M_d + M_v} = \frac{r}{1+r} = \frac{\epsilon e}{p - (1-\epsilon)e} \tag{150}$$

where we have used the definition of the mixing ratio 43, the ratio of the molecular weight of water vapor to the molecular weight of dry air 44 and Dalton's law 42. Another important quantity is the relative humidity, defined as the ratio of the water vapor partial pressure to its saturation value:

$$\mathcal{H} \overset{\text{def}}{=} \frac{e}{e^*} \approx \frac{q}{q^*} \tag{151}$$

We use the subscript $*$ to denote saturated variables.

8.2.2 Thermodynamics of moist but unsaturated air

For a constant volume process, the definition of the specific heat of dry air c_{v_d} and water vapor c_{v_v} at constant volume allow us to write:

$$(M_d + M_v)\dot{Q} = (M_d c_{v_d} + M_v c_{v_v})\dot{T} \tag{152}$$

This leads us to introduce:

- The mass-weighted specific heat of air at constant volume:

$$c'_v \overset{\text{def}}{=} (\frac{\partial Q}{\partial T})_\alpha = c_{v_d} \frac{1 + r\frac{c_{v_v}}{c_{v_d}}}{1+r} \tag{153}$$

- The mass-weighted specific heat of air at constant pressure:

$$c'_p \overset{\text{def}}{=} (\frac{\partial \dot{Q}}{\partial T})_p = c_{p_d} \frac{1 + r\frac{c_{p_v}}{c_{p_d}}}{1+r} \tag{154}$$

Neglecting the mass of liquid water in 35 allows us to relate the specific volume of air and the specific volume of dry air:

$$\alpha = \frac{\alpha_d}{1+r} \tag{155}$$

so that the first and second thermodynamic identities become:

$$\delta Q = c'_v dT + \frac{p}{1+r} d\alpha_d = c'_p dT - \alpha dp \tag{156}$$

According to 156, the natural quantity conserved under adiabatic displacements ($\delta Q = 0$) is the potential temperature defined by:

$$\theta \overset{\text{def}}{=} T(\frac{p_0}{p})^{\frac{R'}{c'_p}} \approx T(\frac{p_0}{p})^{\frac{R_d}{c_{p_d}}} \tag{157}$$

where we have generalized the specific gas constant for moist air:

$$R' \overset{\text{def}}{=} \frac{R_d + rR_v}{1+r} \tag{158}$$

It is sometimes more convenient the density potential temperature, which is an adiabatic invariant that can be directly related to buoyancy:

$$\theta_\rho \overset{\text{def}}{=} T_\rho (\frac{p_0}{p})^{\frac{R_d}{c_{pd}}} \tag{159}$$

8.2.3 Phase transitions

The phase diagram of water substance can be found on figure 72.

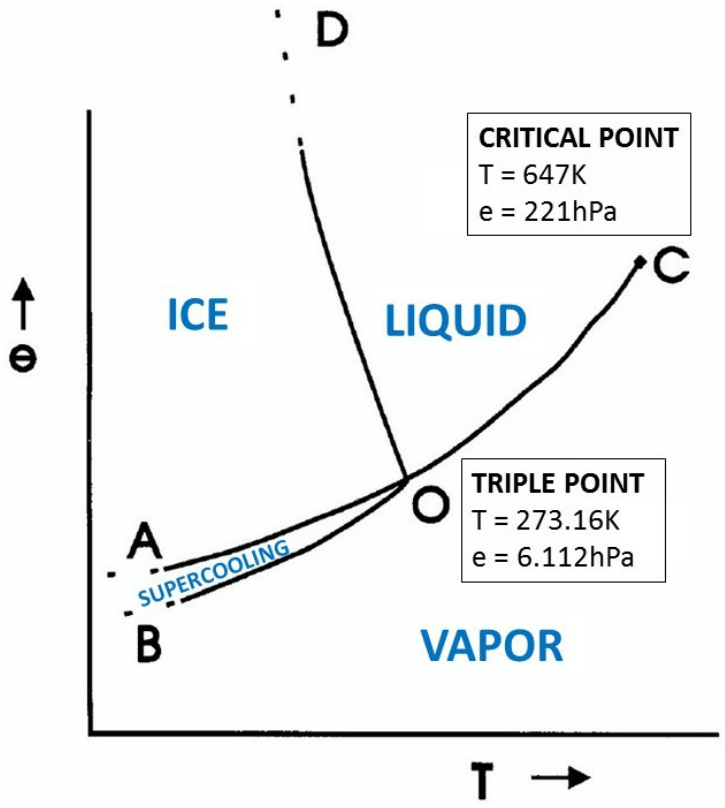

Figure 72: Phase diagram of water substance

Water is one of the few substances where the partial pressure of the liquid/solid equilibrium decreases with temperature, with important atmospheric consequences. Before proving two fundamental laws in phase transition, we introduce Gibbs free enthalpy aka Gibbs potential:

$$g \overset{\text{def}}{=} k - Ts = k + p\alpha - Ts \tag{160}$$

where we use the notations introduced in paragraph 4.3. Taking the differential of definition 160 and using the second thermodynamic identity 49, we derive the fourth thermodynamic identity:

$$dg = \alpha dp - sdT \tag{161}$$

Cross-differentiating 161 and using Schwartz theorem for partial differentials gives another useful Maxwell relation:

$$[\frac{\partial}{\partial T}(\frac{\partial g}{\partial p})_T]_p = [\frac{\partial}{\partial p}(\frac{\partial g}{\partial T})_p]_T \;\Rightarrow\; (\frac{\partial \alpha}{\partial T})_p = -(\frac{\partial s}{\partial p})_T \tag{162}$$

We now study the energetics of phase transition, and introduce the latent heat of the phase change $i \to ii$:

$$L_{i,ii} \overset{\text{def}}{=} k_{ii} - k_i \tag{163}$$

where k_i and k_{ii} are the specific enthalpy of the substance in phases i and ii at the equilibrium point. Physically, $L_{i,ii}$ represents the energy per unit mass that needs to be transferred to the substance at constant temperature and pressure to change from phase i to

phase ii. The specific enthalpy is a thermodynamic state variable and we can write it as $k(T,p)$. According to definition 163, the differential of latent heat can be written:

$$dL_{i,ii} = dT[(\frac{\partial k_{ii}}{\partial T})_p - (\frac{\partial k_i}{\partial T})_p] + dp[(\frac{\partial k_{ii}}{\partial p})_T - (\frac{\partial k_i}{\partial p})_T] \tag{164}$$

- By definition of the specific heat at constant pressure:

$$c_p \overset{\text{def}}{=} (\frac{\partial k}{\partial T})_p \tag{165}$$

- Using the thermodynamic identity 50 and the fourth Maxwell relation 162:

$$(\frac{\partial k}{\partial p})_T = \alpha + T(\frac{\partial s}{\partial p})_T = \alpha - T(\frac{\partial \alpha}{\partial T})_p$$

  For an ideal gas verifying the equation of state 39:

$$T(\frac{\partial \alpha}{\partial T})_p = \alpha \;\Rightarrow\; (\frac{\partial k}{\partial p})_T = 0 \tag{166}$$

  For a more general substance, $(\frac{\partial k}{\partial p})_T$ is not strictly zero but very small.

Combining differential 164 with definition 165 and equation 166, we obtain Kirchhoff's law for the latent heat:

$$\boxed{dL_{i,ii} = dT[c_{p,ii} - c_{p,i}]} \tag{167}$$

Kirchhoff's law is strictly valid for an ideal gas, and approximately valid for a more general substance. Kirchhoff's law 167 tells us how latent heat varies with temperature; for instance the latent heat of vaporization of water decreases with temperature because $c_l > c_{p_v}$ where c_l is the specific heat capacity of liquid water. To study how the pressure varies with temperature for a phase change $i \to ii$, we remember that during a phase change, the system is:

- In thermal equilibrium:

$$T_i = T_{ii} \tag{168}$$

- In mechanical equilibrium:

$$p_i = p_{ii} \tag{169}$$

- In chemical equilibrium:

$$g_i = g_{ii} \tag{170}$$

According to the fourth thermodynamic identity 161:

$$\alpha_i dp - s_i dT = \alpha_{ii} dp - s_{ii} dT$$

$$(\frac{dp}{dT})_{i,ii} = \frac{s_{ii} - s_i}{\alpha_{ii} - \alpha_i} \tag{171}$$

Using the definition of latent heat 163, the definition of specific enthalpy, and the thermal equilibrium 168:

$$L_{i,ii} = k_{ii} - k_i = T(s_{ii} - s_i) \tag{172}$$

Combining equations 171 and 172 leads to Clausius-Clapeyron relation:

$$\boxed{(\frac{dp}{dT})_{i,ii} = \frac{L_{i,ii}}{T(\alpha_{ii} - \alpha_i)}} \tag{173}$$

Clausius-Clapeyron relation 173 allows us to determine the signs of the lines separating the different phases on the water phase diagram 72:

- As ice is less dense than liquid water (very special property of water) $\alpha_{\text{ice}} > \alpha_l \;\Rightarrow\; (\frac{de^*}{dT})_{\text{ice,l}} < 0$ which explains why (DO) has a negative slope.
- As water vapor is less dense than liquid water $\alpha_v > \alpha_l \;\Rightarrow\; (\frac{de^*}{dT})_{l,v} > 0$ which explains why the line (OC) has a positive slope.

More specifically, for the transition from liquid water to water vapor, Clausius-Clapeyron relation 173 yields:

$$(\frac{de^*}{dT})_{l,v} = \frac{L_v}{T(\alpha_v - \alpha_l)} \approx \frac{L_\mathrm{v}}{T\alpha_v} \tag{174}$$

where we have introduced the latent heat of vaporization of water L_v and used the fact that $\alpha_v \gg \alpha_l$. The ideal gas law for water vapor can be written:

$$e^*\alpha_v = R_v T \tag{175}$$

where we have introduced the specific gas constant for water vapor R_v. Combining equations 174 and 175, we obtain Clausius-Clapeyron relation for ideal water vapor:

$$\boxed{(\frac{de^*}{dT})_{l,v} = \frac{L_\mathrm{v} e^*}{R_v T^2}} \tag{176}$$

We can integrate the previous relation 176 if we neglect the variations of the latent heat L_v with temperature:

$$\int_{e_0}^{e^*(T)} \frac{de}{e} = \frac{L_v}{R_v}\int_{T_0}^{T} \frac{dT'}{T'^2} \;\Rightarrow\; e^*(T) \approx e_0 \exp[\frac{L_v}{R_v}(\frac{1}{T_0} - \frac{1}{T})] \tag{177}$$

Formula 177 shows that the saturation pressure of water vapor exponentially with temperature. However, it deviates significantly from observations, not only because we have assumed that the ideal gas law holds and neglected the specific volume of liquid water, but more importantly because we have neglected the variations of L_v with T, which according to Kirchhoff's law 167 is equivalent to making the false assumption $c_l \approx c_{p_v}$. As a consequence, we need to use semi-empirical expressions for the saturation water vapor pressure e^* that require laboratory experiments, such as Bolton's formula:

$$e^*(T) = (6.112\mathrm{hPa}) \exp(\frac{17.67T[^\circ\mathrm{C}]}{243.5 + T[^\circ C]}) \tag{178}$$

Bolton's formula implies a doubling of the saturation water vapor pressure every 10°C. The reference pressure 6.112hPa is the triple point pressure as we can see on figure 72. The triple point is not too far from Earth standard temperature and pressure, which is not a coincidence as life on Earth relies on the coexistence of the three phases of water. In the atmosphere, condensation is a subtle process (responsible of the formation of dew, fog, clouds...), which happens mostly through adiabatic ascent:

- First, the partial pressure e of water vapor, that we can compute using Dalton's law 42:

$$e \overset{\text{def}}{=} p - p_d = p\frac{r}{r+\epsilon} \tag{179}$$

  needs to reach its saturation value $e^*(T)$. As an air parcel ascends in the troposphere, there are two competing effects: the total pressure p decreases, which decreases e through 179. However, the temperature also decreases, which decreases e^* through 176. It can be proven that e^* decreases faster than e as long as the system lies below and on the left of the critical point in the phase diagram 72 (it is always the case in the atmosphere), so that the water vapor in the parcel eventually condensates.

- Then, the condensation process needs to occur. A certain energy is needed as the surface tension energy of the water droplet needs to be provided. This energetic barrier requires high level of supersaturation for this process to occur spontaneously (homogeneous nucleation). However, the atmosphere is full of aerosols, which are very good Cloud Condensation Nuclei (CCN) because of their physical properties, and heterogeneous nucleation dominates in the atmosphere, which explains why supersaturation is practically never observed. To be more precise, the CCN decrease the saturation pressure needed to saturation pressure e^* required to condensate, which can be quantitatively assessed by looking at Köhler's curves on figure 73. Whenever the slop is positive, the droplet is stable whereas it is unstable and grows when the slope is negative, until it reaches its nucleation peak. To summarize, condensation can indeed be approximated as instantaneous for all practical purposes and the relative humidity is always smaller than 1: $\mathcal{H} \leq 1$.

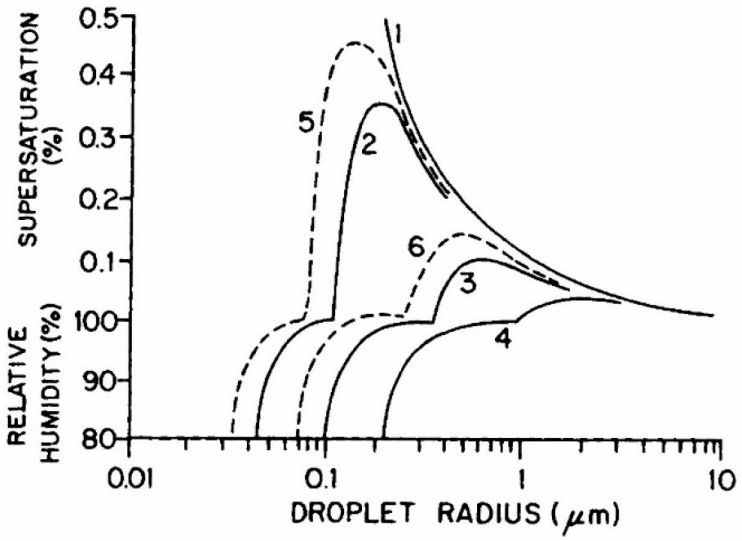

Figure 73: Köhler's curves: Variations of the relative humidity and supersaturation of the air adjacent to droplets of (1) pure water and solution droplets containing higher fixed masses of salts ($2 \rightarrow 6$)

As a consequence, liquid water and water vapor are very close to equilibrium in the atmosphere. It happens that all these aerosols which are very good condensation nuclei are very poor freezing nuclei. The good freezing nuclei are scarce in the atmosphere and their concentration is highly variable from place to place, which explains why liquid water and ice are not in equilibrium in the atmosphere. As a consequence, liquid water exists below the freezing point in the atmosphere: this phenomenon is referred as supercooling and is depicted on the phase diagram of water 72. An alternative to adiabatic ascent for condensation is adiabatic mixing of two samples. Let's consider the example of two unsaturated air samples in (T, q) space, as depicted on figure 74.

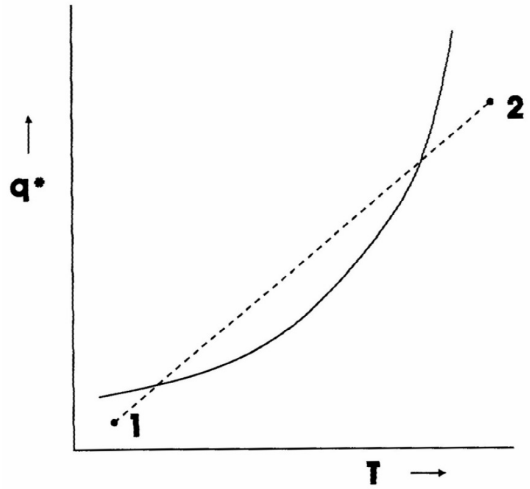

Figure 74: Adiabatic mixing of two unsaturated samples 1 and 2, which approximately mix along the dotted line. The full line represents the saturation specific humidity profile $q^*(T)$.

After they mix adiabatically, the final specific humidity and temperature of the sample will approximately be the mass-weighted average of the initial specific humidities and temperatures of the two samples (true if $e \ll p$). Consequently, the final mixture will lay on the dotted line $(1-2)$ in (T, q) space on figure 74. Because of the nonlinearity of Clausius-Clapeyron, the specific humidity profile $q^*(T)$ will approximately be exponential as according to equations 150 and 177:

$$q^* = \frac{\epsilon e^*}{p - (1-\epsilon)e^*} \approx \frac{\epsilon}{p_0} e^*(T) \approx \frac{\epsilon e_0}{p_0} \exp[\frac{L_v}{R_v}(\frac{1}{T_0} - \frac{1}{T})] \tag{180}$$

As a consequence, we can see on figure 74 that the final mixture will most likely be supersaturated, which means that it will condensate. This is why you can see your breathe condensate on a cold day when the hot air coming from your mouth mixes almost adiabatically with the environmental cold air. Another problem to understand in the atmosphere is: When the droplets form, how do they get big

enough to fall out from clouds. The maximal size of a droplet can be obtained from a balance between gravity and surface tension, leading to the definition of the capillarity length:

$$\ell_c \stackrel{\text{def}}{=} \sqrt{\frac{\sigma}{(\rho_l - \rho_d)g}} \tag{181}$$

We have introduced the surface tension σ : For water the typical value at standard pressure and temperature is 0.07N.m^{-2}, which means that the typical upper bound for a droplet's size will be $\ell_c \approx 3\text{mm}$, corresponding to a terminal fall velocity of $5 - 10\text{m.s}^{-1}$. Several processes can lead to the formation of droplets that will rain:

- **The Bergeron-Findeisen process:** When the cloud top is cold enough for ice crystals to form, if they fall in supercooled water, they will grow rapidly. The presence of supercooled water is very common in cold clouds, as we can see on the sounding depicted on figure 75, where almost no ice crystals are observed in the $-5°\text{C} - 0°\text{C}$ range although the temperature is below the freezing point. The ice crystals will then melt near the ground if the temperature is high enough, and fall out as rain. We have not considered the ice phase in this class, which is an almost reasonable approximation as the latent heat of fusion is only one eighth of the latent heat of vaporization. However, it is impossible to accurately understand the physics of the small water droplets resulting from the Bergeron process without considering the ice phase, making it a crucial microphysical element.
- **The stochastic coalescence process:** In tropical islands, shallow clouds rains although their cloud-top temperature is above the freezing point of water. Rain is actually formed by the random collision of droplets; the efficiency of this process is strongly dependent on the distribution of the droplets sizes. Near the ocean, the aerosols size distribution has a large variance, which explains why this process is dominant in warm islands. In the continents where the particles are numerous but mono-dispersed, this process is much less efficient and the clouds grow to a much bigger size before raining.

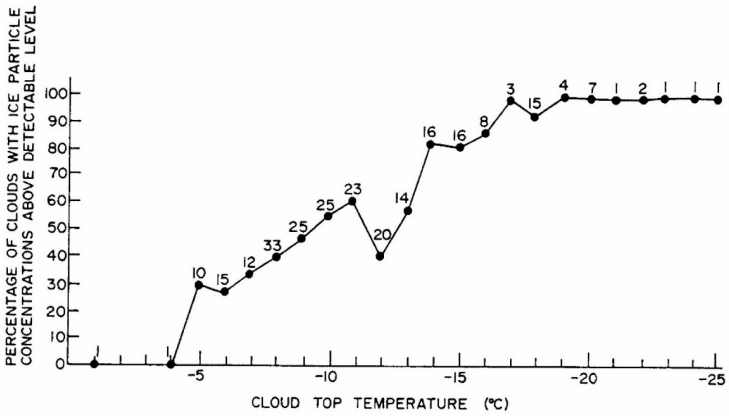

Figure 75: Percentage chance of ice being detected in clouds as a function of the cloud top temperature.

The previous considerations prove that it is impossible to study convection without cloud microphysics if we want to understand phase changes in the atmosphere.

8.2.4 Adiabatic invariants for moist isobaric processes

Since liquid water can be considered to be in thermodynamic equilibrium with water vapor, we can derive a minimal set of conserved variables to be used in moist thermodynamics. At constant pressure, the enthalpy is by definition conserved for adiabatic (not necessarily reversible) transformations. In an atmospheric context, it is convenient to normalize variables by using the total mass of dry air, as we have done in paragraph 4.2:

$$M_\text{d} k = M_d k_\text{d} + M_v k_v + M_l k_l$$

Using the definition of the mixing ratio previously introduced in 43, we can write the specific enthalpy k as:

$$k = k_d + r k_v + r_l k_l = k_d + r(k_v - k_l) + r_T k_l = (c_{p_d} + c_l r_T)T + L_v r \tag{182}$$

where we have:

- Introduced the mixing ratio of liquid water:

$$r_l \stackrel{\text{def}}{=} \frac{M_l}{M_d} \tag{183}$$

- Used the definition 163 of latent heat:

$$k_v - k_d \stackrel{\text{def}}{=} L_v \tag{184}$$

- Used the definition 165 of the specific heat at constant pressure.

Note that we could have eliminated r instead of r_l in equation 182, giving the following expression for the specific enthalpy:

$$k = (c_{p_d} + c_{p_v} r_T)T - L_v r_l \tag{185}$$

From 182, it is possible to derive a set of more simple variables, which are almost conserved and very commonly used. We start by taking the derivative of the second thermodynamic identity 49 in time:

$$T\frac{Ds}{Dt} = \dot{Q} = \frac{Dk}{Dt} + \alpha\frac{Dp}{Dt} \tag{186}$$

Here, $\dot{Q}$ is the diabatic heating, which does NOT include latent heating; in the atmosphere $\dot{Q}$ is usually dominated by the radiative heating. In moist thermodynamics, latent heating should not be treated as an external heat source and moisture needs to be incorporated in the conservation statement. Multiplying 186 by the density $\rho = \alpha_d^{-1}$ and using equation 35 to relate α to the density, we obtain our moist thermodynamic equation:

$$\rho\dot{Q} = \rho\frac{D}{Dt}[(c_{p_d} + r_T c_l)T + L_v r] - (1 + r_T)\frac{Dp}{Dt} \tag{187}$$

We now need to express $\frac{Dp}{Dt}$ using the dynamics of the fluid; we naturally start with the Navier-Stokes equation:

$$\rho\frac{D\overrightarrow{v}}{Dt} = -\overrightarrow{\nabla p} + \rho\overrightarrow{g} + \rho\overrightarrow{F} \tag{188}$$

Taking the dot-product of 188 with the velocity field $\overrightarrow{v}$ gives an equation for the evolution of the kinetic energy:

$$\rho\frac{D}{Dt}\frac{|\overrightarrow{v}|^2}{2} = -\overrightarrow{v}\cdot\overrightarrow{\nabla p} - \rho g w + \rho\overrightarrow{v}\cdot\overrightarrow{F} = -\overrightarrow{v}\cdot(\frac{\partial p}{\partial t} - \frac{Dp}{Dt}) - \rho g\frac{Dz}{Dt} + \rho\overrightarrow{v}\cdot\overrightarrow{F} \tag{189}$$

where we have used the notations introduced in section 4.1. Combining equations 187 and 189 allows to eliminate $\frac{Dp}{Dt}$ and leads to an equation for the total energy of moist air:

$$\boxed{\frac{D\mathcal{E}}{Dt} = \underbrace{\dot{Q}}_{\text{Diabatic heating}} + \underbrace{\overrightarrow{v}\cdot\overrightarrow{F}}_{\text{Friction}} + \underbrace{\frac{1+r_T}{\rho}\frac{\partial p}{\partial t}}_{\text{Wave radiation term}}} \tag{190}$$

where the total energy of moist air is defined to be:

$$\mathcal{E} \overset{\text{def}}{=} \underbrace{(1+r_T)\frac{|\overrightarrow{v}|^2}{2}}_{\text{Kinetic energy}} + \underbrace{(c_{p_d} + r_T c_l)T + L_v r}_{\text{Enthalpy}} + \underbrace{(1+r_T)gz}_{\text{Pontential energy}} \tag{191}$$

Note that the kinetic energy and the wave radiation term are not Galilean invariant quantities, and make it hard to conserve energy in numerical models of the atmosphere. Thu usual approximation is to neglect the kinetic energy, typically smaller than the other terms by a factor of 100 (eg lifting a parcel only 5m up in the atmosphere gives a potential energy that corresponds to a kinetic energy of velocity 10m.s^{-1}, which is the order of magnitude of the wind velocity in the atmosphere). To not generate inconsistent energy, we often use the Moist Static Energy (MSE) as our energy variable:

$$h \overset{\text{def}}{=} (c_{p_d} + r_T c_l)T + L_v r + (1 + r_T)gz \tag{192}$$

Neglecting the wave radiation term in 190, the MSE equation reduces to:

$$\boxed{\underbrace{\frac{Dh}{Dt}}_{\text{Evolution MSE}} \approx \underbrace{\dot{Q}}_{\text{Diabatic heating}} + \underbrace{\overrightarrow{v}\cdot\overrightarrow{F}}_{\text{Friction}}} \tag{193}$$

which means that MSE is conserved for frictionless and adiabatic motion. However, it is not strictly speaking an adiabatic invariant because we have neglected the kinetic energy and the wave radiation term in equation 190. This has to be taken into account when studying hurricane physics, where the kinetic energy term is not small. Another common quantity is the Dry Static Energy (DSE), where condensation is not taken into account, and the mixing ratios are constant ($r = r_T = \text{Constant}$):

$$h_d \overset{\text{def}}{=} (c_{p_d} + r c_l)T + gz \tag{194}$$

The definition of DSE 194 gives a very straightforward way of computing the dry adiabatic lapse rate 54. Indeed, we simply need to define the lapse rate as the variation of temperature with altitude at constant DSE:

$$\Gamma \stackrel{\text{def}}{=} (\frac{\partial T}{\partial z})_{h_d} = -\frac{g}{c_{p_d} + rc_l} \approx \frac{1^\circ\text{C}}{100\text{m}} \tag{195}$$

If we define the specific enthalpy using equation 185 instead than equation 182, the equivalent of the moist static energy is the liquid water enthalpy:

$$h_w \stackrel{\text{def}}{=} (c_{p_d} + r_T c_{p_v})T - L_v r_l + (1 + r_T)gz \tag{196}$$

which involves the liquid water mixing ratio r_l rather than r. Note that the moist static energy 192 and the liquid water enthalpy 196 are only approximately conserved for isobaric adiabatic processes. If the process is adiabatic and reversible but not isobaric, enthalpies are not conserved anymore and it is convenient to introduce entropy-variables.

8.2.5 Adiabatic invariants for moist reversible processes

We have seen that liquid water and water vapor can be assumed to be in thermodynamic equilibrium in the atmosphere to a reasonable approximation. We want to write the moist entropy s as a function of the (T, p, r, e). In that purpose, we remember that the moist entropy can be defined as the mass-weighted sum of the dry air entropy, water vapor entropy, and liquid water entropy:

$$s \stackrel{\text{def}}{=} s_d + rs_v + r_l s_l = s_d + r(s_v - s_l) + r_T s_l = s_d + r(s_v^* - s_l) + r(s_v - s_v^*) + r_T s_l \tag{197}$$

$$\boxed{s = [c_{p_d} + r_T c_l] \ln(\frac{T}{T_0}) - R_d \ln[\frac{p}{p_0} \frac{1 + r_T}{1 + \frac{r}{\epsilon}}] + \frac{L_v r}{T} - rR_v \ln \mathcal{H}} \tag{198}$$

where we have used:

- Equation 172 to write:
$$L_v = T(s_v^* - s_l)$$
- The definition 68 of dry entropy.
- The definition of water vapor entropy:
$$s_v \stackrel{\text{def}}{=} c_p \ln(\frac{T}{T_0}) - R_v \ln(\frac{e}{e_0}) \tag{199}$$
leading to:
$$s_v - s_v^* = -R_v \ln(\frac{e}{e^*}) = -R_v \ln \mathcal{H}$$
where we have used the definition of the relative humidity $\mathcal{H}$.
- Dalton's law 42 to express p_d as a function of p.

From the definition of specific enthalpy and entropy, it is possible to derive moist Maxwell relations, including the addition and subtraction of water mass. Differentiating 182 and eliminating (dT, dr) for (ds, dp) by using the differential of the moist entropy definition 197, we obtain:

$$dk = Tds + c_l T(1 - \ln T)dr_T + \alpha_d dp \tag{200}$$

Here, we have chosen the entropy constant s_0 such as to eliminate the temperature constant T_0. By cross-differentiating equation 200 and using Schwartz theorem as we have done to prove the dry Maxwell relations 51 and 162, we obtain the moist Maxwell relations:

$$(\frac{\partial T}{\partial p})_{s,r_T} = (\frac{\partial \alpha_d}{\partial s})_{p,r_T} \tag{201}$$

$$(\frac{\partial T}{\partial r_T})_{p,s} = -c_l \ln T (\frac{\partial T}{\partial s})_{p,r_T} \tag{202}$$

$$(\frac{\partial \alpha_d}{\partial r_T})_{p,s} = -c_l \ln T (\frac{\partial T}{\partial p})_{s,r_T} \tag{203}$$

Entropy has to be treated carefully, as many processes are irreversible. The evaporation of water into unsaturated air corresponds to a finite jump of the mixing ratio r for a small displacement of air, which is an irreversible source of entropy. If we assume a global energy balance for planet Earth and do a global entropy budget, the fact that radiation absorbed at a higher temperature than it is emitted back means that entropy is created. The biggest sources of created entropy on Earth are actually:

1. Mixing in the cloud boundary layers.

2. Frictional rain dissipation ($\approx 10\%$).

Frictional wind dissipation constitutes less than 1% of the created entropy. From this entropy budget, we can find very loose upper bounds for different types of renewable energy. Solar energy is limited by the solar constant, whereas wind energy would never reach more than 1% of the incoming solar energy. As frictional rain dissipation constitutes roughly 10% of the entropy budget, the upper bound of hydrological renewable energy lays between the two previous bounds.

8.3 Stability to motions involving phase transitions

8.3.1 Buoyancy of a moist cloudy sample

We have assessed the stability of a dry sample in 4.3. We now want to assess the stability of a moist cloudy sample (a sample that contains water vapor and liquid water). Because of the presence of moisture, the specific volume is now a state variable that depends on three variables. Choosing pressure, entropy, and the total mixing ration as the three variables, we obtain:

$$\alpha = \alpha(p, s, r_T) \;\Rightarrow\; (d\alpha)_p = (\frac{\partial \alpha}{\partial s})_{p,r_T} ds + (\frac{\partial \alpha}{\partial r_T})_{p,s} dr_T \tag{204}$$

By definition (33), the buoyancy of the moist cloudy sample is given by:

$$b = g\frac{\alpha'}{\alpha} = \frac{\Gamma_m[(s^*)' - c_l \ln(\frac{T}{T_0})r'_T] - g r'_T}{1 + r_T} \tag{205}$$

where primes denote the difference of a variable between an air parcel and the environment. We also have defined the moist adiabatic lapse rate:

$$\Gamma_m \overset{\text{def}}{=} -(\frac{\partial T}{\partial z})_{s^*,r} \tag{206}$$

We have introduced a key quantity: s^* , the saturation moist entropy, defined by setting $(r, r_T, \mathcal{H})$ to $(r^*, r_T^*, 1)$ in the moist entropy definition 197:

$$s^* \overset{\text{def}}{=} [c_{p_d} + r_T^* c_l] \ln(\frac{T}{T_0}) - R_d \ln[\frac{p}{p_0}\frac{1 + r_T^*}{1 + \frac{r^*}{\epsilon}}] + \frac{L_v r^*}{T} \tag{207}$$

8.3.2 Stability of an entropy profile

A typical s^* profile is plotted on figure 76.

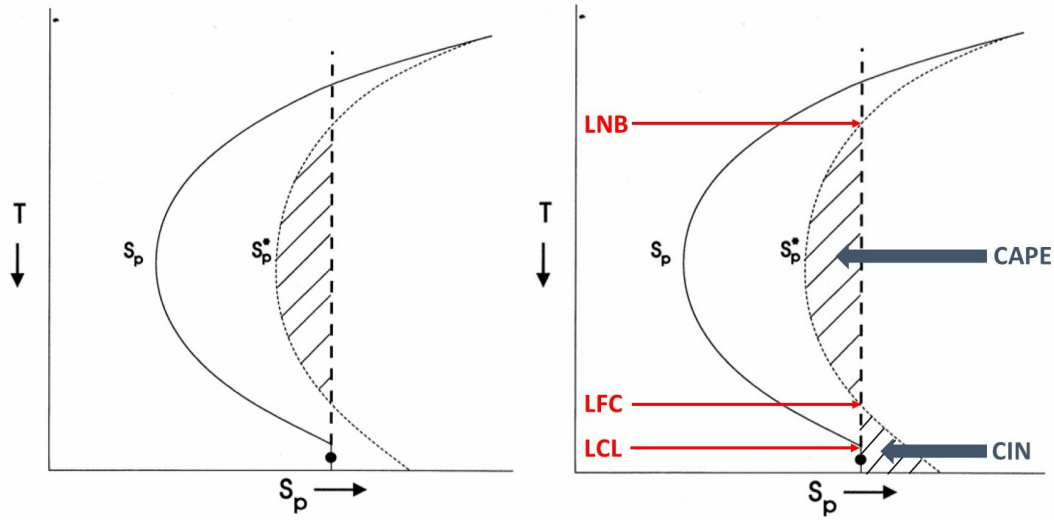

Figure 76: Typical entropy s and saturated s^* profiles; on the right the LNB, LFC, LCL, CAPE and CIN are indicated.

To evaluate the stability of a sample, we look at the buoyancy 205:

- The two terms on the right can be almost canceled by choosing T_0 judiciously.
- The stability thus entirely depends on the saturated entropy s^*: If the saturated entropy of the parcels is larger/smaller than the environmental entropy, the buoyancy force will be directed upwards/downwards. Unlike the dry stability case 53, the buoyancy is not related to an adiabatic invariant as s^* is only conserved for adiabatic saturated motions. This is what makes moist convection so difficult. Latent heating only requires to add a term to the entropy. However, the irreversible fallout of convection making the air sub-saturated, which prevents s^* from being an adiabatic invariant, making it much harder to assess the stability of a profile.

If we take the example of profile 76, when the moist sample (represented by a point) is lifted adiabatically from the ground, its entropy is conserved and is thus represented by the vertical dotted line. If the displacement is not large enough, the entropy of the sample will always be smaller than the environmental s^* and the buoyancy force will be directed downwards, making the sample's displacement stable. If the displacement is large enough to reach the point where the dotted line and the environmental s^* intersect (aka the Level of Free Convection or LFC), then the buoyancy force will be directed upwards and the sample will lift until it reaches the level where the dotted line and the s^* profile intersect again (aka the Level of Neutral Buoyancy or LNB). Thus, an air sample is unstable to large enough displacement, which means it is conditionally unstable (or equivalently metastable). Note that an air sample usually condensates before it reaches the Level of Free Convection; the level at which it condensates is called the Lifted Condensation Level (LCL). From these levels, it is possible to define:

- The Convective Available Potential Energy (CAPE):

$$\text{CAPE}_\text{i} \stackrel{\text{def}}{=} \int_{\text{LFC}_\text{i}}^{\text{LNB}_\text{i}} B dz \tag{208}$$

  Graphically, the CAPE is related to the area between the parcel and the environmental entropy profiles (cf right of figure 76). From the CAPE, it is possible to estimate the maximal vertical velocities available when all the CAPE is used (eg during a very strong storm):

$$\frac{V_{\text{max}}^2}{2} = \text{CAPE} \;\Rightarrow\; V_{\text{max}} = \sqrt{2\text{CAPE}} \tag{209}$$

  For example, the maximal values observed for a CAPE of a profile reach 5000J.kg^{-1}, giving maximal V_{max} of order 100m.s^{-1}. Using the buoyancy of a moist cloudy sample 205, the CAPE 208 becomes:

$$\underbrace{\text{CAPE}_i}_{\text{Potential energy}} \approx \int_{\text{LFC}_\text{i}}^{\text{LNB}_\text{i}} \underbrace{(s^*)' dT}_{\text{Thermodynamic work}} - \underbrace{g(r_T)' dz}_{\text{Work to lift water}} \tag{210}$$

  The expression of the CAPE becomes simpler if we use the definition of the density temperature 47 and assume that the atmosphere is an ideal hydrostatic gas:

$$\text{CAPE}_\text{i} \approx \int_{\text{LFC}_\text{i}}^{\text{LNB}_\text{i}} R_d (T_\rho)' d(\ln p) \tag{211}$$

- The Convective Inhibition (CIN):

$$\text{CIN}_\text{i} \stackrel{\text{def}}{=} -\int_{z_\text{i}}^{\text{LFC}_\text{i}} B dz \tag{212}$$

The subscripts i have been added because the CAPE is defined for a sample lifted from a given altitude z_i. It is thus not unique for a given profile, and if we wanted to rigorously test the stability of a profile, we would have to lift air samples from all the altitudes z_i of the profile. Usually, air samples are lifted form the surface ($p_0 \approx 1000\text{hPa}$) of from the top of the boundary layer ($p_1 \approx 950\text{hPa}$).

8.3.3 Thermodynamic diagrams

A skew-T diagram is presented on the left of figure 77.

- The horizontal scale is density temperature, and the isotherm are skewed 45° to the right, in order to make the graph more compact.
- The vertical scale is the pressure in logarithmic scale, so that according to 208, the CAPE is proportional to the area between the parcel and the environment's profiles.
- The dry-adiabats (constant potential temperature θ defined in 67) are depicted in blue.
- The pseudo moist adiabats are depicted in red. The pseudo-adiabatic ascent of a sample is one where the liquid water is removed from the sample as soon as it is formed by condensation. If we define the pseudo-equivalent potential temperature θ_{ep} as the potential temperature conserved during a pseudo-adiabatic transformation, Bolton's curve fit yields:

$$\theta_{\text{ep}} \approx T\left(\frac{p_0}{p}\right)^{0.2854(1-0.28r)} \exp\left[r(1+0.81r)\left(\frac{3376\text{K}}{T^*} - 2.54\right)\right] \tag{213}$$

  where T^* is the saturation temperature.

Note that it would be impossible to plot a moist adiabat, because its profile not only requires the knowledge of pressure but also of the total mixing ratio.

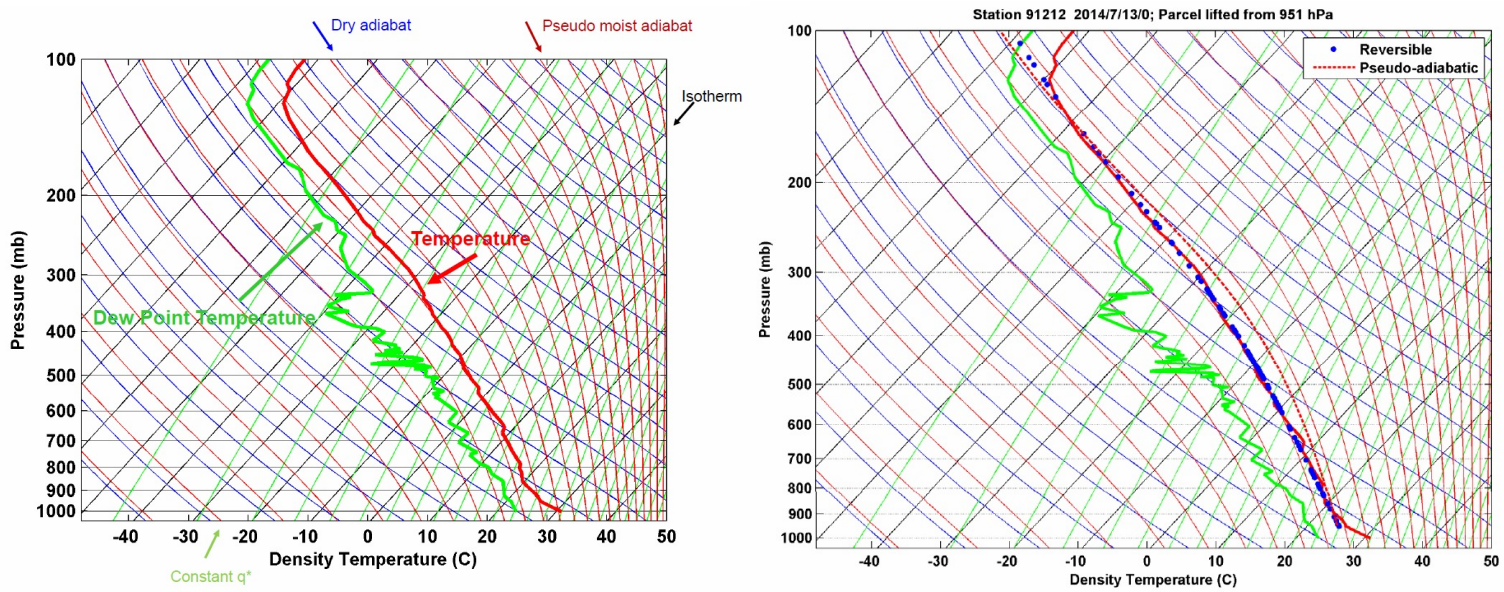

Figure 77: Skew-T diagram; on the right the pseudo-adiabatic and reversible trajectories of a sample lifted from 950hPa have been added

On the right of figure 77, we can see that the sounding (red full line) is very close to the reversible trajectory (blue dots) of an air sample lifted from 950hPa, which is generally true in the Tropics; it is less close to the pseudo-adiabatic trajectory of an air sample lifted from 950hPa (red dotted line). A good way to assess the general stability of a sounding is to plot the contours of the buoyancy for different sample's initial pressures (figure 78).

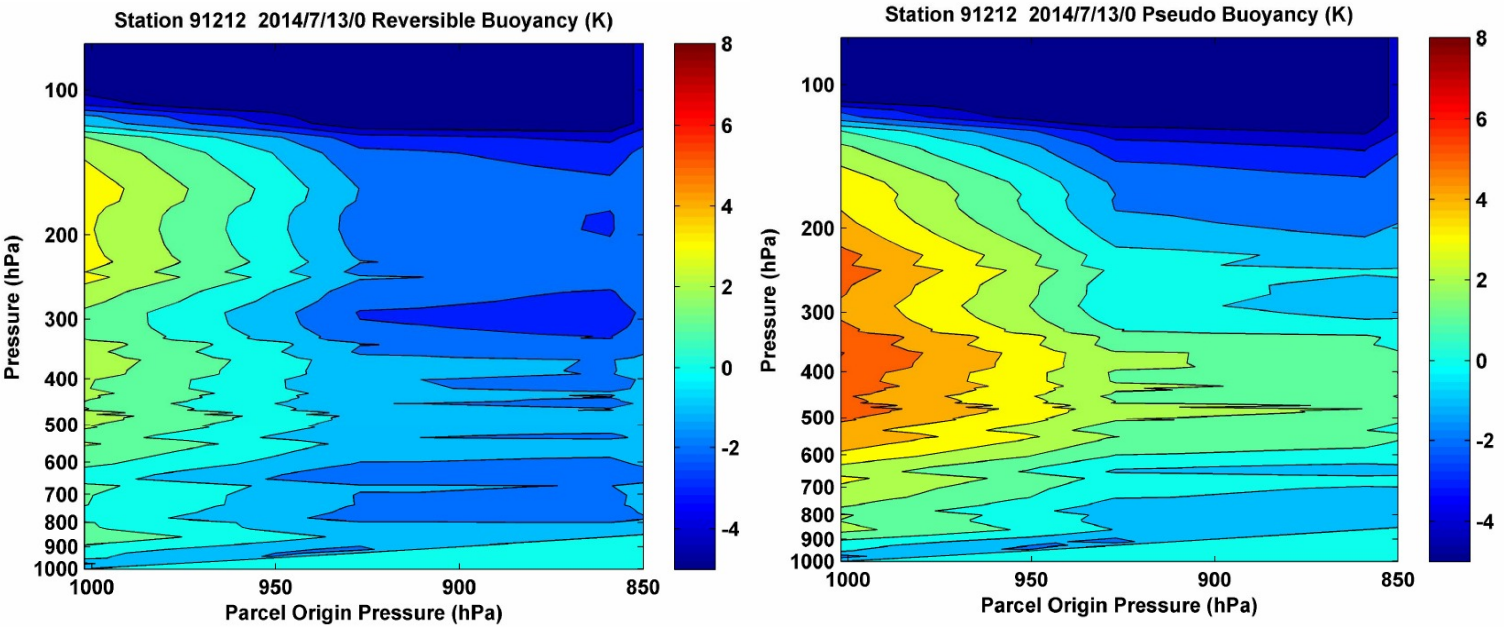

Figure 78: Contours of reversible buoyancy (left) and pseudo-buoyancy (right) of an air sample lifted in the sounding in 77

We see that samples are more unstable when lifted from a high pressure (low altitude) point. The LFC can be defined as the altitude where the buoyancy becomes positive, whereas the LNB is the level at which it becomes negative again. We remember the dry entraining plume model: the mass conservation of a thermal yielded 71. If we had a strictly vertical plume, we could write the conservation of any conserved variable φ (such as heat or buoyancy) using the entrainment parameter α:

$$\frac{d\varphi}{dz} = -\alpha \frac{\varphi_{\text{Plume}} - \varphi_{\text{Environment}}}{z} \tag{214}$$

Taking entrainment into account brings us even closer to the observed sounding, suggesting that it is neutrally stable to an entraining plume.

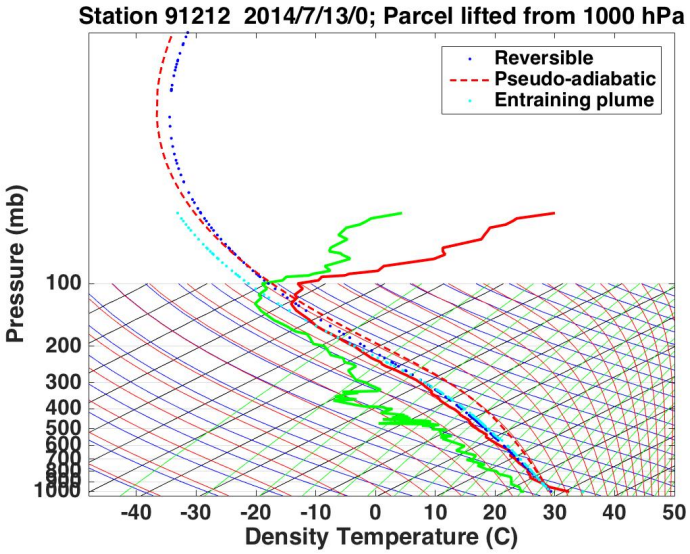

Figure 79: Same sounding as before, but this time taking the entrainment into account

9 Scattering

9.1 Introduction

Scattering plays an important role in the Earth's climatic budget (cf figure 2) and mainly depends on the radiation field (it is only weakly connected to the local values of the gas thermodynamic properties, such as its temperature). The non locality of radiation means that scattering over large distances can make the atmosphere feels the presence of boundaries from far away. For example, the albedos of different surface types can differ by a factor of 10 (cf figure 80).

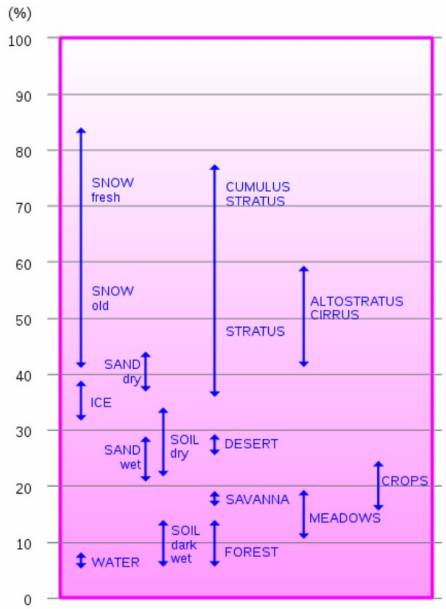

Figure 80: Albedos of different surfaces

We can see that water has the lowest albedo (~8%), making the ocean look very "dark" from space: If Earth looks like a "blue planet", it is mostly because of Rayleigh scattering in the atmosphere. In satellite meteorology, a quantity called the Bidirectional

Reflectance Distribution Function (BRDF) is used:

$$\mathrm{BRDF}(\Omega_i, \Omega_r) \stackrel{\mathrm{def}}{=} \frac{dI_r(\Omega_r)}{I_i(\Omega_i)\cos\theta_i d\Omega_i} \tag{215}$$

where I_i is the incident intensity in the incoming direction defined by its solid angle: $\Omega_i = \Omega_i(\theta_i, \phi_i)$ and I_r is the reflected intensity in the reflected direction defined by its solid angle: $\Omega_r = \Omega_r(\theta_r, \phi_r)$.

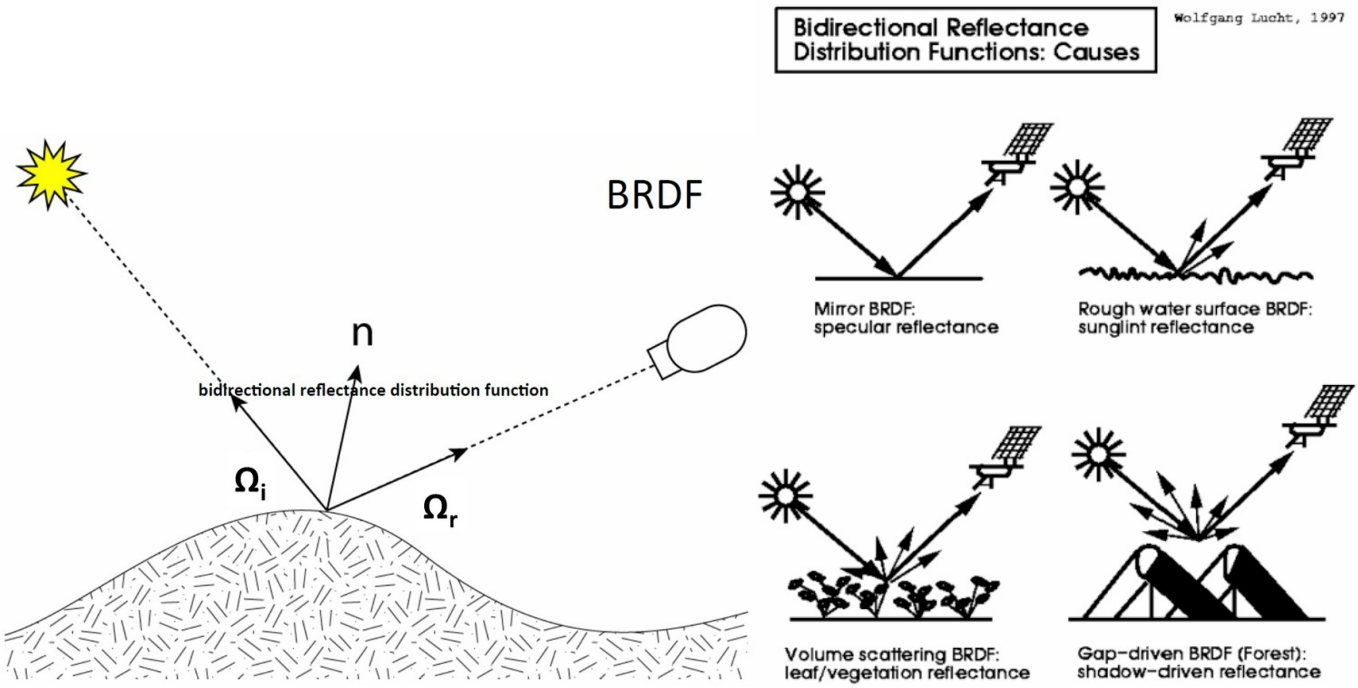

Figure 81: Definition of BRDF (left) and its causes (right)

The different processes that can shape the BRDF distribution defined by 215 are listed on the right of figure 81. For example, if we consider the example of leaf/vegetation reflectance, the albedo is not the most important factor, and the asymmetry of the vegetation (direction of the leaves, trees...) also plays a big role in shaping the BRDF. Three example of surface's BRDF asymmetry are given on figure 82: depending on the position of the sun, the angle Ω_i changes and the scattering of the radiation by the vegetation/ground changes significantly.

This is a black spruce forest in the BOREAS experimental region in Canada. Left: backscattering (sun behind observer), note the bright region (hotspot) where all shadows are hidden. Right: forwardscattering (sun opposite observer), note the shadowed centers of trees and transmission of light through the edges of the canopies. Photograph by Don Deering.

A soybean field. Left: backscattering (sun behind observer). Right: forwardscattering (sun opposite observer), note the specular reflection of the leaves. Photograph by Don Deering.

A barren field with rough surface Left: backscattering (sun behind observer), note the bright region (hotspot) where all shadows are hidden. Right: forwardscattering (sun opposite observer), note the specular reflection. Photograph by Don Deering.

Figure 82: Difference in light transmission between forward-scattering and back-scattering for three different surfaces

Computing the BRDF distribution has been significantly simplified by the use of Monte-Carlo methods and the possibility of tracing individual rays. Furthermore, current databases such as the MERL BRDF database [http://www.merl.com/brdf/] includes reflectance for more than 100 materials (cf figure 83), making numerical computations of the BRDF feasible for simple enough surfaces.

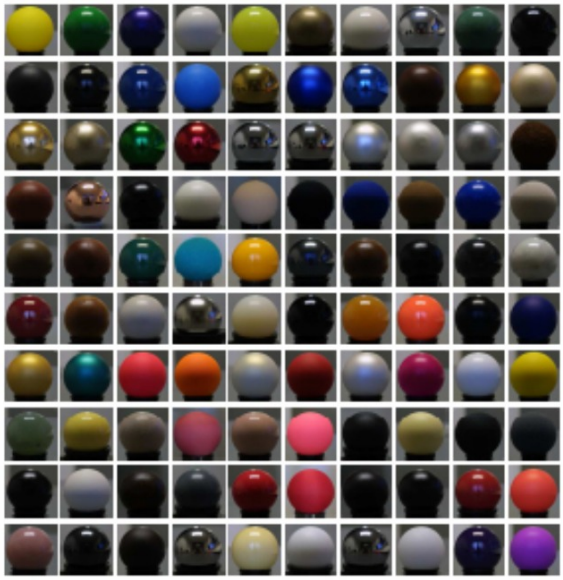

Figure 83: "A Data-Driven reflectance Model" by Wojciech, Matusik, Hanspeter, Pfister, Matt Brand and Leonard McMillan

9.2 The scattering phase function

9.2.1 Definitions

The scattering absorptivity $\varepsilon_{\text{scatter}}$ of radiation coming from a direction $\overrightarrow{\Omega}'$ and scattered in the direction of interest $\overrightarrow{\Omega}$ is computed by introducing the dimensionless single scattering albedo $\tilde{\omega}$:

$$\varepsilon_{\text{scatter}} = \frac{\kappa\tilde{\omega}}{4\pi}\int_{(\Omega')}\mathcal{P}(\overrightarrow{\Omega}', \overrightarrow{\Omega})I(\overrightarrow{\Omega}')d\Omega' \tag{216}$$

where we have used the absorptivity κ defined in 20. The phase function $\mathcal{P}$ determines the contribution from each direction of scattering, and is normalized over a sphere:

$$\int_{(4\pi)}\mathcal{P}(\overrightarrow{\Omega}', \overrightarrow{\Omega})d\Omega' \overset{\text{def}}{=} 4\pi \tag{217}$$

Physically, $\mathcal{P}$ is the probability that a photon coming from a direction $\overrightarrow{\Omega}'$ is scattered in a direction $\overrightarrow{\Omega}$. The functional dependence of the phase function $\mathcal{P}$ can be quite complicated, depending on the sizes and shapes of the particles responsible for the scattering. We will assume:

- That radiation is scattered independently by each particle (particles must be separated by a few times their radius, and the volume of particles should be small enough that the fractional attenuation of light passing through it is much less than unity).
- That the atmospheric particles are spherical or randomly oriented, so that the phase function only depends on the angle Θ between the two units vector $(\overrightarrow{\Omega}, \overrightarrow{\Omega}')$, defined by:

$$\overrightarrow{\Omega}\cdot\overrightarrow{\Omega}' \overset{\text{def}}{=} \cos\Theta = \mu \tag{218}$$

A metric for the anisotropy of the phase function is the asymmetry parameter, defined as the "average value" of μ:

$$g \overset{\text{def}}{=} \frac{1}{4\pi}\int_{(\Omega)}\mathcal{P}(\mu)\mu d\Omega \tag{219}$$

If $g > 0$ the photons preferentially scatter in the forward direction, whereas if $g < 0$, the photons preferentially scatter in the backwards direction.

9.2.2 Examples

Isotropic scattering assumes a homogeneous phase function:

$$\mathcal{P}_{\text{Isotropic}}(\mu) \overset{\text{def}}{=} 1 \;\Leftrightarrow\; g = 0 \tag{220}$$

For a single photon, it means that it has the same probability of going in any direction, which means it follows a 3D random walk It "bounces and never escapes" like a photon in an optically thick cloud), as illustrated by figure 84.

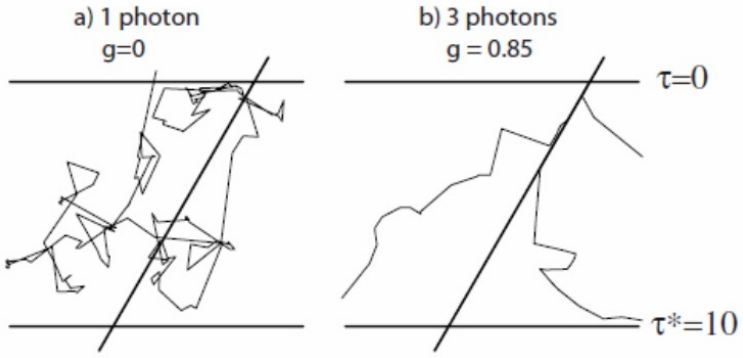

Figure 84: Examples of the random paths of photons in a plane parallel scattering layer of optical thickness 10. Heavy diagonal lines represent the trajectories of unscattered photons while normal lines represent (a) the scattering of a single photon when scattering is isotropic (b) the trajectories of three photons when the asymmetry parameter is equal to 0.85, which is typical for a cloud in solar band

Isotropic scattering is never practically observed in nature. From the radiation of the induced electric dipole moment of the molecules, it can be proven that the phase function for Rayleigh scattering has the following form:

$$\mathcal{P}_{\text{Rayleigh}}(\mu) = \frac{3(1+\mu^2)}{4} \tag{221}$$

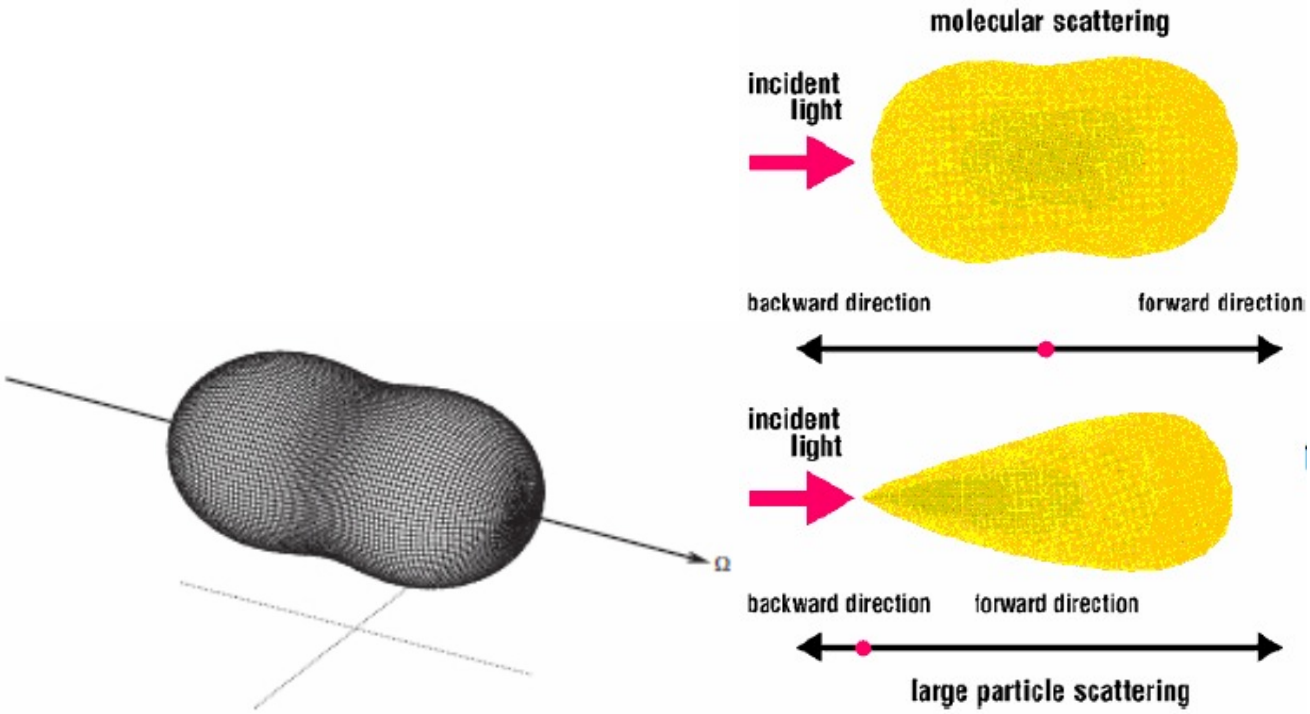

Figure 85: 3D rendering of the Rayleigh phase function (left) and comparison between the Rayleigh phase function 221 and the Henyey-Greenstein phase function 222 (right)

Rayleigh scattering is polarized and maximal for the direction of the incident radiation ($\Theta \in [0, \pi] \Leftrightarrow \mu^2 = 1$), and minimal orthogonally to that direction ($\Theta = \pm\frac{\pi}{2} \Leftrightarrow \mu = 0$). In general, the phase function is quite complicated and it is not necessary to know it in detail for radiative transfer calculations. Often, knowledge of the asymmetry parameter g is enough and it is possible to model the phase function as a Henyey-Greenstein profile (a non-negative explicit function of μ and g that resembles realistic phase functions):

$$\mathcal{P}_{HG}(\mu, g) \overset{\text{def}}{=} \frac{1-g^2}{(1+g^2-2\mu g)^{\frac{3}{2}}} \tag{222}$$

The Henyey-Greenstein phase function is plotted on figure 86 and compared to the Rayleigh function on the right of figure 85.

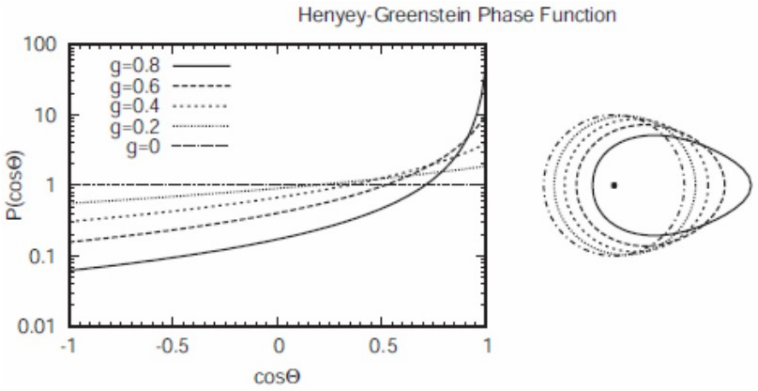

Figure 86: The Henyey-Greenstein phase function plotted versus $\cos\Theta$ (left) and as a log-scaled polar plot (right)

Finally, many particles have a smaller back-scattering peak in addition to the main forward scattering peak. The double Henyey-Greenstein function is able to capture the two peaks:

$$\mathcal{P}_{HG2} \stackrel{\text{def}}{=} b\mathcal{P}_{HG}(\mu, g_1) + (1-b)\mathcal{P}_{HG}(\mu, g_2) \tag{223}$$

where $(g_1 > 0, g_2 < 0, b \in [0,1])$ and $\mathcal{P}_{HG}$ is defined by equation 222.

9.2.3 Influence of the particle's size and the radiation's wavelength

The scattering regimes mainly depend on a key dimensionless parameter, called the size parameter, and defined as:

$$x \stackrel{\text{def}}{=} \frac{2\pi r_{\text{Particle}}}{\lambda} \tag{224}$$

For $x \ll 1$, Rayleigh scattering applies and for $x \gg 1$, it is possible to use ray tracing or geometric optics, whereas for $x \sim 1$, it is necessary to come back to the primitive equations and use Mie theory. A direct example of the different scattering regimes is given on figure 87.

Type	Size	Number
Gas molecule	$\sim 10^{-4}$ μm	$< 3 \times 10^{19}$ cm^{-3}
Aerosol, Aitken	< 0.1 μm	$\sim 10^{4}$ cm^{-3}
Aerosol, Large	0.1–1 μm	$\sim 10^{2}$ cm^{-3}
Aerosol, Giant	>1 μm	$\sim 10^{-1}$ cm^{-3}
Cloud droplet	5–50 μm	10^{2}–10^{3} cm^{-3}
Drizzle drop	~ 100 μm	$\sim 10^{3}$ m^{-3}
Ice crystal	10–10^{2} μm	10^{3}–10^{5} m^{-3}
Rain drop	0.1–3 mm	10–10^{3} m^{-3}
Graupel	0.1–3 mm	1–10^{2} m^{-3}
Hailstone	~ 1 cm	10^{-2}–1 m^{-3}
Insect	~ 1 cm	< 1 m^{-3}
Bird	~ 10 cm	$< 10^{-4}$ m^{-3}
Airplane	~ 10 m	< 1 km^{-3}

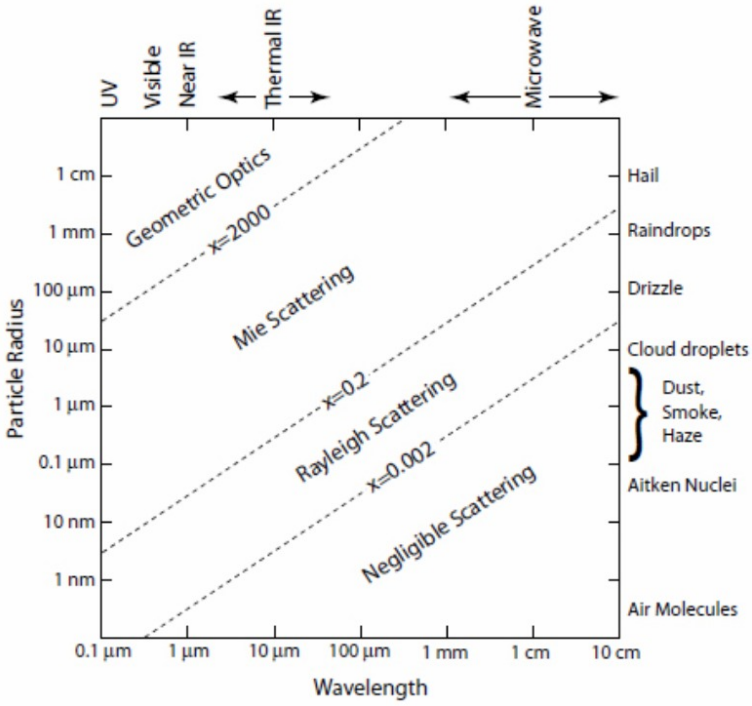

Figure 87: Examples of atmospheric particle types, with representative dimensions and number concentrations (left) and relationship between particle size, radiation wavelength and scattering behavior for atmospheric particles based on the size parameter 224 (right)

An important difference between the different regimes is that for small x, forward and backward scattering are about equal, whereas forward scattering prevails for $x \geq 1$. This behavior is due to constructive interference in the forward direction by waves scattered by the different part of the particles. This asymmetry that increases with x can be seen on the phase functions (figure 87) and the polar plots of Mie-derived scattering phase functions (figure 89).

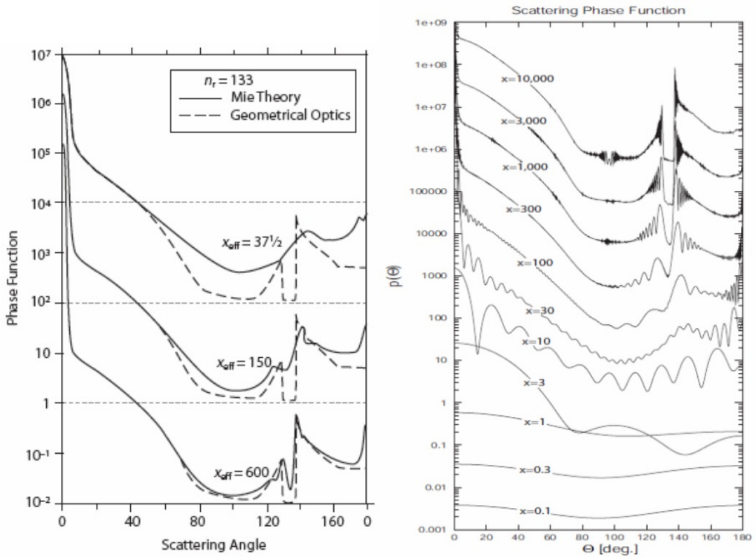

Figure 88: The phase function for single scattering by spherical liquid water droplets (left) and plots of Mie-derived phase functions for various values of x (right)

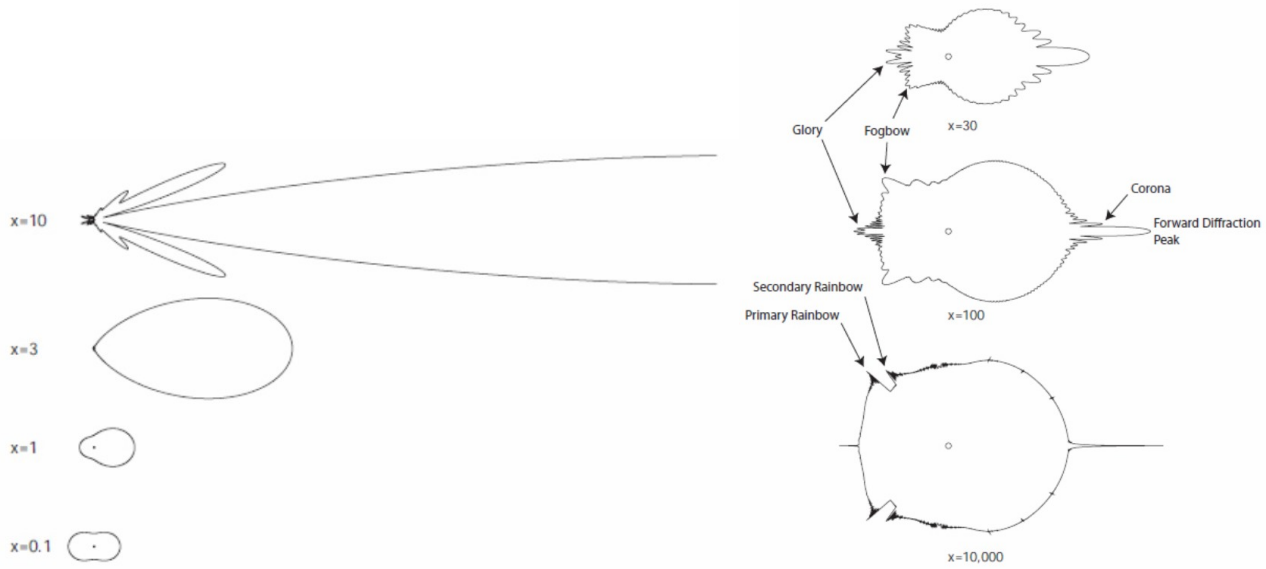

Figure 89: Polar plots of the Mie-derived scattering phase functions for selected values of x (left) and same plot but in logarithmic scale to better accommodate the variations of $\mathcal{P}(\mu)$ for large values of x (right)

Two applications of the previous phase functions are:

1. **The glory:** If you stand on a hill overlooking a fog bank with the sun at your back, you will see a bright patch of ring surrounding the shadow of your head in the manner of medieval paintings of saints (cf left of figure 90 and right of figure 89).

2. **The rainbow:** The primary rainbow can be seen as peaks of the phase functions on the right of figure 89. It can also simply be explain by the reflections and refractions occurring in a droplet (left of figure 91). The rainbow corresponds to the ray $l = 3$ with one internal reflection.

Figure 90: A glory (left) and a rainbow (right)

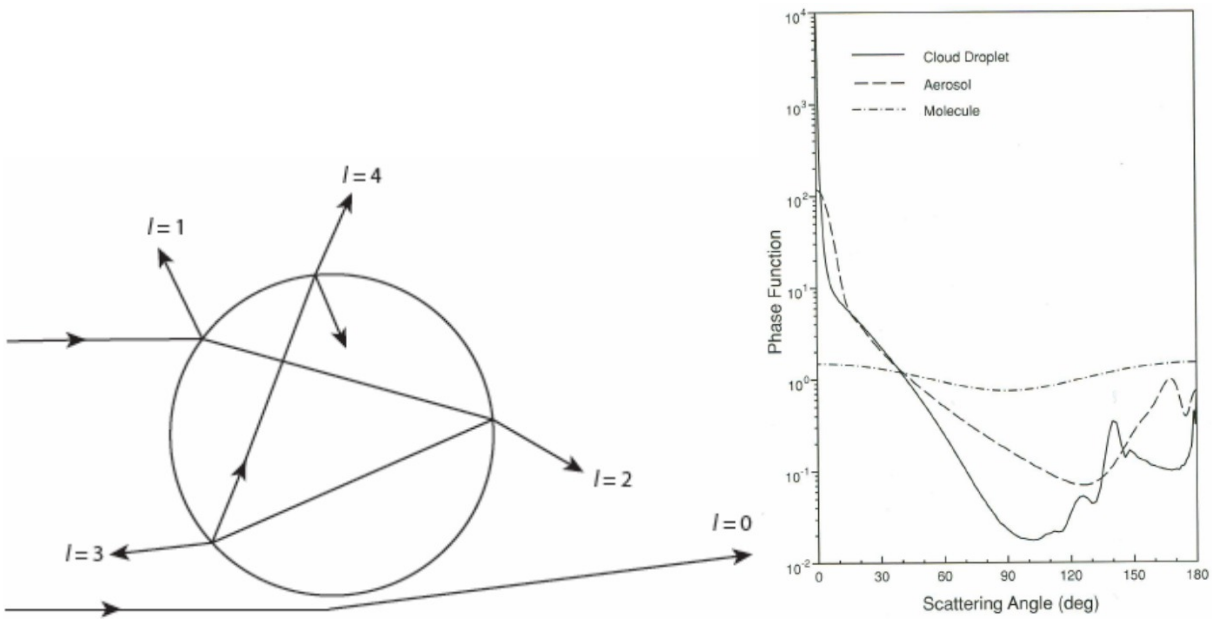

Figure 91: Paths of light rays reflected, refracted or diffracted by a sphere (left) and normalized functions for cloud droplets, aerosols and molecules illuminated by a visible wavelength of 0.5μm (right)

Looking at the right of figure 91, we can see that Mie theory gives complex variations of the phase function for a water droplet, which we can explain by all the paths the light can take in it (left of figure 91). As a consequence, we don't expect a simple fit such as 222 to work in this case. Indeed, according to figure 92, this profile is only helpful to understand the phase function of ocean particles, and the approximate phase function of aerosols.

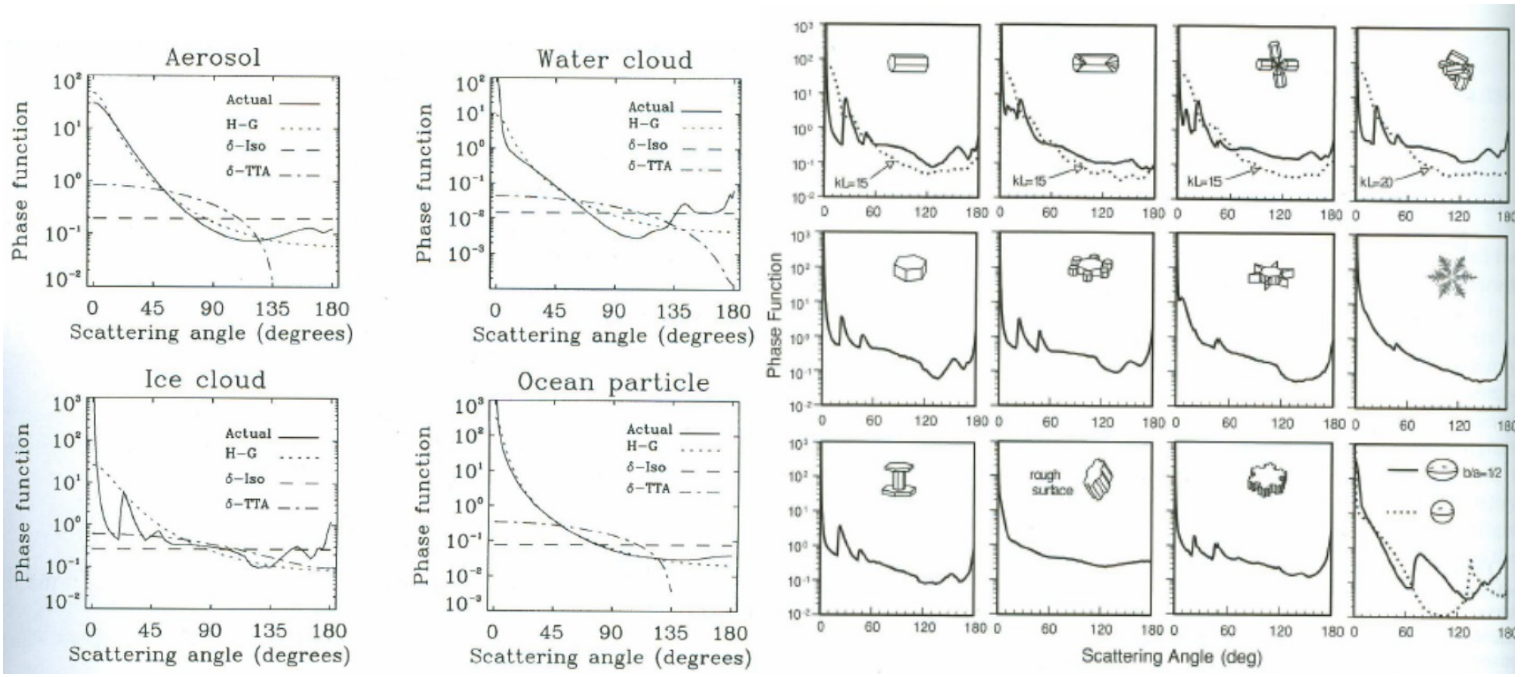

Figure 92: Actual phase function compared to the Henyey-Greenstein profile for different particle types (left) and eleven ice-crystals habits commonly occurring in cirrus clouds generated by computer program, along with their associated phase functions patterns for the 0.63μm wavelength (right)

. The ice clouds phase functions are extremely difficult to capture because of the complex phase functions of their ice crystals which have diverse geometries and sizes (right of figure 92). This explains why it is very difficult to understand the composition of planetary atmospheres with ice clouds, as even the use polarized light does not allow to understand them currently.

9.3 Traditional radiative transfer scattering

9.3.1 Single scattering

In the case of a single scattering and a non-absorbing atmosphere, the intensity 25 can be written:

$$I(\mu,\phi) = I_0\delta(\mu-\mu_0)\delta(\phi-\phi_0)\exp(\frac{\tau}{\mu_0}) \tag{225}$$

where δ is the Dirac Delta function. In that special case, if we assume the phase function to be isotropic (220), the scattering absorptivity 216 becomes:

$$\frac{\varepsilon_{\text{scatter}}}{\kappa} = \frac{\tilde{\omega}}{4\pi}\int_0^{2\pi} d\phi \int_{-1}^{1} d\mu I_0\delta(\mu-\mu_0)\delta(\phi-\phi_0)\exp(\frac{\tau}{\mu_0}) = \frac{\tilde{\omega}I_0}{4\pi}\exp(\frac{\tau}{\mu_0}) \tag{226}$$

9.3.2 Multiple scattering

In the case of multiple scattering, the radiation received by a layer of atmosphere schematically represented on figure 93 (mathematically, the right hand side of the radiative transfer equation 9) is affected by four processes:

1. A reduction by extinction from attenuation of sunlight: $-\kappa(z)I(z,\mu,\phi)$.
2. An increase due to single scattering from direct (unscattered) solar radiation; according to Kirchhoff's law 19: $\varepsilon_{\text{thermal emission}} = \kappa(z)B_\lambda(z)$.
3. An increase from multiple scattering of diffuse intensity from direction $\overrightarrow{\Omega}'$ to $\overrightarrow{\Omega}$ given by equation 216.
4. An increase from emission in the layer into directions $\overrightarrow{\Omega}$, given by:

$$\varepsilon_{\text{direct solar scattering}} = \frac{\tilde{\omega}\kappa I_{\text{Sun}}}{4\pi}\exp(-\frac{\tau}{\mu_0})\mathcal{P}(\overrightarrow{\Omega},\overrightarrow{\Omega_0}) \tag{227}$$

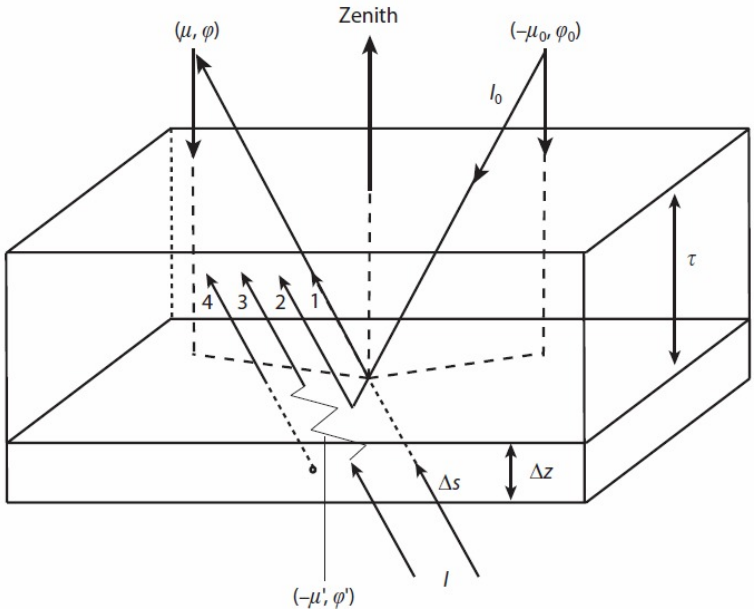

Figure 93: Schematic representation of an atmospheric layer

The two first terms (absorption and thermal emission) couple the radiation field to the local thermodynamic properties of the gas. For example, an absorbed photon gets destroyed and converted to the kinetic energy of the gas. Conversely, thermal emission can transfer energy from the thermal pool of the gas directly into the radiation field, via collisional desexcitation. The two last terms are scattering terms, and as we have already seen, they are non-local and make the atmosphere feel remote boundaries.

9.3.3 Radiative transfer in a plane parallel atmosphere with direct solar scattering

For a plane-parallel atmosphere, we can solve the radiative-transfer equation as we had done in section 3.3, but this time we replace the blackbody radiance $B(\tau) = \varepsilon_{\text{thermal emission}}\kappa^{-1}$ by the more general source term: $S(\tau) \overset{\text{def}}{=} (\varepsilon_{\text{thermal emission}} + \varepsilon_{\text{scatter}} + \varepsilon_{\text{direct solar scattering}})\kappa^{-1}$. We can solve the case of single scattering with small optical thickness τ, that occurs in optically thin cirrus and aerosol atmospheres. Adapting equation 25 to our case and neglecting the additional upward reflected intensity $I(\tau) = 0$, as well as the multiple scattering $\varepsilon_{\text{scatter}} = 0$:

$$I(0,\mu) \approx \int_0^\tau \frac{S(\tau',\mu)}{\mu}\exp(-\frac{\tau'}{\mu})d\tau' = \frac{\tilde{\omega}\kappa I_{\text{Sun}}\mathcal{P}(\overrightarrow{\Omega},\overrightarrow{\Omega_0})}{4\pi\mu}\int_0^\tau d\tau'\exp[-\frac{\tau'}{\mu}-\frac{\tau'}{\mu_0}] = \frac{\tilde{\omega}\kappa I_{\text{Sun}}\mathcal{P}(\overrightarrow{\Omega},\overrightarrow{\Omega_0})\mu_0}{4\pi(\mu+\mu_0)}[1-\exp(-\frac{\tau}{\mu}-\frac{\tau}{\mu_0})] \tag{228}$$

where we have used equation 227 for the direct solar scattering absorptivity. For an optically thin atmosphere $\tau \ll 1$, equation 228 reduces to:

$$I(0,\mu) \approx \frac{\tilde{\omega}\kappa I_{\text{Sun}}\mathcal{P}(\overrightarrow{\Omega},\overrightarrow{\Omega_0})\mu_0\tau}{4\pi\mu\mu_0} \Leftrightarrow \text{BRDF}(\overrightarrow{\Omega},\overrightarrow{\Omega}') \overset{\text{def}}{=} \frac{\pi I(0,\mu)}{\mu_0 I_{\text{Sun}}} = \frac{\tilde{\omega}\mathcal{P}(\overrightarrow{\Omega},\overrightarrow{\Omega_0})\tau}{4\mu\mu_0} \tag{229}$$

where we have used the bidirectional reflectance introduced in 215. Consequently, under the conditions of an optically thin atmosphere, the optical depth τ is proportional to the BRDF that can be determined from satellite measurements. This is as far as we can easily go analytically: the next step is the two-stream approximation of the radiation transfer equation 9 where radiation is only propagating in two discrete directions. Numerically, it is more straightforward to use the Monte-Carlo methods described in paragraph 2.6. However, these methods are too computationally intensive in the case of low absorption and high scattering where the photons bounce too much, or in the case of high absorption where no photons make it to the receptor. They are well-adapted for complex geometries.

10 Radiative heating

10.1 Introduction

We remember that Radiative equilibrium (3.5) can be defined as the balance between total absorbed and emitted radiation (cf equation 29). It can also been expressed as the constancy of the total flux (integrated over all wavelengths):

$$\frac{d\mathcal{F}}{d\tau} = 0 \tag{230}$$

If we are not interested in the precise distribution of the radiation among different wavelengths, we can integrate variables over all wavelengths, which is what we call the "gray atmosphere". We define the three first moments of the intensity:

$$J(\tau) \overset{\text{def}}{=} \frac{1}{4\pi} \int_{(\Omega)} I(\tau, \mu) d\Omega \tag{231}$$

$$H(\tau) \overset{\text{def}}{=} \frac{1}{4\pi} \int_{(\Omega)} \mu I(\tau, \mu) d\Omega \tag{232}$$

$$K(\tau) \overset{\text{def}}{=} \frac{1}{4\pi} \int_{(\Omega)} \mu^2 I(\tau, \mu) d\Omega \overset{\text{Isotropic ideal gas}}{\approx} \frac{J(\tau)}{3} \tag{233}$$

We have used kinetic theory for the second equality of equation 233 and assumes that this relation holds even when the atmosphere is dense (eg near the surface). Since we have assumed that the gas and its intensity were isotropic, we can expand I in powers of μ:

$$I(\tau, \mu) = a_0(\tau) + a_1(\tau)\mu + ... \Rightarrow \begin{cases} J(\tau) = a_0(\tau) \\ H(\tau) = \frac{a_1(\tau)}{3} \\ K(\tau) = \frac{a_0(\tau)}{3} \end{cases} \tag{234}$$

Using this expansion and Stefan-Boltzmann law, it is possible to prove that the effective emission temperature and the temperature are related by:

$$(\frac{T}{T_e})^4 \approx \frac{3}{4}(\tau + \frac{2}{3}) \tag{235}$$

which means that the effective temperature T_e equals the absolute temperature T at a depth $\tau = \frac{2}{3}$. As a consequence, RE allows us to compute the temperature profile from the radiative transfer equation. Once the temperature are obtained, it is possible to compute the radiative heating and cooling rates.

10.2 Radiative heating and cooling rates

The absorption of solar radiation by various gases generates heat in the atmosphere. If all the net radiative flux $\mathcal{F}$ [W.m^{-2}] is turned into heat in each atmospheric layer of thickness dz, specific heat capacity c_p and density ρ, the heating rate [K.s^{-1}] or [K.d^{-1}] can be written:

$$\frac{\partial T}{\partial t} = -\frac{1}{\rho c_p} \frac{\partial \mathcal{F}(z)}{\partial z} \overset{\text{Hydrostatic}}{=} \frac{g}{c_p} \frac{\partial \mathcal{F}(p)}{\partial p} \tag{236}$$

Examples of heating rate are shown on figure 94.

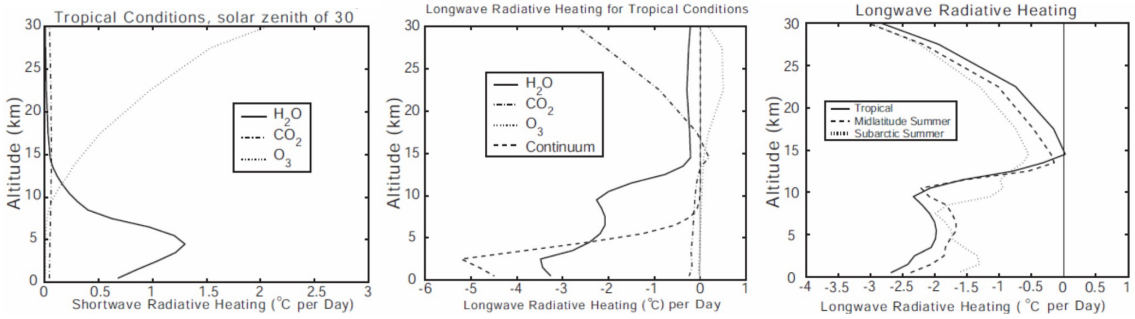

Figure 94: Typical shortwave heating rates (left), longwave heating rates (middle) and heating rates for different model atmospheres

We can see that:

- Water vapor is the main SW absorber in the troposphere and Ozone the main SW absorber in the stratosphere.
- In the LW, Carbon Dioxide plays a significant role, especially in the lower troposphere.
- There are two separate of peaks in the LW cooling rates of water vapor, corresponding to absorbing bands of different strengths.
- The radiative heating and cooling rates not only depend on the chemical composition of the atmosphere, but also on the insolation, which explains the observed variations of the heating rates with latitude.

In practice, computing the magnitude of the heating and cooling rates is tedious because it requires the flux density at each latitude. Numerically, evaluating the various terms in the flux density equations requires a suitable "band transmittance model" which is applied to the atmospheric profile of interest (key variables are the temperature, the humidity and the gas composition).

10.3 Opacity treatment

All IR radiative transfer methods are intended to economize the computation of spectral transmittance by circumventing the integration over the spectral interval and non homogeneous path length (cf 9, 25 and 9.3.3).

10.3.1 Line by line radiative transfer method (LBLRTM)

This method resolves individual spectral lines in the radiative transfer calculation. Absorption cross-section must be computed at wavenumbers that are smaller than the line half-width. However, there are three big limiting factors:

1. A lot of lines are needed: Taking the example of the CO_2 absorption band at $\tilde{\nu} \sim 600 - 800\text{cm}^{-1}$ on the Earth IR spectrum (14), and assuming that the broadened half-widths of each lines is order 0.01cm^{-1}, 2.10^4 lines are needed just to resolve this band.
2. Because of broadening, it is not obvious to know where to cut off the wavenumber for a given line (you can see that the lines have big "wings" on the right of figure 95).
3. There are a lot of "pollutant" lines (from species other than the molecule of interest) that need to be considered.

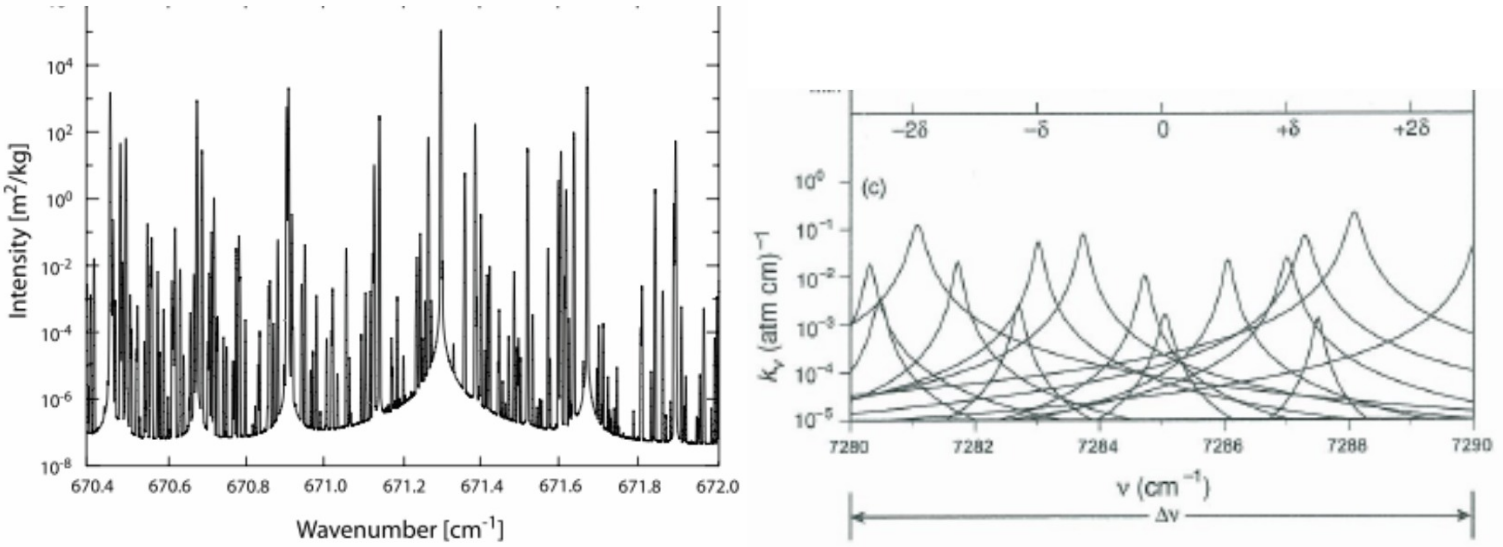

Figure 95: Intensity as a function of the wavenumber (left) and Lorentz-broadened lines in a $10\text{cm} - 1$ interval in the 1.38μm water band (right)

10.3.2 Correlated K-distribution method

This alternative method is based on the grouping of gaseous spectral transmittances according to the absorption coefficient κ. The integration over the wavenumber k is then replaced by an integration over κ, which is possible in a homogeneous atmosphere where the spectral transmittance is independent of the ordering of κ, significantly reducing the number of integration points (and reducing the computational time by at least an order of magnitude).

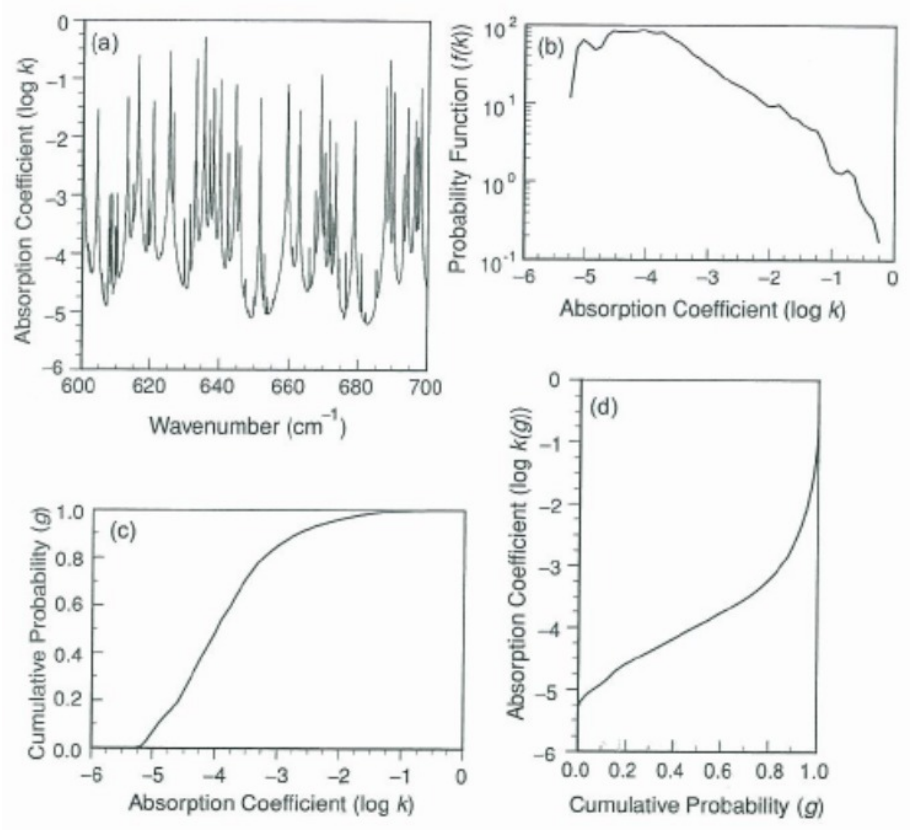

Figure 96: H_2O rotational band: (a) Absorption coefficient vs wavenumber (b) Probability function of the absorption coefficient (c) Cumulative probability function of the absorption coefficient (d) Absorption coefficient vs the cumulative probability function

10.3.3 Numerical implementation and influence on the heating rate

The numerical implementation of this method is presented on figure 97.

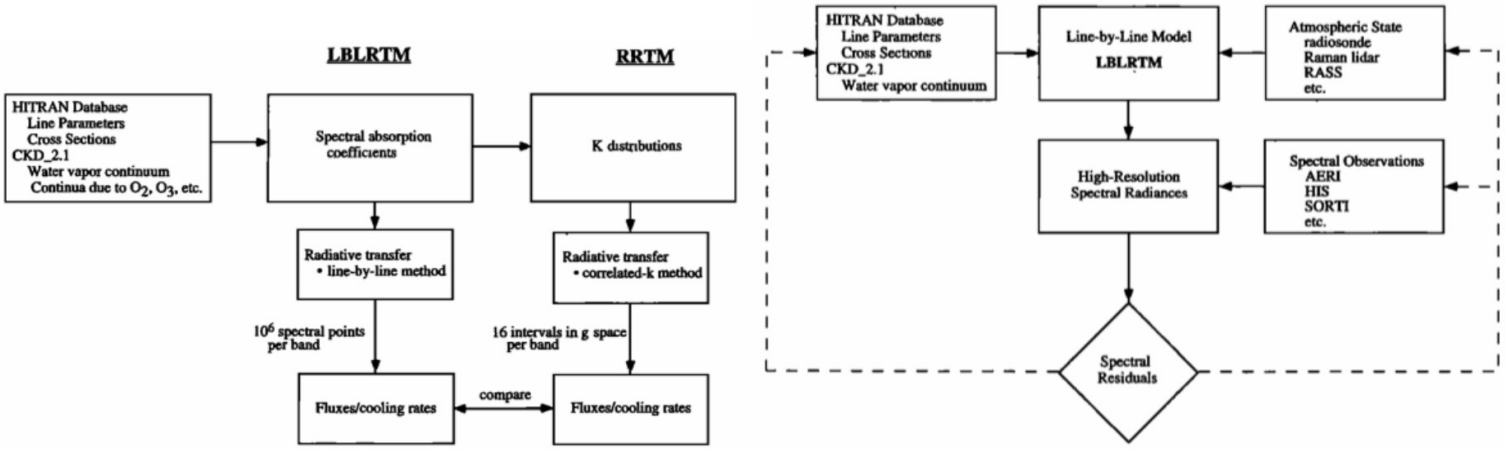

Figure 97: Developmental strategy of RRTM (a K-distribution method) using an LBLRTM (left) and validation strategy of line-by-line radiative transfer model (right)

The influence of choosing the less precise correlated-K distribution on the heating rates is presented on figure 98. We can see that the differences in fluxes never exceed 1% whereas the differences in cooling rates can go up to almost 10%, making it a good method for situations where the uncertainty is bigger than 5-10% (eg studying exoplanets).

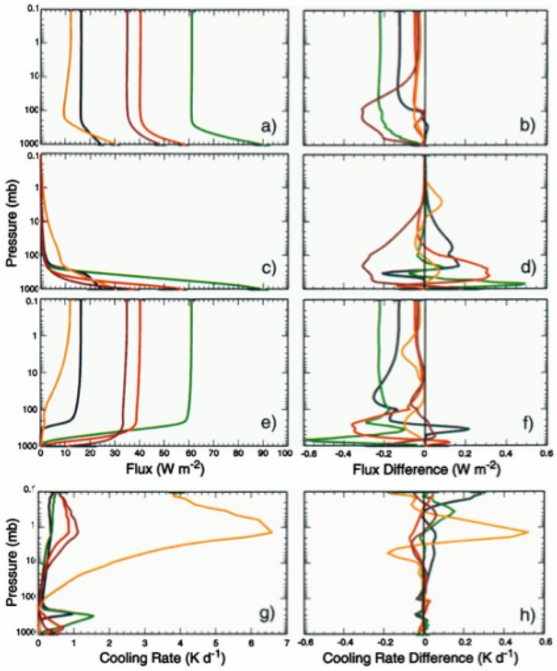

Figure 98: Spectrally integrated (a) up (c) down (e) net fluxes and (g) cooling rates for each of bands calculated by LBLRTM. Differences between RRTM and LBLRTM for these quantities are shown in plates (b,d,f,h).
Reference: Mlawer et al. (1997)

10.4 Band models

10.4.1 Introduction

Band models are traditional approaches that simplify the computation of spectral transmittance: the atmosphere is usually assumed to be homogeneous or to have very simple greenhouse gas distributions so that analytical expressions can be developed.

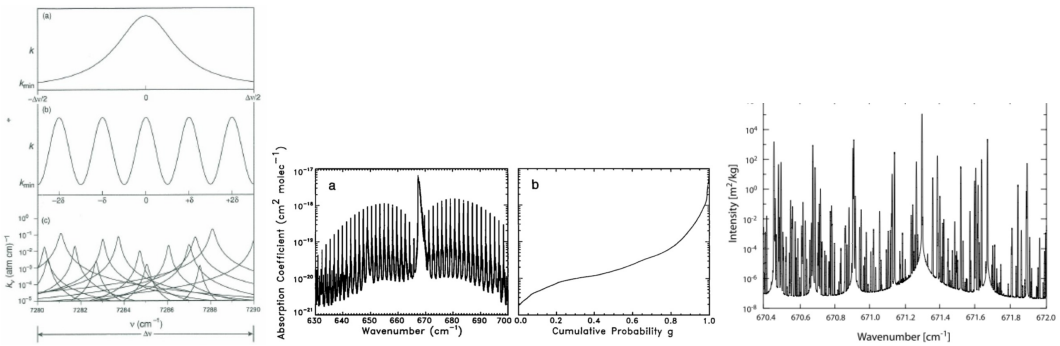

Figure 99: Left: (a) A single line (b) Period lines with a line spacing of δ (c) H_2O lines with Lorentz broadening in a $10cm^{-1}$ interval in the $1.38\mu m$ H_2O band. 15 lines are shown.
Middle: Absorption coefficients due to carbon dioxide for a layer in the mid-latitude atmosphere (a) as a function of wavenumber (b) after being rearranged in ascending order
Right: Absorption Lorentz lines in the SW spectrum of water vapor.

On the left of figure 99, the single absorption lines is only observed in the case of isolated atoms; whereas the periodic lines (regular band) remind us of the vibrational-rotational lines observed for Carbon Dioxide (middle) and the entangled Lorentz lines are similar to the Methane or the Water vapor (right) spectra.

10.4.2 Transmittance and absorptance

We remember the definition of the monochromatic transmittance, which gives the rate of absorption in the simple case where there is no scattering nor emission into the beam (and Beer-Lambert's law 26 applies):

$$T_\nu(\frac{\tau}{\mu}) \overset{\text{def}}{=} \exp(-\frac{\tau}{\mu}) \;\Rightarrow\; \frac{\partial T_\nu}{\partial \tau} = -\frac{T_\nu}{\mu} \tag{237}$$

If we integrate the radiative transfer equation in local thermodynamic equilibrium 24, from the top of the atmosphere $\tau = 0$ to the Earth's surface $\tau = \tau_*$ assuming that the Earth behaves like a blackbody ($I(\tau_*, \mu) = B[T(\tau_*)]$) and no source of downward emission at the top of the atmosphere ($I(0, -\mu) = B[T(0)]$), the formal solution for upward and downward intensities are given by:

$$I^\uparrow(\tau, \mu) = B(\tau_*)T_\nu(\frac{\tau_* - \tau}{\mu}) - \int_\tau^{\tau_*} B(\tau')\frac{d}{d\tau'}T_\nu(\frac{\tau' - \tau}{\mu})d\tau' \tag{238}$$

$$I^\downarrow(\tau, -\mu) = \int_0^{\tau} B(\tau')\frac{d}{d\tau'}T_\nu(\frac{\tau - \tau'}{\mu})d\tau' \tag{239}$$

To discretize in the wavenumber, we consider small enough spectral intervals $\Delta\nu$ such that the Planck function's variation can be neglected. The transmittance 237 can be approximated as:

$$T_{\overline{\nu}}(u) \approx \frac{1}{\Delta\nu}\int_{(\Delta\nu)} \exp(-\sigma_{\overline{\nu}}u)d\nu \tag{240}$$

where $\sigma_{\overline{\nu}}$ is the mass absorption coefficient and u the path-length of absorbing gases, defined as:

$$u \overset{\text{def}}{=} \int_0^s \rho ds' \tag{241}$$

in usual notations. If we assume that the medium is homogeneous, we can assume that $\sigma_{\overline{\nu}}$ is independent of the distance s. The absorptance defined as $A_\nu \overset{\text{def}}{=} 1 - T_\nu$ can also be discretized by using small spectral intervals:

$$A_{\overline{\nu}}(u) \overset{\text{def}}{=} 1 - T_{\overline{\nu}}(u) \approx \frac{1}{\Delta\nu}\int_{(\Delta\nu)} [1 - \exp(-\sigma_{\overline{\nu}}u)]d\nu \tag{242}$$

10.4.3 Absorptance of a single line

To avoid having to deal with multiple lines, it is helpful to define the equivalent width W_ν, which is the width of an infinitely strong line of rectangular shape that is the same as the absorption of a single line.

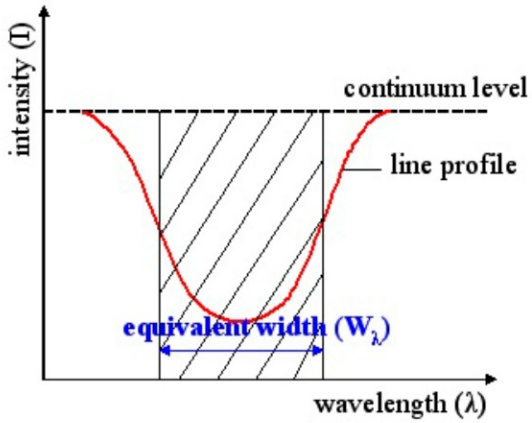

Figure 100: Definition of an equivalent width

The equivalent width plays a central role in the development of band models, and can be defined from the discrete version of the absorptance 242:

$$W_\nu(u) \overset{\text{def}}{=} A_{\overline{\nu}}(u)\Delta\nu \approx \int_{(\Delta\nu)} [1 - \exp(-\sigma_{\overline{\nu}}u)]d\nu \tag{243}$$

We can compute the equivalent width W_ν for different line strengths S (defined by 140).

- In the weak line limit $\sigma_{\overline{\nu}} u \ll 1$, the discrete absorptance 242 becomes:

$$A_{\overline{\nu}}(u) \approx \frac{1}{\Delta\nu} \int_{(\Delta\nu)} \sigma_{\overline{\nu}} u d\nu \approx \frac{Su}{\Delta\nu} \tag{244}$$

  Regardless of the line shape, the absorptance is directly proportional to path length, and this is called the "region of linear absorption".

- In the strong line limit $\sigma_{\overline{\nu}} u \gg 1$, the discrete absorptance 242 can be computed by assuming a Lorentz profile of mass absorption $\sigma_{\overline{\nu}} = \frac{S}{\pi\alpha}$:

$$A_{\overline{\nu}}(u) \approx \frac{1}{\Delta\nu} \int_{-\infty}^{+\infty} [1 - \exp(-\frac{S\alpha u}{\pi[\nu - \nu_0]^2})] d\nu \overset{\frac{Su}{\alpha} \gg 1}{\sim} \frac{2\sqrt{S\alpha u}}{\Delta\nu} \tag{245}$$

  In this "square root absorption" region, the absorptance is proportional to the square root of the path length.

- In the general case $\sigma_{\overline{\nu}} u \in \mathbb{R}$, the discrete absorptance is given by:

$$A_{\overline{\nu}}(u) = 2\pi\alpha L(\frac{Su}{2\pi\alpha}) \overset{\text{def}}{=} \frac{Su}{\pi} \exp(-\frac{Su}{2\pi\alpha}) \int_0^{\pi} \exp(\frac{iSu\cos\theta}{2\pi\alpha})[1 - \cos\theta] d\theta \tag{246}$$

  where we have defined L, the Landeburg and Reiche function.

To conclude, the equivalent width for a single Lorentz line is given by:

$$W(u) = 2\pi\alpha L(\frac{Su}{2\pi\alpha}) = \begin{cases} Su & [\text{weak} - \text{line}] \\ 2\sqrt{S\alpha u} & [\text{strong} - \text{line}] \end{cases} \tag{247}$$

10.4.4 Absorptance of a regular band

If the bands are regularly spaced, the total mass absorption coefficient can be obtained by summing over all the Lorentz lines:

$$\sigma_{\overline{\nu}} = \sum_{k=-\infty}^{+\infty} \frac{S\alpha\pi^{-1}}{(\nu - k\delta)^2 + \alpha^2}$$

where α is the half width at half maximum and δ is the spacing between the Lorentz lines. It can be proven that the discrete absorptance 242 in this case can be written:

$$A_{\overline{\nu}}(u) = \text{erf}(\frac{\sqrt{\pi S\alpha u}}{\delta}) \overset{\text{def}}{=} \frac{2}{\sqrt{\pi}} \int_0^{\frac{\sqrt{\pi S\alpha u}}{\delta}} \exp(-x^2) dx$$

For $\sqrt{\pi S\alpha u} \ll \delta$, we recover the "region of square root absorption" 245. Other analytical band models exist, in particular statistical band models and models for non-homogeneous atmospheres, that we will not cover here.

11 Radiative-convective equilibrium

11.1 Introduction

11.1.1 Definition

We remember that RE (defined as the equilibrium state of the atmosphere in absence of non-radiative enthalpy fluxes in 1.2) is unstable to both moist and dry convection. This instability triggers convection, and leads to RCE in a one-dimensional setting, where all the fluxes are carried by convection and radiation, and the lateral fluxes are ignored (cf 1.4). Unlike RE, RCE is an equilibrium in the statistical sense because convection is intermittent and turbulent. Energetically, RCE is a balance between radiative cooling driving the atmosphere towards state of RE (even if it is tempting to think of it as a Newtonian relaxation, atmospheric ways to relax towards RE are nonlinear), and convective heating that re-stabilizes the entropy profile wherever it is unstable.

11.1.2 Simple models of RE

We remember how radiation is transmitted through the atmosphere (cf figure 3) and the simple analytical one-layer model of RE developed in section 1.2. The models can be easily generalized to two layers (cf left of figure 101). To solve it we write the energy balance of the:

- TOA:
$$\sigma T_2^4 = \sigma T_e^4 \;\Rightarrow\; \boxed{T_2 = T_e} \tag{248}$$
- First atmospheric layer:
$$2\sigma T_1^4 = \sigma T_2^4 + \sigma T_s^4 = \sigma(T_e^4 + T_s^4) \tag{249}$$
- Surface:
$$\sigma T_s^4 = \sigma T_e^4 + \sigma T_1^4 \tag{250}$$

Combining equations 249 and 250 leads to $\boxed{T_s = 3^{\frac{1}{4}} T_e} \approx 336\text{K}$ and $\boxed{T_1 = 2^{\frac{1}{4}} T_e} \approx 303\text{K}$.

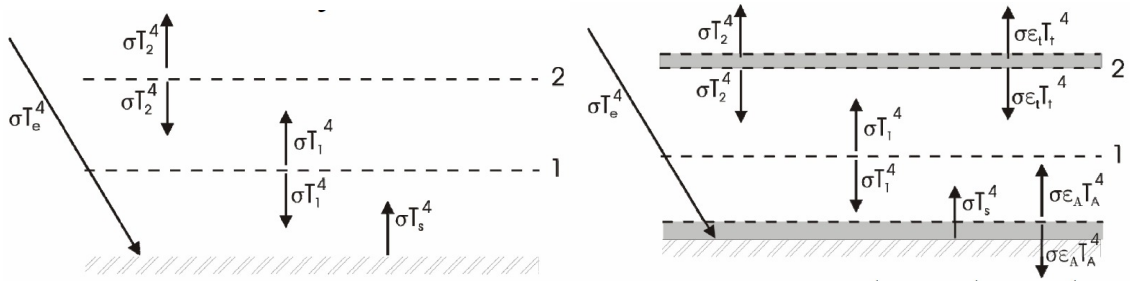

Figure 101: Two-layers model of RE (left) and temperature discontinuities introduced by thin layers (right)

We can see that the lapse rate in RE is strongly negative in the troposphere: $T_2 > T_1 > T_s$. The previous model can be generalized to n opaque layers and gives a surface temperature $T_s = (n+1)^{\frac{1}{4}} T_e$. We can take absorption and emission into account by making the gray atmosphere approximation, which assumes that layers have a constant absorptivity ε (equal to their emissivity according to Kirchhoff's law 19) in the IR. In that case, it is important to understand that a discontinuity in emissivity implies a discontinuity in temperature because we do not take heat diffusion into account in this model. For instance, the discontinuity between the ground that almost absorbs like a blackbody (high ε) and the near surface air with much lower absorptivity (low ε) creates the near-surface temperature disequilibrium in RE, which triggers convection. Quantitatively, we can estimate this discontinuity by introducing very thin layers that do not change the layer temperatures in the previous two-layers model. Following the notations on the right of figure 101, we introduce:

- A near-surface thin layer of emissivity $\varepsilon_A \ll 1$ and temperature T_A.
- A stratospheric (or top of the troposphere) thin layer of emissivity $\varepsilon_t \ll 1$ and temperature T_t.

The very low emissivities of these this layers allows to neglect their influence on the global energetic budget, meaning that we can evaluate their temperature by simply considering their individual energetic balance:

$$2\varepsilon_A \sigma T_A^4 = \varepsilon_A \sigma T_1^4 + \varepsilon_A \sigma T_s^4 \;\Rightarrow\; \boxed{T_A = (\frac{5}{2})^{\frac{1}{4}} T_e} \approx 321\text{K} \approx T_s - 15\text{K} \tag{251}$$

$$2\varepsilon_t \sigma T_t^4 = \varepsilon_t \sigma T_2^4 \;\Rightarrow\; \boxed{T_t = 2^{-\frac{1}{4}} T_e} \approx 214\text{K} \approx T_e - 41\text{K} \tag{252}$$

We can immediately see the large temperature discontinuities introduced by those thin layers that do not behave like blackbodies.

11.1.3 1D models of RCE

In RCE, we need to add convective fluxes to the previous two-layers model, as done in figure 260.

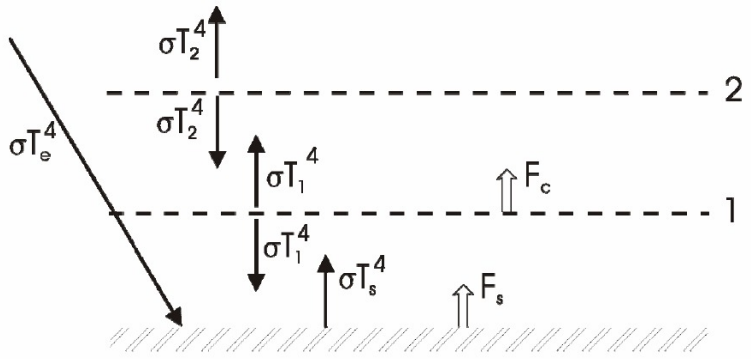

Figure 102: Two-layers model of RCE

We enforce convective neutrality in this model by assuming a constant (positive) lapse rate. Assuming that the layers are equally spaced, this assumption gives $T_1 = T_2 + \Delta T$ and $T_s = T_1 + \Delta T = T_2 + 2\Delta T$. From the two previous equations, it is very easy to compute the temperatures of the system from the TOA energetic balance:

$$\sigma T_2^4 = \sigma T_e^4 \;\Rightarrow\; \boxed{T_2 = T_e} \;\Rightarrow\; \boxed{T_1 = T_e + \Delta T} \;\Rightarrow\; \boxed{T_2 = T_e + 2\Delta T} \tag{253}$$

The surface and mid-tropospheric convective fluxes can be determined from the energetic balance of:

- The surface:
$$F_s + \sigma T_s^4 = \sigma T_e^4 + \sigma T_1^4 \tag{254}$$
- The second atmospheric layer:
$$2\sigma T_e^4 = \sigma T_1^4 + F_c \tag{255}$$

yielding:

$$F_s = \sigma T_e^4[1 + (1+x)^4 - (1+2x)^4] \tag{256}$$

$$F_c = \sigma T_e^4[2 - (1+x)^4] \tag{257}$$

where we have defined the dimensionless number:

$$x \overset{\text{def}}{=} \frac{\Delta T}{T_e} \tag{258}$$

Note that x (and thus ΔT) must be such that $(F_s, F_c) > 0$. In the case where $(F_s, F_c) = (0, 0)$, we recover RE. In reality, even simple models of RCE are much more complex because the layer do not behave like blackbodies and their emissivities ε depend on the greenhouse gas concentrations, especially the water vapor concentration. The full calculation using a band-averaged model has been described in section 1.4 and leads to the graphs presented on figure 10. This full calculation is done by assuming greenhouse gases profiles depicted on the left of figure 103. Gases such as NO_2, CH_4, CO_2 are homogenized in the troposphere which explains why their concentrations do not vary with altitude. O_3 (which is a greenhouse gas even if it absorbs more in the UV than in the IR) is mostly present in the stratosphere, unlike CO, which has significant chemical sinks there. The water vapor profile decreases exponentially with altitude, which comes from the assumption of constant relative humidity $\mathcal{H}$ and the consequences of Clausius-Clapeyron relation on the saturation specific humidity profile (cf 180). The radiative consequences of these greenhouse gases can be seen on the right of figure 103. For example, we can see that the presence of water vapor warms the troposphere the most, consistently with the fact that it is the main greenhouse gas in the atmosphere, and we also observe that removing Carbon Dioxide warms the stratosphere a lot as it is the main IR emitter there.

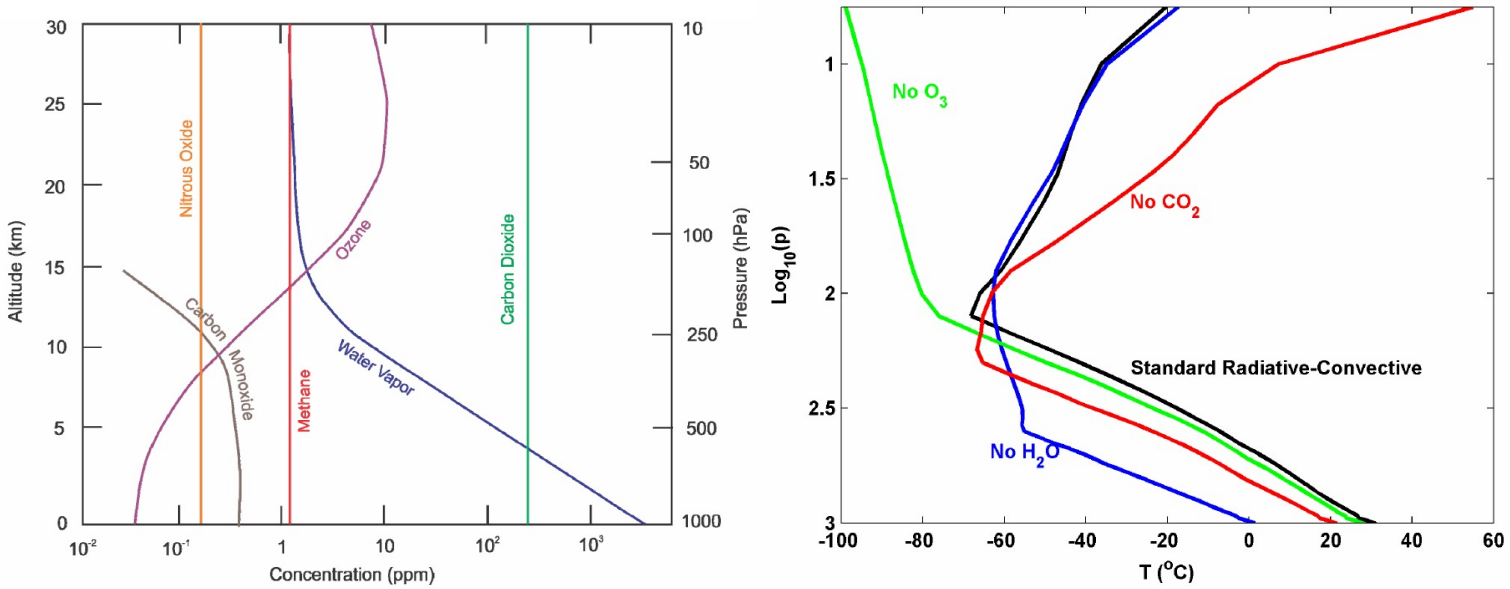

Figure 103: Profile of the main greenhouse gases in the troposphere and stratosphere (left) and contributions of various absorbers to the temperature in RCE (right)

Water vapor has very little effect on the stratosphere, mainly because its concentration is so small there: it is advected through the tropopause by the Brewer-Dobson circulation (that cools the troposphere) and its main chemical source in the stratosphere is the slow oxidation of methane. We also remember that removing Ozone cools the stratosphere because it has strong absorption bands in the UV. Finally, the two effects of Carbon Dioxide (warming the troposphere, cooling the stratosphere) is a good proxy for the effects of anthropogenic climate change: In the past century, the troposphere has been warming but the stratosphere has been cooling.

11.1.4 Vertical velocities in RCE

Bjerknes (1938) had already observed that precipitating convection favored widely spaced clouds (cf figure 104).

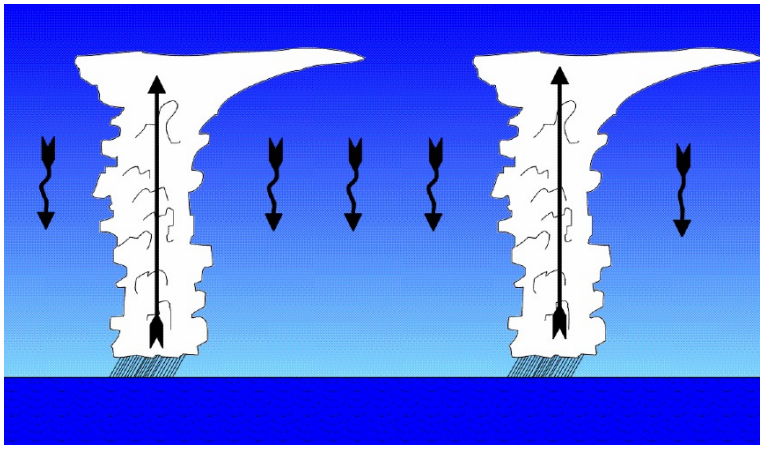

Figure 104: A cartoon of moist RCE

Air rises rapidly within clouds, approximately conserving moist static energy (defined by 192). The clouds cover a very small fractional area $\sigma \ll 1$, so that the return flow is weak. The clear, subsiding air covers a large fractional area $(1-\sigma)$ and approximately follows a moist adiabat (implying a moist adiabatic lapse rate 206). Since mass conservation requires the average vertical velocity of the domain to be zero:

$$0 = \underbrace{(1-\sigma) w_{\text{clear}}}_{\approx w_{\text{clear}}} + \underbrace{\sigma w_{\text{cloud}}}_{M_u} \;\Rightarrow\; w_{\text{clear}} \approx -\sigma w_{\text{cloud}} \tag{259}$$

where we have introduced the net convective updraft velocity M_u. As σ is not larger than a few %, equation 259 explains why the vertical velocity observed in clouds is typically two orders of magnitude above the vertical velocity of the subsiding air. However, even if (w_{clear}, M_u) are easy to estimate and are orders a few m.s^{-1}, it can be hard to estimate σ and w_{cloud} individually. For example, in

computational fluid dynamics, it is important to resolve the turbulent cascade to convert potential energy to kinetic energy in numerical simulations. In the case of RCE, this means a resolution of 10m or better. However, with cloudy updrafts that can be spaced up to 50km apart, the domain size of a cloud resolving simulation needs to be of order 1000km, leading to 10^5 grid points in only one direction (and three dimensions are needed to model convection)! That's why current cloud resolving models have no more than one or two nods per cloud, and processes such as entrainment need to be parametrized, which explains why it is hard to estimate σ and w_{cloud} precisely, even using computationally intensive simulations. Understanding the physical processes that set w_{cloud} to its observed value ($\sim 5\text{m.s}^{-1}$) is still an open research topic; Parodi and Emanuel (2009) have argued that w_{cloud} scales like the terminal velocity of the largest possible size of droplets before they become hydrodynamically unstable. Energetically, the convective updrafts balances the radiative cooling. Using the first law of thermodynamics (or more directly the second thermodynamic identity 49):

$$\dot{Q}_{\text{rad}} = c_p \frac{DT}{Dt} - \frac{1}{\rho}\frac{Dp}{Dt} \overset{\text{Ideal gas}}{=} c_p T\left(\frac{1}{T}\frac{DT}{Dt} - \frac{R}{c_p p}\frac{Dp}{Dt}\right) = \frac{c_p T}{\theta}\frac{D\theta}{Dt} \tag{260}$$

where we have used the definition 67 of potential temperature and introduced the radiative heating per unit mass $\dot{Q}_{\text{rad}}$ (negative since RCE temperatures are larger than RE temperatures). Using the fact that the majority of the area is covered by the dry subsiding air following a moist adiabat (constant saturated entropy s^*), we can estimate the subsidence vertical velocity from the RCE energetic balance 260:

$$\frac{D\theta}{Dt} \approx w_{\text{clear}}\left(\frac{d\theta}{dz}\right)_{s^*} = \frac{\dot{Q}_{\text{rad}}\theta}{c_p T} \;\Rightarrow\; w_{\text{clear}} = \frac{\dot{Q}_{\text{rad}}\theta}{c_p T\left(\frac{d\theta}{dz}\right)_{s^*}} \overset{\text{Typical values}}{\approx} -1\text{cm.s}^{-1} \tag{261}$$

If we look at an entire air column in RCE, the surface enthalpy flux (sum of the latent heat flux and the sensible heat flux) balance the vertically integrated radiative cooling. Finally note that the radiation and convection are highly interactive in RCE, which adds another layer of complexity to this equilibrium. For instance, convection forms clouds, which will have a significant influence on the net SW and LW fluxes above and below the cloud. In return, these fluxes will have consequences on the convection, and this two-way interaction can lead to positive or negative feedbacks depending on the situation.

11.2 Stable perturbations from RCE

11.2.1 Introduction

It is never trivial to think about perturbations from RCE, because of the interactions between temperature and radiation and convection: for example, the vertical structure of the perturbation is very important, and approximating the relaxation to RCE as Newtonian is always a crude approximation. We make experiments to estimate the time scale of approach to equilibrium by initiating the MIT single column model (the same that gives figure 10) with a constant 0°C temperature profile, and letting it relax to RCE on figure 105.

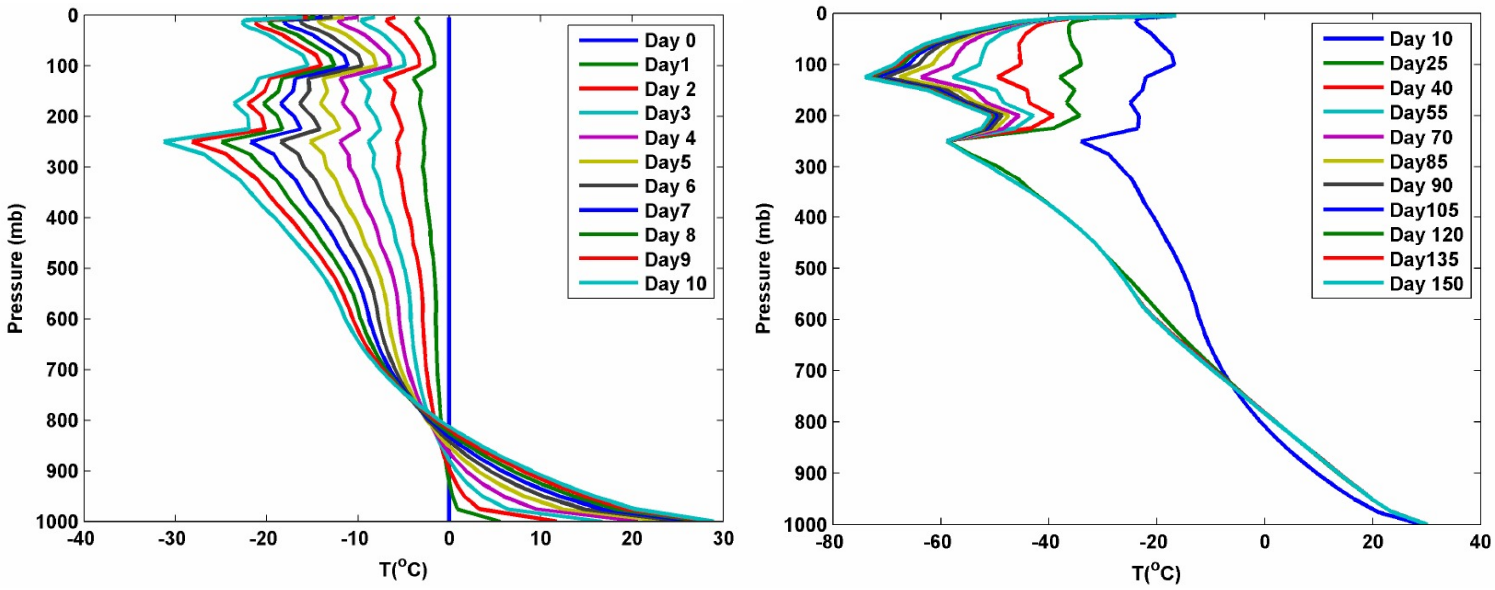

Figure 105: Relaxation of a constant temperature profile to RCE for a week (left) and half a year (right)

Note that the troposphere adjusts within a month whereas it takes almost half a year to the stratosphere to adjust, because there is almost no convection in the stratosphere.

11.2.2 A simple model of RCE

Following Einstein's quote stating "that everything should be as simple as it can be, but not simpler", we try to come up with an analytically tractable model that captures the essence of this timescale, presented on figure 106.

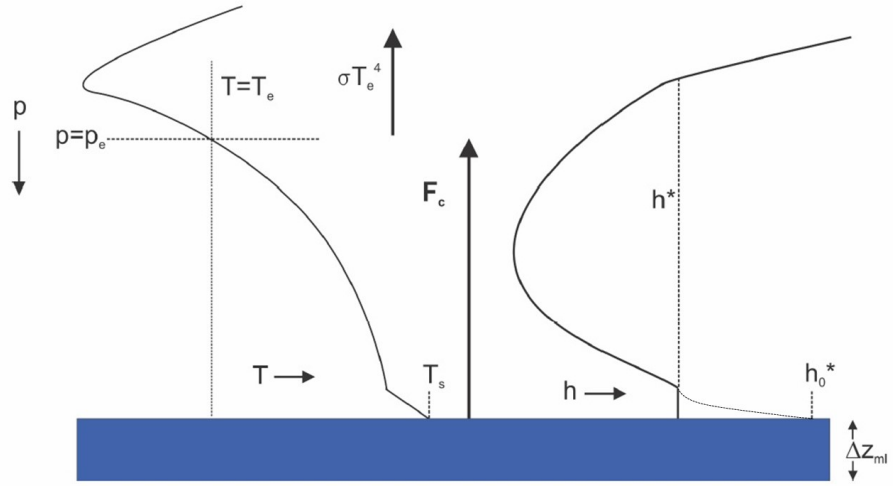

Figure 106: Simple model of RCE; temperature profile (left) and MSE profile (right)

On the left, the temperature profile starts from the warm surface temperature T_s; it then decreases sharply with altitude because of the strong near-surface disequilibrium. Above the boundary layer, the temperature profile follows a moist adiabat until the tropopause. We introduce the effective emission temperature T_e and the pressure p_e at which the environmental temperature equals T_e, corresponding to an optical thickness close to unity. According to its definition 3, T_e is set by the solar constant and the planetary albedo, which we assume to be constant in this model. p_e can also be approximated as steady as the profile of greenhouse gases/clouds do not vary much in time. F_c is the total non-radiative heat flux, which is the sum of the latent heat flux LHF and the sensible heat flux SHF , which are both carried by turbulence. We introduce a thin slab ocean of thickness Δz_{ml}; however it has a high total heat capacity as the specific heat capacity/density of liquid water are much higher than these of water vapor. Physically, it is easier to think about the saturated MSE, defined as:

$$h^* \overset{\text{def}}{=} (c_{p_d} + r_T^* c_l)T + L_v r^* + (1 + r_T^*)gz \approx c_p T + L_v r^*(p, T) + gz \tag{262}$$

The saturated MSE is approximately conserved along a moist adiabat (explaining the vertical profile of h^* on the right of figure 106), and can be looked as a proxy for temperature as it does not depend on the mixing ratio r. This model thus relies on several assumptions:

- The enthalpy is constant in the boundary layer, and the saturated MSE is constant in the free troposphere, and equal to the MSE at the top of the boundary layer: $h_{\text{env}} = h^*$ where h_{env} is the MSE in the boundary layer and h^* is the saturated MSE in the free troposphere. This assumption comes from the convective neutrality assumption. Indeed, if we lift a parcel dry-adiabatically throughout the boundary layer, its saturated MSE will be constant and equal to the boundary layer environmental MSE. Then, it will keep its saturated MSE through the free troposphere, which means that it will only be stable if $h_{\text{env}} = h^*$.
- The boundary layer is assumed to be nearly opaque, consistently with observations in the Tropics, which means there is no net IR flux at the surface.
- We neglect the atmospheric absorption of SW.

Remembering the scaling of mechanically/thermally generated turbulences 6.4, we know that below the Monin-Obukhov length $-L$ defined by 113, mechanically generated turbulence dominate and the surface fluxes are dominated by the effect of the wind. From dimensional analysis, we can estimate the latent heat flux and the sensible heat flux by using the following bulk formulas:

$$\text{LHF} = \rho_s C_k |\overrightarrow{V_{\text{wind}}}| L_v (q_0^* - q_{\text{env}}) \tag{263}$$

$$\text{SHF} = \rho_s C_k |\overrightarrow{V_{\text{wind}}}| c_p (T_s - T_{\text{env}}) \tag{264}$$

where ρ_s is the density of the surface, C_k the dimensionless enthalpy transfer coefficient that we can measure during field experiments, $|\overrightarrow{V_{\text{wind}}}|$ is the typical amplitude of the wind at the surface, and q_0^* the saturation specific humidity of the surface. Adding equations 263 and 264, and using definition 262, we obtain the non-turbulent heat flux at the surface:

$$F_c = \text{LHF} + \text{SHF} = \rho_s C_k |\overrightarrow{V_{\text{wind}}}| (h_0^* - h_{\text{env}}) = \rho_s C_k |\overrightarrow{V_{\text{wind}}}| (h_0^* - h^*) \tag{265}$$

We have used the convective neutrality assumption for the last equality on the right hand side of equation 265. From the simplified energy balance at the top of the atmosphere $F_c = \sigma T_e^4$, which we can combine with 265 to find the saturated MSE at the surface:

$$h_0^* = h^*(T_e, p_e) + \frac{\sigma T_e^4}{\rho_s C_k |\overrightarrow{V_{\text{wind}}}|} \tag{266}$$

The control balance of this steady state (RCE) are thus $(T_e, p_e, |\overrightarrow{V_{\text{wind}}}|)$ that we will hold fixed as we perturb this system from RCE.

11.2.3 Relaxation timescales

We now slightly perturb the entire temperature profile and study how the system relaxes back to RCE. The evolution of the free tropospheric saturated MSE's perturbation is directly related to the variations of the convective and radiative fluxes:

$$\frac{dM_{\text{atm}}}{dS}\frac{\partial (h^*)'}{\partial t} \approx \frac{\Delta p}{g}\frac{\partial (h^*)'}{\partial t} = F_c' - F_{\text{rad}}' = F_c' - \frac{\partial F_{\text{rad}}}{\partial h^*}(h^*)' \tag{267}$$

where $\frac{dM_{\text{atm}}}{dS}$ is the mass of the free troposphere per unit surface, that we can approximately relate to the pressure thickness Δp of the free troposphere through the hydrostatic relationship. In the slab ocean, the evolution of the surface temperature perturbation is only related to the perturbation of the turbulent surface flux because we have assumed that the near-surface atmosphere was opaque:

$$c_l \rho_l \Delta z_{\text{ml}} \frac{\partial T_s'}{\partial t} = -F_c' \tag{268}$$

The perturbation of the surface saturated MSE is by definition 262 given by:

$$(h_0^*)' = c_p T_s' + L_v \frac{\partial q_0^*}{\partial T_s} T_s' \approx c_p T_s' (1 + \frac{L_v^2 q_0^*}{c_p R_v T_s^2}) \tag{269}$$

where we have linearized the Clausius-Clapeyron relation for water vapor 176. We introduce the climate sensitivity B [W.m^{-2}.K^{-1}] to evaluate how the radiative flux evolves with the surface temperature:

$$B \overset{\text{def}}{=} \frac{\partial F_{\text{rad}}}{\partial T_s} \tag{270}$$

and assume it is a given property of the system. Combining 269 and 270 allows to evaluate how the radiative flux evolves when the saturated MSE of the free troposphere changes:

$$\frac{\partial F_{\text{rad}}}{\partial h^*} = \frac{\partial F_{\text{rad}}}{\partial T_s}\frac{\partial T_s}{\partial h^*} = \frac{B}{1 + \frac{L_v^2 q_0^*}{c_p R_v T_s^2}} \tag{271}$$

We are now in measure of expressing the evolution of (h^*, h_0^*) as a function of (h^*, h_0^*). We simplify this linear system of ordinary differential equations by introducing:

- The variation of the dry turbulent flux with temperature for a steady atmosphere:

$$x \overset{\text{def}}{=} (\frac{\partial F_c}{\partial T_s})_{q_0^*, h^*} = \rho_s C_k |\overrightarrow{V_{\text{wind}}}| (\frac{\partial h_0^*}{\partial T_s})_{q_0^*, h^*} = \rho_s C_k |\overrightarrow{V_{\text{wind}}}| c_p \tag{272}$$

- The dimensionless variation of surface saturated MSE with surface temperature:

$$y \overset{\text{def}}{=} \frac{1}{c_p}\frac{\partial h_0^*}{\partial T_s} = 1 + \frac{L_v^2 q_0^*}{R_v c_p T_s^2} \tag{273}$$

- The combination of the two previous sensitivities to surface temperature changes:

$$\chi \overset{\text{def}}{=} \frac{xy}{B + xy} \tag{274}$$

- The atmospheric timescale (corresponding to an ocean of fixed temperature/infinite heat capacity):

$$\tau_{\text{atm}} \overset{\text{def}}{=} \frac{c_p y \Delta p}{g(B + xy)} \approx 10\text{d} \tag{275}$$

- The oceanic timescale (corresponding to a fixed atmosphere):

$$\tau_{\text{oce}} \overset{\text{def}}{=} \frac{c_l \rho_l \Delta z_{\text{ml}}}{xy} \approx 100\text{d} \tag{276}$$

leading to the following evolution equation:

$$\tau_{\text{atm}} \frac{d(h^*)'}{dt} = -(h*)' + \chi h'_s \tag{277}$$

$$\tau_{\text{oce}} \frac{\partial h'_s}{\partial t} = (h^*)' - h'_s \tag{278}$$

The linear system of equations (277,278) has two eigenvalues $\lambda_\pm$, corresponding to two timescales $\tau_\pm = -\lambda_\pm^{-1}$:

$$\tau_\pm = \frac{2\tau_{\text{oce}}}{1 + \frac{\tau_{\text{oce}}}{\tau_{\text{atm}}} \pm \sqrt{(1 + \frac{\tau_{\text{oce}}}{\tau_{\text{atm}}})^2 - 4(1-\chi)\frac{\tau_{\text{oce}}}{\tau_{\text{atm}}}}} \tag{279}$$

We are especially interested in the longest timescale τ_-, that govern how long the system takes to relax back to RCE when perturbed. Formula 279 is not very transparent; it is thus useful to look at the two limits where:

- $\tau_{\text{oce}} \gg \tau_{\text{atm}}$:

$$\tau_- \approx \tau_{\text{atm}} + \frac{\tau_{\text{oce}}}{1-\chi} \tag{280}$$

- $\tau_{\text{oce}} \ll \tau_{\text{atm}}$:

$$\tau_- \approx \frac{\tau_{\text{atm}}}{1-\chi} \tag{281}$$

As χ is very close to 1, the longest timescale is much bigger than the sum of the atmospheric and oceanic timescale: the coupling of the system considerably increases its relaxation time. It is possible to estimate B from the MIT single column model, which allows us to compare our theory to the MIT single column model relaxation time (cf figure 107).

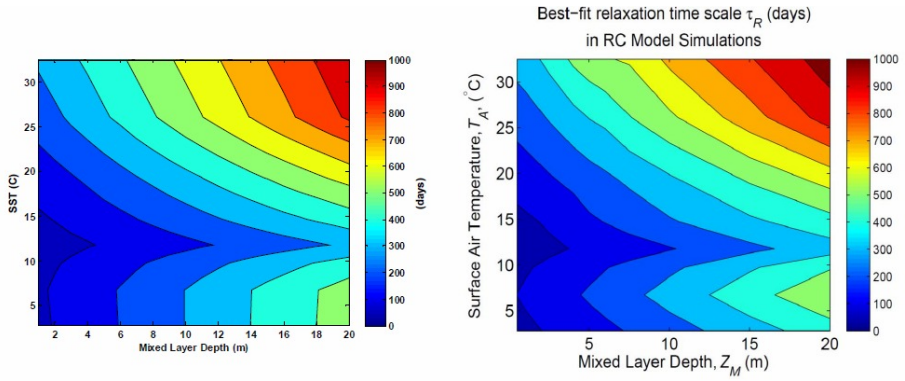

Figure 107: Relaxation time (days) as a function of the surface temperature and the mixed layer depth, given by the theory (left) and the MIT single column model (right)

However, it should be noted that we have fixed the greenhouse gas concentration, which is unrealistic on Earth, given that the high variability of water vapor, the main greenhouse gas. For example, if the precipitation efficiency (the fraction of liquid water of a sample falls out as precipitation in the model) is changed, the relative humidity profile varies strongly, as we can see on figure 108.

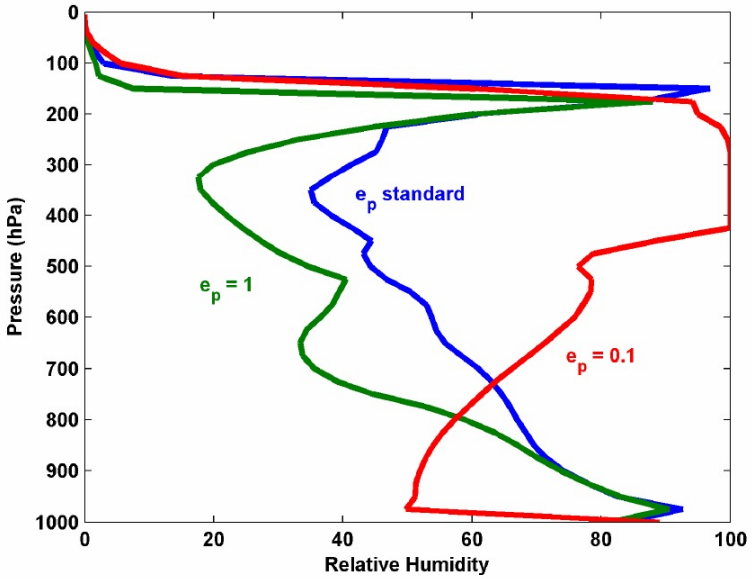

Figure 108: Dependence of the relative humidity profile on the precipitation efficiency

For example, for low precipitation efficiency (ep = 0.1), all the water vapor stays in the atmosphere, which makes it very humid. If the precipitation efficiency is maximal (ep = 1), the atmosphere becomes very dry, except very close to the surface where all the rain evaporates, and near the tropopause because of the upwards flux of water vapor. If models are poorly resolved in the vertical, numerical experiments make the water vapor behave diffusively, and this nonlinear effect of precipitation efficiency can not be observed, underlying the importance of high vertical resolution and precise microphysical schemes in global circulation models.

11.3 Shallow convection

11.3.1 Observation of clouds

We define shallow convection as cumulus convection that does not go all the way through the troposphere (ie typically doesn't go above the top of the boundary layer, cf top left of figure 109). Observing the middle of figure 109, we can see that clouds are envelopes of multiple complex convective structures, with new thermal emerging from the top of the "cloud" because their water vapor concentration is higher. Consequently, clouds are always loosely defined. Shallow convective clouds are common around a deep cumulus cloud, such as the one on the top right of figure 109. The fibrous cloud on the bottom left of figure 109 is typical of a cloud containing ice crystals. As the saturation water vapor over ice is smaller than the saturation water vapor pressure over liquid water (cf figure 72), the "ice cloud sucks water vapor out of the supercooled cloud around it", explaining the "hole of clear air" around it. Another example of this physical phenomenon is presented on the bottom middle of figure 109. We remember that the sea aerosols tend to be very hygroscopic (they attract and hold water vapor molecules from the environment very easily), which explains why the relatively small cloud on the bottom right of figure 109 is precipitating.

Figure 109: Pictures of clouds produced by shallow convection

An important noticeable feature when we watch movies of cumulus cloud convection (snapshots of such movies are presented on figure 110) is the importance of downwards motion in moist plumes. After the thermals ascend, they go down as we can see from looking at the cloud tops, because entrainment of dry air makes them too diluted. As the day progresses, two processes help the clouds reaching a higher and higher altitude:

1. The surface temperature gets warmer and warmer.
2. The entrainment makes the environment surrounding the cloud moister and moister.

Figure 110: Snapshots of cumulus convection movies

Another question is understanding why clouds preferentially form over the mountain. A first thought would be that the mean air currents are up-slope because of the no-normal flow condition along the topographic slopes, which explains why the air ascends and condensates above the mountain. However, in the case of figure 110, the clouds form above the peak of the mountain. An interested thermodynamic interpretation is based on how RCE is affected by the presence of topography. First, it should be noted that the surface temperature at the top of a mountain is colder because there is a smaller mass of atmosphere above the surface, meaning that it receives less IR radiation. Since the air still follows a dry and then a moist adiabat, we can see on figure 111 that it implies that the entire temperature profile is colder.

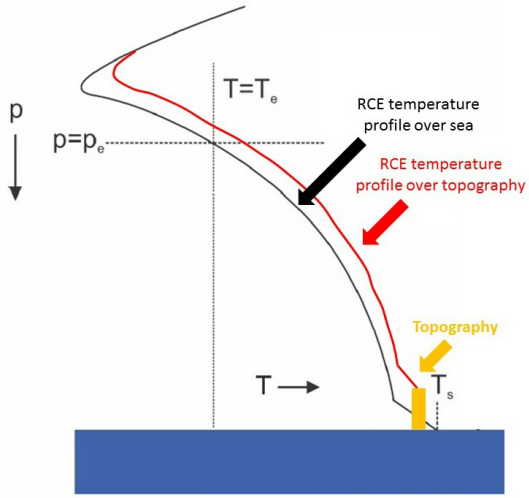

Figure 111: RCE temperature profile over the sea (black line) and over topography (red line)

Coming back to the right part of figure 110, once an air parcel reaches the tropopause, it overshoots and its buoyancy become negative, initiating a downdraft. This is only possible for moist thermals as we had seen that for dry thermals, the buoyancy was always positive, and that it never went below the value $b = 0$ that represents the "top of the plume" (cf paragraph 5.3).

11.3.2 Thermodynamics of shallow convection

To understand shallow convection, it is helpful to introduce the appropriate thermodynamic invariant. We start from the virtual potential temperature θ_v, which is a special case of the density potential temperature θ_ρ (defined by 159) where we neglect the presence of liquid water and ice in the sensible heat budget of the air parcel. However, we do take into account the latent heat coming from the condensation of water vapor in the heat budget:

$$T c_{p_d} \frac{d\theta_v}{\theta_v} \approx dQ + L_v dr_l \;\Rightarrow\; c_{p_d} T \frac{d\theta_{\mathrm{lv}}}{\theta_{\mathrm{lv}}} \approx dQ \tag{282}$$

where we have introduced our new adiabatic invariant, namely the liquid water virtual potential temperature:

$$\theta_{\mathrm{lv}} \overset{\mathrm{def}}{\approx} \underbrace{T_v \left(\frac{p_0}{p}\right)^{\frac{R_d}{c_{p_d}}}}_{\theta_v} \underbrace{\exp\left(-\frac{L_v r_l}{c_{p_d} T}\right)}_{\text{Latent heating}} \tag{283}$$

θ_{lv} is conserved during reversible adiabatic processes, as long as precipitation does not fall. When two samples containing liquid water mix adiabatically, their liquid water virtual potential temperature almost linearly mixes. As a consequence, following the left of figure 112, when a reversibly lifted sample mixes with its environment, its θ_{lv} will be less than that of the uncontaminated environment. Physically, the mixing evaporates water into the entrained dry environmental air, making the net buoyancy of the mixture negative, which explains why the presence of downdrafts is only possible for moist air.

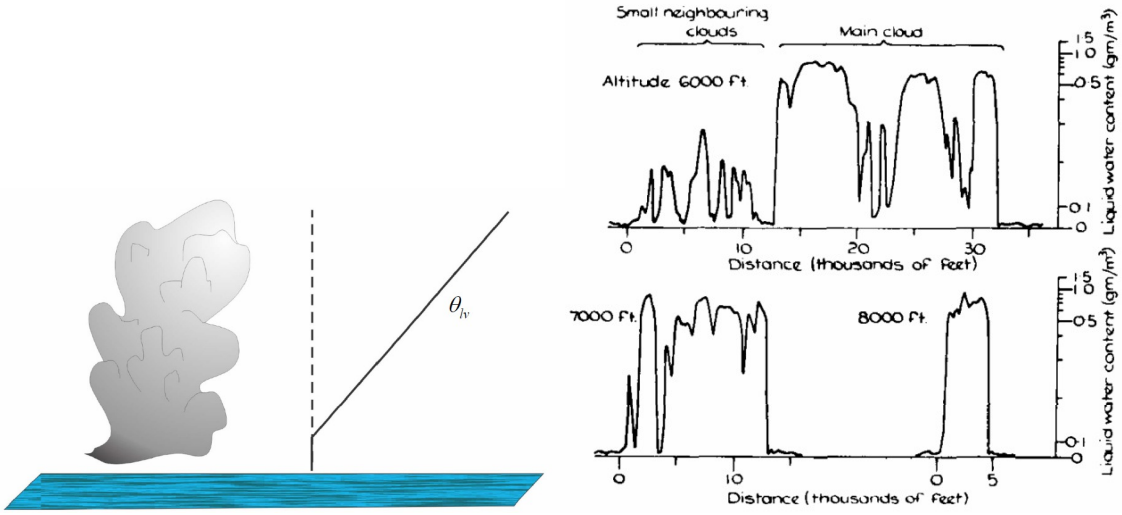

Figure 112: Typical vertical profile of liquid water in the environment of non precipitating cumulus clouds (left) and liquid water content (g.m^{-3}) on successive traverses through cumulus clouds at altitudes of 2000, 2350, and 2650 meters (right)

The conservation of $\theta_{\rm lv}$ yields:

$$\frac{D\theta_{\rm lv}}{Dt} = 0 \;\Rightarrow\; \frac{\partial \theta_{\rm lv}}{\partial t} = -w\frac{\partial \theta_{\rm lv}}{\partial z} \tag{284}$$

Using the mass conservation statement 259 in steady state ($\frac{\partial}{\partial t} = 0$), integrating 284 over the volume ($V_{\rm cloud}$) of a cloud and its lifetime ($t_{\rm cloud}$), we obtain:

$$\int_{(V_{\rm cloud})}\int_{(t_{\rm cloud})} M_u \frac{\partial \theta_{\rm lv}}{\partial z} dV dt = 0 \tag{285}$$

The constraint 285 on non-precipitating convective clouds means that over the lifetime and volume of each cloud, there can be no net heating by condensation. Consequently, there must be significant downward motion somewhere over the lifetime and volume of a non-precipitating cloud.

11.3.3 Observations of shallow convection

Observationally, using aircrafts, it is possible to measure the liquid content of a cloud and its neighbors (cf right of figure 112). On the left of figure 113, vertical velocity data are presented; they have been obtained through the technique of inertial navigation, which is based on measuring the acceleration and the rotation using accelerometers and gyroscopes to obtain the velocity and the position of the airplane by integration.

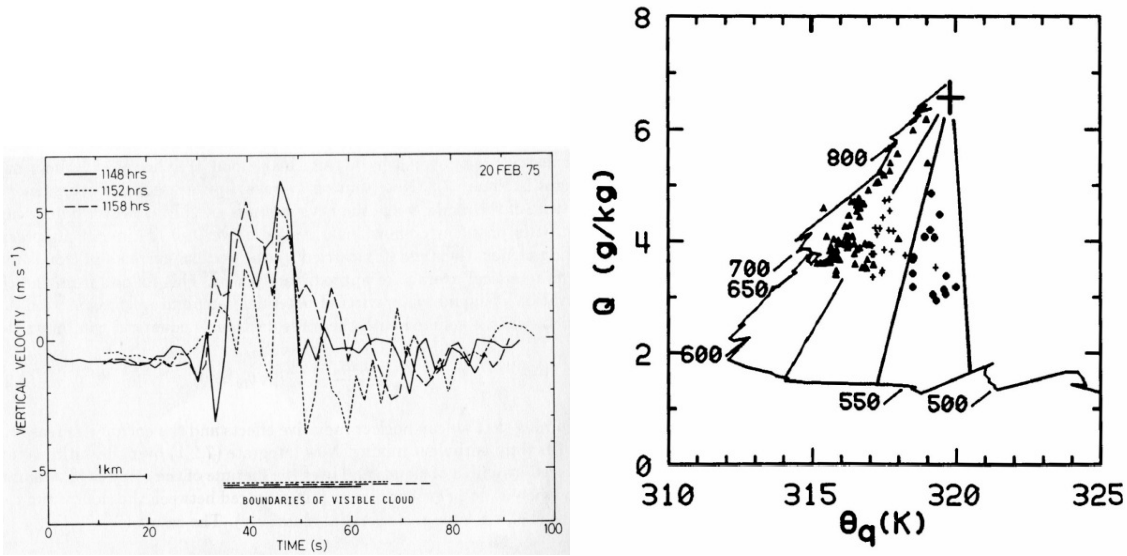

Figure 113: Filtered vertical velocity data from successive penetrations of a cumulus cloud (left) and measurements in Montana cumuli plotted on a $\theta_e - r_T$ diagram

IR imaging shows that it is hard to find a place in the Tropics where there is no shallow convection (114), confirming the importance of taking it into account when we study RCE or deep convective systems.

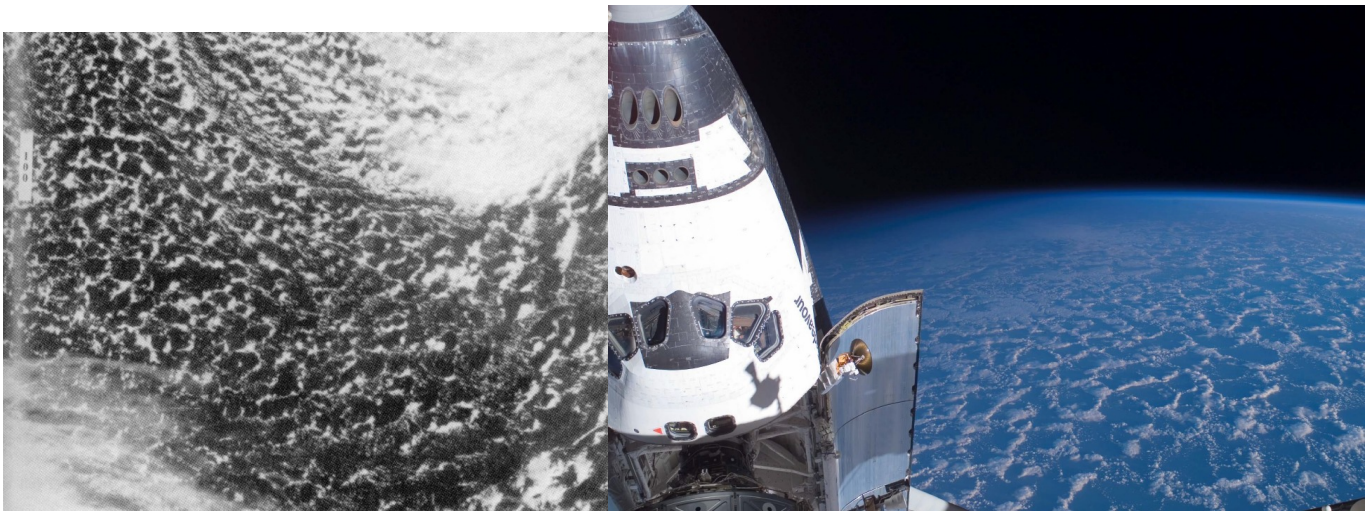

Figure 114: Open cellular cumulus convection over the sea (left) and space-based observations of clouds produced by shallow convection (right)

Coming back to RCE, shallow convection help balance out the net increase in MSE produced by deep convection that brings water vapor (and thus latent heat) in the troposphere. Because they help producing downdrafts and entrain dry air around them, they indeed have a net cooling effect on the system. If we look at a profile of θ_{lv}, the trade cumuli can be found below the trade inversion (sharp increase of θ_{lv}), approximately located at an altitude of 2km in the Tropics.

11.4 Deep, precipitating convection

11.4.1 Introduction

From observations of cumulus cloud tops, the distribution of cumulus heights is continuous but bimodal, with a lot of shallow clouds (1-2km) and a lot of clouds reaching the tropopause, hence the distinction between "shallow" and "deep" convection. On figure 115, we can see that there are clearly more storms in the Tropics where the climate is warmer and moister.

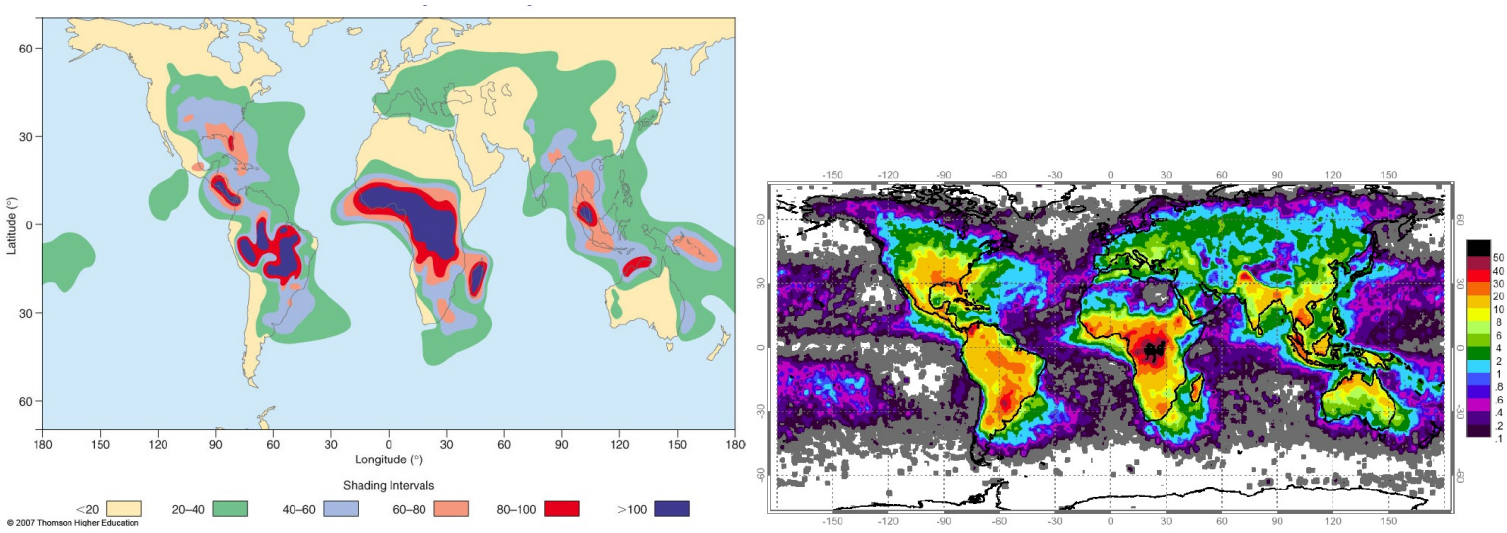

Figure 115: Average number of thunderstorms days in a year (left) and annual lightning frequency from satellite (right)

It would seem that there are much more storms on the land (of course the left of figure 115 does not give any information because storms happening over the ocean are under-reported), or at least that storms are more violent and produce more lightning over land (even if they still rain a lot over the ocean in the Tropics). The main difference between sea and land-surface temperatures is the strong diurnal cycle over land. As the convection is lagged and typically happens five hours after the peak in solar radiation, MSE (or

the CAPE for a parcel released at ground level) has time to build up before it is released, explaining the intensity of observed storms. A higher value of CAPE leads to higher updrafts values (according to 209), allowing for the interaction between snow crystals and supercooled droplets that creates graupel. Flying aircrafts through deep convective clouds has allowed to study their time evolution, that can be (artificially) divided in three phases, as we can see on figure 116.

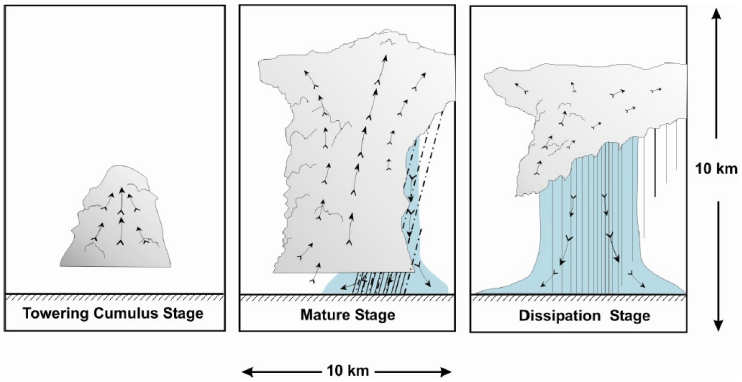

Figure 116: Three stages of "air-mass" showers

The evolution of a cumulus cloud typically lasts 45min: first, deep convection leads to strong updrafts and builds a cumulus tower, then the clouds spreads out as it reaches the tropopause (creating what is called a "cloud anvil") and water starts raining out of the cloud after it has condensed by being lifted; finally, the cold, low-entropy air chokes off the potentially warm air and creates strong downdrafts leading to the dissipation of the cumulus tower. Note that the average droplet loses half of its mass before it reaches the ground because of partial re-evaporation. Once the cold downdraft hits the ground, it propagates laterally as a density current (called a "cold pool"), which can be simulated in laboratory (cf figure 117).

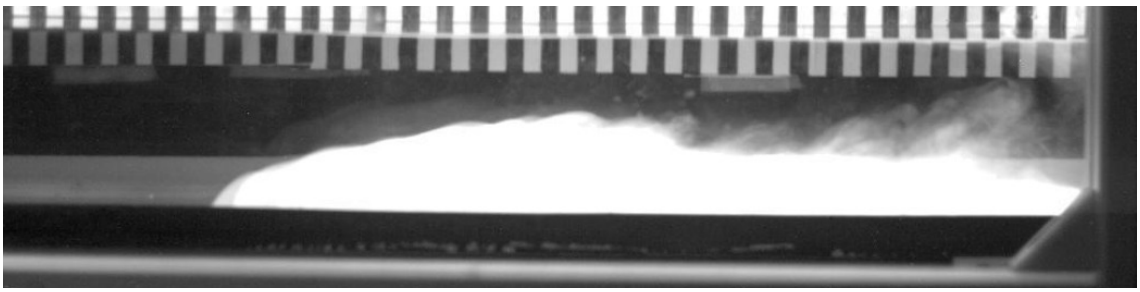

Figure 117: Laboratory experiment of a density current (the denser water is fluorescent)

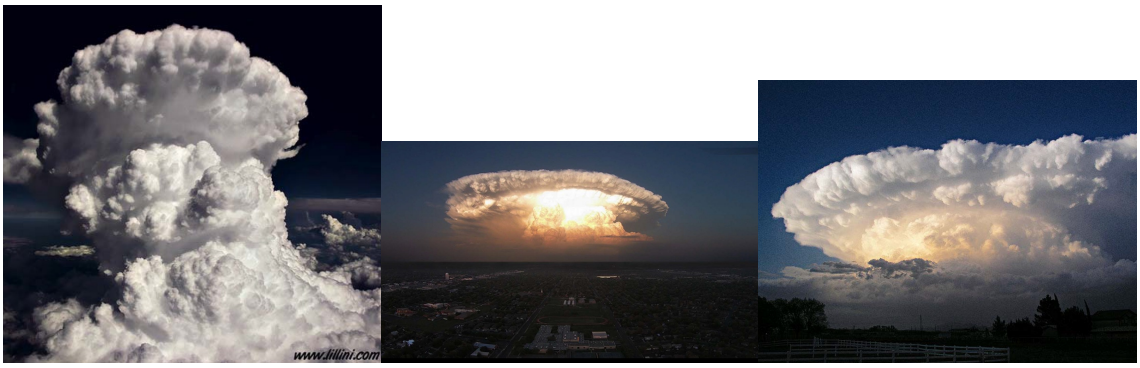

Figure 118: Photo of deep convective clouds, spreading as they hit the tropopause

Figure 120: Arcus clouds (air mechanically lifted from the cold pools and condensing as thin clouds)

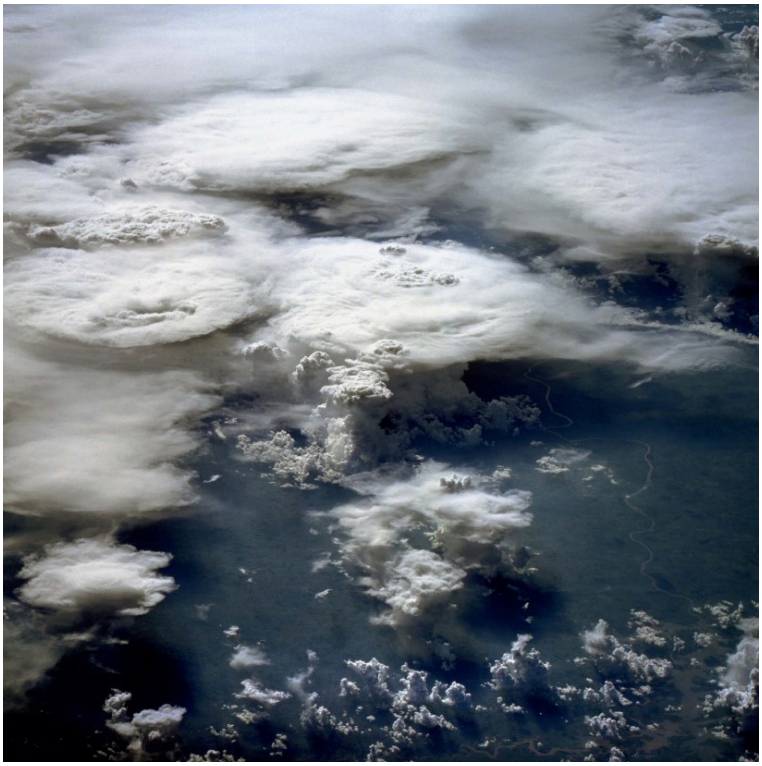

Figure 119: Convective shower observed from space

Figure 121: Mammatus clouds

Mammatus clouds (121) form on the bottom of ice clouds, on the underside of the cloud anvil. They are believed to form when the liquid water enthalpy (196) of the cloud $h_{\mathrm{w,cloud}}$ is smaller than the liquid water enthalpy of the environment $h_{\mathrm{w,env}}$. Then, if it the cloudy air mixes with the environmental air and its liquid water evaporates, its buoyancy will be negative and it will undershoot, and then go back up, explaining the form of the Mammatus cloud.

11.4.2 Mesoscale organization of convection

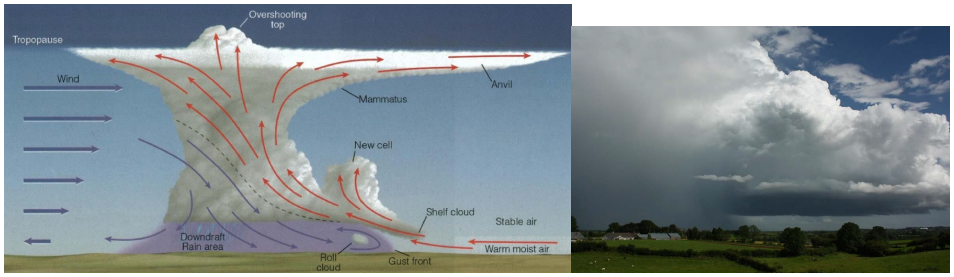

Figure 122: Left: Schematic of a multi-cell thunderstorm (red arrow≡warm updraft; blue arrow≡cool downdraft). The new cell forms downshear. The rain falls down relatively to the mean current, which means it will not actually fall down if the updrafts are strong enough (right).

An important form of organized convection is the squall line. It is a set of individual intense thunderstorms cells arranged in a line. They occur along a boundary of unstable air, such as a cold front. Strong environmental wind shear causes the updrafts to be tilted and separated from the downdraft, which dense cold air forms a "gust front".

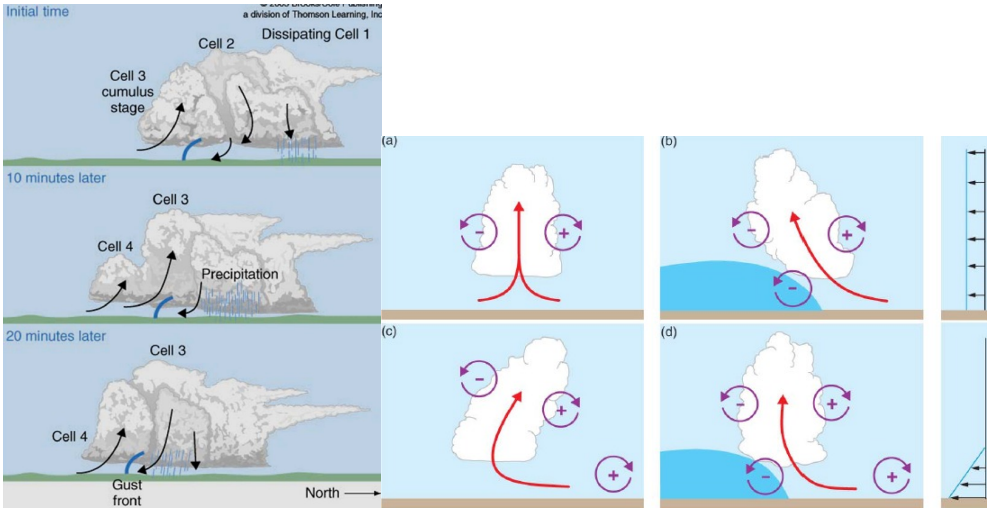

Figure 123: Left: The squall line propagates to the left because of the mechanism of formation of new cells.
Right: Schematic diagram showing how a buoyant updraft may be influenced by environmental wind shear and/or cold pool (RKW theory: the sign of $-\xi$ is indicated by purple arrows)
(a) With no environmental wind shear and no cold pool, the axis of the updraft produced by the thermally created symmetric vorticity distribution is vertical.
(b) With a cold pool, the distribution is biased by the positive vorticity of the underlying cold pool, causing the updraft to tilt over the cold pool.
(c) With environmental shear and no cold pool, the distribution is biased toward negative vorticity, causing the updraft to lean downshear.
(d) With both a cold pool and shear, the two effects may negate each other and promote an erect updraft, and thus create a squall line.

Dynamically, we can understand squall lines by studying the evolution of the meridional component of the relative vorticity:

$$\xi \overset{\text{def}}{=} \overrightarrow{e_y} \cdot (\overrightarrow{\nabla} \times \overrightarrow{v}) = \frac{\partial w}{\partial x} - \frac{\partial u}{\partial z} \tag{286}$$

Using the Boussinesq equations with a given environmental buoyancy profile b_{env}, we can see that the zonal gradient of environmental buoyancy is responsible for the evolution of ξ:

$$\frac{D\xi}{Dt} = \frac{\partial b_{\text{env}}}{\partial x} \tag{287}$$

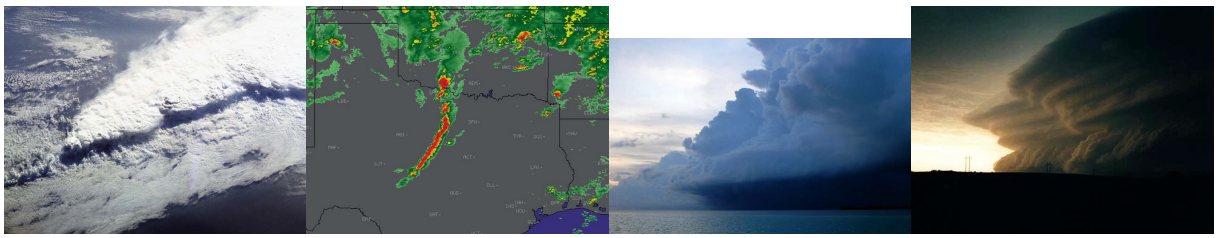

Figure 124: Squall lines seen from space (left), appearing on radar (middle left) and clouds formed by gust fronts (right)

A less understood form of organized convection is the Mesoscale Convective Complex (MCC), which are circular, as we can see from radar observations on figure 125.

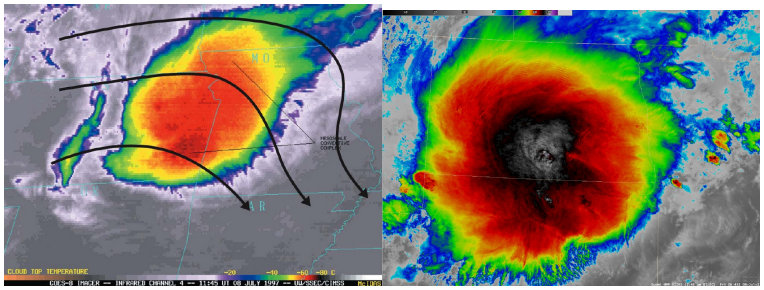

Figure 125: Radar images of mesoscale convective complexes

A MCC is composed of multiple single-cell storms in different stages of development; the individual thunderstorms must support the formation of other convective cells. In order to last a long time, a good supply of moisture is required at low levels in the atmosphere. As a consequence, MCC over land only occur in the middle of the Summer. They are recognizable as large areas of low effective temperature, which is indicative of a thick cloud, and many convective cells (with a typical aggregated radius of 300km). The streamlines of a MCC have a strong anticyclonic motion, unlike the eastwards mean flow observed normally (the individual clouds are chaotic so it is impossible to predict them individually). The aggregation of moisture will have a strong influence on the external flow, and large collections of clouds interact in a non trivial way with the radiation, influencing the TOA infrared emission and the local climatology. In some rare cases, even bigger aggregates of thunderstorms called super-cells can be observed. The required conditions are a low-level wind shear and a large amount of CAPE. In specific regions of the world, such as the "tornado alley" of the United States, a lot of CAPE can be climatologically built. First, we need to introduce a useful approximate adiabatic invariant, starting from the virtual potential temperature θ_v, and taking into account the potential energy due to the water vapor content of a parcel that can be potentially released as latent heat; the first law of thermodynamics can be written in this case:

$$T c_{p_d} \frac{d\theta_v}{\theta_v} + L_v dr \approx dQ \;\Rightarrow\; c_{p_d} T \frac{d\theta_e}{\theta_e} \approx dQ \tag{288}$$

where we have introduced the equivalent potential temperature θ_e:

$$\theta_e \overset{\text{def}}{\approx} \underbrace{T_v \left(\frac{p_0}{p}\right)^{\frac{R_d}{c_{p_d}}}}_{\theta_v} \underbrace{\exp\left(\frac{L_v r}{c_{p_d} T}\right)}_{\text{Potential latent heating}} \tag{289}$$

Note that in this definition, because θ_e only increases linearly with the virtual temperature T_v but exponentially with the water vapor mixing ratio r, a moist and cold air mass is likely to have a higher equivalent potential temperature than a dry and hot air mass, because of all the latent heat it can release by condensing its water vapor content. Coming back to the "tornado alley" and following the schematic on the left of figure 126, the high temperature but dry lowθ_e air mass coming from the West will go above the moist cold highθ_e air mass coming from the Gulf of Mexico, allowing to build a CAPE by creating a temperature inversion (visible on the middle of figure 126). The temperature inversion creates some CIN, which prevents deep convection from happening and allows to build up a lot of CAPE. Using equation 209, we can see that the values of CAPE listed on the right of figure 126 correspond to velocities of 100m.s^{-1}! In practice, updrafts of 80m.s^{-1} can be observed in those regions in the case of a strong storm. Forming a super-cells is one way of releasing this CAPE, which explains why they are observed in the Great Plains during Spring. We have seen that the wind shear $\frac{\partial U}{\partial z}$ is another important factor in the genesis of supercells; it is by definition an invariant Galilean quantity, which means that the curvature of the wind shear has a physical meaning.

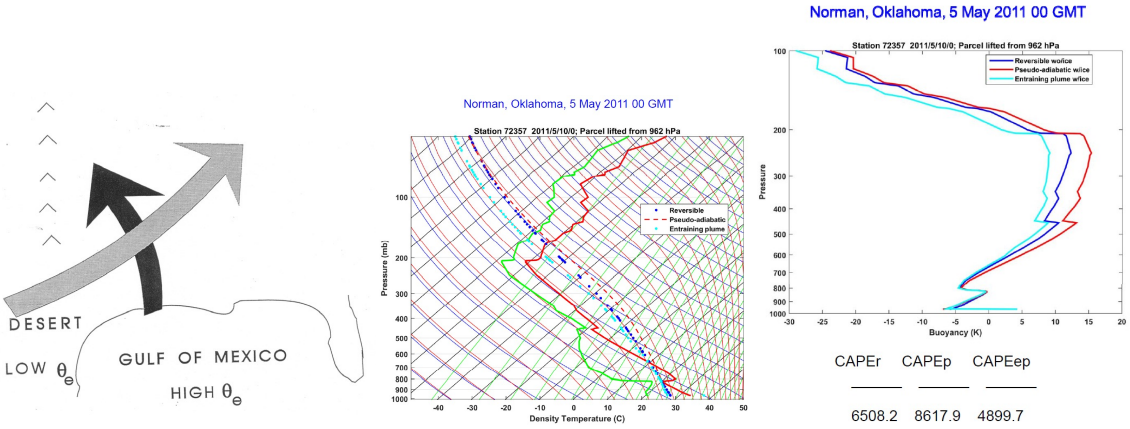

Figure 126: Intersection of two air masses leading to CAPE build-up (left), sounding of Norman, Oklahoma during a tornado event (middle), and CAPE in Norman, Oklahoma at the same time (right)

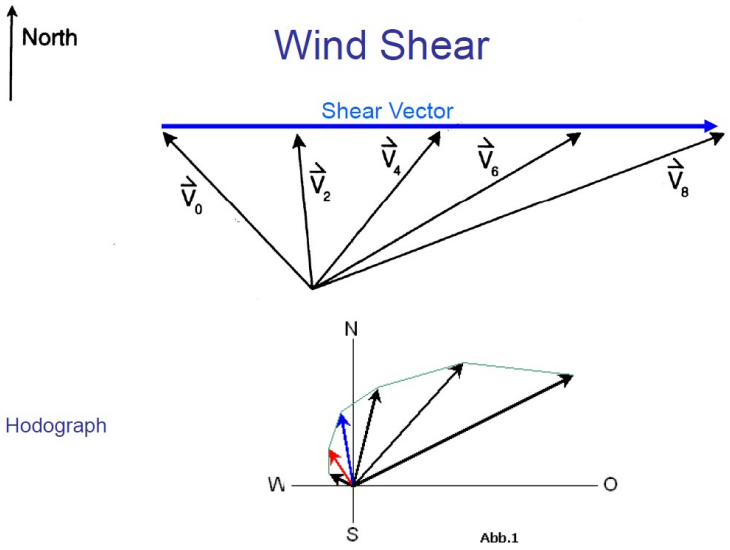

Figure 127: Wind shear constructed by finite-differencing a hodograph; straight (top) and curved (bottom) wind shear vector

If the wind shear is straight, like on the top of figure 127, squall lines are more likely to be generated, whereas if the wind shear is curved, like on the bottom of figure 127, supercells are more likely to be generated.

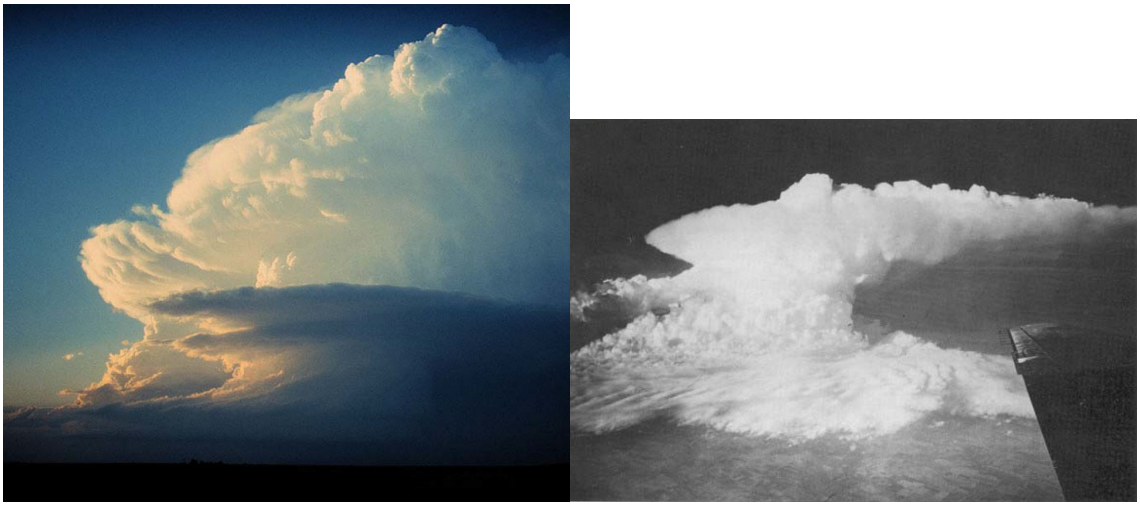

Figure 128: Supercell cloud images

From the visible and the infrared images of a supercell (figure 129), a qualitative understanding of the conditions for their formation and their schematic can be deduced (figure 130).

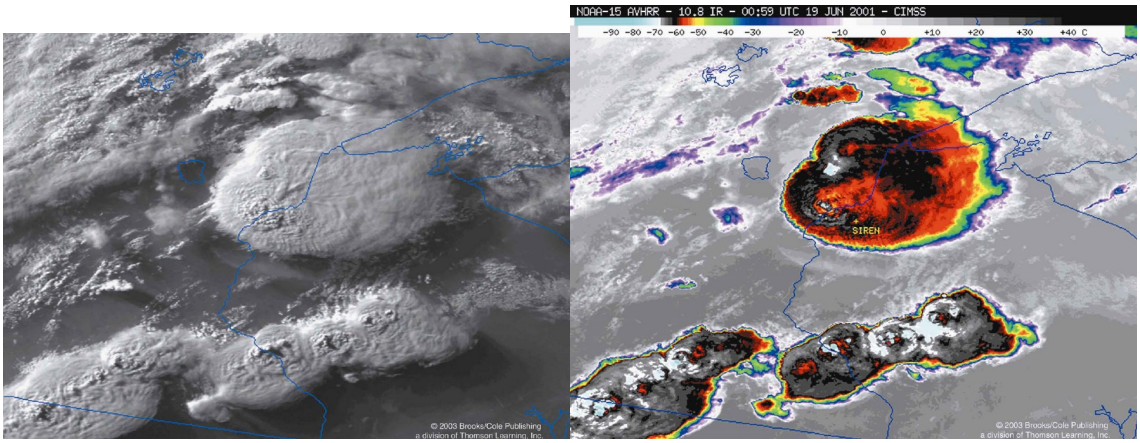

Figure 129: Visible (left) and infrared (right) images of a supercell

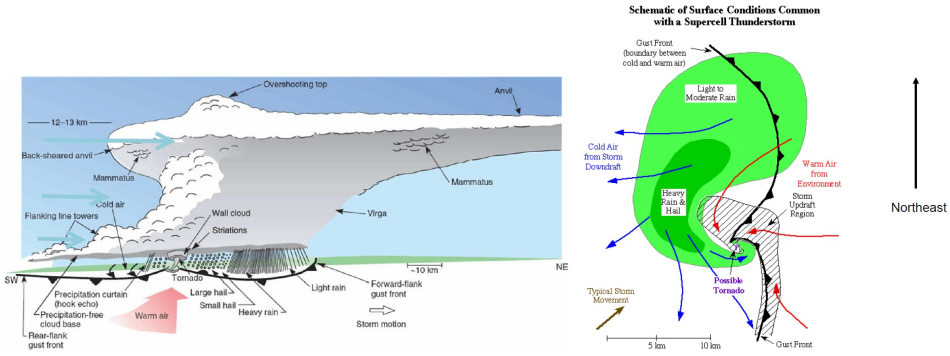

Figure 130: Schematic of a supercell (left) and the conditions for its formation (right)

. The reason why supercells rotate is tightly linked to the conservation of meridional relative vorticity in the absence of environmental buoyancy gradients, according to equation 287.

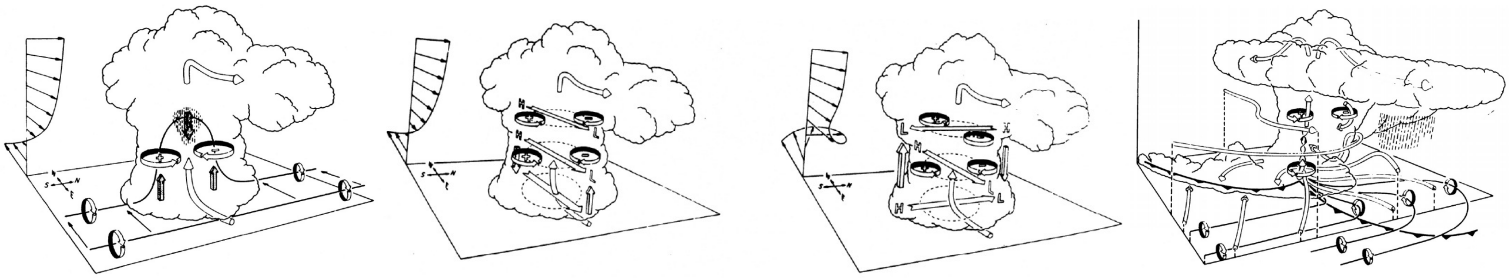

Figure 131: Production of vorticity within a supercell: Tilting of vortex lines (left), pressure perturbations (middle) and vorticity production (right)

According to figure 131, if the supercell rotates clockwise, it strengthens the cyclonic and weakens the anticyclonic air flows within it. If the pressure gradients are properly aligned, vorticity can be produced, by the environmental air flow, reinforcing the supercell.

Figure 132: Supercell cloud images

Figure 133: Supercell cloud images

Figure 134: Supercell cloud images

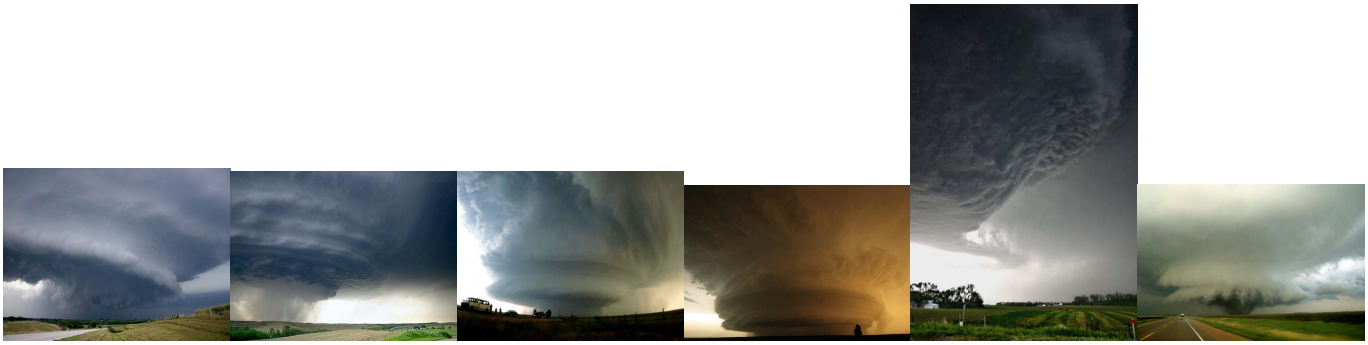

Figure 135: Supercell cloud images

The tilting of vorticity within a supercell can produce tornadoes, which only happen in very specific places on Earth (US Great plains, Bangladesh, Argentina pampas...). Looking at the distribution of tornadoes in the US in the second half on the twentieth century, we can clearly see that they mostly happen in the "tornado alley", East from the Rockies.

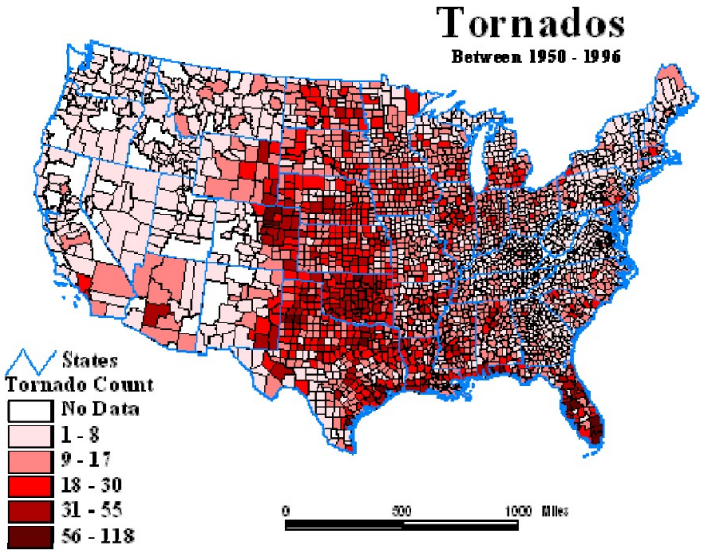

Figure 136: Tornado count in the US per county between 1950 and 1996

Often, waterspouts that form on the ocean because of low level cut-offs will be counted as tornadoes, which explains their presence in Southern California on figure 136,for instance.

11.5 Interaction of radiation and convection

11.5.1 Numerical simulation of RCE

We remember that it is possible to explicitly simulate the details of RCE using cloud resolving models (CRM). Unlike what their names suggest, CRM are not actually able to simulate clouds; however, they can resolve convection and the physical processes associated to it. An example of a CRM is the system for atmospheric modeling, presented on figure 137.

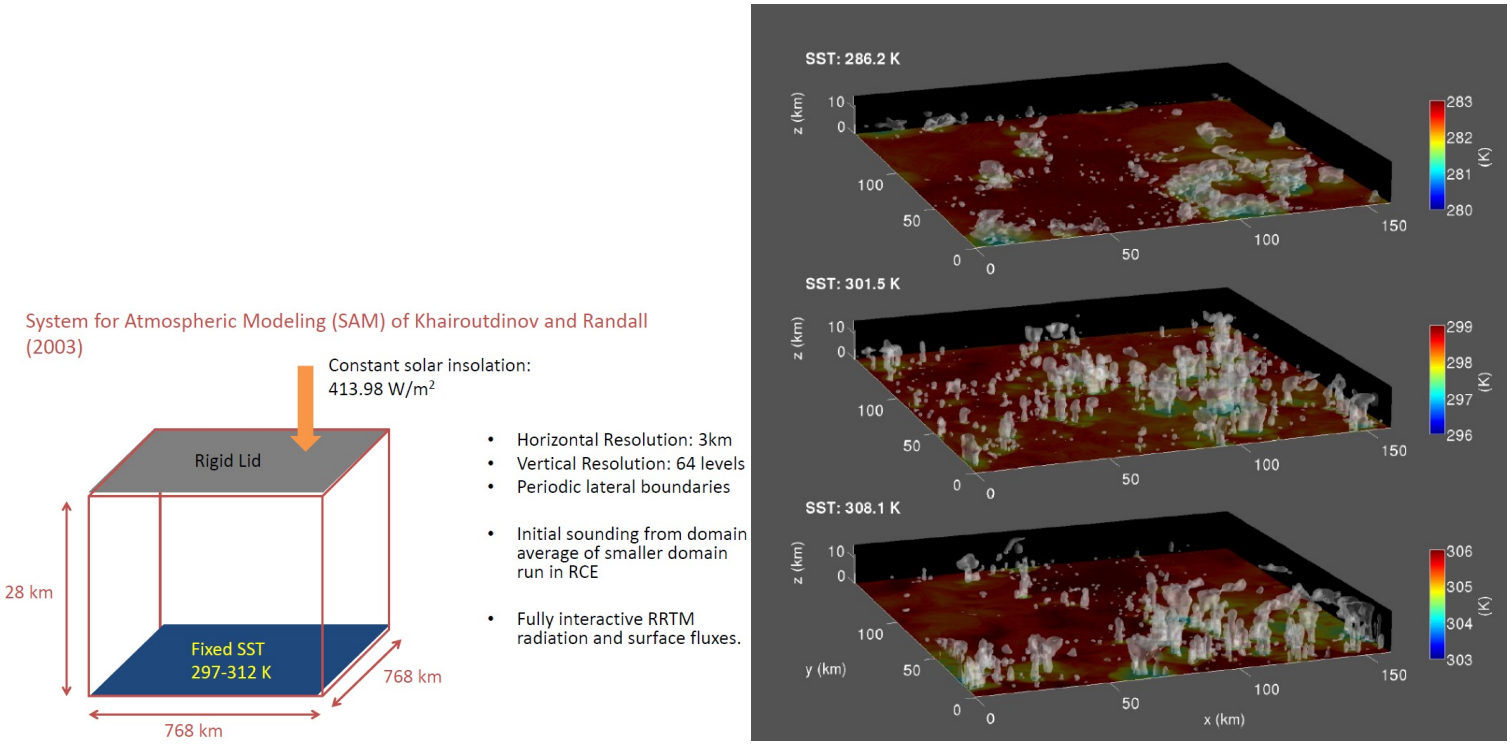

Figure 137: Characteristics of SAM (left) and snapshots of condensed water in RCE using SAM for different values of fixed sea surface temperature (right)

The vast majority of comprehensive simulations of RCE have been done using a fixed sea surface temperature, as it would be very computationally expensive to run CRM with an interactive slab ocean (for instance, the relaxation timescales to RCE shown of figure 107 can become very long as soon as the heat capacity of the slab ocean decreases a little). Simulating RCE confirms the general characteristics described in section 11.1.4, including the chaotic aspect of convection, making it seem random (although rigorously a cloud is less likely to appear in a place where convection just happened because of the presence of cold pools). It is very insightful to study the total precipitation, which can be written as a product of the rainfall velocity and the area of the domain over which precipitation is happening:

$$\text{Precipitation} = \underbrace{\text{Rainfall velocity}}_{V_t} \cdot \underbrace{\text{Rainfall } \textit{Area}}_{\sigma} \tag{290}$$

Determining which physical processes are associated to V_t and to σ and how they affect the total precipitation is still an open area of research. The rainfall terminal velocity V_t plays a central role in RCE:

- If the mean precipitation is held constant (for instance by specifying the radiative cooling), according to 290, the rainfall intensity will increase with the terminal velocity. This effect is shown on figure 138.
- Because of that effect, and noticing that the rainfall area is not affected, an increase in V_t will cause an increase in the updraft velocity $w_{\text{cloud}} = M_u \sigma^{-1}$, which explains why it can be argued that w_{cloud} scales like V_t.

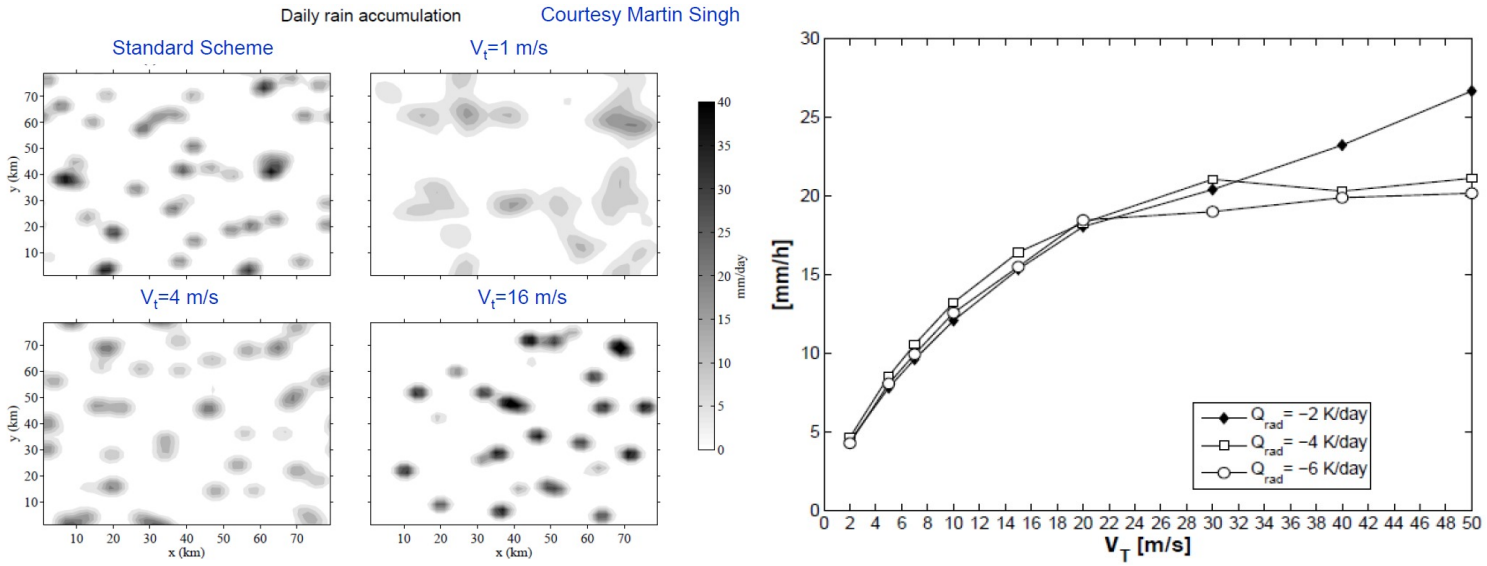

Figure 138: Daily rain accumulation (left) and rainfall intensity vs terminal fall speed (right)

According to simulations of RCE, the rainfall area itself seems to be determined by the large-scale circulation, or by the radiative forcing/cooling, as we can see on the left of figure 139, whereas the rainfall intensity seems not to be affected in this case.

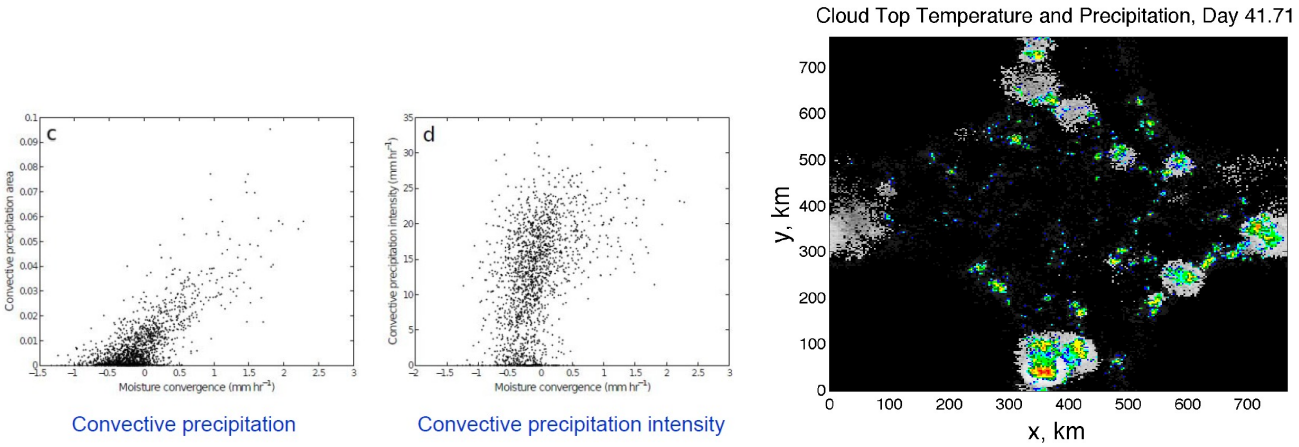

Figure 139: Comparison of large-scale moisture convergence to radar-derived convective quantities (left) and cloud top temperature and precipitation in the case where convection has self-aggregated (right)

11.5.2 Self-aggregation of convection

When run under specific conditions, we can see on the right of figure 139 that convection can spontaneously self-aggregate. First, a dry patch forms, which forces all the convection to cluster in a random area of the domain. As there is no characteristic physical horizontal length, the cluster scales like the domain size, and does not disaggregate easily once it has formed. The self-aggregation phenomenon can be seen by looking at any variable related to convection, especially water vapor, as we can see on figure 140.

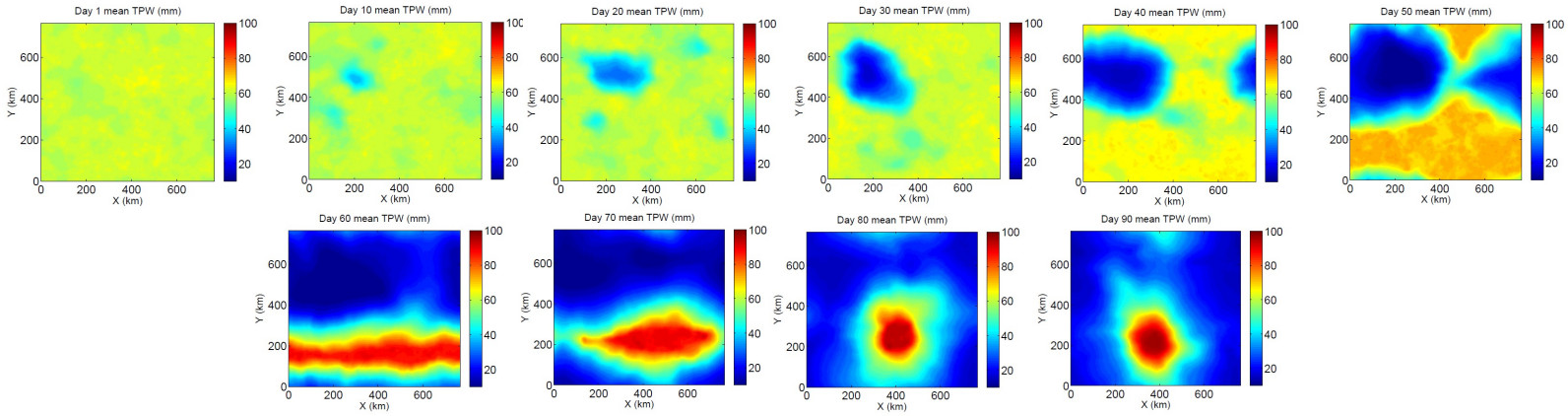

Figure 140: Evolution of vertically integrated water vapor during self-aggregation

Good examples of convective clusters are mesoscale convective systems (defined in 11.4.2). The left of figure 141 shows a good example of self-aggregation in nature: on the top of the picture, convection is seemingly random, as expected in classical RCE. In the center of the picture, a dry patch has formed around a moist precipitating cluster surrounded by gust fronts.

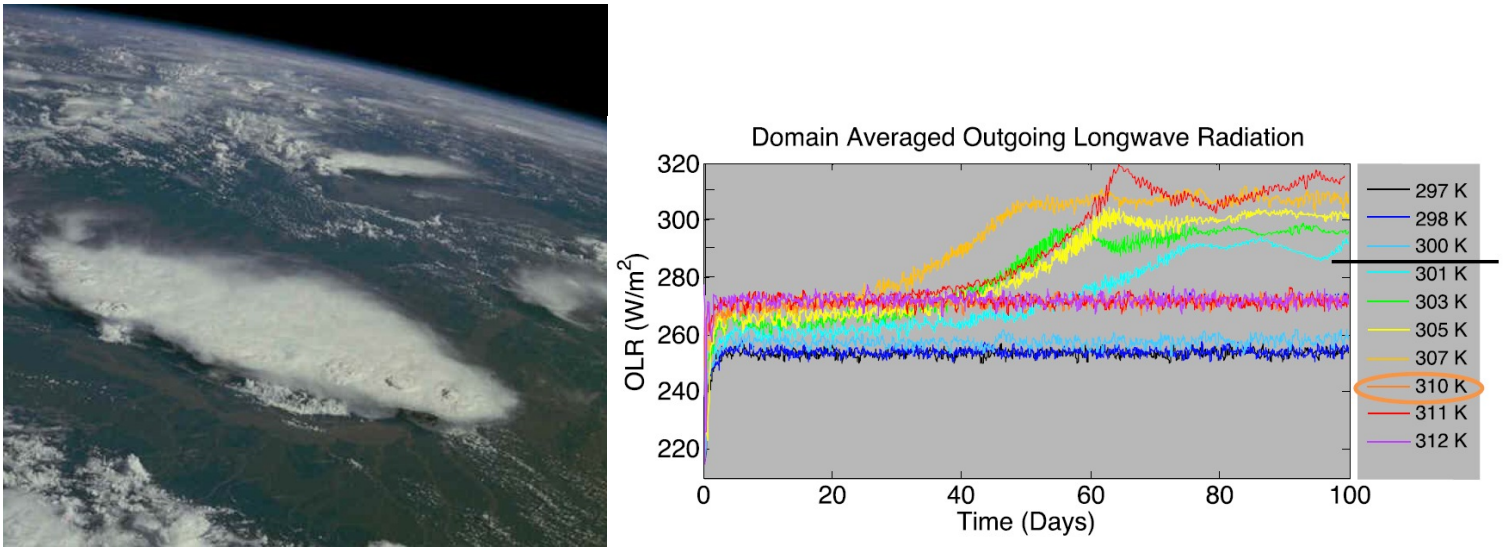

Figure 141: Monsoonal thunderstorms, Bangladesh and India, July 1985 (left) and surface temperature dependence of the domain averaged outgoing longwave radiation (right)

On the right of figure 141, we can see that the amount of outgoing longwave radiation increases when the system has self-aggregated, as the area of the moist blob is much smaller than the area of the dry region. Thus, self-aggregation tends to dry out the system, which can also be seen by looking at the average water vapor in the domain. By noting that all the simulations that have an increase in the outgoing longwave radiation have self-aggregated, we can see that the system does not aggregate for too small sea surface temperatures (because the system is then too dry) or for too high temperature. We remember that for high sea surface temperatures, the moist adiabatic lapse rate $(\frac{d\theta}{dz})_{s^*}$ increases, since the upper tropospheric temperature stays the same. According to 261, the updrafts w then become weaker, which means that the moist cluster extends further in the domain, since you need a bigger area σ to maintain the same convective mass flux M_u. As a consequence, we can hypothesize that the non-occurrence of self-aggregation for high temperatures is an artifact of a too small domain, which is confirmed by the fact that when the 310K case is re-run in a larger domain, we observe self-aggregation in the simulation (red curve). A good metric of self-aggregation is based on the vertically integrated moist static energy (192):

$$\hat{h} \stackrel{\text{def}}{=} \int_{(\text{Column})} \rho h dz \approx \int_{(\text{Column})} \frac{h dp}{g} \tag{291}$$

If neglect export of kinetic energy by the wave field, 291 cannot be changed by convection. Thus the budget of 291 only involves the surface turbulent fluxes and the net radiative fluxes:

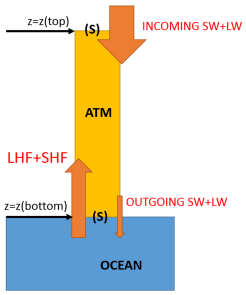

Figure 142: Budget of vertically integrated MSE for an air column

$$\underbrace{\frac{D\hat{h}}{Dt}}_{\text{Evolution MSE}} = \underbrace{\text{LHF} + \text{SHF} + \text{NetLW} + \text{NetSW}}_{\text{Diabatic terms}} \tag{292}$$

When the RCE is nearly random, the water vapor is nearly homogeneous in the domain (as well as the temperatures), so the same thing can be said for $\hat{h}$. However, when the system self-aggregates a very moist cluster (zone of high $\hat{h}$) is surrounding by dry subsiding air (small $\hat{h}$). As a consequence, the spatial variance of $\hat{h}$ increases when the system self-aggregate. To find out how the spatial variance of $\hat{h}$ evolves, we take a domain-average $\{\}$ and denote the deviation from this average by primes. Subtracting the average of 292 to 292 and multiplying the resulting equation by $\hat{h}'$, we obtain a budget for the time-evolution of the spatial variance of $\hat{h}$:

$$\underbrace{\frac{1}{2}\frac{\partial(\hat{h}')^2}{\partial t}}_{\text{Increase MSE variance}} = \underbrace{\hat{h}'\text{LHF}' + \hat{h}'\text{SHF}' + \hat{h}'\text{NewLW}' + \hat{h}'\text{NetSW}'}_{\text{Correlation between MSE perturbations and diabatic terms}} - \underbrace{\hat{h}'\overrightarrow{\nabla}\cdot(\overrightarrow{u}\hat{h})}_{\text{Convergence of MSE variance}} \tag{293}$$

Each term on the right hand side of equation 293 can be seen as a feedback term: if the perturbation of the vertically integrated MSE has the same sign as the spatial perturbation of a diabatic term, then the feedback is positive, and vice-versa. The Hovmuller plots of the feedback terms are shown on figure 143.

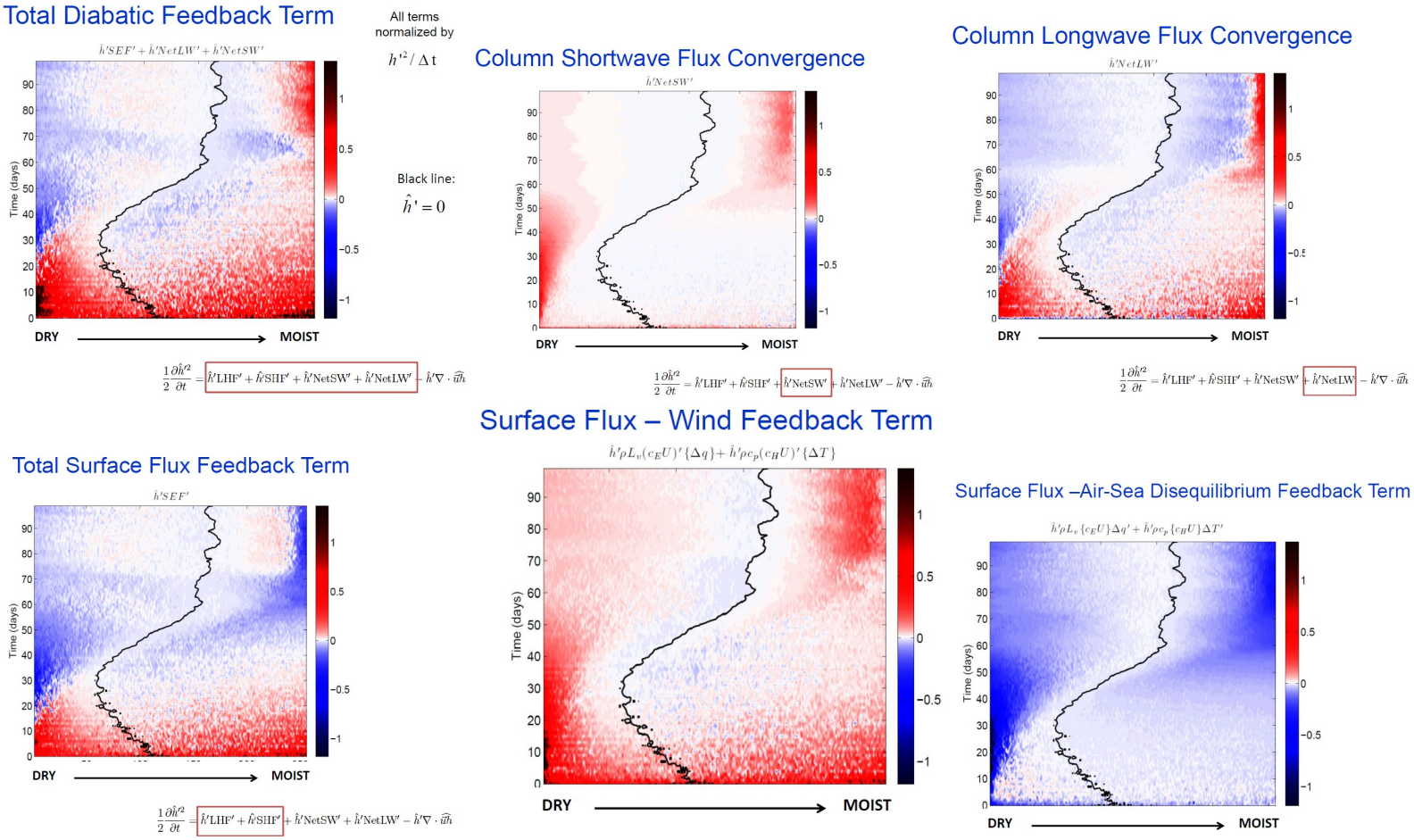

Figure 143: Hovmuller plots of the feedback terms. From left and right and top to bottom:
Total diabatic feedback term; Column SW flux convergence; Column LW flux convergence;
Total surface flux feedback term; Surface flux - Wind feedback term; Surface flux - Air sea disequilibrium feedback term.

For example the LW feedback is positive everywhere ($\hat{h}'\mathrm{NetLW}' > 0$) during the process of self aggregation: in the dry zones ($\hat{h}' < 0$), the net LW flux (directed towards the surface) decreases ($\mathrm{NetLW}' < 0$) because there is less water vapor, and vice-versa for the moist zones. It then becomes negative everywhere when the cluster is formed because of the cloud cover above the moist zone which has the opposite effect. We remember the bulk formulas for the latent heat flux (263) and the sensible heat flux (264). The perturbation of the surface enthalpy flux, which is the sum of both turbulent fluxes (following 265), can be partitioned in different flux anomalies:

$$\frac{F_c'}{\rho_s} \approx \underbrace{(C_k|\overrightarrow{V_{\mathrm{wind}}}|)'(L_v\{\Delta q\} + c_p\{\Delta T\})}_{\text{Wind feedback term}} + \underbrace{C_k|\overrightarrow{V_{\mathrm{wind}}}|(L_v\Delta q' + c_p\Delta T')}_{\text{Air}-\text{sea disequilibrium feedback term}} \tag{294}$$

that are plotted on figure 143. The wind feedback, called WISHE (Wind Induced Surface Heat Exchange) is always positive because of the absence of background winds in the simulation: In that case the amplitude of the wind at the surface is directly related to the intensity of downdrafts, so that when it increases, the surface fluxes increase, increasing the intensity of convection, increasing the intensity of downdrafts to first order, which explains the positive feedback. It is even possible to make the MIT Single column self-aggregate. We rely on the Weak Temperature Gradient (WTG) approximation: In the Tropics, the Coriolis force is low, and it is thus very hard to sustain horizontal temperature gradients because the thermal wind relations would imply a too strong atmospheric flow; the temperature can then be approximated as horizontally homogeneous to a good approximation. We compensate the thermodynamic disbalance between radiative cooling and convective heating by a large-scale ascent/descent in the atmospheric column. The experience is the following: We run the MIT Single Column Model into RCE state with fixed sea surface temperature, and then reinitialize it in WTG mode with temperature fixed above 850hPa. We then introduce a small water vapor perturbation in the system and see if the model significantly drifts from RCE state or not. The system effectively migrates towards a state with mean large-scale ascent or descent for sea surface temperatures above 32°C. On figure 144, we show the time-evolution of the system when the experience was an initial 20% drying of the atmospheric column.

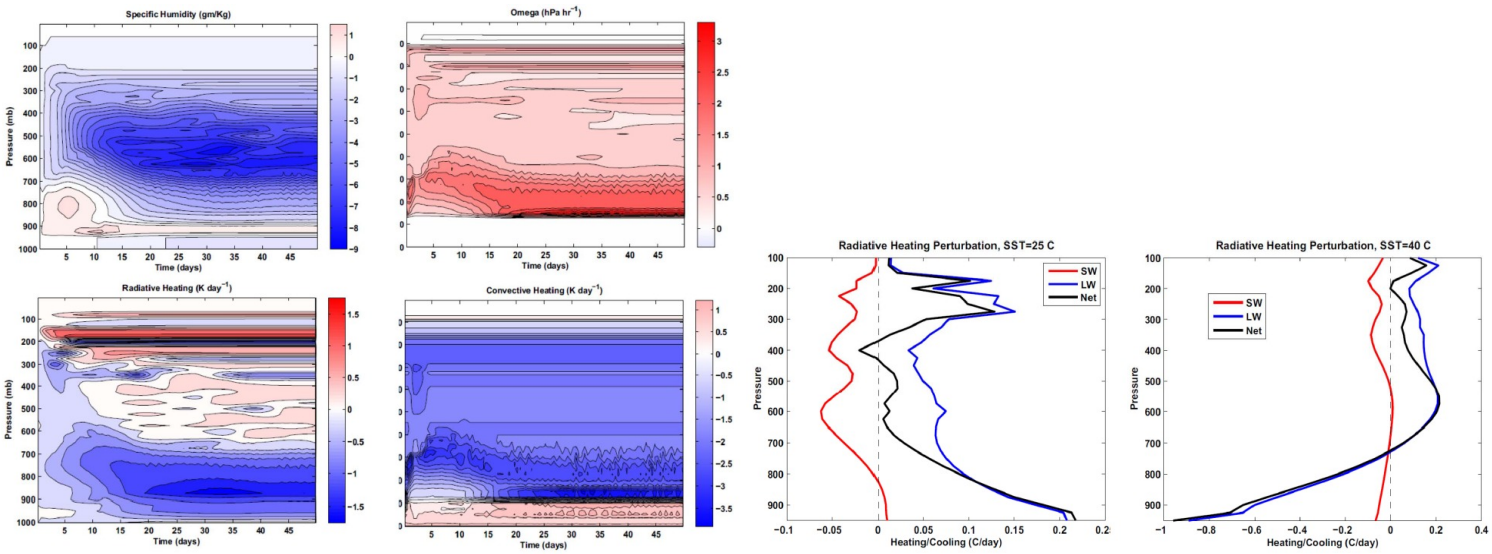

Figure 144: Left: Time-evolution of the specific humidity, vertical velocity, radiative heating and convective profiles of the system when it was initialized in WTG mode with a 20% dry perturbation for a fixed sea surface temperature of 40°C.
Right: Perturbation SW (red), LW (blue) and net (black) radiative heating rates in response to an instantaneous reduction of specific humidity of 20% from the RCE state for fixed surface temperatures of 25°C (left) and 40°C (right).

11.5.3 Radiative-convective instability

For low SSTs, the response to an instant drying is a local response: because the concentration of water vapor is decreased, there is less radiative cooling which corresponds to a LW heating, and there is less absorption which corresponds to a SW cooling. As the role of water vapor as a greenhouse gas is more important than its role as an absorber energetically, the net perturbation is a heating. For warmer SSTs, something very unexpected happens, which is the key of radiative-convective instability: the LW response to a dry perturbation is a net cooling! This is due to the non-local effect of radiation. We can think of the bottom of the atmosphere as so moist at this temperature that it is almost opaque: a dry perturbation will not change that, and so it will not change the local radiative cooling of the lower troposphere. However, the drying of the upper layer means that less of the LW radiation emitted by the lower troposphere will be trapped by the upper troposphere and radiated back (there will be less greenhouse effect, or more radiation escaping to space, explaining the cooling perturbation). If we repeat this experiment for different fixed sea surface temperatures (figure 145), we can see that the transition between the local stable effect and the non-local unstable effect occurs at a sea surface temperature of roughly 32°C (between 30°C and 35°C in this experimental setting).

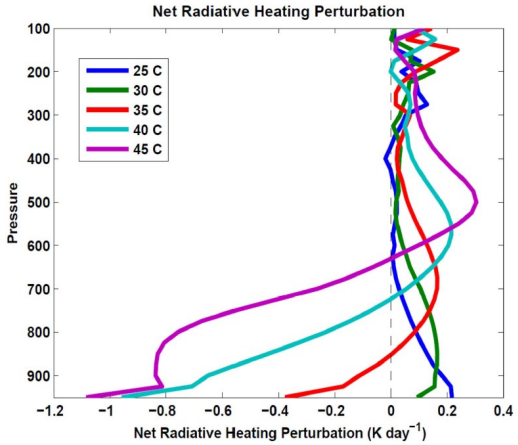

Figure 145: Perturbation net radiative heating rates in response to an instantaneous reduction of specific humidity of 20% from the RCE states for SSTs ranging form 25°C to 40°C

Since this instability relies on the non-local effect of radiation, a simple atmospheric model of this instability requires at least two layers. The temperatures are held constant (WTG approximation), the IR emissivities ε_i depend on the specific humidities q_i, and the convective mass fluxes are calculated from the boundary layer quasi-equilibrium, while the large-scale vertical velocities are computed

from the WTG approximation (to compensate the extra cooling/heating and allowing for the vertical advection of water vapor from layer to layer).

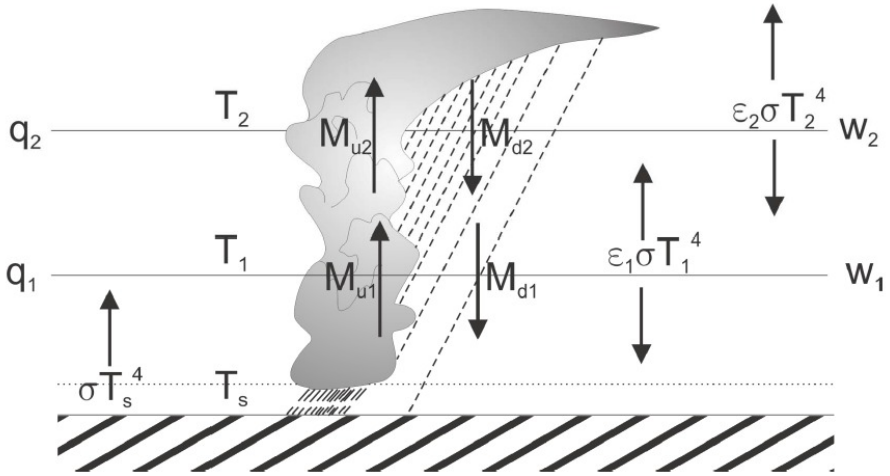

Figure 146: Two-layer model of RCE and radiative-convective instability

The criterion for instability in the case of equal layers can be mathematically written:

$$\underbrace{\overbrace{\frac{\overline{\dot{Q}_1}}{\varepsilon_1}\frac{\partial \varepsilon_1}{\partial q_1}}^{\rightarrow 0 \text{ for opaque lower layer}}}_{(<0)\text{ Local lower layer}} + \underbrace{\overbrace{(1-\epsilon_p)\frac{\overline{\dot{Q}_2}}{\varepsilon_2}\frac{\partial \varepsilon_2}{\partial q_2}}^{\text{Small for large } \epsilon_p}}_{(<0)\text{ Local upper layer}} + \underbrace{\overbrace{\epsilon_p \frac{S_2}{S_1}\frac{\sigma \varepsilon_1 T_2^4}{\rho}\frac{\partial \varepsilon_2}{\partial q_2}}^{\text{Can be large if upper layer not opaque}}}_{(>0)\text{ Non-local term}} > 0 \tag{295}$$

where $\overline{\dot{Q}_i}$ are the radiative heating/cooling in RCE, S_i the dry static stabilities and ϵ_p the precipitation efficiency (the proportion of the updrafts that falls out as rain). From equation 295, we can see that RCE becomes linearly unstable when the IR opacity of the lower troposphere becomes sufficiently large, and when precipitation efficiency is large.

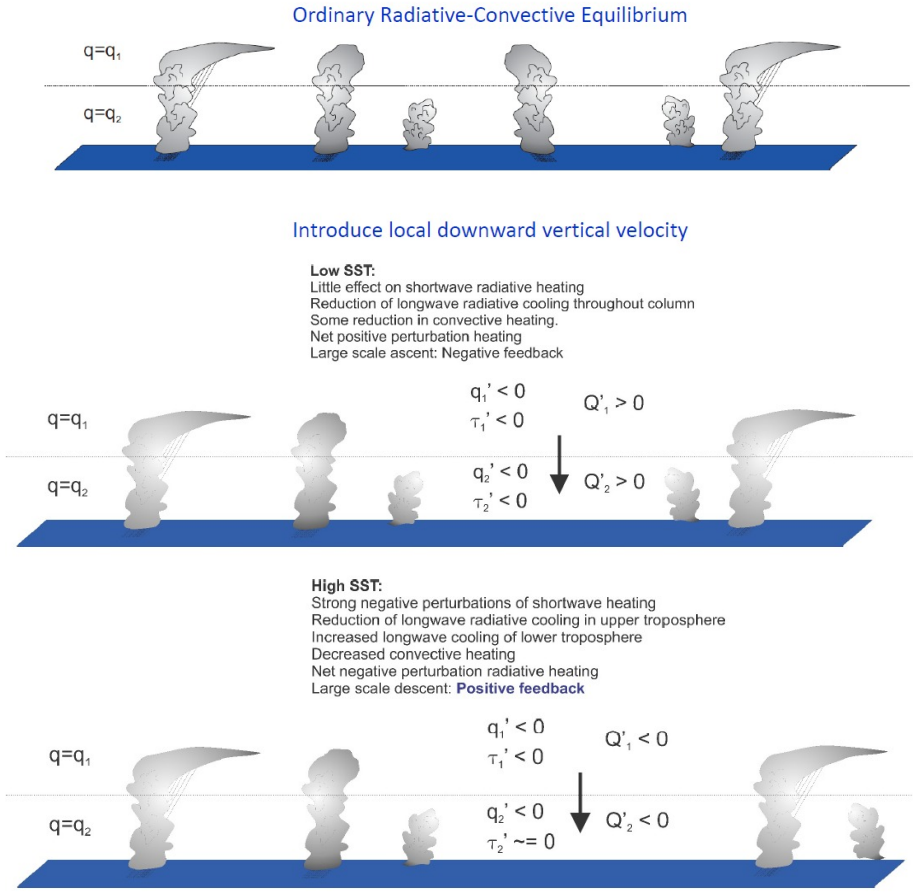

Figure 147: Physical interpretation of radiative convective instability

Once the cluster forms, it is strongly maintained by the intense negative outgoing LW anomaly associated with the central dense cloud overcast. However, cloud feedbacks are not important when the instability is developing, and thus they are not important in instigating the instability. This leads to a strong hysteresis in the radiative-convective system. From the behavior of radiative-convective instability, it seems that there is a critical SST above which the system is always unstable. Under that critical SST, the system will be unstable to large enough finite amplitude perturbation.

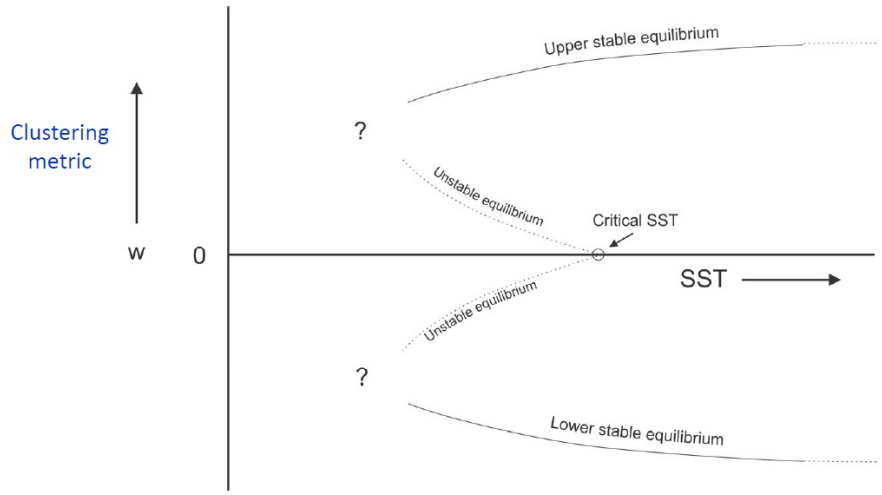

Figure 148: Hypothesized subcritical bifurcation. The vertical axis is a clustering metric, eg large-scale vertical velocity.

11.5.4 Climatic consequences of self-aggregation

Because the dry part of this instability is larger than the moist part, self-aggregation is observed to dry out the atmosphere, in simulations and in nature.

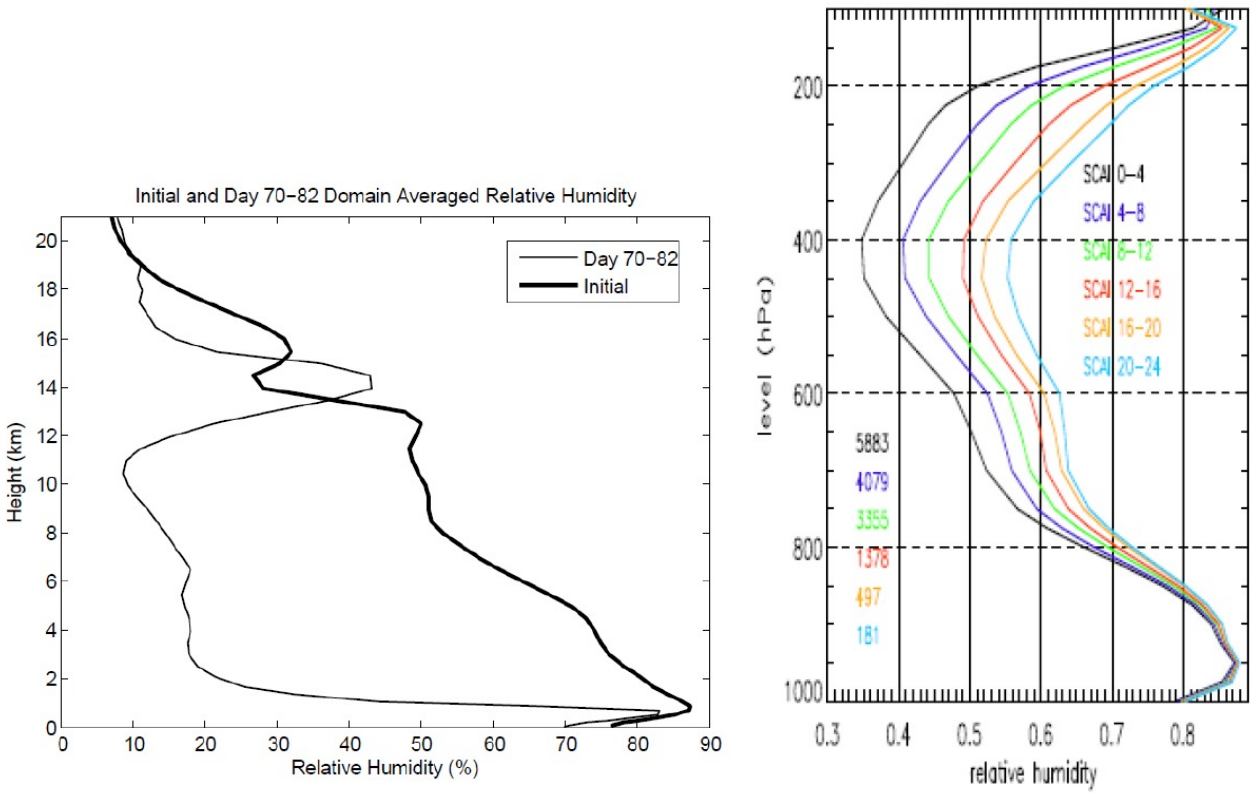

Figure 149: Left: Drying of the domain averaged humidity through self-aggregation in a cloud resolving model. Right: Variations of tropical relative humidity profiles in nature with a simple convective aggregation index.

This leads to a possible hypothesis on how self-aggregation drives the climatic system to a critical humidity:

1. At high temperature, convection self-aggregates.
2. The horizontally averaged humidity then drops dramatically.
3. The reduction of the greenhouse effect then cools the system.
4. The convection thus disaggregates.
5. Without aggregated convection, the humidity increases and the system warms.

If the climatic system followed that cycle, it could be qualified of self-organized. The self-organized criticality theory means that the sea surface temperature would be regulated by self-aggregation, implying power-law distributions for quantities such as the convective cluster sizes (more precise assumptions are required for this theory to apply rigorously).

11.5.5 Self-aggregation on a f-plane and cyclogenesis

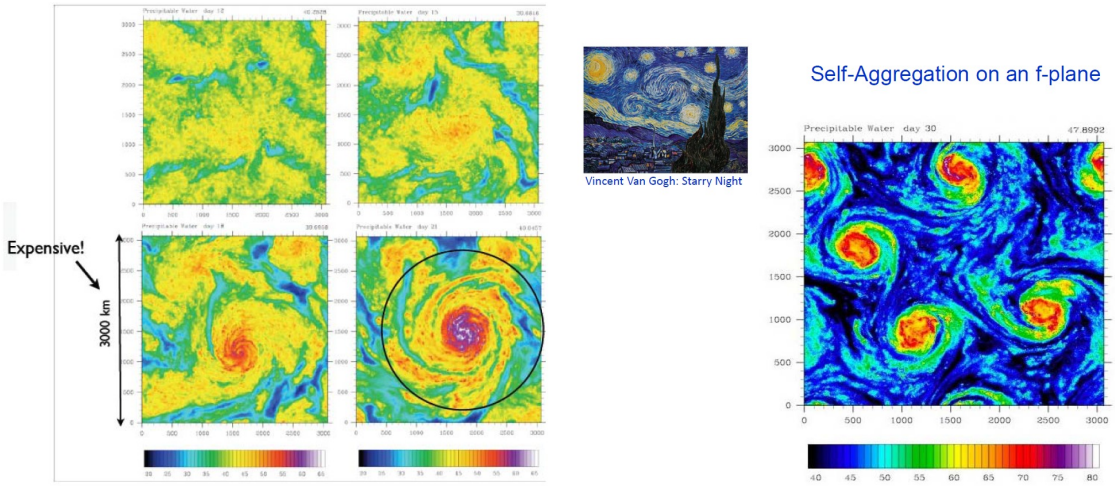

Figure 150: Cloud resolving simulations of self-aggregation on a f-plane

CRM simulations of self-aggregation on a f-plane make vortices form spontaneously (figure 150), and the physics of self-aggregation on a f-plane are believed to be very similar to those of cyclogenesis. If we approximate the energy production of a cyclone as a Carnot cycle, following the left of figure 151, we can obtain the surface turbulent flux and thus the maximal wind amplitude (through bulk formulae similar to 265) as a function of the surface temperature T_s and the outflow temperature T_o:

$$\underbrace{|\overrightarrow{V_{\text{wind,max}}}|^2}_{\text{Square potential intensity}} \approx \underbrace{\frac{C_k}{C_D}}_{\text{Ratio exc coef enthalpy momentum}} \underbrace{\frac{T_s - T_o}{T_o}}_{\approx\text{Carnot efficiency}} \underbrace{(k_0^* - k)}_{\text{Air-sea enthalpy deseq}} \tag{296}$$

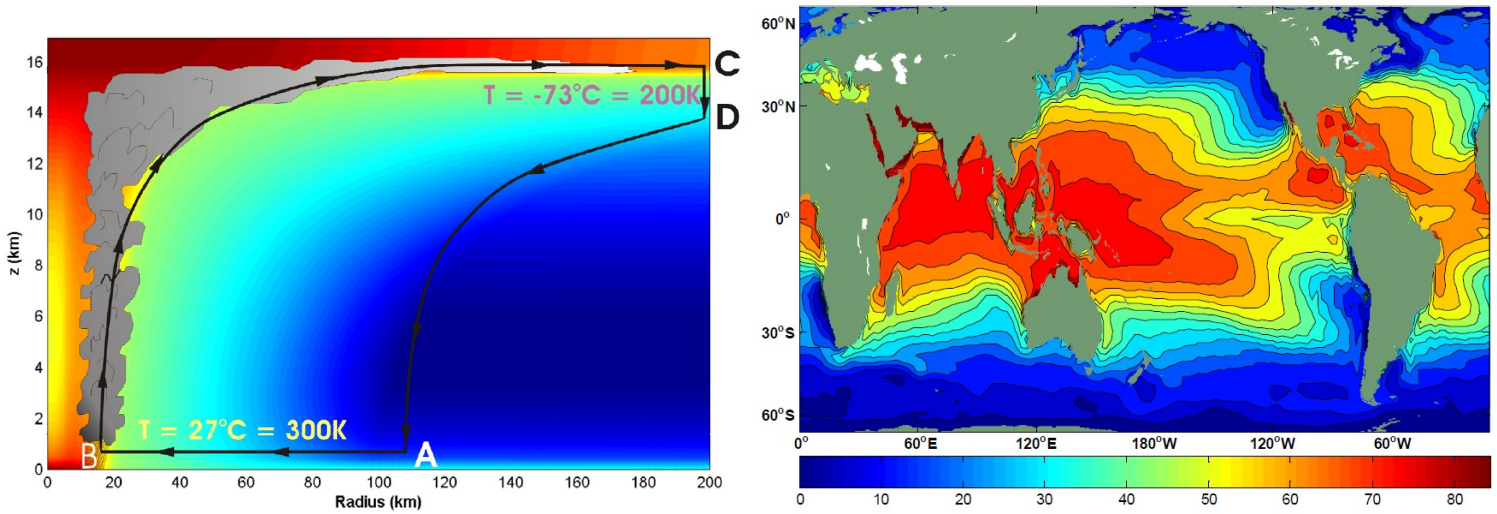

Figure 151: Carnot cycle for the energy production of a cyclone (left) and world map of the annual maximum potential intensity $|\overrightarrow{V_{\text{wind,max}}}|$ (right)

Because we have introduced an external frequency, the Coriolis parameter f, the cluster size (here the vortices sizes) are not self-similar anymore, and scale like the external parameter of the system; the radius of maximal winds scales like $|\overrightarrow{V_{\text{wind,max}}}|f^{-1}$. Since the distance between storm centers scales like the moist deformation radius $f^{-1}\sqrt{L_v q^*}$, the number density n of storms scales like $f^2(L_v q^*)^{-1}$. Furthermore, it is also possible to obtain a scaling for the potential intensity of the cyclones $|\overrightarrow{V_{\text{wind,max}}}|$ from:

- The modified Carnot thermodynamic efficiency $\epsilon_C = \frac{T_s - T_o}{T_o}$.
- The net TOA upward radiative flux $\mathcal{F}_{\text{TOA}}$.

- The net surface radiative flux $\mathcal{F}_s$.
- The momentum exchange coefficient C_D.

$$|\overrightarrow{V_{\text{wind,max}}}|^3 \sim \frac{\epsilon_C(\mathcal{F}_{\text{TOA}} - \mathcal{F}_s)}{C_D} \tag{297}$$

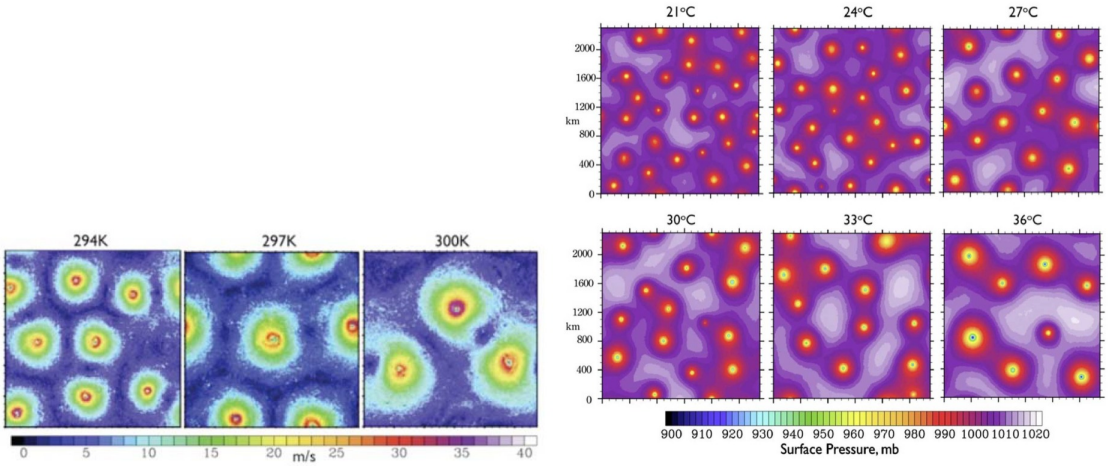

Figure 152: Snapshots of near-surface wind (in m.s^{-1}, left) and pressure (in mbar, right) in RCE for three different values of the SST

12 Introduction to remote sensing

12.1 Exoplanet atmospheres

12.1.1 Introduction

On the left of figure 153, we can see the impressive diversity among the few dozens of exoplanets, which atmospheres are observable in a broad sense.

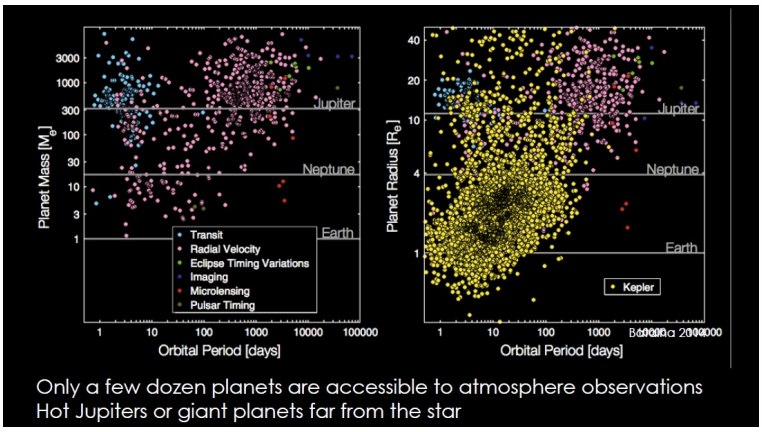

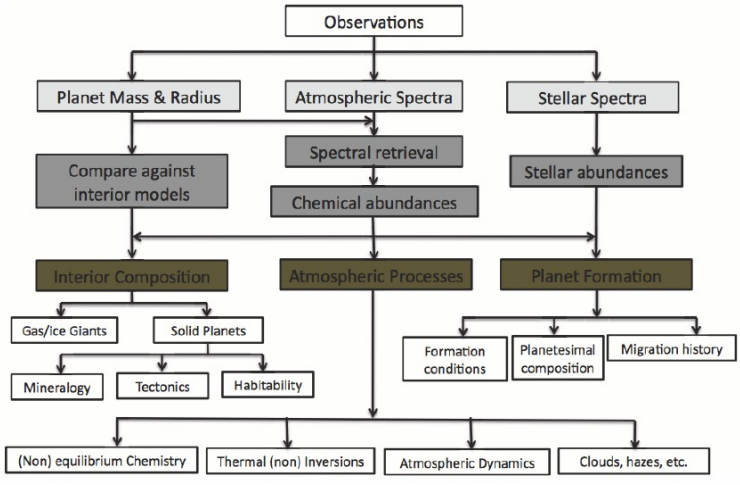

Figure 153: Accessible exoplanet atmospheres in different parameters spaces (left) and hierarchy of analysis to go from observations to exoplanetary processes (right, Madhusudan 2014)

"Observing" an exoplanet's atmosphere generally means inferring atmospheric properties from how the atmosphere alters the different electromagnetic fluxes passing through it. More generally, the graph on the right of figure 153 shows how specific properties can be deduced from observing exoplanets; everything below the gray blocks is very uncertain given the current precision of astronomical measurements. The common tools/approximations used to understand these processes include the radiative transfer equation 9, global conservation of energy (cf 2), hydrostatic equilibrium 31, the ideal gas law 39 and photo-chemical simplified equillibria. From these tools, we want to approximate the profiles of the radiative fluxes, the temperature, the pressure, the density and the chemical composition

of exoplanetary atmospheres. However, there are many sources of uncertainties, for example clouds. Strong variations in chemical compositions and in temperatures generate many different types of clouds, which can be either gaseous or liquid, as we can see on figure 154. Common unknowns about clouds include the aerosol size distribution, composition, and shape, the fraction of condensed gas, the vertical extent of the cloud...

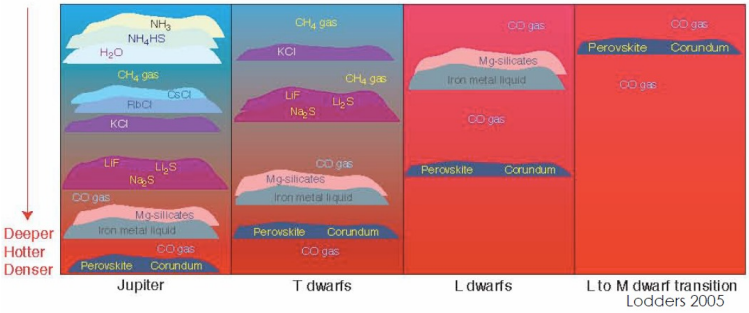

Figure 154: Different types of clouds on different planet's types

There are also large chemical, radiative and dynamical uncertainties as the only known inputs are the surface gravity and the radiation coming from the star.

12.1.2 Exoplanet atmosphere observation methods

Direct imaging Let's consider the HR8799 solar system, which is a very expanded solar system because some of its planets are very far from its star (it is assumed that its formation resulted from the instability of a disk).

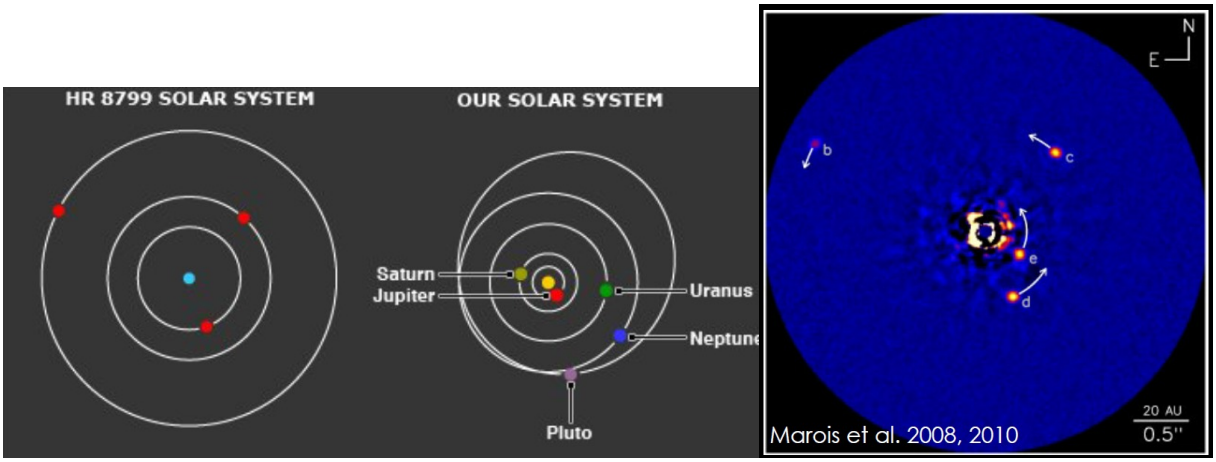

Figure 155: HR8799 solar system compared to the Solar system (left) and observations of it at near-IR wavelengths (right)

To study it, the starlight is blocked out in order to see the planets directly. The result is shown on figure 156: although it is really hard to obtain the molecular absorption from the spectrum, some thin rotational lines are well-modeled by the knowledge of the planet's temperature and the assumption that Carbon and Oxygen are major radiative elements of its atmosphere.

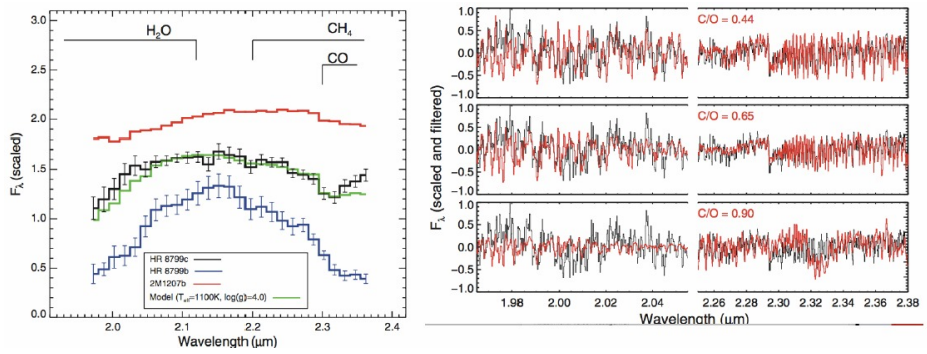

Figure 156: Monochromatic flux as a function of wavelength obtained from direct imaging: on the left $\frac{\lambda}{\Delta\lambda} \sim 50$ whereas $\frac{\lambda}{\Delta\lambda} \sim 4000$ on the right

High spectral resolution cross-correlation When the planets orbit very close to their stars (for instance some planets can reach velocities as high as 100km.s^{-1}), their radiation will be Doppler-shifted (144 shows why the Doppler shift in frequency is positive when the planet is "approaching the satellite" - blue shift - and negative when the planet is "moving away" from the satellite - red shift -).

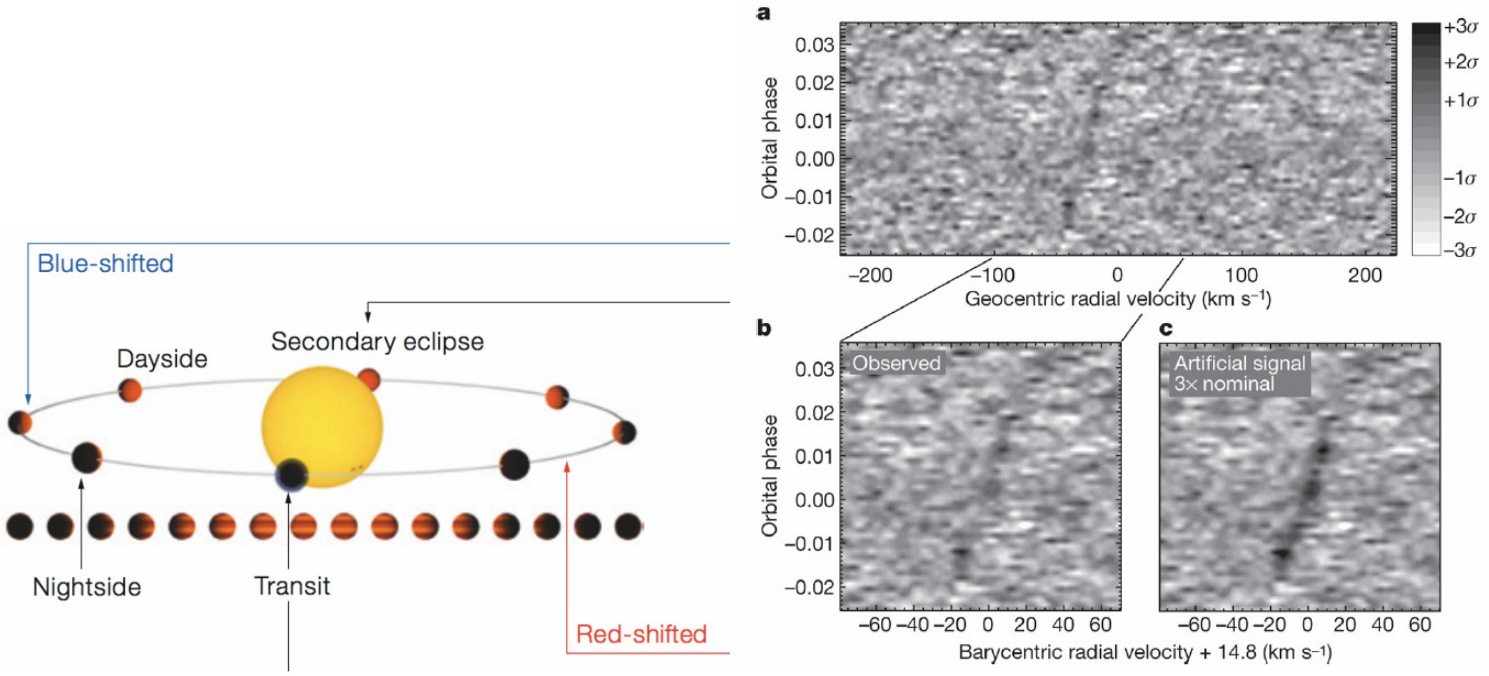

Figure 157: Influence of the orbit of a planet on the detected radiation (left) and resulting CO signal in black (right)

From analyzing the Doppler shifts of the different frequencies of the radiation received from the exoplanet as a function of its orbital velocity, it is possible to detect the main gas composing this atmosphere (eg CO and H_2O).

Transits Because the atmospheric opacity depends on the radiation's wavelength, the atmosphere of a planet will be visible or not from a satellite depending on its orbital position, as we can see on figure 158.

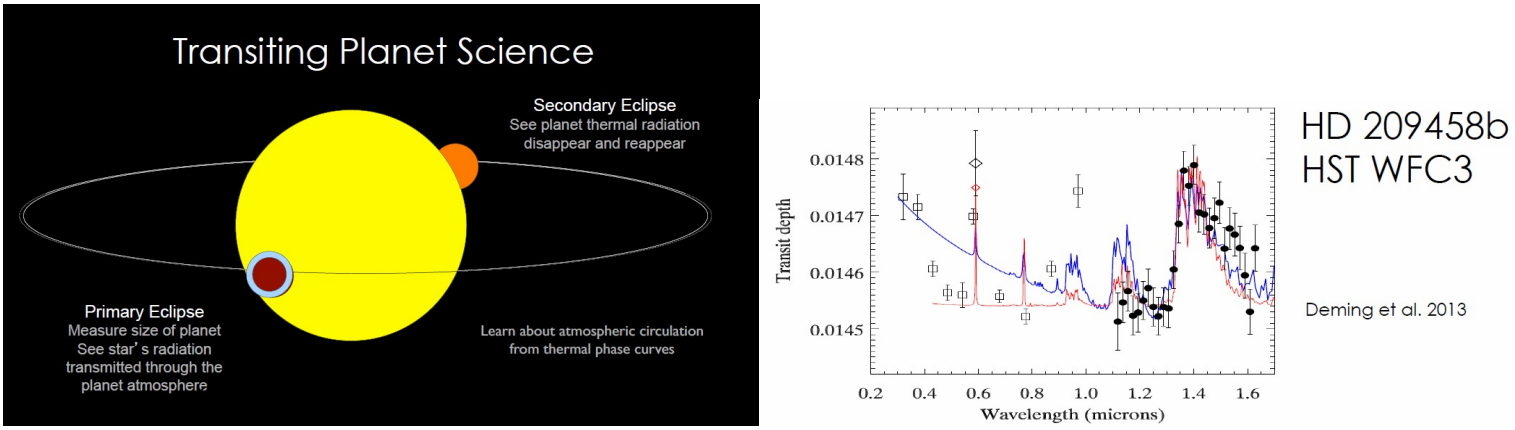

Figure 158: Influence of the planet's orbital position on its thermal emission (left) and resulting spectrum [black dots] compared to an isothermal model [red line] (right)

The order of magnitude of the signal can be obtained by comparing the surface of the atmosphere (approximately obtained from the radius r_p of the planet and the scale height H of its atmosphere) to the surface of the star of radius r_{star}:

$$\frac{\pi(r_p + 5H)^2 - \pi r_p^2}{\pi r_{\text{star}}^2} \approx \frac{10 r_p H}{r_{\text{star}}^2} \sim 10^{-4}$$

However, since planets such as gas giants contain Hydrogen and Water Vapor, the presence of clouds causes huge uncertainties in this method as discussed in 38 and 39.

12.1.3 Earth as an exoplanet

We've already discussed how Earth's spectrum would look like if we would observe the Earth as an exoplanet (figure 35).

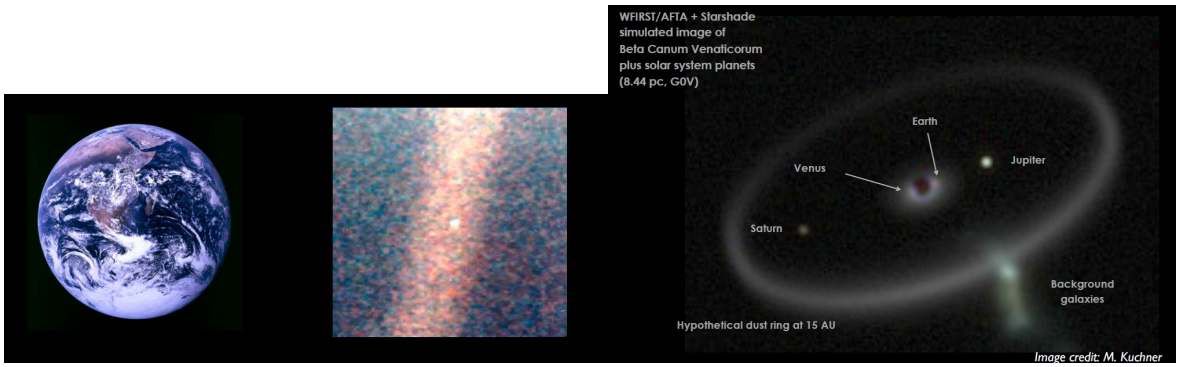

Figure 159: Galileo's view of Earth (left), Earth's star-shade in the Solar system (zoom on Earth in the middle, complete view of the Solar system on the right)

It is possible to "detect signs of life" on Earth by noticing the effect of vegetation on the emission spectrum. On figure , we can see that the chlorophyll bump is detectable, but minor compared to the red edge, which is the strong absorbing feature of the vegetation in the IR.

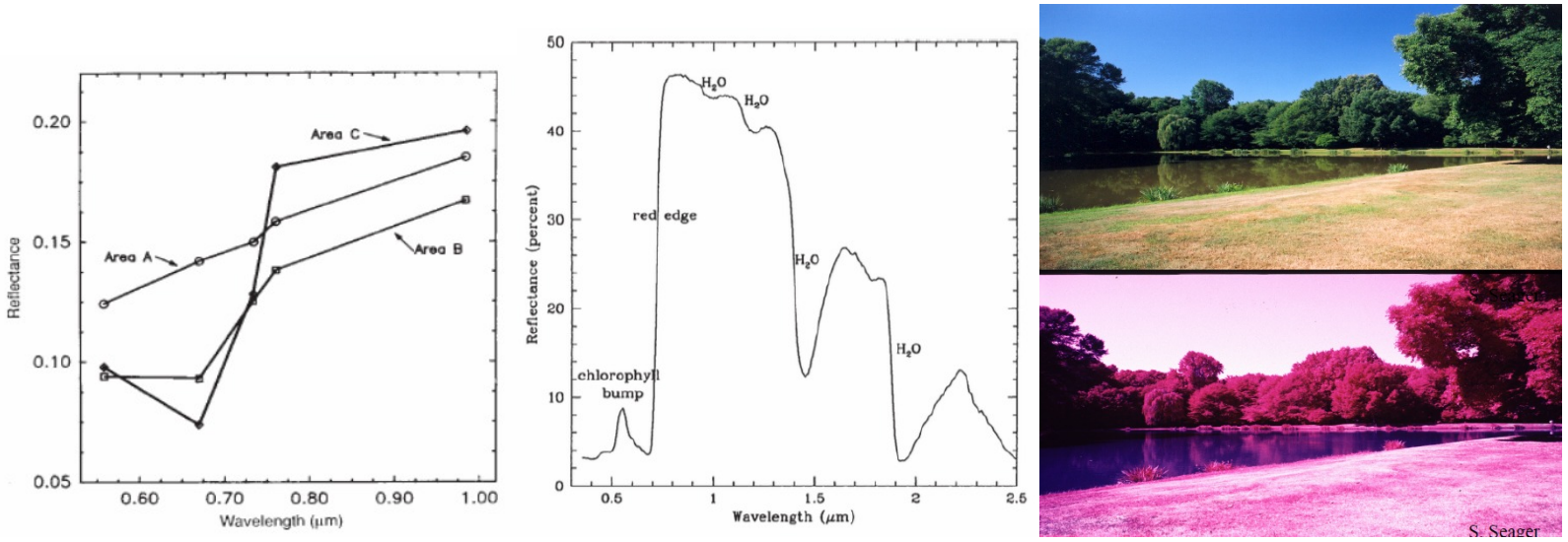

Figure 160: Left: Spectra for a gently sloping spectrum representative of rock or soil (a), and intermediate spectrum (b) the typical spectrum (c) is believed to be associated with photosynthetic pigments
Middle: Earth's annotated thermal emission spectrum
Right: Vegetation red edge

If Earth is observed as an exoplanet through measuring the something close to the disk-integrated spectra or using the Earth shine (scattered line reflected from the Moon), we obtain the spectra shown on figure 161.

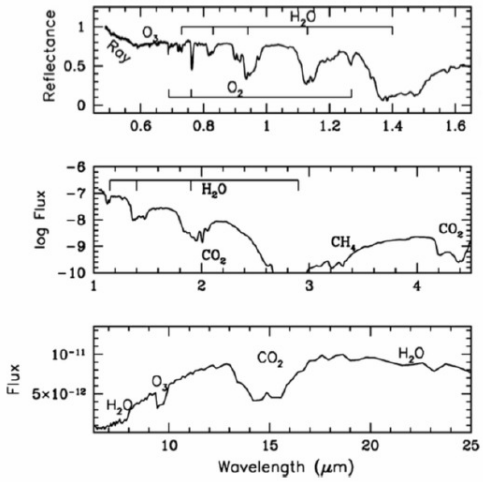

Figure 161: Spectra from Earth shine measurements (top) the NASA's Extrasolar Planet Observation (middle), and the Mars Global Surveyor (bottom)

From Earth brightness, it is possible to estimate the land-sea distribution (left of figure 162) as land has a much higher albedo than the very dark oceans (in a radiative sense). For example, the Sahara has a very high albedo, which makes it a significant pattern of Earth's outgoing radiation. It is also possible to reconstruct the diurnal cycle and measure Earth's rotation period as the ocean currents and continents result in relatively stable averaged global cloud patterns (right of figure 162).

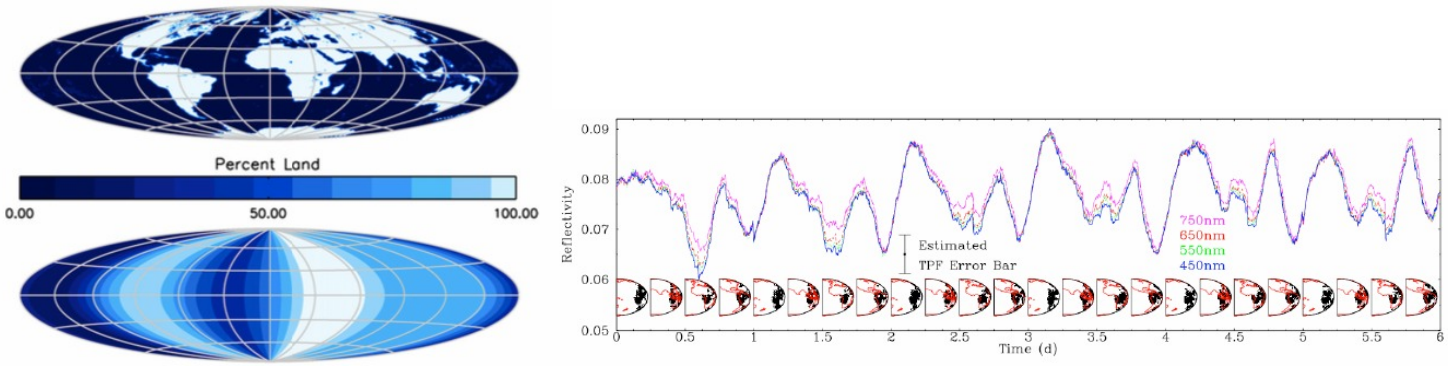

Figure 162: Aitoff projection showing the land distribution on Earth in a cloud-free map (top left) and the latitudinally-averaged distribution of land from the telescope EPOXI's observations (bottom left) and diurnal light curves from the Earth's reflectivity as a function of time (right)

As we have seen in 33, the difference between the reflected and transmitted spectra can also give crucial information about the Earth as an exoplanet. To summarize, from observing Earth as an exoplanet, we can obtain information about the chemical composition of its atmosphere (Water vapor, oxygen, ozone, and carbon dioxide), detect its vegetation, observe the presence of continents and darker spots (which correspond to oceans, but oceans are unlikely to be detectable form specular reflection), detect fixed large-scale cloud patterns which give the Earth's rotation rate.

12.2 Temperature sounding

12.2.1 Introduction

We remember the concept of optical depth (2.4). Because of the difference of absorption for each sounded wavelength, we will always preferentially "see" a zone looking from above the atmosphere. If the atmosphere is transparent, this zone will be the surface of the Earth; if the atmosphere is perfectly opaque it will be the top of the atmosphere. For intermediate cases, such as the spectrum of CO_2 shown on figure 163, this zone will be at different pressure levels in the atmosphere.

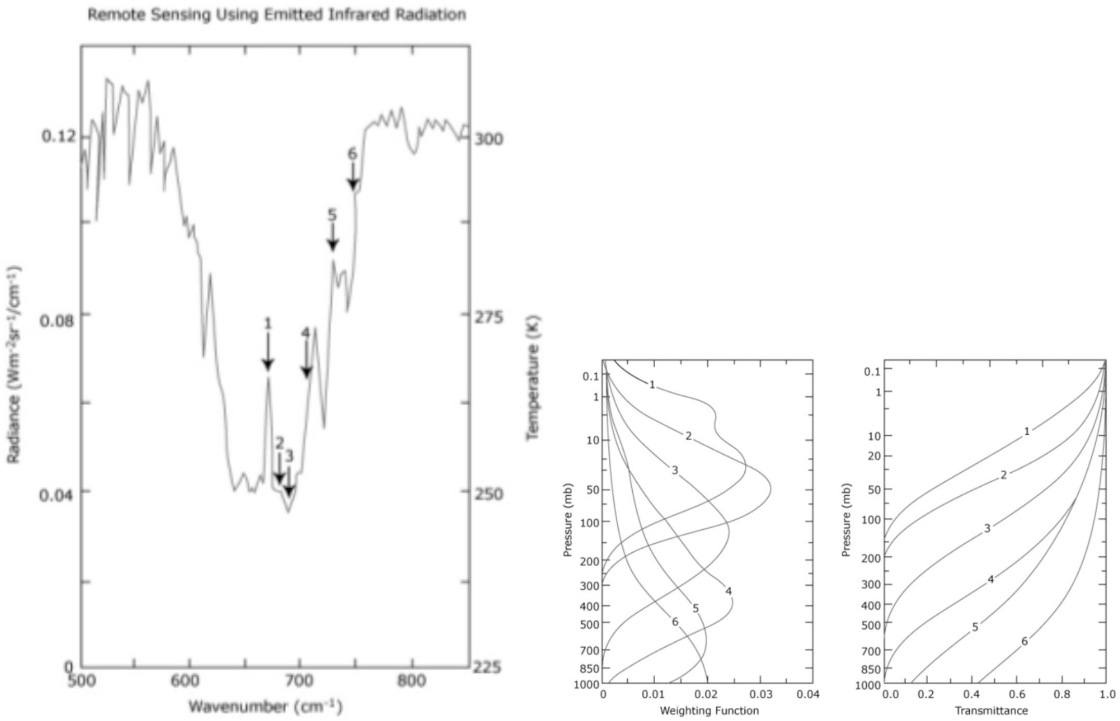

Figure 163: Left: Outgoing radiance in terms of blackbody temperature in the vicinity of 15μm CO_2 band observed by the IRIS on Nimbus 4. The arrows denote the spectral regions sampled by the VTPR instrument.
Right: The weighting function and transmittance of each region sampled by the VTPR instrument.

In principle, this zone would be marked by an ideal delta weighting function. In practice, the weighting function has a finite width, and must be constructed using known line-by-line absorption data and a program for transmittance calculations. Note that there is a slight temperature dependence of the weighting function. One can select spectral bands to achieve an array of weighting functions that span the atmosphere and are distributed in a reasonable manner.

12.2.2 Computing the weighting functions

From equation 238, we can write the intensity at the top of the atmosphere as a function of the transmittance T_ν:

$$\underbrace{I(0,\mu)}_{\text{Upwelling radiance}} = \underbrace{B[T(\tau_*)]T_\nu(\frac{\tau_*}{\mu})}_{\text{Radiance surface}} + \underbrace{\int_{\tau_*}^{0} B[T(\tau_*)]\frac{\partial T_\nu(\tau')}{\partial \tau'}d\tau'}_{\text{Absorption by atmosphere}} \tag{298}$$

In remote sensing, the radiance equation 298 is usually written in terms of altitude or pressure as the independent variable. Using the definition 11 of optical depth, the definition 43 for the mixing ratio of any gas and the hydrostatic balance 31, 298 becomes:

$$\underbrace{I(0,\mu)}_{\text{Upwelling radiance}} = \underbrace{B(T_s)T_\nu(p_s)}_{\text{Radiance surface}} + \underbrace{\int_{p_s}^{0} B_\nu[T(p)]\frac{\partial T_\nu(p)}{\partial p}dp}_{\text{Absorption by atmosphere}} \tag{299}$$

where the subscript (s) refers to the surface. The effective spectral interval for the instrument response's function is usually small enough that the variation of the Planck function is insignificant. We can thus integrate and replace the quantities in 299 by averaged quantities over small wavenumbers ranges. The upwelling radiance is a product of the Planck function $B(T)$, the spectral transmittance T_ν and the weighting function $\frac{\partial T_\nu}{\partial p}$. The temperature T is encoded in the Planck function while the density profiles of the relevant absorbing gases are involved in the transmittance (however recall that the absorption coefficient T_ν depends weakly on the temperature T. Extracting the relevant information about the atmospheric state and composition from observed IR radiances is the essence of remote sensing from space. In practice, to determine atmospheric temperatures from measurements of thermal emission, the source of emission must be a relatively abundant gas of known and uniform distribution, otherwise uncertainties will make the determination of temperature from the measurement ambiguous. In the Earth's atmosphere, Oxygen O_2 and Carbon Dioxide CO_2 are greenhouse gases that can be considered to have a uniform abundance below 100km. They also show emission bands in spectral bands that are convenient for measurement. However, recall that low concentration of a gas does not necessarily mean weak spectroscopic features, for example if the corresponding molecule has strong absorption cross-sections. In general, the weighting function $\frac{\partial T_\nu}{\partial p}$ can be used in two ways:

1. Using a well-mixed gas with known concentration, derive the temperature vs pressure $T(p)$ profile.
2. Using the $T(p)$ profile, derive the concentration of a gas (eg H_2O).

12.2.3 GOES weighting function

http://cimss.ssec.wisc.edu/goes/wf/viewwf.php?day=T0&5me=00&sat=GE&band=ir

- *Compare weighting functions from:*

1. *High altitude(s) to low altitude(s).*
2. *Cloudy scenes to clear scenes.*
3. *Dry scenes to wet scenes.*
4. *Pay attention to where the different bands peak during these situations (this may tell you a lot about the amount of water vapor in the atmosphere or where vertically it appears).*

- *Which molecules are absorbing in the following bands?*

1. *Sounder Bands: 10 (7.4 μm) 11 (7.0 μm) 12 (6.5 μm).*
2. *Imager Bands: 2 (3.9μm) 3 (6.5 μm) 4 (11.0 μm) 6 (13.3 μm).*

12.2.4 Retrieval theory

Example 1: Surface temperature determination In the window region where the atmospheric effect is at a minimum, the upwelling radiance at the top of the atmosphere must be closely associated with emission from the surface. Defining a mean temperature T_a for the atmosphere, the retrieval equation 299 can be approximately integrated to yield:

$$I_{\overline{\nu}}(0,\mu) \approx B(T_s)T_{\overline{\nu}}(p_s) + B(T_a)[1 - T_{\overline{\nu}}(p_s)] \tag{300}$$

The goal is to solve for the surface temperature T_s, which we do by using a "split-window" technique, using observations at two channels $(\overline{\nu},1)$ $(\overline{\nu},2)$ to eliminate the term involving the atmospheric temperature T_a; following the approximation 300:

$$I_i = B_i(T_{bi}) = B_i(T_s)T_{\overline{\nu},i} + B_i(T_a)[1 - T_{\overline{\nu},i}] \text{ for } i \in \{1,2\} \tag{301}$$

where T_{bi} are the brightness temperatures for the frequency ranges $(\overline{\nu},i)$. T_a generally varies by less than 1K in the window region $10.5\mu\text{m} - 12.5\mu\text{m}$, in which the surface emissivity's variability is insignificant, which justifies the use of the "split-window" technique. Taylor-expanding the Planck functions B_i to first order about T_a and eliminating the temperature dependence yields:

$$B_2(T) = B_2(T_a) + \frac{\partial B_2}{\partial T}(\frac{\partial B_1}{\partial T})^{-1}[B_1(T) - B_1(T_a)] + \mathrm{O}[(\mathrm{T} - \mathrm{T_a})^2] \tag{302}$$

Combining 302 applied for $T = \{T_s, T_{b2}\}$ with 301 leads to:

$$B_1(T_{b2}) \approx B_1(T_s)T_{\overline{\nu},2} + B_1(T_a)(1 - T_{\overline{\nu},2}) \;\Rightarrow\; B_1(T_s) = B_1(T_{b1}) + \eta[B_1(T_{b1}) - B_1(T_{b2})] \tag{303}$$

In this window region, the atmospheric transmittance is primarily produced by the continuous absorption of water vapor and can be approximated as $T_{\overline{\nu}} \approx \exp(-\sigma_{\overline{\nu}}u) \approx 1 - \sigma_{\overline{\nu}}u$. We can thus write:

$$\eta \stackrel{\text{def}}{=} \frac{1 - T_{\overline{\nu},1}}{T_{\overline{\nu},1} - T_{\overline{\nu},2}} \approx \frac{\sigma_{\overline{\nu},1}}{\sigma_{\overline{\nu},2} - \sigma_{\overline{\nu},1}} \tag{304}$$

where $\sigma_{\overline{\nu},i}$ are the mass absorption coefficients. In practice, the Planck functions in equation 303 are replaced by the brightness temperatures, since a local linear relation can be established between the two in a small spectral temperature:

$$T_s \approx T_{b1} + \eta(T_{b1} - T_{b2}) \tag{305}$$

Sea surface temperatures have routinely be inferred from satellites using two narrow spectral band channels (such as the NOAA AVHRR 10.9μm and 12μm channels. The SST may be expressed by a general form of regression as:

$$\mathrm{SST} = aT_{b1} + b(T_{b1} - T_{b2}) - c \tag{306}$$

where (a,b,c) are empirical coefficients derived from in situ observations obtained from drifting buoys.

Example 2: Inference of temperature profiles The goal is to solve for the Planck function $B[T(p)]$ given a set of observed radiances corresponding to different wavenumbers ν and the "known" weighting functions $\frac{\partial T_\nu}{\partial p}$.

- We start from the main retrieval equation 299.
- We assume that the transmittance at the ground is zero: $T_{\overline{\nu}}(p_s) \approx 0$.
- We can eliminate the Planck dependence on wavenumber by considering it is smooth and in a small spectral interval can be approximated in a linear form:
$$B_{\overline{\nu}}(T) = c_{\overline{\nu_0}}B_{\overline{\nu_0}}(T) + d_{\overline{\nu}} \tag{307}$$
where the 0 subscript refers to a fixed reference wavenumber and c and d are fitting coefficients.

We obtain a Fredholm equation equation of the first kind with $K(p)$ the weighting function and $f(p)$ the function to be recovered from a set of g:

$$g = \int_{p_s}^{0} f(p)K(p)dp \tag{308}$$

where we have defined:

$$g \stackrel{\text{def}}{=} \frac{I_{\overline{\nu}} - d_{\overline{\nu}}}{c_{\overline{\nu}}} \tag{309}$$

$$f(p) \stackrel{\text{def}}{=} B_{\overline{\nu_0}}[T(p)] \tag{310}$$

$$K(p) \stackrel{\text{def}}{=} \frac{\partial T_{\overline{\nu}}(p)}{\partial p} \tag{311}$$

For this equation to work in order to determine atmospheric temperatures from measurements for thermal emission, the source of emission must be a relatively abundant gas of known uniform distribution. Otherwise, its uncertainty will make the determination of temperatures from the measurements ambiguous.

Example 3: Non-linear temperature retrieval based on iteration Note that:

- The retrieval procedures we have discussed so far are linear and empirical.
- The problem we face is that the radiative transfer equation may not always have a solution.
- Atmospheric gases for retrieval may be inhomogeneously distributed.
- The measurements and the calculated transmission contain experimental uncertainties.
- We have approximated integrals by sums, again introducing an error.

We will now outline a non-linear approach. We start by measuring the intensity at the top of the atmosphere given by equation 299 in different channels i and switch the independent variable to $\ln p$:

$$I_{i,\text{obs}} = B_i(T_s)T_{\overline{\nu},i,\text{obs}}(p_s) + \int_{\ln(p_s)}^{-\infty} B_i[T(p)]\frac{\partial T_{\overline{\nu},i,\text{obs}}(p)}{\partial \ln p}d\ln p \approx B_i(T_s)T_{\overline{\nu},i,\text{obs}}(p_s) + B_i[T(p_i)][\frac{\partial T_{\overline{\nu},i,\text{obs}}(p)}{\partial \ln p}]_{p_i}\Delta_i \ln p \tag{312}$$

where we have approximated the integral using the mean value theorem at the pressure level where the maximum of the weighting function is located for each channel $(\overline{\nu}, i)$. If the guessed temperature profile is $T_{\text{guessed}}(p)$, the expected radiance is:

$$I_{i,\text{guessed}} \approx B_i(T_s)T_{\overline{\nu},i,\text{guessed}}(p_s) + B_i[T_{\text{guessed}}(p_i)][\frac{\partial T_{\overline{\nu},i,\text{guessed}}(p)}{\partial \ln p}]_{p_i}\Delta_i \ln p \tag{313}$$

Dividing equation 312 by equation 313, we obtain:

$$\frac{I_{i,\text{obs}} - B_i(T_s)T_{\overline{\nu},i,\text{obs}}(p_s)}{I_{i,\text{guessed}} - B_i(T_s)T_{\overline{\nu},i,\text{guessed}}} \approx \frac{I_{i,\text{obs}}}{I_{i,\text{guessed}}} \approx \frac{B_i[T(p_i)]}{B_i[T_{\text{guessed}}(p_i)]} \tag{314}$$

where we have used frequencies $(\overline{\nu}, i)$ where the surface contribution to the upwelling radiance is small. Approach 314 was pioneered by M. Chahine and is referred to as the relaxation equation; a number of variants of this procedure have been developed and are used operationally today. The iteration works as follows:

1. Make an initial guess for the temperature profile: $T^{(0)}(p_i) = 0$.
2. Substitute in equation 312, using an accurate quadrature formula to compute the expected upwelling radiance $I_i^{(n)}$ for each sounding channel.
3. Compare the computed radiance values $I_i^{(n)}$ with the measured data $I_{i,\text{obs}}$. If the residuals:

$$R_i^{(n)} \overset{\text{def}}{=} \frac{|I_{i,\text{obs}} - I_i^{(n)}|}{I_{i,\text{obs}}} \tag{315}$$

   are less than a tolerance threshold, such as 10^{-4}, then $T^{(n)}(p)$ is a solution. Otherwise, the iteration must be continued.
4. Apply the relaxation equation 314 as many times as the number of spectral channels to generate a new guess $T^{(n+1)}(p)$ for the temperature profile. We go from $T^{(n)}(p)$ to $T^{(n+1)}(p)$ by inverting the Planck function 12:

$$T^{(n+1)}(p_i) = \frac{hc}{k\ln\{1 - [1 - \exp(\frac{hc\nu_i}{kT^{(n)}(p_i)})]\frac{I_i^{(n)}}{I_{i,\text{obs}}}\}} \tag{316}$$

5. Carry out the interpolation between the temperature values at each pressure level p_i to obtain the desired profile.
6. Finally, go back to step 2 and repeat until the residuals 315 are less than the preset criterion.

12.3 Remote sensing

12.3.1 Introduction

The interaction of radiation with a medium M leaves a signal S that depends on the composition and the thermal structure of the medium that we want to retrieve. We can symbolically write this interaction using a non-linear function f:

$$S = f(M) \overset{\text{goal}}{\Rightarrow} M = f^{-1}(M) \tag{317}$$

f relates to absorption (depends on composition), emission (depends on composition and temperature) and scattering & polarization (depend on the size, the shape and the orientations of the particulates). Furthermore, the computation of f^{-1} presents mathematical problems (f might not be an injective function, ie several physical processes have the same radiative signature; the inverse method might not be stable...). There are two types of remote sensing:

1. **Active:** Use of a radiation source generated by artificial means (eg lasers used for LIDAR or microwaves used for RADAR); a beam of radiation is sent out and a backscattered signal is measured.

2. **Passive:** Use of natural radiation sources, such as the sun or the emission of the surface and the atmosphere of the Earth. Wavelengths from UV to IR are accessible for scattered radiation (for example, the thermal emission by the Earth atmospheric system is available for a wavelength of about 4μm to the far IR and microwave region).

Figure 164: The Earth Observing System is a coordinated series of polar-orbiting and low inclination satellites for long-term global observations of the land, surface, biosphere, solid Earth, atmospheres and oceans.

12.3.2 Vegetation remote sensing

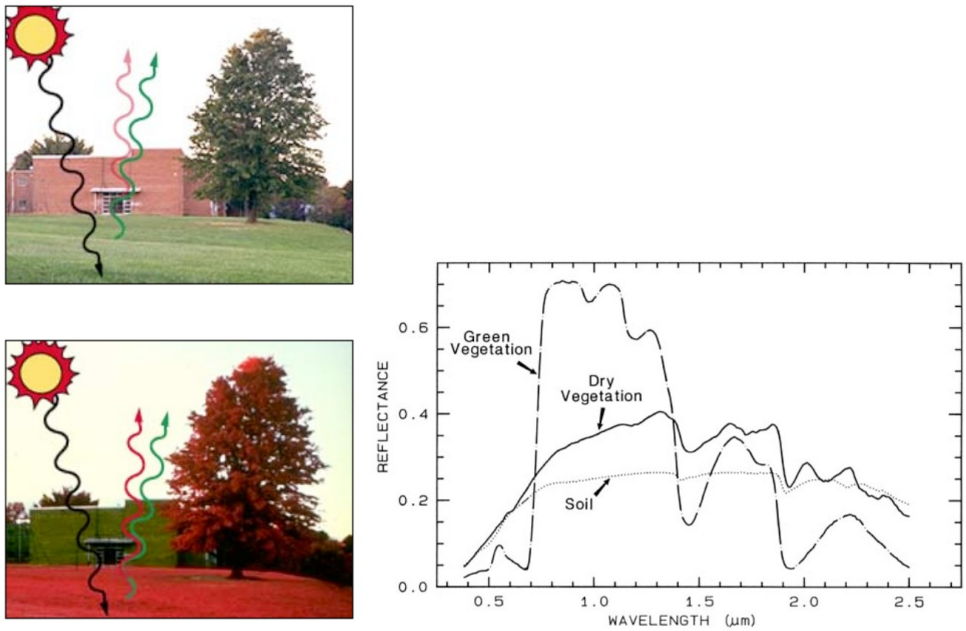

Figure 165: Left: IR photography of vegetationRight: Reflectance spectra of different vegetation types

We've already mentioned the importance of vegetation for remote sensing in section 9.1. Live plants are dark at visible wavelengths and bright at near IR; no other gas or mineral behaves exactly in this way, making this property extremely useful in practice.

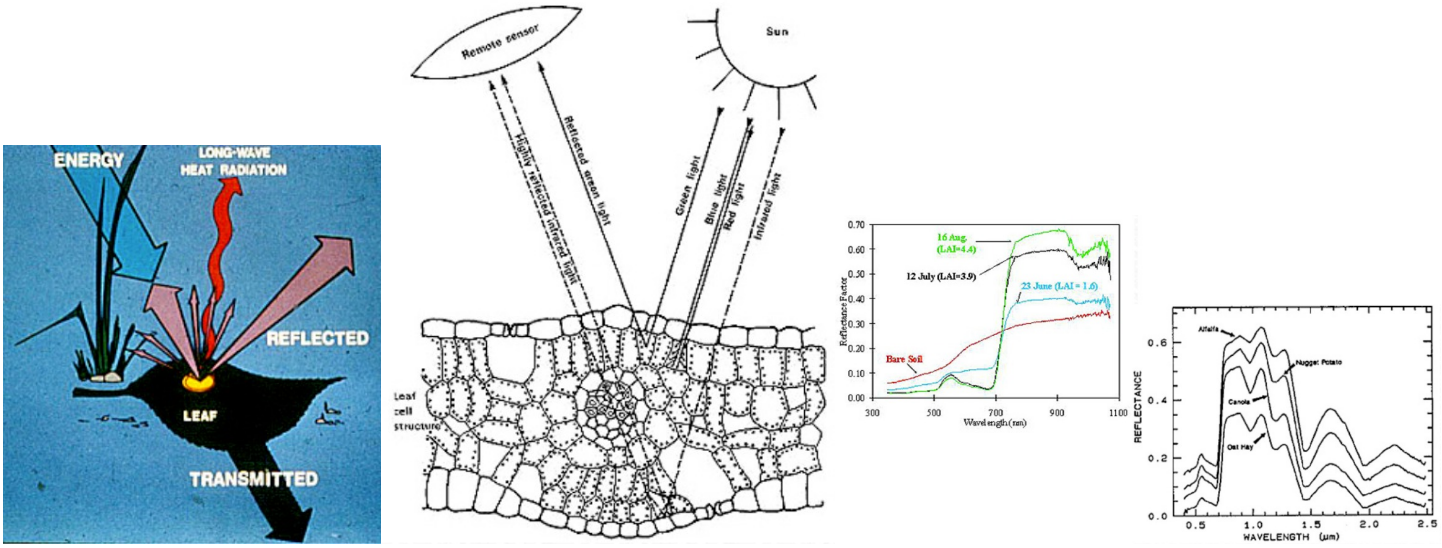

Figure 166: Left and middle: Radiation budget for a leaf.Right: Spectra of different vegetation types.

A useful quantity is the normalized difference vegetation index (NDVI): it is a simple numerical indicator used to assess whether the observed target contains vegetation or not, and is defined as:

$$\text{NDVI} \stackrel{\text{def}}{=} \frac{\text{NIR} - \text{RED}}{\text{NIR} + \text{RED}} \tag{318}$$

RED (typically 0.5-0.7) and NIR (typically 0.7-1.3) are the spectral reflectance measurements (ratio of reflected over incoming radiation in an individual spectral band) acquired respectively in the red and near IR regions, making NDVI range from (-1) to (+1). It works well because of the sharp transition between IR and near IR observed on the spectrum of live vegetation (cf right of figure 166). More subtle indicators exist, such as where plants are thriving and where they are under stress, and even what type of crop is growing.

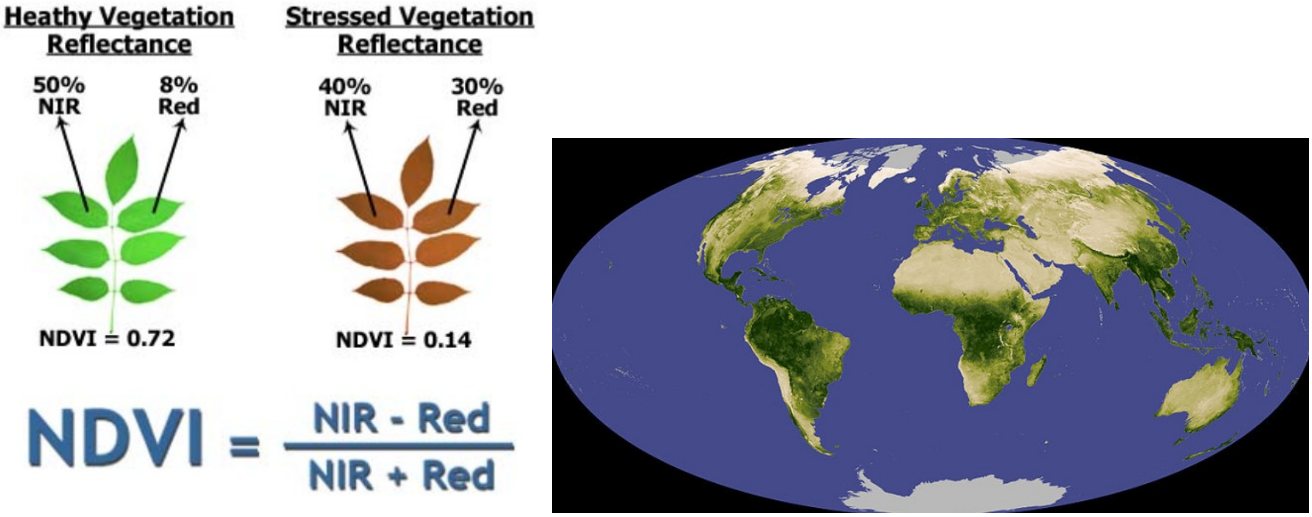

Figure 167: Left: Examples of NDVI for live (left) and decaying (right) vegetation.
Right: Earth Observatory: Measuring vegetation from space.

Little dips are due to water vapor; nothing is that reflective (except snow) on planet earth; if plant absorbed everything by photosynthesis would it overheat; whole field pas=sun act=radar to understand vegetation remote sensing.

12.3.3 Remote sensing by transmitted sunlight

We start by defining the "airmass factor" as the inverse of the solar zenith cosine $m \stackrel{\text{def}}{=} \cos^{-1}\theta$, which allows us to write the solution of the radiative transfer equation 9 without emission as:

$$I(\lambda) = I_{\text{sun}}(\lambda)\exp[-m\tau(\lambda)] = I_{\text{sun}}(\lambda)\exp[-m(\tau_{\text{aerosol}} + \tau_{\text{Rayleigh}} + \tau_{\text{O}_3} + \tau_{\text{NO}_2})(\lambda)] \tag{319}$$

where we have considered a specific example where the main absorbing gases are Ozone and Nitrogen dioxide. Equation 319 can be used to retrieve the Ozone concentration in the atmosphere, for example using two wavelengths windows centered at λ_1 and λ_2.

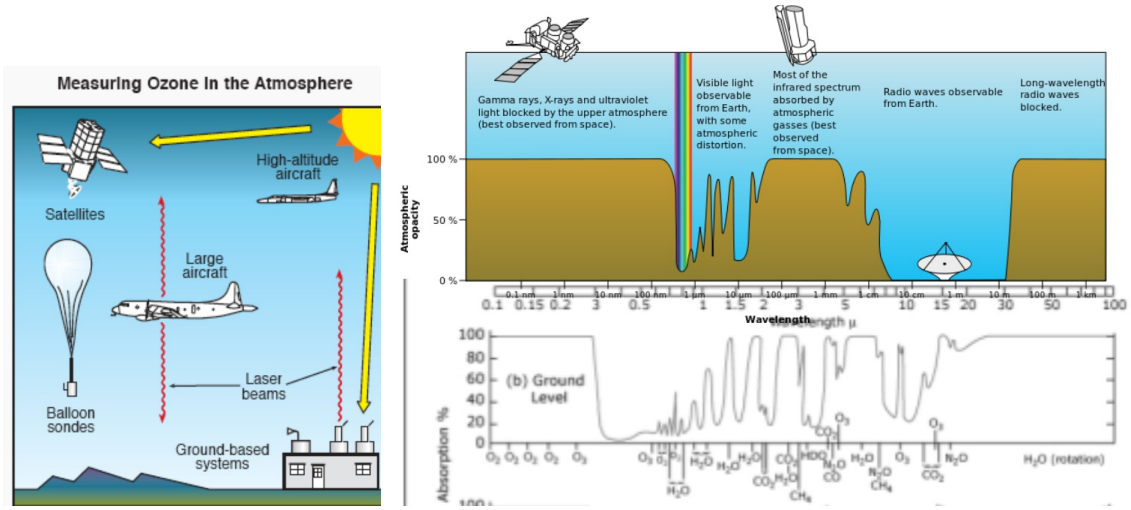

Figure 168: Left: Ozone measurements throughout the atmosphere with instruments on the ground and on board aircraft, high-altitude balloons and satellites.
Right: Measurements techniques rely on the UV absorption cutoff due to ozone.

If we assume the Ozone absorption coefficient $\sigma_{O_3}(\lambda)$ to be homogeneous along the ray's path, we can write $\tau_{O_3}(\lambda) \approx \Omega\sigma_{O_3}(\lambda)$, where Ω is the integral of the Ozone's concentration along the ray's path:

$$\Omega \stackrel{\text{def}}{=} \int_{(s)} \rho_{O_3} ds \tag{320}$$

Using this approximation and equation 319 in the two wavelength windows gives:

$$\Omega m \sigma_{O_3}(\lambda_i) \approx \ln[\frac{I(\lambda_1)}{I_{\text{sun}}(\lambda_1)}] - m(\tau_{\text{aerosol}} + \tau_{\text{Rayleigh}} + \tau_{NO_2})(\lambda_i) \text{ for i} \in \{1, 2\} \tag{321}$$

We need to choose two pairs of wavelengths so that the optical depth of aerosols can be subtracted out: the standard wavelength pairs for O_3 are $(1) \equiv (0.3055, 0.3254)\mu$m and $(2) \equiv (0.3176, 0.3398)\mu$m; at these wavelengths there is significant Rayleigh scattering, but as it makes the sky blue and not opaque, it can either be neglected (very rough approximation) or parametrized and included in τ_{Rayleigh}. Combining the two equations 321 leads to:

$$\Omega = \Delta_i^{-1} \sigma_{O_3} m^{-1} \underbrace{\ln[\frac{I(\lambda_1) I_{\text{sun}}(\lambda_2)}{I(\lambda_2) I_{\text{sun}}(\lambda_1)}]}_{N} - m(\Delta_i \tau_{\text{aerosol}} + \Delta_i \tau_{\text{Rayleigh}} + \Delta_i \tau_{NO_2}) \approx \frac{N^{(2)} - N^{(1)}}{(\sigma_{O_3}^{(2)} - \sigma_{O_3}^{(1)}) m(\theta)} - C^t p_s \tag{322}$$

where in our specific case $(\sigma_{O_3}^{(2)} - \sigma_{O_3}^{(1)}) \approx 1.388 \text{atm}^{-1}.\text{cm}^{-1}$ and $C^t \approx 0.009$. Usually, for Ozone, the Dobson unit (DU) is used: it is the vertical thickness of the atmosphere in thousands of cm that is occupied by the Ozone when it is concentrated into a uniform layer of pure gas at the standard temperature and pressure. The total column ozone concentration normally ranges from 200 to 500 DU.

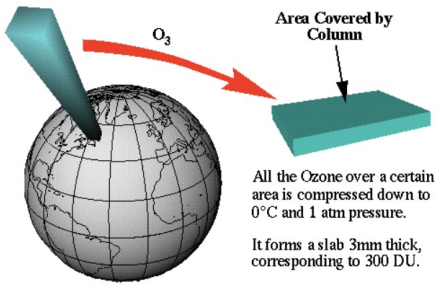

Figure 169: Schematic explaining the definition of the Dobson unit

We now try to retrieve the aerosol concentration. Its optical depth:

$$\tau_{\text{aerosol}}(\lambda) = m^{-1} \ln[\frac{I_{\text{sun}}(\lambda)}{I(\lambda)}] - \tau_{\text{Rayleigh}}(\lambda) - \tau_{O_3}(\lambda) - \tau_{NO_2}(\lambda) \tag{323}$$

can be determined if:

- The other optical depths are evaluated (either measured or parametrized).
- The position of the sun (and thus $m(\theta)$) is known.
- A measurement of the direct solar intensity is taken.

$\tau_{\text{aersol}}(\lambda)$ in equation 323 is referred to as the turbidity (the "haziness" of a fluid or air), which is a measurement of atmospheric aerosols, both natural and man-made. We remember the expression of the bidirectional reflectance in the case of direct solar scattering 229, which can be determined from satellite measurements. We also remember that from Mie theory (cf section 9.2.3), one can input the complex index of refraction and the particle size distribution, which are necessary to calculate the scattering efficiency (and cross-section), the extinction efficiency (and cross-section), and the phase function, all as a functions of wavelength vs particle size. Not only do aerosol scatter radiation, but they also form clouds, which cover more than half of the Earth's surface. Despite the complexity of aerosol's scattering, three general principles hold:

1. At visible wavelengths, scattering is primarily a function of optical depth.
2. In the near IR, scattering largely depends on the particle's size.
3. Polarization measurements helps separate the effect of the size distribution, the refraction index, the particles phase and shapes, and the cloud optical depth.

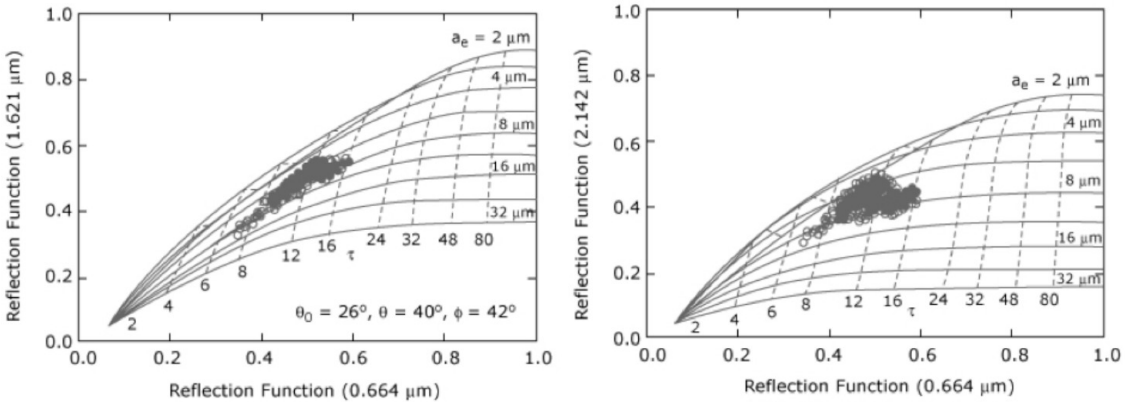

Figure 170: Left: Theoretical relationship between the reflectance at 0.664μm and 1.621μm for various values of the optical depth at 0.664μm and effective droplet radii.
Right: Same figure for the reflectance at 0.664μm and 2.142μm.

To retrieve the aerosol size distribution, we recognize that the turbidity depends on the cross-section which itself depends on the particle's size:

$$\tau_{\text{aerosol}}(\lambda) = \int_{(\text{Path length})} \int_{a_1}^{a_2} n(a,z)\sigma(a,\lambda) da ds \tag{324}$$

where $n(a,z)$ is the distribution of the aerosol radii a that we are trying to retrieve and $\sigma(a,\lambda)$ is their cross-sections. A typical distribution for the aerosols is the Junge size distribution:

$$n_{\text{Junge}}(a,z) \overset{\text{def}}{=} C(a,z) \cdot a^{-(\nu^*+1)} \tag{325}$$

where C is a scaling factor proportional to the aerosol concentration and ν^* represents a shaping constant, usually between 2 and 4. In general, we separate the column aerosol size distribution in a slow varying function $f(a)$ and a rapidly function $h(a)$:

$$n_{\text{column}}(a) \overset{\text{def}}{=} \int_0^{\text{TOA}} n(a,z)dz = f(a)h(a) \tag{326}$$

For instance, for a Junge-profile, $f(a) = \int_0^{\text{TOA}} C(a,z)dz$ and $h(a) = a^{-(\nu^*+1)}$. Combining equations 324 and 326, we obtain:

$$\tau_{\text{aerosol}}(\lambda) = \int_{a_1}^{a_2} f(a)h(a)\sigma(a,\lambda)da = \int_{a_1}^{a_2} f(a)h(a)\pi a^2 Q_e(m, \frac{a}{\lambda})da \tag{327}$$

where we have introduced the extinction efficiency Q_e from Mie's theory. Note that equation 327 is a Fredholm equation of type 308 and can be solved by using classical mathematical methods.

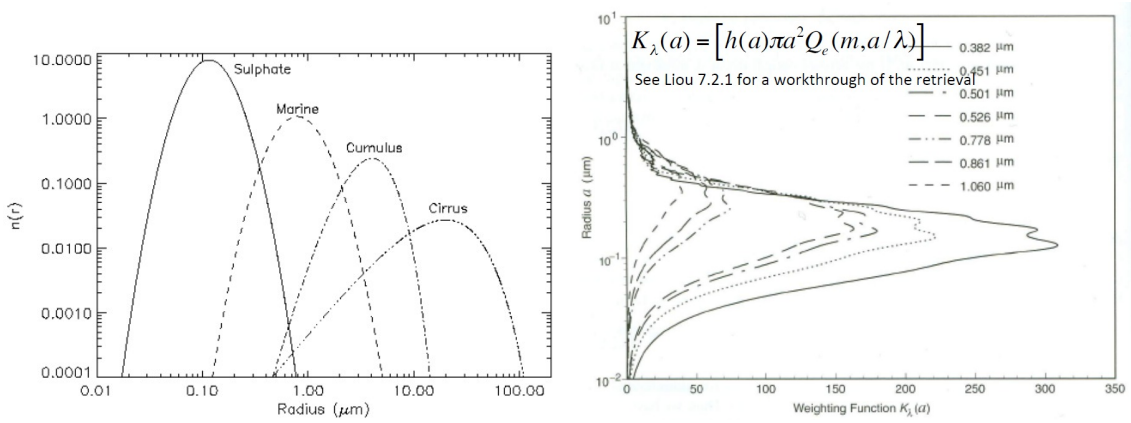

Figure 171: Left: Aerosol model size distributions for the four aerosol types discussed.
Right: Weighting function as a function of aerosol radius for seven sun photometer wavelengths, using the Junge distribution.

In conclusion, there are many different retrieval techniques, all relying on the radiative transfer equation. They often involve complex numerical approaches as there is no exact direct linear inversion.

13 Cloud microphysics

13.1 Climatic importance of clouds

Coming back to the radiative balance of the planet, the left of figure 172 shows the radiative forcing of different agent categories on the climate. Note that anthropogenically produced particles can produce a positive forcing (like greenhouse gases) as well as a negative forcing (scattering agents, cf net effects of aerosols and clouds).

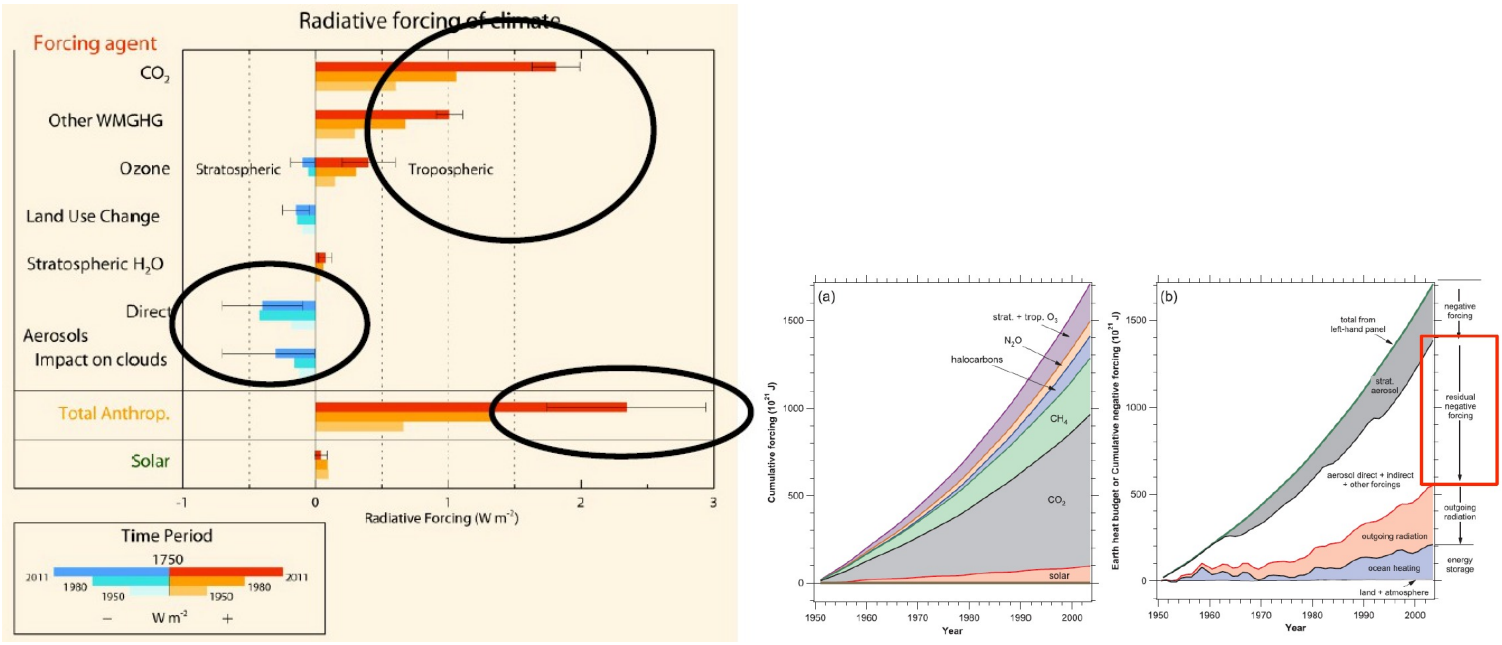

Figure 172: Left: Global average radiative forcing estimates and ranges for various drivers and three successive time periods (1750-1950; 1750-1980; 1750-2011)
Right: Cumulative energy budget for the Earth since 1950 (a) Mostly positive and mostly long-lived forcing agents from 1950 through 2004 (b) The positive forcings have been balanced by stratospheric aerosols, direct and indirect forcing, increased outgoing radiation from a warming Earth and the amount remaining to heat the Earth.

In the balanced large-scale circulation, a large part of the cloud formation can be explained by dynamical effects, but microphysical considerations are key when it comes to link the anthropogenic forcing, the cloud cover, and the radiative forcing. On the right of figure 172, we can see how much extra terrestrial energy there is in the atmosphere because of the extra anthropogenically introduced greenhouse gases. The direct and indirect effects of aerosols can help explain that a big part of this energy has been lost to space, and corresponds to a negative forcing of roughly $1 W.m^{-2}$.

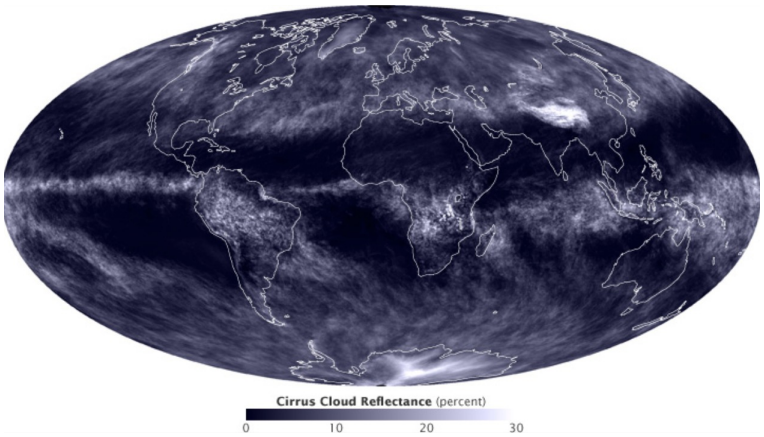

Figure 173: Cirrus cloud reflectance

Figure 173 shows the amount of radiation reflected back by cirrus clouds. Cirrus clouds have a very important role because of their high position: they are the first ones to reflect the SW back to space and the last one to reflect the LW terrestrial radiation; they cover one third to one half of the Earth's surface. Their coverage is very sensitive to forcing, as we can see by the important effects of ships (ship tracks can be seen in the cirrus's reflection map we considerably zoom in). As we have seen in section 8.2.3, condensation is not automatic when the relative humidity hits 100%: it strongly relies on the atmospheric aerosols concentration. The homogeneous nucleation process has a strong energy barrier and requires a relative humidity of 400%, which is never observed in practice. Even homogeneous ice nucleation, which only requires 160% relative humidity, only very rarely happens.

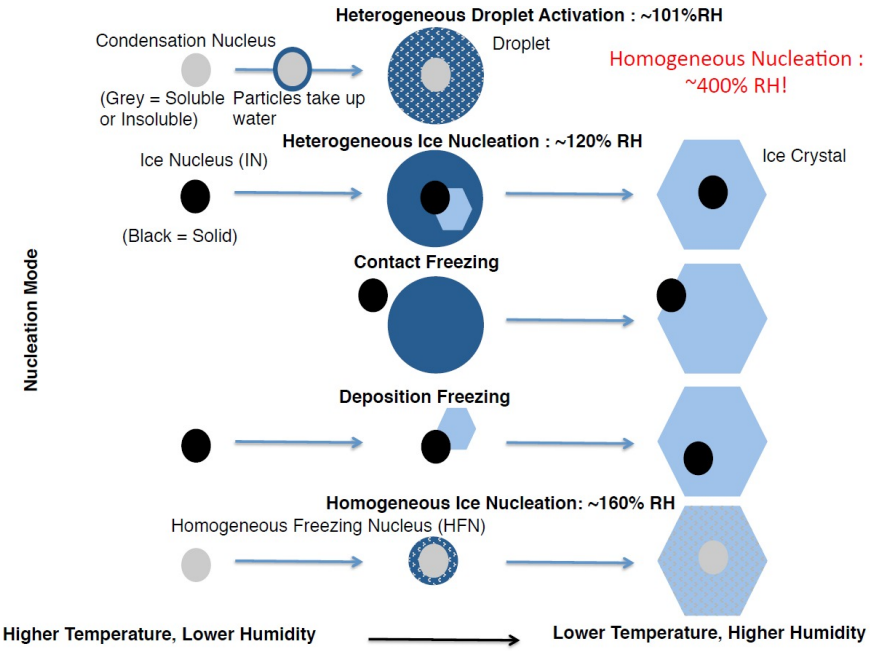

Figure 174: Different nucleation modes

Ice nucleation is thus mostly heterogeneous as long as the atmosphere contains ice freezing nuclei (cf figure 174). As there are many different ways of heterogeneously condensing water vapor, it is very important to understand the corresponding relative humidity and temperature conditions to know which "mode" of condensation happens in a given atmosphere.

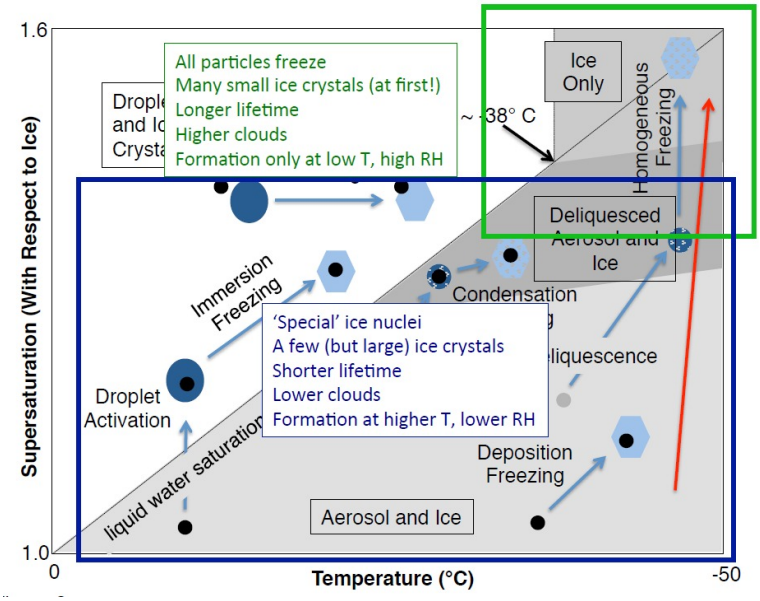

Figure 175: Different "modes" of condensation

Because of the specific conditions for heterogeneous condensation, the local aerosol concentration can strongly affect the cloud coverage and thus the direct radiative forcing, as we can see on the left figure 176.

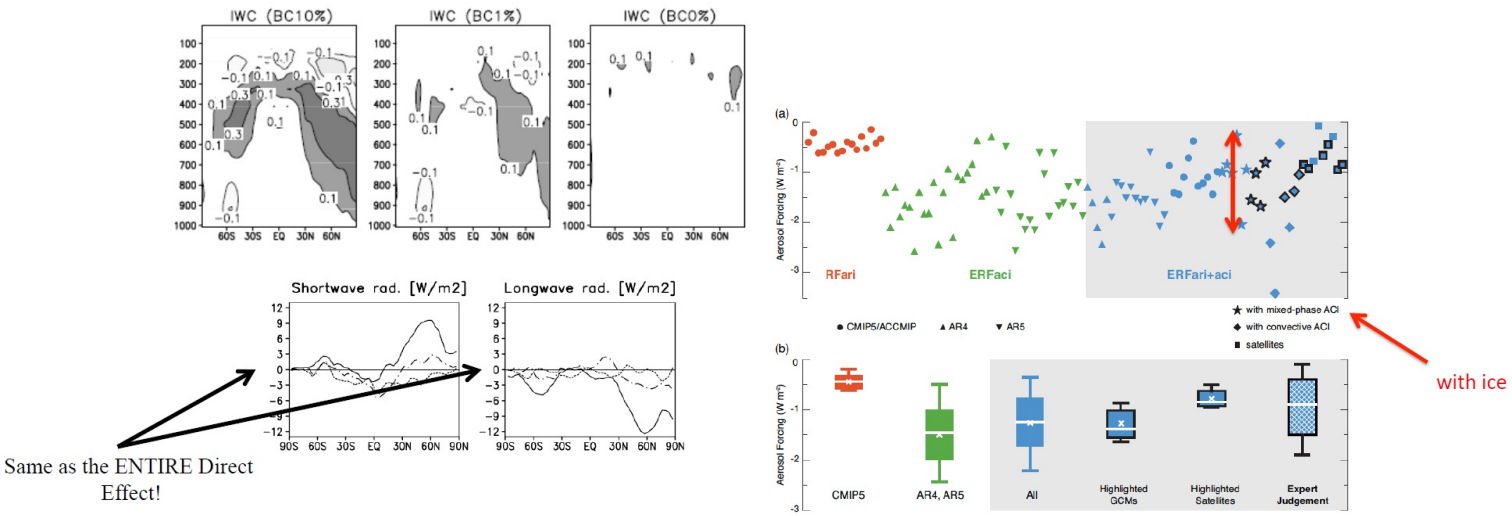

Figure 176: Left: Effect of the concentration of black carbon on the cloud covering and thus on the SW and LW radiative forcing.
Right: Discrepancies between the different aerosol forcings in General Circulation Models.

On the right of figure 176, we can see that even within the "good" microphysical schemes that include ice-condensation and convection, there are very large relative uncertainties on the aerosol forcing (typically of order 100%) in current climate models.

13.2 How to find a cloud

Flying through a cloud is the easiest way to observe it. However, many of the particles contained in the cloud are not good condensation nuclei. To separate the condensation nuclei from the other particles, we rely on the fact that the condensation nuclei have a water phase in formation which typically makes them a million times heavier.

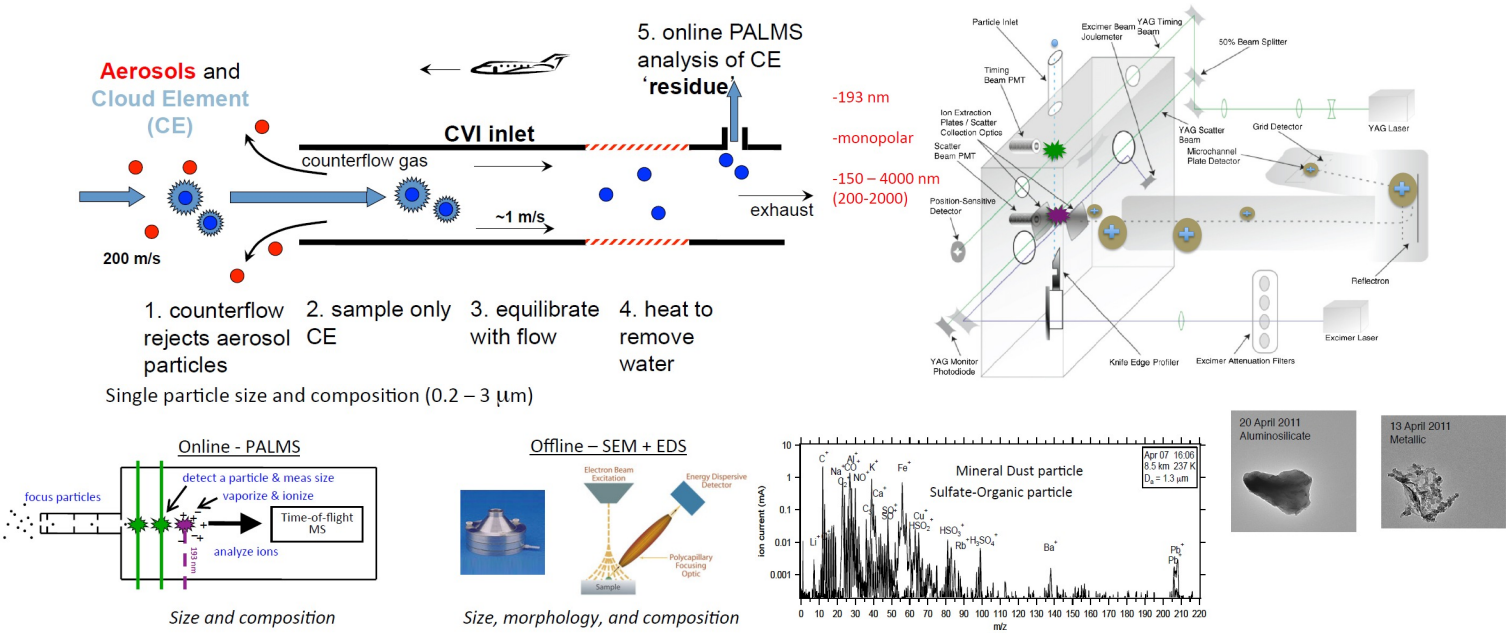

Figure 177: Top left: Counter-flow Virtual Impactor (CVI) used to physically obtain the condensation nuclei.
Top right: Mass spectrometer, used to analyze the chemical composition of the collected particles.
Bottom: Steps to analyse the size, morphology and composition of the condensation nuclei.

The left of figure 177 gives the details of the process, relying on a strong counter-flow ejecting the lighter particles, which have less inertia than the condensation nuclei. For modeling purposes, it is impossible to follow every condensation nuclei and its radiative effect (there is typically a million of particles per cm^3 of air), and the aerosol are classified into a few categories which are each attributed a given radiative forcing.

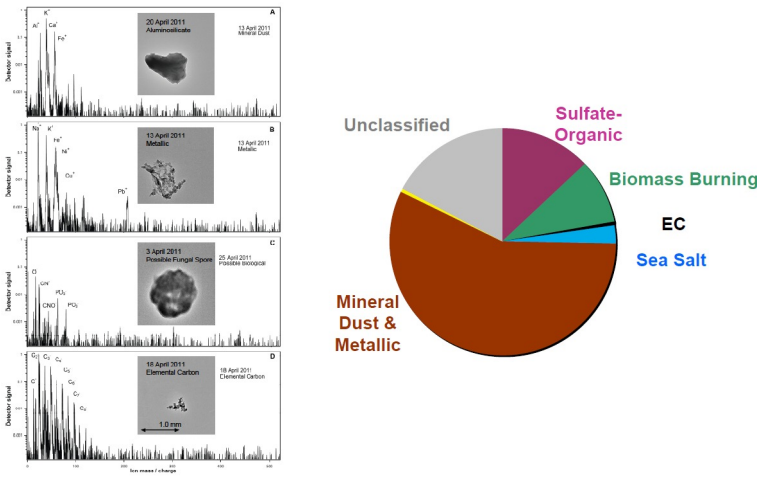

Figure 178: Categories of aerosol particles for modeling purposes

13.3 How to make a cloud

The problem with observing clouds is that you can only fly a cloud once you see it, which means that you will always miss the initial conditions of its formation (and be biased towards relative humidity already very close to saturation values etc). Consequently, laboratory experiments that allow you to form clouds play a central role in microphysical research.

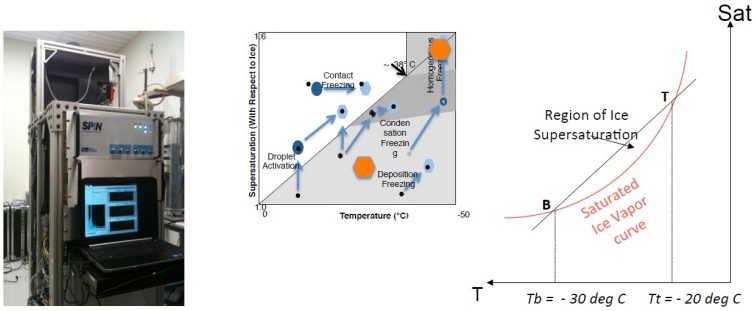

Spectrometer for Ice Nuclei (SPIN)
Commercially available from DMT, Boulder, CO
Based on Zurich Ice Nucleation Chamber (Stetzer & Lohmann)

Relationship between the saturation vapor pressure over ice and temperature.

Figure 179: Spectrometer for ice nuclei (left), condensation in supersaturation vs temperature space (middle) and relationship between the saturation vapor pressure over ice and temperature (right)

We remember from 74that the non-linearity of Clausius-Clapeyron relation allows condensation by mixing of two air samples. In a spectrometer for ice nuclei such as on figure 179, by establishing a constant temperature gradients between two points, it is possible to test different domain and "modes of condensation". An interesting finding is that during the first phase of heterogeneous condensation, metallic particles play an important role as well as mineral dust, which are both strongly influenced by human activities. Indeed, even if mineral dust is a natural aerosol, human activities such as land usage (overgrazing). Using these particles in the laboratory (figure 180) allows to exactly determine the relative humidity and temperature conditions for this heterogeneous nucleation to happen.

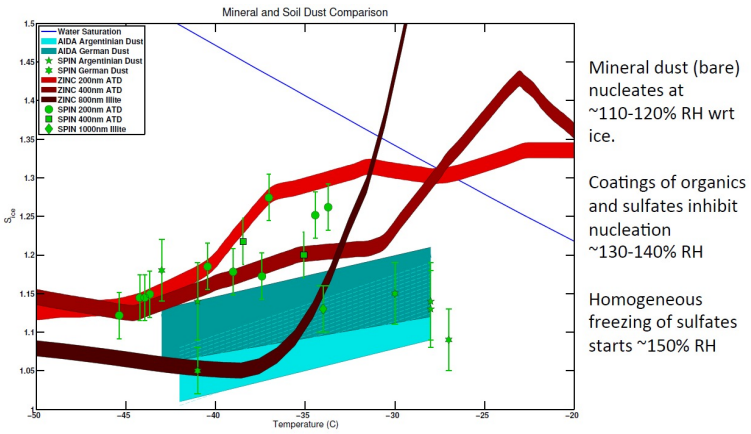

Figure 180: Nucleation condition determination

13.4 Conclusion

- Field studies are so important, because they are the only way to know what really " makes" clouds in the atmosphere. For instance, it is not because a material is a good ice nuclei that it is what happens in the atmosphere.
- Lab studies are really important, because it is important to understand the context of what is being observed, such as the activation relative humidity as a function of temperature and/or size, or the influence of minor chemical components on microphysics.

To conclude, we show the example of lead forcing on the ice nucleation on figure 181.

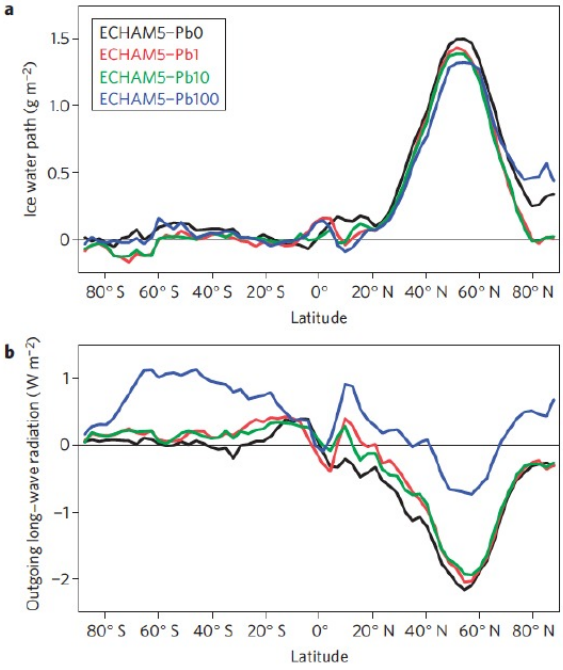

Figure 181: Atmospheric properties with and without the influence of anthropogenic lead. (a) Ice water path and (b) outgoing LW radiation difference between the present day and the per-industrial time

Lead was unintentionally introduced in the 1970s (more than 99.5% of the atmospheric lead at that time was anthropogenically introduced), and is believed to have been responsible to as much as 80% of the ice clouds formation at that time. It is possible that because of this strong anthropogenically induced negative forcing (1 $W.m^{-2}$), the greenhouse gas effect was less noticeable at that time.